eman ta zabal zazu

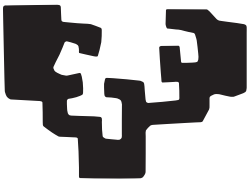

Universidad del País Vasco
Euskal Herriko Unibertsitatea

SUPERCONDUCTING PHENOMENA AT THE NANOSCALE

DOCTORAL THESIS by:

JON ORTUZAR ANDRES

Thesis supervisors:

José Ignacio Pascual Chico

&

F. Sebastian Bergeret Sbarbaro

December 2024

This thesis was carried out at CIC nanoGUNE BRTA

Abstract

Superconductors exhibit macroscopic quantum ordering that allows their unique properties to emerge even at mesoscopic scales, enabling practical applications in electronics and quantum computing. This distinctive behavior makes superconductivity one of the most studied topics in condensed matter physics, valued for both its theoretical elegance and broad physical relevance. In this thesis, we investigate superconductivity at the nanoscale using Scanning Tunneling Microscopy and Ultra-High-Vacuum (UHV) synthesis. By combining superconductors with atomic magnetism, normal metals, and confinement near the pairing limit, we examine these systems' unique nanoscale behaviors both experimentally and theoretically.

The exchange interaction between magnetic adatoms and electrons in a superconductor induces Yu-Shiba-Rusinov (YSR) subgap states. Here, we develop a theory based on a classical spin approximation to describe these states and demonstrate that the shape of the superconductor's Fermi contour significantly influences their spatial extension and their interactions in multi-impurity structures. Scattering wavevector nesting focuses the decay of these states in the directions perpendicular to the flat regions of the Fermi contour, maximizing their extension in these orientations and rendering direction-dependent impurity interactions. Our theoretical predictions are compared with experimental measurements of single V adatoms and Mn structures on the multiband β-Bi_2Pdsuperconducting surface. Additionally, we analyze the quasiparticle interference patterns around V adatoms to extract insights into the complex formation of the condensate in this multiband superconductor.

Once the exchange coupling exceeds a critical threshold, the positive and negative YSR states cross at zero energy and invert, marking the onset of a parity-changing quantum phase transition. The classical spin approximation does not account for this parity change nor the formation of a singlet state between the impurity and itinerant electrons (Kondo singlet), thus overlooking any parity or spin effects observable by Scanning Tunneling Spectroscopy (STS). To address this, we develop a single-site Hamiltonian that models the effects of a magnetic impurity on a thin metallic layer proximitized by a superconductor. This model is applied to explain STS measurements performed on magnetic molecules on the proximitized Au(100)/V surface. Furthermore, we describe a novel singlet-based spin qubit formed by two interacting magnetic impurities, immune to decoherence from spin-orbit and hyperfine coupling, demonstrating its potential for advanced quantum applications.

As the size of a superconductor shrinks, the separation between electronic energy levels widens, lowering superconducting pairing until it vanishes at a critical size known as the Anderson limit. Conversely, the Coulomb energy, the onset energy of single-particle tunneling into a small metal, increases as size decreases. By growing Pb islands on graphene under UHV conditions, we create an ideal platform to study superconductivity and Coulomb blockade phenomena in nanoscale metallic grains. Fitting STS

data with effective theory, we disentangle the combined effect of superconductivity and Coulomb blockade in the measured spectral gap, revealing their evolution with grain size. Moreover, we demostrate that the paricle-hole (ph) symmetry of the system can be controlled with bias pulses applied with the tip, which acts as an effective gate potential.

The zero-bias peak measured in low-resistance ($R < 100$ kΩ) tunneling junctions between bulk superconductors—typically related to incoherent Cooper pair tunneling—appears split in Pb islands. The magnitude of this splitting follows a trend similar to Coulomb energy as island size decreases, and the relative positions of the positive and negative peaks can be adjusted with bias pulsing. Using a current-biased setup, we measure the I-V characteristics and observe non-reciprocal behavior when particle-hole symmetry is broken, resembling diode functionality. We verify this by measuring AC rectification and microwave photon detection.

Acknowledgments

Tesi honen lehen horrixetan esaten dodan bezala, ez da sekula bakarka egindako lanik egon. Edozein ikerketa lehenago egindako lanetan oinarritzen da, zientzia zentzudun eta koherente bat egiteko era bakarra baita hau. Honez gain, ikerketa alde batera itzita, ikerlaria bera begiratzien, edozein zientzialarik ondoan dituen pertsonak aztertu biherko genituzke honek eukindako edozein inspirazio ulertu ahal izateko.

Edonoren pentsamoldea bere inguruagatik bideratuta dago, uste dogunean baino neurri handiagoan. Horregatik uste dot izaera eta pentsatzeko era desberdineko jendez inguratu biher garela, ez bakarrik hobekuntza pertsonalerako, baina profesionalerako ere. Kalitate hobeko zientzia egiten da ingurune mistoetan, lehiaketan baino elkarlanien.

Tesia hau eta ni neu ezin izango ginen garatu betidanik ondoan izan dodan jendea eta azken urte honetan ziher esagututako jendiegaitzik ez bazan izengo. Eskerrik asko Ama eta Asi, zeuokin sortutako bizigiroagatik naz pertsona hau. Beti babestute sentitzen nazen leku bat sortu dozue. Mila esker Laiene azken urte eta erdixegatik, itzela izen da, ez neban ezer aldatuko, prozesu hau piloa erreztu dozu. Pello, Katerina eta Marita, eskerrik asko pisuen lana erraz ahaztuteko moduko bizigiro bat sortziarren. Stefano, zeu hasi zinen lan zelan ein irakasten eta batera bukatu dogu ikasten, zeu barik tesi hau ezinezkoa izengo zan. Nacho eta Sebas, mila esker nire bizi profesionala bideratzen laguntzearren eta eztabaida luzeak jasatearren.

Beste pertsona asko ditut buruen eskertzeko, eta danon izena idatzi biher badot norbaitena ahaztuko dot, beraz taldeka. Eskerrik asko Kuadrilari, gernikeko laguneri, izandako taldekide guztixeri, Lup eta lehenago Monday Lupeko bandakideei eta baita lezako neure lagunei.

Let me use this last paragraph to describe the specific scientific work my several collaborators did in this thesis. Most of the measurements presented in this thesis have been taken by Stefano and me. We are a team and have been working together since before I started my thesis. The experiments presented in Sec 3.4 were done by Javi Zaldivar and are extended in his PhD thesis [1]. The experiments on FeTPP-Cl molecules presented in Sec. 4.3 were mainly done by Katerina Vaxevani [2] and Stefano Trivini [3, 4]. Section 4.4 is a collaboration with Miguel A. Cazalilla and ChenHow Huang, who did the NRG calculations of the system. The theory of Sec. 6.3 was done in partnership with Lu Yao. Thanks to all of them for their help in my professional development.

Contents

List of symbols and abbreviations

The following list is a compilation of all acronyms and terminology used in the thesis. the most common cases (e.g. the abreviation of the elements) are not listed. For the hole work, we take $\hbar = 1$.

- The $\hat{}$ symbol is used for operators.
- The $\check{}$ symbol is used for matrices.
- H: 'Hamiltonian'
- S: 'Spin'
- E and ω are energy or frequency. Equivalent due to $\hbar = 1$.
- Δ: 'Superconducting gap'
- ϕ: 'Superconducting phase'
- T_C: 'Superconducting critical temperature'
- B_C: 'Superconducting critical magnetic field'
- $\beta = (k_B T)^{-1}$
- $p_F = k_F$: 'Fermi momentum'
- $E_C = e^2/2C$: 'Coulomb energy'
- Q, q: 'Charge'
- q_0: 'Excess charge'
- $\mathcal{Z}$: 'Partition function'
- $\hat{c}^\dagger$ ($\hat{c}$): 'Momentum electron creation (annihilation) operator'
- $\hat{\psi}^\dagger$ ($\hat{\psi}$): 'Real space electron creation (annihilation) operator'
- $\hat{\gamma}^\dagger$ ($\hat{\gamma}$): 'Bogoliubovnic creation (annihilation) operator'
- τ_i, σ_i and η_i: 'Nambu, spin and band Pauli matrices'
- τ: 'Imaginary time'
- J: 'Exchange coupling'
- G: 'Green's functions'
- ρ: 'Density of states'
- C: 'Capacitance'
- R: 'Resistance'
- V: 'Voltage'
- I: 'Current'
- BCS: 'Bardeen-Cooper-Shrieffer'
- STM: 'Scanning Tunneling Microscope'
- STS: 'Scanning Tunneling Spectroscopy'
- JT-STM: 'Joule Thomson-STM'
- UHV: 'Ultra-High Vacuum'
- FC: 'Fermi Contour'
- YSR: 'Yu-Shiba-Rusinov
- GF: 'Green's Function'
- QPI: 'Quasiparticle interference'
- SOC(I): 'Spin-Orbit Coupling (Interaction)'
- HI: 'Hyperfine Interaction'

- QP: 'Quasiparticle'
- AFM: 'Antiferromagnetic'
- FM: 'Ferromagnetic'
- dGSJ: 'de Gennes Saint James'
- AR: 'Andreev Reflection'
- CPE: 'Cooper Pair Excitation'
- QPT: 'Quantum Phase Transitions'
- CB: 'Coulomb Blockade'
- (L)DoS: '(Local) Density of States'
- SET: 'Single Electron Trnasistor'
- DBTJ: 'Double Tunneling Junction'
- Gr: 'Graphene'
- a.u.: 'arbitrary units'
- CPD:'Cooper Pair Diode'

1 Introduction

The developments of the Scanning Tunneling Microscope (STM) [5] opened the door to the study of many fundamental aspects of matter at the nanoscale, becoming one of the pillars of surface science with ramifications to biology, chemistry, material science, condensed matter physics and more. The STM is based on the tunneling effect between metals achieved by approaching a sharp, single-atom-ended, metallic tip to a conducting substrate. The exponential dependence of the tunneling current enables the atomic precision of its measurements; moreover, the dependence of the current on the local density of states [6] facilitates access to the electronic properties of the substrate.

The STM has significantly impacted the progress of the research on superconductivity. The superconducting gap Δ, first hypothesized by F. London [7] and formally introduced by Bardeen, Cooper and Schrieffer [8], was first measured in a tunneling experiment [9, 10] proving that an energy separation between the ground state of the superconductor and its single-particle excitations exits [8, 11]. The Bardeen-Cooper-Schrieffer (BCS) theory of superconductivity [8] describes this state of matter as a condensate of Cooper pairs [12]: a state of paired electrons formed due to an attractive interaction between each other originated from the electron-phonon interaction [13, 14]. The Cooper pairs generate an even parity ground state with a macroscopic coherence length that repeals any external magnetic field [15] up to a critical value, with a penetration length given by the London equations [16]. This condensate prevents single electron tunneling into a superconductor with an energy $E < \Delta$. The tunneling spectroscopy shows two sharp peaks, the coherence peaks, at the onset of energy of single-particle excitations.

A magnetic impurity exchange coupled to a superconductor acts as a local magnetic field, distorting the superconducting order in its vicinity and lowering the minimum energy required for single-particle excitations. This system was first described through the Anderson impurity model [17] and later resolved under a classical spin approximation [18–20] using a Kondo Hamiltonian framework [21]. Both approaches are shown to be equivalent [22] and predict a renormalization of the spectral weight from the superconducting coherence peaks into two subgap peaks, now known as Yu-Shiba-Rusinov (YSR) states [18, 19, 23].

Although the first STM measurement of YSR states was performed in 1997 [24], the research around it in the last decade has thrived due to several proposals utilizing these states as the building block for topological quantum computing, based on Majorana bound states [25, 26]. The capability of the STM to control the position of magnetic adatoms with atomic scale opens the door to forming chains of magnetic impurities on superconductors. These YSR bands have been proposed as a platform that can host topological edge states [27, 28].

The study of YSR states also reveals fundamental aspects of atomic scale mag-

netism. Close to the adatoms, STM experiments reveal information about the shape and hybridization of the d-shell orbitals of the impurities with the substrate [29]. Moreover, due to the long-range superconducting correlations, YSR states extend several nanometers away from the impurity. The nature of this spatial distribution is closely related to the superconductor's Fermi Contour (FC). In Chapter 3, we develop an effective theory to compute the Green's Function (GF) of a bare 2D superconductor with an arbitrary Fermi contour (FC), applying this framework to analyze the effects of multiple impurities on the superconducting state. This approach is then used to compare theoretical predictions with STM measurements obtained from Mn and V adatoms on the β-Bi_2Pdsuperconducting surface.

β-$Bi_2Pd$is a 2D multiband superconductor with anisotropic square-shaped FCs [30, 31]. Vanadium impurities on this surface host YSR states with a long-range extension due to Fermi surface nesting [32, 33]. By calculating the Green's function for a square-shaped FC, we observe that the YSR state decay resembles that of a 1D superconductor. The FC's anisotropy and extended decay modify impurity coupling in diluted atomic structures [34], which we experimentally probe by assembling Mn adatom structures with atomic precision using the STM tip [1, 4]. Additionally, analyzing the quasiparticle interference pattern around V adatoms allows us to reconstruct the FC shape [1] and gain insights into the multiband BCS ground state of β-Bi_2Pd.

The classical spin approximation properly describes both V and Mn impurities on β-Bi_2Pd. Still, when more complex spin dynamics, such as magnetic anisotropy and spin-flip tunneling, are combined with a high spin impurity, a quantum approach is needed. Motivated by results on magnetic impurities on proximitized surfaces [2, 3, 35], in Chapter 4, we develop a single-site model [36] that captures the entangled impurity and electron spin nature of YSR states. The model facilitates a phenomenological understanding of all possible single-particle excitations of impurities on ballistic proximitized metals without any numerically costly approaches, such as numerical renormalization group [37, 38] or continuous time Montecarlo [39].

We check the validity of the approximation within the Poor Man's scaling method [40] and apply the single-site model to disentangle the complex excitation spectrum of a FeTPP-Cl molecule on top of the Au(100)/V proximitized surface [2]. We modify the exchange coupling by approaching the STM tip to the molecule [41] and drive the system through a parity-changing quantum phase transition [23, 42], shifting to an odd-parity ground state. This transition enables two-particle (Cooper pair) excitations [8], typically accessed only via microwaves in bulk superconductors [43]. Additionally, we use the model to propose a singlet-based spin qubit architecture formed by two interacting magnetic impurities, avoiding decoherence from spin-orbit and hyperfine interactions [44].

This thesis is divided into two main topics, both regarding superconductivity. In Chapters 3 and 4, we focus on the effects of magnetic impurities on superconductors. In contrast, in Chapters 5 and 6, we measure and analyze the effects of the size of superconductors in their properties.

When the size of a metal is reduced below an electron's screening length (around 100 nm), and a charge is added to it, the other electrons do not have enough space to screen the charge. This generates Coulomb repulsion between charges, and the single-

particle excitation onset increases by an energy E_C, known as the Coulomb energy [45]. In such small metallic grains, the charge tunnels sequentially [46], making this system a very sensitive electrometer. When the grain is embedded in a three-terminal device (source, drain, and gate), the system is known as a single electron transistor [46]. The gate can control the excess charge of the island, which is e-periodic and follows a shape known as Coulomb diamonds [45].

If the grain is a superconductor, the system is split into even and odd parity states, and the periodicity of excess charge changes to 2e [47, 48]. Moreover, contrary to bulk superconductors, having an odd parity ground state is possible when the Coulomb interactions prevail over the superconducting pairing $E_C > \Delta$. In Chapter 5, we perform spectroscopic measurements on small Pb islands suspended on graphene [4, 49] and observe a spectral gap larger than that of bulk Pb, attributed to Coulomb interactions in the grain. By applying a magnetic field up to 2.5 T, superconductivity is suppressed, and we can separate the contributions of E_C and Δ to the gap. Additionally, size-dependent measurements reveal that the pairing energy decreases with reduced island size due to increasing electronic level spacing [50], while the Coulomb energy increases, following an inverse trend.

The islands' excess charge can be controlled by applying bias pulses with the STM tip, resembling a three-terminal device. This control breaks particle-hole symmetry, which appears as an asymmetry in the spectral gap in the dI/dV measurements. In Chapter 6, we further investigate this system by moving the STM tip closer to the islands, turning on current terms that are second order in tunneling transmittance, e.g., the tunneling of Cooper pairs. We find that the zero bias Josephson peak, expected in a low resistance ($R < 100$ kΩ) tunneling junctions between bulk superconductors [45, 51], is split onto two finite voltage peaks. They arise from a resonant transport of Cooper pairs [52, 53] mediated by the interaction with the environmental modes [45, 54].

The separation between peaks in the spectrum scales with the island's size and remains unaffected when the excess charge of the island is changed. However, the relative positive and negative positions of these peaks shift with excess charge, generating a non-reciprocal response to an applied voltage. To further explore this effect, we switch to a current-biased setup [55] and discover that the break in particle-hole and inversion symmetry induces a diode effect [56], with polarity controlled via bias pulses. We demonstrate the system's applicability as a rectifier and photodetector.

2

Theoretical and experimental methods

Finite memory comes with several drawbacks, not only for everyday things, but it also shapes some societies' beliefs and behaviors. One mistake we make as a society is to remember only a few of the authors of a lengthy investigation; this simplification can misrepresent the collaborative nature of scientific progress. It is expected to pinpoint a few breakthroughs done by one or two people in a long line full of investigators and forget many collaborators. We glorify these few names and slowly forget the rest, but science has never been a single-handed job, and no one has ever started from scratch [1]. This does not mean that the people we remember did not make said breakthroughs in their investigation; it just means that we are inclined to forget the predecessors. Even Newton, regarded as the father of calculus, modern physics, and even modern science, had people like Kepler, Galileo, and sometimes the forgotten Avicenna and Alhazen [2] before him. This section will be a historical introduction and a state-of-the-art for the main topic of the thesis: Superconductivity.

It is always challenging to find the starting point of any scientific discovery. One could always go back in time and find previous knowledge needed to give some steps the researchers needed. Following these steps, one would have to start with Aristotle to explain what a smartphone is, and as the thesis should be finite and focus on superconductivity, I will start from Heike Kamerlingh Onnes. Onnes, working at Leiden's University [3], was the first person to achieve the liquefaction of Helium at 4.5K. He managed to do so by using the Joule-Thomson effect, which we still use to lower the temperature of our instruments to 1.3K. Once he had liquefied Helium, trying to disprove the prevailing theories about electrical conductivity at low temperatures [4], he checked the electrical conductivity of Hg, Li, and Pb to find out that Hg and Pb had zero resistivity below a threshold temperature.

While Heike Kamerlingh Onnes initially theorized a quantum explanation for superconductivity (inspired by Planck's quantum theory), early superconductors were still broadly classified as "perfect" conductors within the classical theory. During World War I, research in the Netherlands paused due to the halt of cryogenics, even though the country was neutral. After the war, research resumed, and by 1924, nine superconducting elements had been identified. Early measurements of Uranium Lead also hinted at the isotope effect (later crucial to the microscopic theory) and measured critical magnetic fields that disrupt superconductivity, with much of this foundational work carried out at Leiden University.

It was not until 1933 that Walther Meissner and Robert Ochsenfeld's research proved that superconductors were perfect diamagnets, i.e., could repulse magnetic fields perfectly while maintaining their superconducting state. This was a game-changing discovery, as superconductivity was no longer a perfect conductor [5]. Two

years after the discovery, the London brothers, who had actively worked in the theory of superconductivity before this discovery, presented a theory to explain the experimentally observed effect. The theory can be condensed into the two London equations [16]:

$$\frac{\partial \mathbf{j}_s}{\partial t} = \frac{n_s e^2}{m}\mathbf{E} \qquad\qquad \boldsymbol{\nabla} \times \mathbf{j}_s = -\frac{n_s e^2}{m}\mathbf{B} \tag{2.1}$$

where $\mathbf{j}_s$ is the superconducting current density, $\mathbf{E}$ and $\mathbf{B}$ are the electric and magnetic fields, respectively; m is the electron mass, e the electron charge and n_s is a phenomenological constant connected to the superconducting carrier density. This density is introduced in the two-fluid model of Gorter and Casimir [43, 57]. From the second equation, one can get the penetration depth of the superconductor, i.e., the amount a magnetic field can penetrate the material, namely $\lambda_s = \sqrt{\frac{m}{\mu_0 n_s e^2}}$.

The first theoretical framework that could explain superconducting phenomena was developed by Vitaly Ginzburg and Lev Landau in 1950 [58]. Their theory preceded the microscopic BCS theory of superconductivity, introduced by Bardeen, Cooper, and Schrieffer seven years later. Building on Landau's 1937 phase transition theory, Ginzburg and Landau proposed that superconductivity involves an order parameter: a measurable quantity that emerges during a phase transition, lowering the system's symmetry. The Cold War's limited flow of information between the sides of the Iron Curtain and the phenomenological foundation of theory hindered its spread [6].

2.1 BCS Formalism

On the other side of the Iron Curtain, in 1950, E. Maxwell [59] and C.A. Reynolds [60] discovered that the superconducting transition temperature of mercury depends on its isotopic mass, supporting an idea first suggested by Onnes during his work with uranium lead [61]. This isotope effect hinted at a phononic mechanism in superconductivity, as phonon behavior is tied to atomic mass. In the same year, H. Fröhlich [13] and later J. Bardeen [62] independently proposed that superconductivity arises from an electron pairing mediated by phonons. Then, in 1956, L. N. Cooper demonstrated that an attractive electron-electron interaction can create a paired state of electrons with opposite momentum and spin, now known as a Cooper pair [12]. This concept, together with the established phonon-mediated origin of superconductivity, set the stage for J. Bardeen, L. N. Cooper, and J. R. Schrieffer to develop the BCS theory in 1957, forming the basis of our modern understanding of superconductivity [8]. The BCS Hamiltonian, which they proposed, reads:

$$\hat{H}_{BCS} = \sum_{\mathbf{k}\sigma} \xi_k \hat{c}^\dagger_{\mathbf{k}\sigma}\hat{c}_{\mathbf{k}\sigma} - \frac{\gamma}{V}\sum_{\mathbf{k}} \hat{c}^\dagger_{\mathbf{k}\uparrow}\hat{c}^\dagger_{-\mathbf{k}\downarrow}\hat{c}_{-\mathbf{k}\downarrow}\hat{c}_{\mathbf{k}\uparrow}\,. \tag{2.2}$$

$\xi_k = \epsilon_k - \mu$ is the electronic energy measured from the chemical potential and $\hat{c}^\dagger_{\mathbf{k}\sigma}$ ($\hat{c}_{\mathbf{k}\sigma}$) is the creation (annihilation) operator of an electron with momentum $\mathbf{k}$ and spin σ. This theory considers electron-electron and electron-phonon interaction and finds that

an attractive interaction can exist, modeled by the second term in Eq. (2.2), $\gamma > 0$, so the interaction is attractive. The theory also assumes a non-zero constant interaction for all frequencies below the Debye frequency ω_D. This attractive force lowers the system's free energy by forming a new state of matter composed of Cooper pairs: the superconducting condensate. The authors of the BCS theory (contrary to Frölich [13]) assumed infinite-range interaction for energies lower than the Debye frequency, ω_D, consequently having an exact solution of the problem within a mean-field approach [63]. Treating the interaction in terms of a mean-field approximation, the Hamiltonian reads

$$\hat{H}_{BCS} = \sum_{\vec{k}\sigma} \xi_k \hat{c}^\dagger_{\mathbf{k}\sigma} \hat{c}_{\mathbf{k}\sigma} + \sum_{\vec{k}} \Delta_{\mathbf{k}} \hat{c}^\dagger_{\mathbf{k}\uparrow} \hat{c}^\dagger_{-\mathbf{k}\downarrow} + \Delta^*_{\mathbf{k}} \hat{c}_{-\mathbf{k}\downarrow} \hat{c}_{\mathbf{k}\uparrow} \,. \tag{2.3}$$

with

$$\Delta_{\mathbf{k}} = |\Delta_{\mathbf{k}}| e^{i\phi} = -\frac{\gamma}{V} \sum_{|\epsilon_{\mathbf{k}}|<\omega_D} \langle \hat{c}^\dagger_{\mathbf{k}\uparrow} \hat{c}^\dagger_{-\mathbf{k}\downarrow} \rangle \,, \tag{2.4}$$

which is the order parameter, a complex parameter containing an amplitude and a phase, and its fluctuations are negligible in the thermodynamic limit. This thesis only focuses on s-wave isotropic superconductors, hence $\Delta_{\mathbf{k}} = \Delta$.

The ground state of Eq. (2.3) is a coherent superposition of Cooper pairs, which reads

$$|BCS\rangle = \prod_{\vec{k}} (u_{\mathbf{k}} + v_{\mathbf{k}} \hat{c}^\dagger_{\mathbf{k}\uparrow} \hat{c}^\dagger_{-\mathbf{k}\downarrow}) \, |0\rangle \,. \tag{2.5}$$

with

$$|u_{\mathbf{k}}|^2 = \frac{1}{2}\left(1 + \frac{\xi_{\mathbf{k}}}{\sqrt{|\Delta|^2 + \xi^2_{\mathbf{k}}}}\right) \qquad |v_{\mathbf{k}}|^2 = \frac{1}{2}\left(1 - \frac{\xi_{\mathbf{k}}}{\sqrt{|\Delta|^2 + \xi^2_{\mathbf{k}}}}\right) \tag{2.6}$$

A few months after the BCS theory was published, Bogoliubov found a canonical transformation to the Hamiltonian (2.3) [11, 64]. This canonical transformation defined a new basis formed from a combination of particles and holes that diagonalized Eq. (2.3) [7],

$$\hat{\gamma}^\dagger_{\mathbf{k}\uparrow} = u_{\mathbf{k}} \hat{c}^\dagger_{\mathbf{k}\uparrow} - v_{\mathbf{k}} \hat{c}_{-\mathbf{k}\downarrow} \qquad \hat{\gamma}_{-\mathbf{k}\downarrow} = u_{\mathbf{k}} \hat{c}_{-\mathbf{k}\downarrow} + v_{\mathbf{k}} \hat{c}^\dagger_{\mathbf{k}\downarrow} \,, \tag{2.7}$$

The $\hat{\gamma}$ operators define the Bogoliubov quasiparticles, linear combinations of particles and holes, which are the single-particle excitations of the superconductor. The operators diagonalize the Hamiltonian (2.3) and describe the BCS ground state as the state with no Bogoliubov quasiparticles, i.e., $\hat{\gamma}_{\mathbf{k}\sigma} |BCS\rangle = 0$.

The BCS theory quickly gained acceptance by successfully consolidating prior discoveries about superconductivity: the phononic origin for electron pairing explained the isotope effect, while the condensate of Cooper pairs in the ground state confirmed the existence of long-range order at the heart of the theory, a concept foreshadowed by F. London and Pippard [8]. The BCS theory also aligned well with the phenomenological London equations and the Meissner effect, describing magnetic behavior accurately. However, its prediction of a ground state that breaks particle-number symmetry, $\mathcal{U}(1)$, initially met resistance.

Due to the $\mathcal{U}(1)$ symmetry break, the BCS ground state breaks gauge invariance, so although Eq. (2.2) is invariant under $\hat{c}^\dagger_{\mathbf{k}\sigma} \to e^{i\phi}\hat{c}^\dagger_{\mathbf{k}\sigma}$, Hamiltonian (2.3) is not, see, e.g., Ref. [63]. As a consequence, the phase and the particle number are conjugated operators [9],

$$\hat{N} = -i\frac{d}{d\hat{\phi}} \qquad\qquad [\hat{N}, \hat{\phi}] = 2i\ . \tag{2.8}$$

This relation is handy when considering the effects of size in superconductors, see Chp. 6.

A new formalism, equivalent to solving the Schrödinger equation with Hamiltonian (2.3), came from the works of Nambu [65] and Gor'kov [66], which employs Green's Functions (GF). This formalism is used in Chps. 3 and 4. The superconducting Hamiltonian can be expressed in a spinor basis $\hat{\Psi}_{\mathbf{k}} = (\hat{c}_{\mathbf{k}\uparrow}, \hat{c}_{\mathbf{k}\downarrow}, -\hat{c}^\dagger_{-\mathbf{k}\downarrow}, \hat{c}^\dagger_{-\mathbf{k}\uparrow})^T$ as

$$\hat{H} = \sum_{\mathbf{k}} \mathrm{Tr}\left[\hat{\Psi}^\dagger_{\mathbf{k}} \check{H}_{\mathbf{k}} \hat{\Psi}_{\mathbf{k}}\right] \qquad\qquad \check{H}_{\mathbf{k}} = \xi_{\mathbf{k}}\tau_3\sigma_0 + \Delta\tau_1\sigma_0\ , \tag{2.9}$$

where Δ is the superconducting gap, obtained from the mean-field approximation as expressed in Eq. (2.4), and τ and σ are Pauli matrices describing the particle-hole and spin degrees of freedom, respectively. From now on, we use the $\check{}$ symbol to represent any matrix in the Nambu-Spinor basis or any higher dimensions. The GFs of the system can be obtained from

$$\check{G}_{\mathbf{k},\mathbf{k}'}(\omega) = (\omega\check{\mathbb{1}} - \check{H}_{\mathbf{k}})^{-1}\delta_{\mathbf{k},\mathbf{k}'} = -\frac{\delta_{\mathbf{k},\mathbf{k}'}}{|\Delta|^2 - \omega^2 + \xi^2_{\mathbf{k}}}(\omega + \xi_{\mathbf{k}}\tau_3 + \Delta e^{i\phi\tau_3}\tau_1)\ , \tag{2.10}$$

where the 0th Pauli matrices, i.e., the identity matrices, are implicit. The retarded (advanced) GF is obtained by shifting the energy by an imaginary infinitesimal value $\omega \to \omega + (-)i\epsilon$,

$$\check{G}^R_{\mathbf{k},\mathbf{k}'} = \check{G}_{\mathbf{k},\mathbf{k}'}(\omega - i\epsilon) \qquad\qquad \check{G}^A_{\mathbf{k},\mathbf{k}'} = \check{G}_{\mathbf{k},\mathbf{k}'}(\omega + i\epsilon) \tag{2.11}$$

The GF formalism can be used to extract the spectrum of quasiparticle excitations of a superconductor. In the following, we present a general formula to calculate the Density of States (DoS) of a system and apply it to calculate the spectrum of a bare superconductor.

2.1.1 Single-particle excitations.

The quasiparticle excitations are the lowest-lying excitations in a superconductor, separated from the ground state by an energy Δ. Also known as Bogoliubov excitation, they do not correspond to breaking a Cooper pair, which requires energy 2Δ, but instead exist in a distinct Hilbert space, the odd-particle space. The quasiparticle

excitation spectrum, related to DoS, is convenient to calculate using the GF formalism. It reads

$$\rho(\omega) = \sum_k \pm\frac{1}{4\pi}\,\mathrm{Tr}\left[\mathrm{Im}\,\check{G}^{A,R}_{\mathbf{kk}}(\omega)\right] = \pm\frac{1}{4\pi}\,\mathrm{Tr}\left[\mathrm{Im}\,\check{G}^{A,R}(\omega)\right]\ , \tag{2.12}$$

where $\check{G}^{A,R}(\omega)$ is the real-space GF at the origin, obtained as the Fourier transform of Eq. (2.10). The real space GF at the origin reads

$$\check{G}(\omega) = \nu_0 \frac{\omega + |\Delta| e^{i\phi\tau_3}\tau_1}{\sqrt{|\Delta|^2 - \omega^2}}, \tag{2.13}$$

The form of the DoS for single-particle excitations is given by

$$\rho(\omega) = \frac{1}{4\pi}\,\mathrm{Tr}\left[\mathrm{Im}\,\check{G}(\omega + i\epsilon)\right] = \nu_0\,\mathrm{Im}\left(\frac{\omega + i\epsilon}{\sqrt{|\Delta|^2 - (\omega + i\epsilon)^2}}\right), \tag{2.14}$$

where $\nu_0 = mk_F/\pi^2$ is the normal metal DoS. Figure 2.1(a) illustrates this spectrum, showing a gap of 2Δ. The two van Hoove-like singularities at $\omega = \pm\Delta$ are called coherence peaks. At higher energies, the DoS plateaus at $\rho(\omega \gg \Delta) = \nu_0$, meaning that at large energies, the superconductor behaves similarly to a normal metal. Moreover, $u(\omega \gg \Delta) = 1$ and $v(\omega \gg \Delta) = 0$; consequently, at large energies, the Bogoliubov excitations are equal to electronic excitation [see Fig. 2.1(b)]. The superconducting phenomena happen in a small energy window around the Fermi energy.[1]

2.1.2 Two-particle excitations

As stated in the original BCS paper [8], there are two possible excitations from the ground state of a superconductor: single-particle or Bogoliubov excitations, which we already discussed and two-particle or Cooper Pair Excitations (CPE). The two-particle excitation of a superconductor comes from a double Bogoliubov excitation that can be represented as

$$\hat{\gamma}^\dagger_{\mathbf{k}_0\uparrow}\hat{\gamma}^\dagger_{\mathbf{k}_0\downarrow}\,|BCS\rangle = (v_{\mathbf{k}_0} - u_{\mathbf{k}_0}\hat{c}^\dagger_{\mathbf{k}_0\uparrow}\hat{c}^\dagger_{-\mathbf{k}_0\downarrow}) \prod_{\mathbf{k}\neq\mathbf{k}_0} (u_{\mathbf{k}} + v_{\mathbf{k}}\hat{c}^\dagger_{\mathbf{k}\uparrow}\hat{c}^\dagger_{-\mathbf{k}\downarrow})\,|0\rangle\ . \tag{2.15}$$

which is orthogonal to the ground state. As two quasiparticles have to be excited, the minimum energy for this excitation is 2Δ. The CPEs generated from operators with the same momenta have the same excitation energy 2Δ, so the spectrum looks like replicas of the coherence peaks starting at an energy 2Δ instead of Δ.

2.2 Tunneling between Superconductors

The first tunneling experiments between superconductors were conducted by I. Giaever [9], followed by J. Nicol *et al.* [10], where they measured the current between superconductors separated by an oxide barrier. In both studies, the authors

[1] If it is not written explicitly, we assume Δ to be a real number.

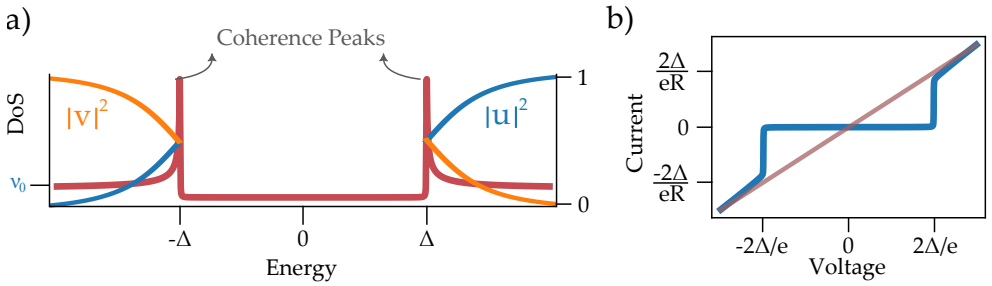

Figure 2.1: **Spectrum of a superconductor. (a)** The DoS of a superconductor, as calculated from Eq. (2.14). The functions $|u|^2$ and $|v|^2$ superposed on top of the spectrum represent the particle and hole components of the Bogoliubov excitations for each energy. **(b)** The current between two superconductors in the tunneling regime, as calculated from the Eq. (2.20). The red curve is the current expected for the tunneling between normal metals with the same tunneling resistance.

suggested that the tunneling current depends on the single-particle DoS of the leads, which J. Bardeen later formalized [6] with a microscopic theory based on the wave function overlap between drain and source, now foundational in STM analysis. Based on Bardeen's theory, the Hamiltonian describing electron tunneling between two leads is

$$\hat{H}_{\text{tunel}} = \sum_{\mathbf{k},\mathbf{k}',\sigma,\sigma'} \hat{c}^{\dagger}_{L\mathbf{k}\sigma} \hat{\mathcal{T}}_{\mathbf{k},\mathbf{k}',\sigma\sigma'} \hat{c}_{R,\mathbf{k}'\sigma'} + \text{h.c.}, \tag{2.16}$$

where $\hat{\mathcal{T}}_{\mathbf{k},\mathbf{k}',\sigma\sigma'}$ is the probability amplitude of one electron tunneling from the left (L) to the right (R) electrode and $\hat{c}_{i\mathbf{k}\sigma}$ ($\hat{c}_i$) is the creation (annihilation) operator of an electron with momentum $\mathbf{k}$ and spin σ in the $i = L$ or $i = R$ electrode. For a time-reversal symmetric system without any magnetic impurities $\hat{\mathcal{T}}_{\mathbf{k},\mathbf{k}',\sigma\sigma'} = \mathcal{T}_{\mathbf{k},\mathbf{k}'}\delta_{\sigma\sigma'}$.

In certain cases it is important to consider finite energy for charging the junction, given by [45, 54, 67]

$$\hat{H}_{\text{charging}} = \frac{e^2}{2C}\left(\sum_k \frac{\hat{c}^{\dagger}_{L\mathbf{k}\sigma}\hat{c}_{L\mathbf{k}\sigma} - \hat{c}^{\dagger}_{R\mathbf{k}\sigma}\hat{c}_{R\mathbf{k}\sigma}}{2}\right)^2 = \frac{\hat{Q}^2}{2C}\,. \tag{2.17}$$

C is the capacitance of the junction, defined by the material's geometry and properties that act as the insulating barrier between superconductors. The tunneling current is given by the average of the current operator, which reads

$$\hat{I} = e\frac{d}{dt}\hat{N}_L = ie\sum_{\mathbf{k},\mathbf{k}'} \hat{c}^{\dagger}_{L\mathbf{k}\sigma}\mathcal{T}_{\mathbf{k},\mathbf{k}'}\hat{c}_{R,\mathbf{k}'\sigma} - \text{h.c.}, \tag{2.18}$$

In the following, we simplify the calculation of $\langle\hat{I}\rangle$ by assuming that $\mathcal{T}_{\mathbf{k},\mathbf{k}'} = \mathcal{T}$, i.e., the transmittance is momentum independent. This approximation is valid for STM

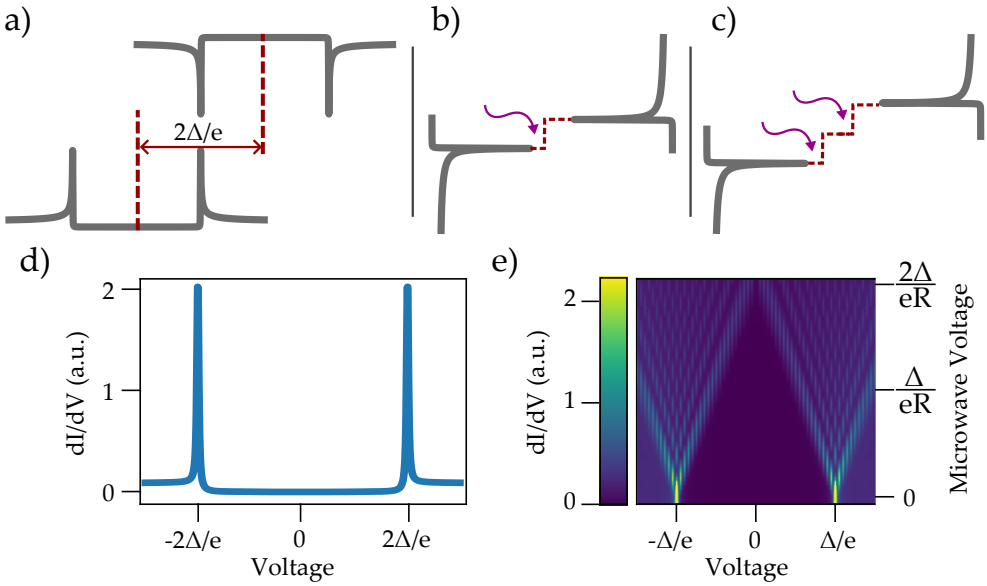

Figure 2.2: **Single-particle tunneling.** **(a)** Sketch of the tunneling between superconductors. When $V = 2\Delta/e$, the negative coherence peak of the upper DoS aligns with the positive peak of the lower one. **(b)**, **(c)** Sketch of the single and two photon-assisted tunneling processes. Only absorption is shown. The photons add an energy equal to $n\Omega$ to the tunneling electron. Similarly, the tunneling electron can emit a photon with the same energy. The purple waves represent the photons. **(d)** Calculated dI/dV for tunneling between superconductors, the coherence peaks appear at $\pm 2\Delta/e$. **(e)** Calculated evolution of the conductance between superconductors as a function of the applied microwave field voltage. Calculated from Eq. (2.19).

experiments, where the main contribution for the tunneling arises from the last atom in the apex of the tip [see Sec 2.5].

In the next sections, we discuss the expressions for the current due to quasiparticle tunneling and Cooper pair tunneling when the two electrodes are superconductors. The extended calculation of these two is shown in App. D.1.

2.2.1 Single Particle Tunneling.

The tunneling current when a DC as well as an AC bias voltage with frequency Ω is applied, i.e., $V(t) = V + V_{\text{ac}} \cos(\Omega t)$, reads

$$I = \sum_{n=-\infty}^{\infty} J_{n'} \left(\frac{eV_{\text{ac}}}{\Omega} \right)^2 4e\pi^2 |\mathcal{T}|^2 \int_{-\infty}^{\infty} d\omega \rho_L(\omega) \rho_R(\omega + eV + ne\Omega) \\ [f(\omega) - f(\omega + eV + ne\Omega)] \,, \tag{2.19}$$

where ρ_i are the Local Density of States (LDoS) of the left and right electrodes on the position of the tunneling, $J_n(x)$ is the nth Bessel function, and $f(\omega)$ is the Fermi-Dirac distribution. When only a DC voltage is applied, the current response is equal to the n=0 term in Eq. (2.19):

$$I = 4e\pi^2|\mathcal{T}|^2 \int_{-\infty}^{\infty} d\omega \rho_L(\omega)\rho_R(\omega + eV)[f(\omega) - f(\omega + eV)] \, . \tag{2.20}$$

The calculated tunneling current between two superconductors with the same gap is shown in Fig. 2.1(a). Figure 2.2 illustrates the phenomenology of Eq. (2.20). It shows that the single-particle tunneling is a convolution between the DoS of the L and R electrodes with an energy shift given by eV. For a symmetric junction between two superconductors, the onset of single-particle tunneling is at $V = 2\Delta/e$, where the negative coherence peak of the left electrode aligns with the positive coherence peak of the right electrode [43]. Figure 2.2(d) shows the calculated dI/dV of the same process, which will come in handy when we describe the measurements performed by the STM [see Sec. 2.5].

The terms with finite n in Eq. (2.19) are the corrections due to an applied AC signal. This approach is known as the Tien-Gordon theory [68], and each term displayed in Eq. (2.19) can be regarded as a photon-assisted tunneling process of the nth order. Figures 2.2(b) and (c) illustrate the first and second-order processes, respectively. The AC field further shifts the left and right DoS in the convolution, so for the nth photon-assisted tunneling, the onset voltage of single-particle tunneling is $V = 2\Delta/e - n\Omega/e$. Figure 2.2(e) illustrates the evolution of the dI/dV as a function of the applied AC voltage. Replicas of the coherence peaks with a separation of $n\Omega/e$ appear. The larger the applied AC voltage, the more replicas are observed.

2.2.2 Josephson Current

A few years after the BCS theory was proposed, the British scientist Brian Josephson proposed that when two superconductors are put in close contact, and a hopping term (such as a tunneling Hamiltonian [Eq. (2.16)]) is added to the system, a zero bias current of Cooper pair appears [69]. The most technical steps of the calculation are shown in App. D.1. The tunneling of Cooper pairs for no applied voltage reads

$$I = I_c \sin(\phi) \, , \tag{2.21}$$

where

$$I_c = \frac{\pi\Delta}{2eR} \tanh \frac{\Delta}{2k_B T} \tag{2.22}$$

is the critical current [70], and $\phi = \phi_L - \phi_R$ is the phase difference between superconductors, R is the junction's resistance, and we assumed a symmetric junction, i.e., $\Delta_L = \Delta_R = \Delta$. Equation (2.21) is known as the first Josephson relation [69] and implies that, with a fixed phase difference between superconductors, a zero-voltage Cooper pair current, or supercurrent, is generated. The second Josephson relation

relates the phase difference with the applied voltage;

$$\frac{d\phi}{dt} = 2eV(t). \tag{2.23}$$

The phase in Eq. (2.21) is not an operator, which is the case for bulk superconductors when the particle number is not well-defined. When the particle number is well-defined, the phase fluctuates, and we have to consider a quantum mechanical operator. In Chp. 6, this is the case due to the small size of the superconducting grains. In this scenario, we exploit the relation between phase and particle number in Eq. (2.8) to describe $\exp\{i\phi\}$ as the translation operator of Cooper pairs. Then, the current operator reads

$$\hat{I} = I_c \sin\left(\hat{\phi}\right) = i\frac{I_c}{2}\sum_{2N} |2N+2\rangle\langle 2N| - |2N\rangle\langle 2N+2| \ . \tag{2.24}$$

and the Hamiltonian generating this current as

$$\hat{H} = E_J \cos\left(\hat{\phi}\right) = -\frac{E_J}{2}\sum_{2N} |2N+2\rangle\langle 2N| + |2N\rangle\langle 2N+2| \ . \tag{2.25}$$

where $E_J = \frac{I_C}{2e}$ represents the Josephson energy. This Hamiltonian captures the tunneling of a Cooper pair between the left and right electrodes.

In the most common STM tunneling configuration, a bias voltage is applied, and the current response is measured. In this setup, the phase difference remains unfixed, leading Eq. (2.21) to vanish, yet incoherent Cooper pair tunneling remains measurable. So far, we have omitted effects from the charging Hamiltonian in Eq. (2.17) as well as the effects of the environment on the tunneling electrons. With finite junction capacitance and a non-zero circuit impedance, Z, a second-order incoherent Cooper pair tunneling current appears. This current is given by

$$\begin{aligned} I &= \pi e E_J^2 \left(P'(2eV) - P'(-2eV)\right), \text{ with } P'(\omega) = \int dt e^{4J(t)+i\omega t} \\ J(t) &= \frac{e^2}{\pi}\int_0^\infty d\omega \frac{\mathrm{Re}\, Z_c(\omega)}{\omega}\left[\coth(\omega/2k_BT)(\cos(\omega t)-1) - i\sin(\omega t)\right] \ . \end{aligned} \tag{2.26}$$

The $P'(\omega)$ is a distribution named Probability of Emission (PoE) function that describes the effects of the environment on the tunneling Cooper pairs [45, 51, 71, 72]. The step-by-step calculation is extended in App. D.1.2. The current is proportional to the square Josephson energy, E_J^2, which indicates that this formula corresponds to a second-order tunneling transport mechanism.

The phenomenology of this equation is similar to the Tien-Gordon theory presented in Sec. 2.1.1. The PoE accounts for the tunneling assisted by the bosonic modes of the environment. As these modes do not have a defined frequency but rather a distribution of frequencies given by the circuit impedance, we can not separate the assisted tunneling in different contributions as in Eq. (2.19). The tunneling is then given by a probability distribution.

2.3 Double tunneling junctions and the Coulomb blockade.

In the following, we present the current response of a Double Tunneling Junction (DBTJ) for ultrasmall tunnel junctions, i.e., the limit where the charging, Eq. (2.17), has an essential role in tunneling electrons. We describe the working principle of the Single Electron Transistor (SET), first described by D. V. Averin and K. K. Likharev in 1986 [46] and measured by T. Fulton and G. Dolan [73] two years later. In this device, the charge does not flow continuously but in a quantized way, making it exceptionally sensitive for electrometry applications. No superconductivity is considered in this section. The effects of finite pairing energy are considered in Chapters 5 and 6, as well as in App. D.

The charging Hamiltonian for two junctions reads

$$\begin{aligned}\hat{H}_{\text{charging}} &= \frac{e^2}{2C_1}\left(\sum_k \frac{\hat{c}^\dagger_{L\mathbf{k}\sigma}\hat{c}_{L\mathbf{k}\sigma} - \hat{c}^\dagger_{c\mathbf{k}\sigma}\hat{c}_{c\mathbf{k}\sigma}}{2}\right)^2 + \frac{e^2}{2C_2}\left(\sum_k \frac{\hat{c}^\dagger_{c\mathbf{k}\sigma}\hat{c}_{c\mathbf{k}\sigma} - \hat{c}^\dagger_{R\mathbf{k}\sigma}\hat{c}_{R\mathbf{k}\sigma}}{2}\right)^2 \\ &= \frac{\hat{Q}_1^2}{2C_1} + \frac{\hat{Q}_2^2}{2C_2} = \frac{\hat{q}^2}{2C} + \frac{\hat{Q}^2}{2C_\Sigma}\,,\end{aligned} \tag{2.27}$$

where, c refers to the central region, $\hat{Q}_i$ is the charge in the ith junction, $\hat{q} = \hat{Q}_1 - \hat{Q}_2$ is the excess charge in the island and $\hat{Q} = \kappa_1\hat{Q}_1 + \kappa_2\hat{Q}_2$ the excess charge in both junctions, with $C = C_1 + C_2$, $C_\Sigma = \frac{C_1C_2}{C}$ and $\kappa_1 = \frac{C_2}{C}$ and $\kappa_2 = \frac{C_1}{C}$. When the central region of the DBTJ is small enough and is isolated from the left and right electrodes, charge fluctuations decrease. Then, the charge of the central grain is quantized, i.e., $\hat{q} = \hat{n}e$.

Moreover, when a gate potential is added as a third terminal to the circuit, as illustrated in Fig. 2.3(a), the tunneling through each junction has a directionality. Adding or extracting a charge from the central grain costs different energy. For this reason, the charge of the central grain transforms to $\hat{q} = \hat{n}e - V_G/C_G = \hat{n}e - q_0$, i.e., it can host an excess fractional charge q_0, which can be controlled with the gate voltage.

The energy distribution of the different charge states on the island is described by the first term in the last formula in Eq. (2.27):

$$\hat{H} = \frac{(\hat{n}e - q_0)^2}{2C}\,. \tag{2.28}$$

the dispersion of the $n = -1, 0, 1$ states of the grains is illustrated in Fig. 2.4(a). We note that the parabolas cross at $q_0 = \pm 0.5$e. Moreover, the system is e periodic. Any q_0 value and $q_0 \pm e$ have the same energy. The energy separation between the state $n = 0$ and states $n = \pm 1$ at $q_0 = 0$, depicted by the green arrow in 2.4(a), is the Coulomb energy: $E_C = e^2/2C$.

Once a voltage is applied between the left and right electrodes, see Fig. 2.3(a), tunneling in the first and second junctions turns on. This varies the population of each charge state; consequently, a non-equilibrium problem must be solved to calculate the populations, p_n. This is done with a Master equation, which is described in App. C.1.

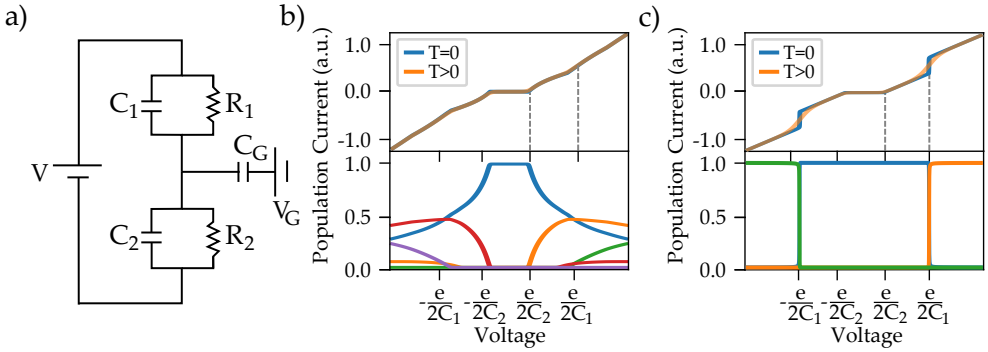

Figure 2.3: **The double tunneling junction. (a)** Sketch of the circuit representing the DBTJ. A voltage source, V, is applied to two junctions characterized by a resistor R_i and a capacitance C_i in parallel. A third terminal is added to account for the fractional excess charge ($q_0 = V_G/C_G$). **(b)** Current through a DBTJ for $R_1 = R_2$ and $C_1 < C_2$ for zero and finite temperatures (top) and the population of each charge state (bottom). **(c)** Same DBTJ in the tunneling limit ($R_1 \gg R_2$) for zero and finite temperatures (top) and the population of each charge state (bottom). The Coulomb gap and the charging steps can be distinguished.

Once the master equation is solved, the current through the DBTJ is a sum of the transition probabilities for all possible charge states of the island weighted by the population of the state. See Eq. (C.4).

The current for $q_0 = 0$ on a DBTJ is shown in Figs. 2.3(b) and 2.3(c) (top). The former is the current response of a junction with $R_1 = R_2$ and $C_2 > C_1$. We observe a spectral gap of magnitude $e/C_{\max}$, where $C_{\max} = \max(C_1, C_2)$, i.e., the sepctral gap is e/C_2. This is known as the Coulomb gap. It represents the minimum voltage needed for current to flow. Beyond this threshold, the DBTJ shows an approximately ohmic response, with slight slope variations due to changes in the central grain's population, as illustrated in Fig. 2.3(b) (bottom).

On the other hand, Fig. 2.3(c) shows the current response of a junction with the same parameters in the tunneling regime, i.e., $R_1 \gg R_2$. In this scenario, the Coulomb gap is the same, but when a voltage equal to $\pm e/C_1$ is reached, the island's population changes to $n = \pm 1$ sharply. See Fig. 2.3(b) (bottom). This is observed in the current as a step or as a peak in the dI/dV, known as a charging peak.

Finally, we examine the influence of gate voltage on the current. With an applied gate voltage, the Coulomb gap and charging steps adjust. Figures 2.4(b) and 2.4(c) show the dI/dV evolution relative to excess charge, displaying the expected e-periodic behavior in a shape commonly referred to as Coulomb diamonds [45]. Both plots are calculated in the tunneling regime, with Fig. 2.4(b) representing a symmetric junction ($C_1 = C_2$) and Fig. 2.4(c) an asymmetric one ($C_1 \neq C_2$).

For $q_0 = 0.5e$, the Coulomb gap closes because the $n = 0$ and $n = 1$ grain states intersect [Fig. 2.2(a)]. In the symmetric BDTJ, the Coulomb diamonds remain

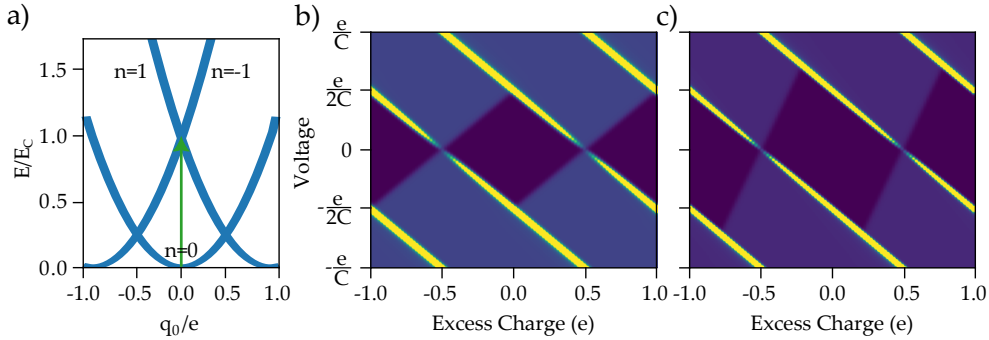

Figure 2.4: **Effect of excess charge in the DBTJ. (a)** Energy level dispersion as a function of q_0. The $n = -1, 0, 1$ levels are shown. The green arrow represents the energy needed to add an electron at the charge neutrality point. **(b)** and **(c)** Dependence of the dI/dV on the excess charge for a symmetric and asymmetric junction, respectively.

symmetric, meaning dI/dV is identical for positive and negative voltages at all excess charges. However, in the asymmetric case, a non-reciprocal response to applied current is observed, where dI/dV asymmetrically responds to voltage inversion. This non-reciprocity results from the simultaneous breaking of charge conjugation and inversion symmetry, a necessary condition for a non-reciprocal current response [see Chapter 6]. In Chapter 5, we expand this formalism to consider superconducting electrodes and central grain and use the formalism to fit the measured spectra.

2.4 Magnetic impurities on superconductors

One of the main topics of this thesis is the effects of magnetic impurities on superconductors at the nanoscale. In this section, we shift gears and discuss these theoretically, foundational for the experimental findings discussed in Chapters 3 and 4.

The first effects due to magnetic impurities on normal metals were first found in the 1930s [15, 74] when an increase in the resistance of the material at low temperatures was measured. This effect happened for several pure metals and alloys, so its importance was immediately pointed out. The resistance was thought to lower with temperature as the electron-phonon scattering decreased. It was not until 1964 that Sarachik *et al.* [75] comprehended the crucial role of magnetic impurities in such a system. The theoretical microscopic theory modeling the phenomena was first introduced by J. Kondo in the same year [21]. The lowering of the resistance due to magnetic impurities is now called the Kondo effect [Sec. 2.4.1], and the Hamiltonian describing it reads

$$\hat{H}_{\text{Kondo}} = \sum_{\mathbf{k}\mathbf{k}',\sigma\sigma'} J_{\mathbf{k}\mathbf{k}'} \hat{c}^{\dagger}_{\mathbf{k}\sigma} \hat{\mathbf{S}} \cdot \mathbf{s}_{\sigma\sigma'} \hat{c}_{\mathbf{k}'\sigma'} \ . \tag{2.29}$$

$J_{\mathbf{kk'}}$ is the exchange coupling, $\hat{\mathbf{S}}$ is the spin of the magnetic impurity, and $\check{\mathbf{s}} = (\sigma_1, \sigma_2, \sigma_3)$. The model assumes an impurity scattering between any two momenta. Note that this is a Heisenberg-like Hamiltonian between a localized spin and the spin of the itinerant electrons.

Kondo was not the first researcher to point out the importance of magnetic impurities in metals, and certainly, his model is not the first microscopic theory describing the adatoms. The work of Friedel [76], motivated by higher temperature experiments [77], has to be mentioned here. He was the first to discuss the effects of impurities (magnetic and non-magnetic) in metals in the context of scattering theory. He described the perturbation of the charge around an impurity, later known as Friedel oscillations, and gave a phenomenological description of a microscopic model that described the interaction between the d-orbitals of an impurity and the substrate.

Following Friedel's lead, Anderson was [17] the first to develop a microscopic Hamiltonian describing magnetic impurities on metals. Anderson described the model for a superconductor, as he was motivated by the experimental work of B. T. Matthias *et al.* [78], who proved that an ensemble of magnetic impurities lowered the critical temperature of a superconductor.

2.4.1 The Kondo Hamiltonian and the Yu-Shiba-Rusinov States

Soon after Kondo proposed his model [21], Schrieffer and Wolff proved that it was equivalent to the Anderson model when the magnetic moment of the impurity was well-defined [79] (see Ref. [80] for the superconducting case). Then, the Hamiltonian describing a magnetic impurity on a superconductor reads

$$H_{\text{Kondo}} = \sum_{\sigma\sigma'} \hat{\psi}^{\dagger}_{\sigma}(0)(J\hat{\mathbf{S}} \cdot \mathbf{s}_{\sigma\sigma'} + U\delta_{\sigma\sigma'})\hat{\psi}_{\sigma'}(0) \,, \tag{2.30}$$

where we assumed a momentum-independent exchange coupling J and the position of the impurity to be at $\mathbf{r} = 0$. Moreover, $\hat{\psi}^{\dagger}_{\sigma}(0)$ ($\hat{\psi}_{\sigma}(0)$) is the creation (annihilation) operator of an electron with spin σ at $\mathbf{r} = 0$, and we added a scalar potential scattering term U to account for particle-hole symmetry break, which is the case for most STM experiments on magnetic impurities.

Three independent works from Yu, Shiba, and Rusinov [19, 23, 81] solved the problem of a single magnetic impurity on top of a superconductor within a classical spin approximation. These authors simplified the problem by assuming that the spin was big enough not to consider quantum effects from its fluctuations. The problem of a magnetic impurity on a superconductor can be approached using the GF formalism introduced in Sec. 2.1. One needs to calculate the exact GF of the superconductor plus magnetic impurity system. This can be done using the Dyson equation, which relates the bare GF of the superconductor to the exact GF of the system. The Dyson equation for a Dirac-like local impurity can be written in the following simple form

$$\begin{aligned} &\check{G}(\omega, \mathbf{r}, \mathbf{r}') = \check{G}_0(\omega, \mathbf{r}, \mathbf{r}') + \check{G}_0(\omega, \mathbf{r}, 0)\check{V}\check{G}(\omega, 0, \mathbf{r}') \Rightarrow \\ &\check{G}(\omega, \mathbf{r}, \mathbf{r}') = \check{G}_0(\omega, \mathbf{r}, \mathbf{r}') + \check{G}_0(\omega, \mathbf{r}, 0)\check{V}\left[\check{\mathbb{1}} - \check{V}\check{G}(\omega, 0, 0)\right]^{-1}\check{G}(\omega, 0, \mathbf{r}') \,, \end{aligned} \tag{2.31}$$

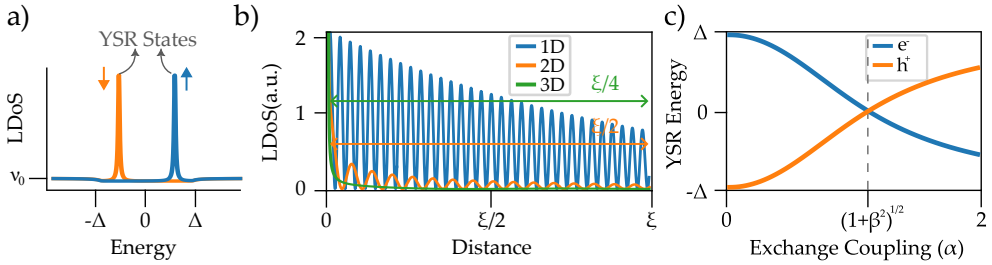

Figure 2.5: **Characterization of YSR states. (a)** Spin-dependent DoS on a local magnetic impurity on a superconducting surface calculated from Eq. (2.31). The positive and negative YSR states have the opposite spin polarization. **(b)** Evolution of the DoS of the YSR states away from the impurity for a 3D (blue), 2D (orange) and 1D (green) superconductor. **(c)** Evolution of the YSR state energy as a function of exchange coupling.

where $\check{G}_0(\omega, \mathbf{r}, \mathbf{r'}) = \sum_{\mathbf{k}} G_{0\mathbf{k},\mathbf{k}}(\omega) e^{i\mathbf{kr} - i\mathbf{k'r'}}$ is the real space GF of a superconductor. $G_{0\mathbf{k},\mathbf{k'}}$ is defined in Eq. (2.10). As explained before, we have assumed that the impurity is located at $\mathbf{r} = 0$. The matrix $\check{V}$ reads

$$\check{V} = U\tau_3 + J\mathbf{S} \cdot \check{\mathbf{s}} \,. \tag{2.32}$$

We are interested in the system's Local Density of States (LDoS), which incorporates information about distortions in the local charge distribution coming from the impurity. The LDoS is obtained by substituting the exact GF in Eq. (2.31) into the expression (2.12). This is a magnitude we can access with STM.

The first term in Eq. (2.31) is the bare superconducting GF, the second gives the correction due to the impurity. We note that the second term has two poles inside the superconducting gap given by the solution of $\det\left[\check{\mathbb{1}} - \check{V}\check{G}(\omega, 0)\right] = 0$, which read

$$\epsilon_{\pm} = \pm\Delta \frac{1 - \alpha^2 + \beta^2}{\sqrt{(1 - \alpha^2 + \beta^2)^2 + 4\alpha^2}} \xrightarrow{\beta \to 0} \pm\Delta \frac{1 - \alpha^2}{1 + \alpha^2} \tag{2.33}$$

with $\alpha = \pi\nu_0 J$ and $\beta = \pi\nu_0 U$. These energies correspond to two states that develop inside the superconducting gap, localized around the impurity, known as the Yu-Shiba-Rusinov (YSR) states [19, 23, 81]. The LDoS on top of the impurity calculated as $\frac{1}{4\pi}\,\mathrm{Tr}\left[\check{G}(\omega, 0, 0)\right]$, with $\check{G}$ given by Eq. (2.31), is shown in Fig. 2.5(a), where the colors represent the spin-dependent DoS. We note two major features: (1) the DoS of the superconducting coherence peaks is suppressed, and the spectral weight is transferred to the YSR states. (2) the YSR states are spin-dependent, the positive and negative states being oppositely polarized.

The first property reflects the conservation of total DoS, $\int d\omega \rho(\omega) = \nu_0$. As two new states are created inside the superconducting gap, the DoS of the coherence peaks is redistributed to form the YSR states. The second feature arises from the chosen approximation. In principle, Eq. (2.30) preserves time-reversal symmetry, no intrinsic

spin-polarized states are generated. However, modeling the impurity spin as a vector acts similarly to a Zeeman field, breaking this symmetry and producing spin-dependent YSR states.

Equation (2.31) also describes the dependence of the LDoS on positions away from the magnetic impurity ($\mathbf{r} \neq 0$), which involves two length scales: a long-range scale determined by the superconducting coherence length ξ_S, which provides an exponential decay, e^{-r/ξ_S} of the YSR wavefunction, and a short length equal to the inverse of the Fermi momentum k_F^{-1}, over which the wave function oscillates and exhibits an algebraic decay $\sim (k_F r)^{-1}$. This decay law is valid for three-dimensional systems. For a general isotropic superconductor, the decay law depends on the dimensionality of the superconducting band, namely the YSR amplitude decays as $\sim (k_F r)^{(1-d)/2}$ with dimension $d = 1, 2, 3$ [32]. Summarizing, the LDoS is given by [23, 82]

$$\rho^{\pm}(\omega) \sim \frac{1}{(k_F r)^{(d-1)/2}} e^{-r/\xi_S} \sin^2(k_F r + \delta^{\pm}), \tag{2.34}$$

where $\delta^{\pm}$ is the scattering phase, which considers the dephasing between the particle and hole component, i.e., it can be different for the hole (-) or particle (+) component of the YSR states. This evolution is depicted in Fig. 2.5(b). The exact evolution for a 2D superconductor is presented in Sec. A.1, and the discussion about their extension is extended in Chapter 3

Figure 2.5(c) shows the evolution of the YSR energy as a function of the value α. At $\alpha = \sqrt{1+\beta^2}$, the positive and negative YSR peaks cross. In the classical limit, this is nothing more than a level crossing. As we explain in the following section it represents a Quantum Phase Transition (QPT) [23, 42] from a free spin to the strong coupling or Kondo-screened regime. As this approximation can not capture the intricate evolution of the system's ground state, we propose a single-site approach that can better describe the QPT without any computationally costly methods [36].

2.4.2 Single-site model for a magnetic impurity on a superconductor

The simple solution of the classical approximation arises from disregarding any quantum effect due to the spin on a local impurity. Still, this method is a good approximation for weak exchange couplings before the perturbative approach breaks down [40]. Larger couplings require sophisticated but numerically costly methods such as the numerical renormalization group [37, 38] or continuous time Montecarlo [39]. A simplified approach to consider the quantum nature of the impurity is reducing the superconductor to a single superconducting atom (a single site), exchange coupled to a quantum spin. The single-site model for a magnetic impurity on a superconductor can be described with the following Hamiltonian [36],

$$\hat{H} = \Delta \hat{c}_{\uparrow}^{\dagger} \hat{c}_{\downarrow}^{\dagger} + \Delta \hat{c}_{\downarrow} \hat{c}_{\uparrow} + \sum_{\sigma\sigma'} \hat{c}_{\sigma}^{\dagger} (J \hat{\mathbf{S}} \cdot \mathbf{s}_{\sigma\sigma'} + U \delta_{\sigma\sigma'}) \hat{c}_{\sigma} \ , \tag{2.35}$$

where J is the exchange coupling between the impurity and the superconducting site, U is a scattering potential, and Δ is the superconducting pairing energy. Without loss of generality, we take $U = 0$ in the following discussion.

As discussed in sections Secs. 2.1.1 and 2.1.2, excitations of the superconductor have a onset energy, Δ and 2Δ, for single- and two-particle excitations, respectively. At these threshold energies, a sharp peak develops (coherence peaks). The first two terms in Eq. (2.35) correspond to the single-site model for a superconductor without magnetic impurities. This Hamiltonian considers a single superconducting atom, with creation and annihilation operators $\hat{c}_\sigma^\dagger$ and $\hat{c}_\sigma$. The eigenstates of Eq. (2.35) for $J = U = 0$ read

$$\left\{ |BCS\rangle = \frac{1}{\sqrt{2}}(|0\rangle - |2\rangle), \overline{|BCS\rangle} = \frac{1}{\sqrt{2}}(|2\rangle + |0\rangle), |\uparrow\rangle, |\downarrow\rangle \right\}. \tag{2.36}$$

$|BCS\rangle$ is the GS lying at $-\Delta$ energy, $\overline{|BCS\rangle}$ is the Cooper pair excited state, with an energy Δ and $|\uparrow\rangle$ and $|\downarrow\rangle$ are the two possible single-particle excitations, which lie at 0 energy. Here, $|2\rangle = |\uparrow\downarrow\rangle$ represents a Cooper pair. The electron-induced excitations from the ground state, $|BCS\rangle$, into $|\uparrow\rangle$ and $|\downarrow\rangle$ amounts to Δ and represent the coherence peaks of a superconductor. The higher energy continuum is disregarded.

Figure 2.6(a) plots the energy diagram for $J = U = 0$, which we compare with the spectrum discussed in Secs. 2.1.1 and 2.1.2. This single-site Hamiltonian considers only the onset of excitations (gets rid of the k-dependence of the ground state), which, as discussed below, is handy when the effects of magnetic impurities on superconductors are considered.

When the exchange coupling is turned on, the Hilbert space is doubled due to the spin degrees of freedom. For a spin 1/2 and $J < \frac{4}{3}\Delta = J_{cr}$ one can show by exact

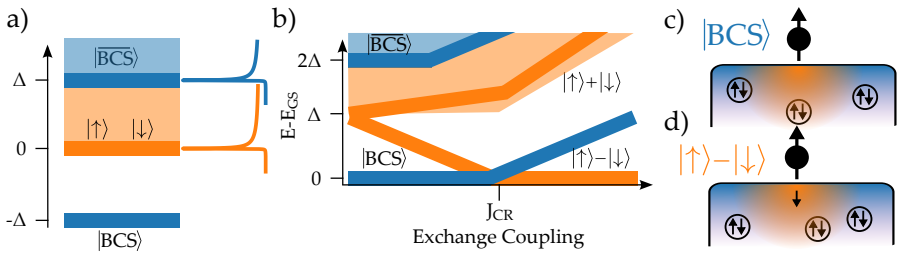

Figure 2.6: **Single-site model for a magnetic impurity on a superconductor. (a)** The blue and orange states correspond to the even and odd parity states, respectively. At $J = J_{cr}$, we observe the crossing between the even BCS and the od singlet YSr state. The shaded area represents the onset of the continuum of single-particle excitations (orange) and the Cooper pair excitations (blue). **(b)**, **(c)** Sketch of the even and odd ground states, respectively

diagonalization of Hamiltonian (2.35) that the ground state is given by

$$|GS\rangle_{\text{weak}} = |BCS\rangle \left|\frac{1}{2}\right\rangle \text{ or } |BCS\rangle \left|-\frac{1}{2}\right\rangle , \tag{2.37}$$

where $\left|\pm\frac{1}{2}\right\rangle$ refer to the spin state of the impurity. The regime where $J < J_{cr}$ is known as the weak or free spin regime [36], where the interaction between spin and substrate is not big enough to screen the impurity spin, so it is free, see Fig. 2.6(b). The ground state has a total spin 1/2 and can be described as the product of two different subspaces: one for the electronic degrees of freedom and another for the spin's degrees of freedom. Furthermore, the parity of the system is even, as the superconductor has 0 or 2 electrons.

When $J > J_{cr}$, the ground state changes to

$$|GS\rangle_{\text{strong}} = \frac{1}{\sqrt{2}} \left(\left|\uparrow, -\frac{1}{2}\right\rangle - \left|\downarrow, \frac{1}{2}\right\rangle \right) . \tag{2.38}$$

This is a singlet state formed between the spin of the itinerant electrons on the substrate and the impurity spin, i.e., it has a total spin 0, see Fig. 2.6(c). The exchange coupling term in Eq. (2.35) does not couple to even states, which are singlets, i.e., spin-0 states. Consequently, the energy of $|BCS\rangle\,|\pm 1/2\rangle$, which represents the BCS condensate with a free spin, does not depend on J. The QPT happens when the singlet state in Eq. (2.38), formed between the impurity spin and a quasiparticle, has a lower energy than the BCS condensate. As it is formed with a bound quasiparticle, the parity in the strong coupling regime is odd.

In the weak coupling regime, the YSR state is the transition from the BCS ground state to the Kondo singlet, and *vice versa* in the strong coupling regime. The single-site model, contrary to the classical approximation, captures the change of total spin and parity through the QPT. Notice that within the single-site model the spatial dependence is lost.

In this thesis, we compare these approaches. In Chapter 3, we focus on the spatial extension of the YSR states away from the impurity, so the classical approximation is used. On the other hand, in Chapter 4, we are interested in identifying the origin of the YSR states in a high-spin molecule, so the single-site model is used.

In the upcoming, we contextualize the theoretical concepts discussed thus far by introducing the scanning tunneling microscope, the key experimental platform used for the measurements in this thesis.

2.5 The Scanning Tunneling Microscope on superconductors

In 1972, R. Young *et al.* [83] took the initial step toward nanoscale topographical measurements of metallic surfaces by developing a device capable of mapping surface contours with submicrometer precision. This pioneering instrument, named the "topographiner", worked on a principle akin to that of the modern Scanning Tunneling Microscope, but with a key difference: it utilized field emission current instead of

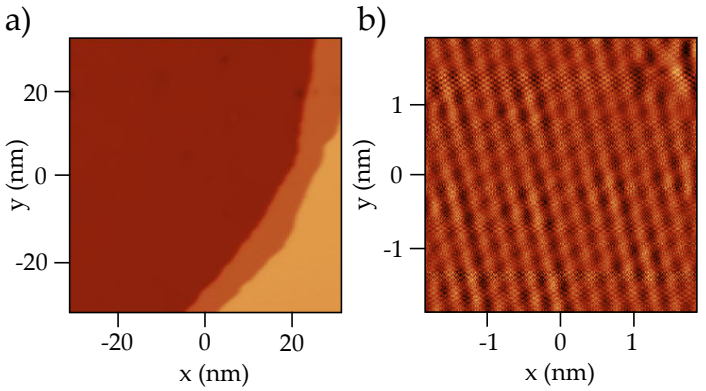

Figure 2.7: **Topography and Current measurements on Pb(111) (a)** Constant current topographic image of a large area of bulk Pb (V=1 V, I=100 pA). **(b)** Constant height topographic image of a small area of bulk Pb. The atomic resolution is observed (V=50 mV).

tunneling current for its measurements. In 1981, G. Binnig and H. Rohrer [5] introduced the first STM, which revolutionized surface analysis by leveraging the tunneling current between a sharp metallic tip and a conducting surface, the sample. The distance between the tip and sample was regulated using piezoelectric materials, which adjust the z-position to maintain the tunneling current. Additional piezoelectric components controlled the x and y movements, enabling the tip to scan the surface in a raster pattern and generate a detailed topographical map.

The theoretical foundation of the tunneling current was introduced in Sec. 2.2.1 and is described, in the absence of inelastic processes, by Eq. (2.20). A key innovation of the STM is its sharply pointed metallic probe, often fabricated by electrochemical etching for tungsten tips or mechanical shearing for platinum-iridium tips, creating a single-atom apex. The tunneling transmittance decays exponentially with distance, expressed as $|\mathcal{T}|^2 \propto e^{-|z|}$ [6], where z is the distance between tip and sample. A slight increase of 1 Å reduces $|\mathcal{T}|^2$ by an order of magnitude. Due to the tip's sharpness and the transmittance's exponential dependence, only the DoS at the outer atom at the apex of the tip contributes to the tunneling current. Similarly, only the DoS at the nearest surface point contributes to the current, allowing the STM's raster scan to resolve the sample's topography at an atomic level.

The STM has evolved to enable measurements under increasingly optimal conditions, enhancing resolution and precision [84]. The STM used in this thesis is a Joule-Thomson STM (JT-STM), operated in Ultra-High Vacuum (UHV) at a pressure of 10^{-10} mbar. The Joule-Thomson cycle lowers the temperature from 4.2 K, the boiling temperature of He at atmospheric pressure, to 1.3 K, where all measurements are conducted. The low temperatures allow for the observation of superconducting phenomena, as the critical temperature of most superconductors is a few Kelvin degrees, enhancing the energy resolution.

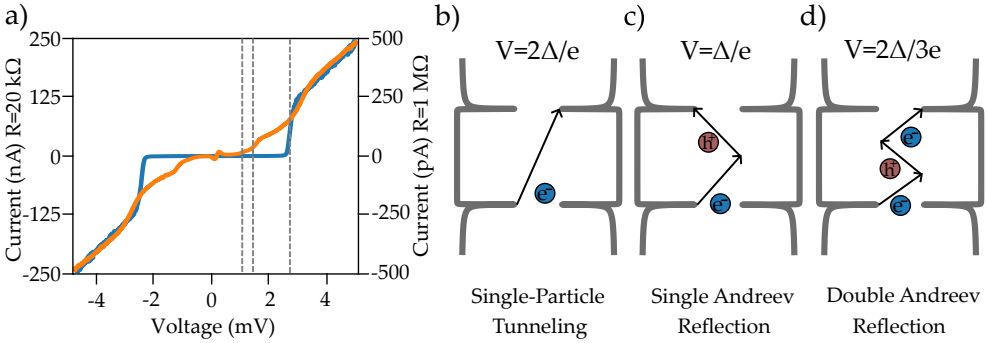

Figure 2.8: **I-V characteristics of a superconducting tunneling junction.** **(a)** Current response of a Pb-Pb tunneling junction upon an applied voltage at $R = 1$ MΩ (blue) and $R = 20$ kΩ (orange). **(b)** Sketch of the single particle-tunneling. **(c)** Sketch of the first-order Andreev reflection. **(c)** Sketch of the second-order Andreev reflection. Applied voltages in the sketches is taken assuming $\Delta_{\text{tip}} = \Delta_{\text{sample}}$.

Figures 2.7(a) and 2.7(b) illustrate both a large-scale scan and atomic-resolution images of bulk Pb. The large-scale scan in Fig. 2.7(a) is conducted in constant-current mode, where a feedback loop maintains a steady current as the tip scans across the sample in a raster pattern. The sample's topography is mapped by recording changes in the tip's z-position, reflected in the adjustments of the piezo voltage required to keep the current constant. For atomic-resolution imaging, shown in Fig. 2.7(b), the constant-height mode is used. Here, the tip height remains fixed, and variations in current, dependent on the tip-sample distance, are measured to reveal atomic-level details.

Constant-current mode is ideal for large-area scans, where surface features like step edges [see Fig. 2.7(a)] may exceed the typical tip-sample separation. For smaller, high-resolution scans, constant-height mode provides optimal atomic-scale detail.

2.5.1 Scanning tunneling spectroscopy on superconductors

When two metallic electrodes are in contact, their chemical potential is fixed to be equal, i.e., their Fermi energies are aligned [Sec. 2.2]. When a voltage between the tip and sample is applied, the alignment of the chemical potentials changes. Measuring the output current as the input voltage is swept, we measure the convolution between the tip and sample DoS [Eq. (2.20)]. If the tip DoS is known, the DoS of the sample can be inferred. Combining topographic information with the voltage sweeps, we obtain the LDoS of the sample. Moreover, the system's differential conductance or dI/dV can improve the current resolution. This is known as Scanning Tunneling Spectroscopy (STS). In STS, a small AC signal is added to the DC voltage, and the output is measured using a lock-in amplifier set at the AC frequency of choice.

Quasiparticle tunneling

Figure 2.7(c) shows the I-V curve measured on a flat region of the superconducting Pb(111) surface. For these measurements, a tungsten tip with its apex coated in Pb is used, inducing superconductivity. Using a superconducting tip enhances the energy resolution by reducing thermal broadening due to the superconducting gap, which is larger than the thermal broadening at 1.3 K. At high junction resistances ($R > 1$ MΩ), illustrated in the blue curve in Fig. 2.7(a), a voltage of $\sim (\Delta_{\text{tip}} + \Delta_{\text{sample}})/e$ must be applied to overcome the two superconducting gaps, and initiate tunneling, where Δ_{tip} and Δ_{sample} are the gap of the tip and sample, respectively. This is indicative of single-particle tunneling [Sec. 2.2]. In this regime, no current can tunnel between the two superconducting gaps, and the supercurrent is absent since there is no fixed phase between the superconductors.

The quasiparticle tunneling mechanism is illustrated in Fig. (2.8)(b). The applied voltage has to be enough for a quasiparticle to tunnel from the negative coherence peak of the tip to the positive peak in the sample or *vice versa*. The dI/dV measurement corresponding to the high resistance I-V curve is shown in Figs. 2.9(a). The onset of quasiparticle tunneling is observed as a sharp peak, which enhances the resolution of the measurement.

Andreev Tunneling

As the tip approaches the sample, the resistance is lowered, and higher-order tunneling processes are activated. Figure 2.8(a) displays the I-V curve at $R = 20$ kΩ, compared with the high resistance measurement. Beyond the single-particle tunneling onset at $V = \pm(\Delta_{\text{tip}} + \Delta_{\text{sample}})/e = 2.7\,\text{meV}$, two additional characteristic jumps in the current appear at $V = \pm(\Delta_{\text{tip}} + \Delta_{\text{sample}})/2e = 1.35\,\text{meV}$ and $V = \pm(\Delta_{\text{tip}} + \Delta_{\text{sample}})/3e = 0.9\,\text{meV}$. Figure 2.9(b) is the corresponding differential conductance measurement where the current steps are observed as peaks at the same energies. These steps correspond to the first- and second-order Andreev reflections between the tip and sample [85–89].

An Andreev reflection is a scattering mechanism where an incident electron is retroreflected as a hole. For $E < \Delta$, no quasiparticle states exist in a superconductor, only the condensate of Cooper pairs. Any incident electron with $E < \Delta$ sees an infinite potential well and can not access it except by generating a Cooper pair in the superconductor. If the incident electron generates a Cooper pair, a retroreflected hole has to be formed for charge and momentum to be conserved.

The first-order Andreev tunneling process is depicted in Fig. 2.8(c). When the onset voltage of $V = (\Delta_{\text{tip}} + \Delta_{\text{sample}})/2e$ is applied, an electron traveling from the left electrode to the right generates a Cooper pair in the right electrode and is retroreflected as a hole. The tunneling electron's energy is $(\Delta_{\text{tip}} + \Delta_{\text{sample}})/2$, matching the hole's energy, resulting in a total energy transfer of $(\Delta_{\text{tip}} + \Delta_{\text{sample}})$.

Following the same principle, the second-order Andreev tunneling process is shown in Fig. 2.8(d). Here, an applied voltage of $V = (\Delta_{\text{tip}} + \Delta_{\text{sample}})/3e$ gives the tunneling electron an energy of $(\Delta_{\text{tip}} + \Delta_{\text{sample}})/3$. The electron creates a Cooper pair in the

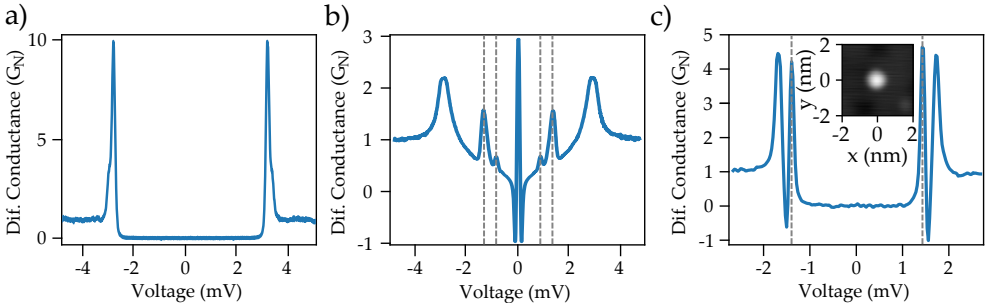

Figure 2.9: **STS on a superconductor. (a)** Spectra at $R = 1$ MΩ in a Pb-Pb tunneling junction. Equivalent to Fig. 2.7(c). **(b)** Spectra at $R = 20$ kΩ in the same junction, equivalent to Fig. 2.8(a) **(c)** STS on top of a Ti magnetic impurity on the superconducting β-Bi_2Pdsurface (V=5 mV, I=500 pA). The inset is a topographic image of the adatom (V=100 mV, I=100 pA).

right electrode and is retroreflected as a hole. This hole lacks sufficient energy to create a quasiparticle in the left electrode, leading to the formation of a Cooper pair in the left electrode and the retroreflection of another electron. The total energy of the tunneling quasiparticles again adds up to $(\Delta_{\text{tip}} + \Delta_{\text{sample}})$.

As the order of Andreev reflection increases, the required voltage decreases while the order of transmittance increases. Single-particle tunneling is proportional to $|\mathcal{T}|^2$, while the first- and second-order Andreev reflections are proportional to $|\mathcal{T}|^4$ and $|\mathcal{T}|^6$, respectively.

Cooper Pair tunneling

Another feature is visible in the low-resistance I-V curve shown in Fig. 2.8(a). Close to zero applied voltage, two small peaks emerge. In the corresponding differential conductance measurement [Fig. 2.8(b)], these appear as a sharp peak at zero voltage, referred to as the Josephson peak [45, 51, 71, 72, 86, 90, 91].

As discussed in Sec. 2.2.2, the STM tunneling junction lacks a fixed phase difference between superconductors, eliminating the DC Josephson current. However, due to the finite interaction between environmental modes and the tunneling charge, incoherent Cooper pair tunneling emerges. The zero-voltage peak corresponds to this process, mediated by environmental modes.

The shape of the Josephson peak is determined by the PoE function, providing information about the distribution of environmental modes, which is further elaborated in Chp. 6, where measuring the Josephson peak in small-sized superconductors, we observe a large deviation from Fig. 2.8(b).

Yu-Shiba-Rusinov states in STM

The STM's subnanometer resolution and capability to access the sample spectrum make it a perfect platform for probing superconductivity and its consequences at the nanoscale. The YSR states are an ideal system to measure the effects of a local magnet on a superconductor. These subgap excitations arise from the interaction between the magnetic moment of an impurity's spin and the itinerant electron. Because they lie within the band gap, these excitations are long-lived and, hence, appear as very narrow resonances in tunneling experiments [29, 92]. YSR states are the elementary states forming sub-gap bands in atomic chains of magnetic impurities [27, 28, 34, 93–99]. Owing to its narrow line shape, the study of YSR states also reveals fundamental aspects of atomic scale magnetism with high precision. For example, STM experiments on superconductors with magnetic impurities revealed valuable information about molecular [41, 100–108] and atomic properties, as hybridization of orbitals, anisotropy, etc [39, 109–122].

An example of an STS measurement on a Ti adatom on the superconducting β-Bi_2Pdsurface is shown in Fig. 2.9(c), and the corresponding topographic image of the adatom and its surroundings in the inset. Two peaks at symmetric positive and negative voltages can be observed inside the superconducting gap. Their voltage reads $V = 1.40$ mV. The energy of the YSR can be calculated by subtracting the gap of the tip $\epsilon_{\pm} = \pm(eV - \Delta) = \pm 0.62$ meV. We also measure some reminiscence of the coherence peaks, probably due to a non-zero transmittance between the tip and superconductor.

The YSR states are studied in Chps. 3 and 4. In the former, the classical approach, introduced in Sec. 2.4.1, is used to understand the nanoscopic phenomena arising from magnetic adatoms on β-Bi_2Pd. In the latter, we generalize the single-site model, described in Sec. 2.4.2, to comprehend the complex entangled states formed in a magnetic molecule on a proximitized superconductor.

3

Classical Impurities in s-wave Superconductors

The microscopic behavior of metals is deeply connected to the Fermi Contour (FC) of the material. For superconductors, the gap is created around a small energy window near the FC. Consequently, the Yu-Shiba-Rusinov (YSR) states are created at low energies. At shorter scales ($\mathcal{O}(1/k_F) \sim 1nm$), the spatial distribution of their wave function may reveal the shape of the atomic or molecular orbitals responsible for the creation of the YSR states [97, 102, 107, 117, 123, 124]. In contrast, at longer scales, due to the exponential decay of superconducting correlations, the distribution of the YSR amplitude reflects the shape of the bands (at the FC) of the superconductor [32, 33, 103, 123, 125, 126].

As a consequence of the dependence of the decay of the YSR states on the FC, their measurement can be used as a method to assess the shape of the FC, or vice versa, knowing the FC of the sample can be used as a method to analyze the behavior of these extensions. The STM is the perfect platform for these local measurements. A well-studied method for obtaining k-space information is the analysis of Quasiparticle Interference (QPI) patterns [127, 128]. Using local scatterers on the surface of a sample, one can obtain all possible wave-vector shifts due to scattered quasiparticles; the interference between the incoming and outgoing states creates standing waves that perturb the Local Density of States (LDoS), which the STM can access. These extensions are the superconducting equivalent of the Friedel oscillations of an impurity on a metallic substrate. Contrary to QPI on a normal metal, the superconducting gap protects the in-gap YSR states, which prolong for larger scales.

This chapter is structured into four sections. In Sec. 3.1, we introduce the system under study: magnetic impurities (V and Mn) on the Bi-terminated surface of the β-Bi_2Pd superconductor. The intricate band structure of the superconductor and its potential implications on the measurements are examined. In Sec. 3.2, an effective theory is proposed to account for the observed spatial extension of the YSR states. This theory demonstrates that the decay of the YSR states and their spatial profile are closely linked to the FC of the superconductor. Section 3.3 extends the effective theory to explore the interactions between multiple magnetic impurities and various structural configurations, which we compare to experiments performed on Mn adatoms on the β-Bi_2Pd. Lastly, in Sec. 3.4, we investigate the effects of spin-polarized bands on QPI measurements. Analyzing the QPI patterns offers deeper insights into the intricate band structure of the β-Bi_2Pd, a superconductor characterized by two surface bands alongside two projected bulk bands, all with a square FC. A discussion of the conclusions and future outlook follows this.

3.1 The β-Bi_2PdSuperconductor

The β phase of Bi_2Pd is a layered s-wave multiband type-II superconductor with a superconducting homogenous gap (same for all bands) of $\Delta = 0.78$ meV [129], and a critical temperature of $T_C = 5.4$ K [130, 131]. Figure 3.1(a) shows the material's atomic structure. Upon cleavage, the Bi-terminated face becomes the surface, which is shown in the topographic STM measurements in Fig. 3.1(b). The surface exhibits both bright and dark spots. These could be Pb atoms from the last cleaved layer or regions where Bi atoms are missing, likely due to the cleavage (or other unknown atomic substitutional impurities in the topmost Bi layer). Additionally, some shadows can also be observed, probably caused by impurities in the lower layers. Previous ARPES measurements and DFT calculations [30, 31] suggest that the FC is composed of four different bands: two projected bulk bands, α and β, and two surface bands, S1 and S2 [Fig. 3.1(c)].

All the bands crossing the Fermi level have a square-like shape; see the sketch in Fig. 3.1(c) [1, 30, 31]. Extended FC regions with parallel flat portions suggest strong vector nesting in this surface: the scattering is focused on the direction specified by the FC. In this case, the nesting is on the (100) and (010) crystallographic directions, orientations perpendicular to the parallel flat areas of the FC. Moreover, due to the strong Rashba Spin-Orbit Coupling (SOC) of the material, the spin degeneracy at the surface is broken, and the bands become spin-polarized [30, 31]. At the surface, momentum and spin are locked so that the spin is reversed for each pair of opposing faces of the square-like FC [Fig. 3.1(c)]. The FC's shape and polarization affects the YSR states' extensions, so their consideration is important when analyzing possible scattering mechanisms from the impurities.

The non-circular shape of the FC and a multiband, spin-dependent nature of the superconducting state characterizes β-Bi_2Pd. These properties are not unique to β-Bi_2Pd; many superconducting materials exhibit significant effects of a non-circular FC on the properties of YSR states [32, 33]. Moreover, multiband superconductivity is a common feature of many materials, such as Pb, $NbSe_2$, and FeSe [93, 127, 132].

In the following, we first solve these problems with a generalist approach so that our methods can be applied to any material; then, we focus on results for magnetic impurities on the β-Bi_2Pdsuperconducting surface.

3.2 Yu-Shiba-Rusinov states in Superconductors with arbitrary Fermi Contour

Several STM experiments observe YSR decaying several nanometers in conventional superconducting systems [32, 33, 123, 125], which were attributed to a combination of two effects, a reduced dimensionality of the superconducting bands [see Eq. (2.34)] and the anisotropic character of their Fermi surfaces or contours. This last effect is connected with the accumulation of multiple scattering wavevectors along specific substrate directions due to flat segments in the FC. These "nesting vectors" cause an "electronic focusing" effect along specific directions [133], propagating the

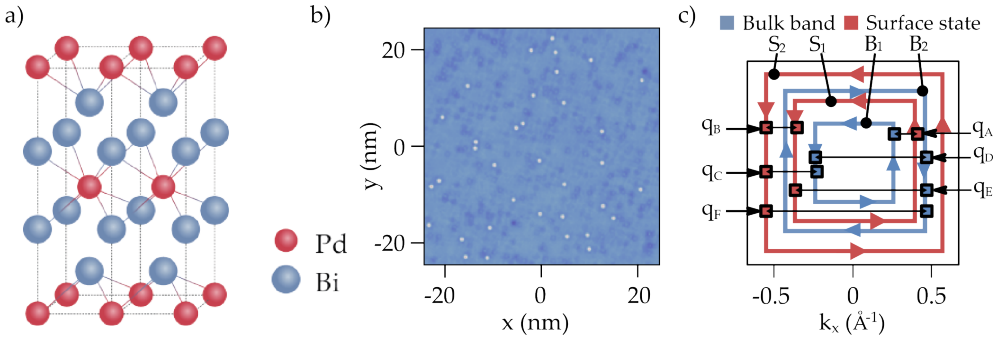

Figure 3.1: **An overview of the characteristics of the β-Bi_2Pd: (a)** Structure of the layered β-Bi_2Pdsuperconductor. **(b)** STM topographic image of said surface: a few bright and dark spots arising from imperfections can be distinguished (V=100 mV, I=100 pA). **(c)** Sketch of the spin-dependent surface FC based on the calculations in Refs. [30, 31]. The spin of the bands is illustrated by the blue and red arrows. Four main bands are depicted, two surface bands (S_1 and S_2) and the surface projections of two bulk bands (B_1 and B_2). All possible spin-conserving scattering vectors are shown (q_i).

wavefunction amplitude for larger distances. Due to the clear relevance of this effect, especially for highly anisotropic superconductors, we propose a detailed analytical study on its role in the decay of superconducting quasiparticle states, which does not rely on high-throughput numerical simulations to incorporate complex Fermi surfaces and contours.

In what follows, we derive a compact expression for the Green's Functions (GFs) in real space to account for the effect caused on the superconductor by multiple atomic impurities.

3.2.1 General expression for the GF in the presence of multiple impurities

To obtain the spectrum of the system, we introduce the equation of motion for the 4×4 matrix GF, the so-called Gor'kov equation [82] which, in real frequency ω space, reads,

$$\left[\omega - \check{H}_0(\mathbf{r}) - \sum_{n=1}^{N} \check{V}_n \delta(\mathbf{r} - \mathbf{r}_n)\right] \check{G}(\mathbf{r}, \mathbf{r}'; \omega) = \delta(\mathbf{r} - \mathbf{r}') \, . \tag{3.1}$$

$\check{H}_0$ is given by the Fourier transform of the Hamiltonian (2.9) and $\check{V}_n$ is the nth impurity's potential [see Eq. (2.32)]. The spectrum of a single impurity can be found explicitly by solving Eq. (3.1) analytically [Sec. 2.4.1], as well as the case of multiple impurities. In this subsection, we provide a useful expression to compute $\check{G}(\mathbf{r}, \mathbf{r})$ in the presence of N impurities at arbitrary position $\mathbf{r}_i$. We start writing the solution of

Eq. (3.1) in the form of a Dyson series:

$$\check{G}(\mathbf{r},\mathbf{r}') = \check{G}_0(\mathbf{r}-\mathbf{r}') + \sum_n \check{G}_0(\mathbf{r}-\mathbf{r}_n)\check{V}_n\check{G}(\mathbf{r}_n,\mathbf{r}'), \tag{3.2}$$

where $\check{G}_0(\mathbf{r}-\mathbf{r}')$ is the GF of the 2D superconductor without impurities. To simplify the notation, we drop the ω-dependence of the GFs. We aim to write the right-hand side of this equation only in terms of the unperturbed $\check{G}_0$. For this, we write the N equations for the matrices $\check{G}(\mathbf{r}_n,\mathbf{r}')$, with $n = 1,\ldots,N$ in a compact form:

$$\check{\overline{G}}(\mathbf{r}') = [\check{\mathbb{1}} - \check{M}]^{-1}\check{\overline{G}}_0(\mathbf{r}')\ , \tag{3.3}$$

where is $\mathbb{1}$ is the $4N \times 4N$ identity matrix and we have introduced the shorthand notation:

$$\check{\overline{G}}(\mathbf{r}') = \begin{pmatrix} \check{G}(\mathbf{r}_1,\mathbf{r}') \\ \check{G}(\mathbf{r}_2,\mathbf{r}') \\ \vdots \\ \check{G}(\mathbf{r}_N,\mathbf{r}') \end{pmatrix}, \quad \check{\overline{G}}_0(\mathbf{r}') = \begin{pmatrix} \check{G}_0(\mathbf{r}_1-\mathbf{r}') \\ \check{G}_0(\mathbf{r}_2-\mathbf{r}') \\ \vdots \\ \check{G}_0(\mathbf{r}_N-\mathbf{r}') \end{pmatrix}, \tag{3.4}$$

and the $4N \times 4N$ matrix

$$\check{M} = \begin{pmatrix} \check{G}_0(0)\check{V}_1 & \check{G}_0(\mathbf{r}_1-\mathbf{r}_2)\check{V}_2 & \cdots & \check{G}_0(\mathbf{r}_1-\mathbf{r}_N)\check{V}_N \\ \check{G}_0(\mathbf{r}_2-\mathbf{r}_1)\check{V}_1 & \check{G}_0(0)\check{V}_2 & \cdots & \check{G}_0(\mathbf{r}_2-\mathbf{r}_N)\check{V}_N \\ \vdots & \vdots & \ddots & \vdots \\ \check{G}_0(\mathbf{r}_N-\mathbf{r}_1)\check{V}_1 & \check{G}_0(\mathbf{r}_N-\mathbf{r}_2)\check{V}_2 & \cdots & \check{G}_0(0)\check{V}_N \end{pmatrix}. \tag{3.5}$$

The matrix $(\check{\mathbb{1}}-\check{M})$ contains information about the bound states of a system of N magnetic adatoms and their hybridization. In particular, the YSR states are determined from the condition $\det(\check{\mathbb{1}} - \check{M}) = 0$.

By solving the set of equations (3.3), and after substitution into Eq. (3.2), one can obtain the full GF in terms of G_0, the GF in the absence of impurities. In most previous works, superconductors with a spherical Fermi surface were considered. In the next subsection we obtain $\check{G}_0(\mathbf{r}-\mathbf{r}')$ for FCs with arbitrary shape that can be approximated by a polygon. In section 3.3, we use Eqs. (3.2-3.5) to obtain the spectrum of some multiimpurity structures.

3.2.2 Real space GF for superconductors with non-circular FC

In this subsection, we present the method to obtain the GF of a 2D superconductor with an arbitrary FC, which we then apply to calculate $\check{G}_0(\mathbf{r}-\mathbf{r}')$ in a M-sided regular polygon centered at $\mathbf{k} = \mathbf{0}$ [App. A.1]. We selected the 2D case because the bands forming the superconducting state in β-$Bi_2Pd$are either surface bands or surface projections of bulk bands, i.e., they are 2D.

The real space GF of the two-dimensional clean superconductor reads,

$$\check{G}_0(\mathbf{r}-\mathbf{r}') = \int \frac{d^2\mathbf{k}}{(2\pi)^2}\check{G}_0(\mathbf{k})e^{i\mathbf{k}\cdot(\mathbf{r}-\mathbf{r}')}, \tag{3.6}$$

where $\check{G}_0(\mathbf{k})$ is given by the Gor'kov equations of the hosting media in momentum space [Eq. (3.1)]. We transform the integral in Eq. (3.6) to an integral over the quasiparticle energy ξ [see Eq. (2.13)] by writing $d^2k = d\mathcal{C}dk_n$, where $d\mathcal{C}$ is a differential element on a constant energy contour and k_n the perpendicular component of the momentum, normal to such contour, with $dk_n = d\xi/|\partial\xi/\partial\mathbf{k}|$ [Fig. 3.2]. The relevant contribution to the integral is around the FC, where the GFs have poles. Therefore, it is convenient to linearize ξ around the FC.

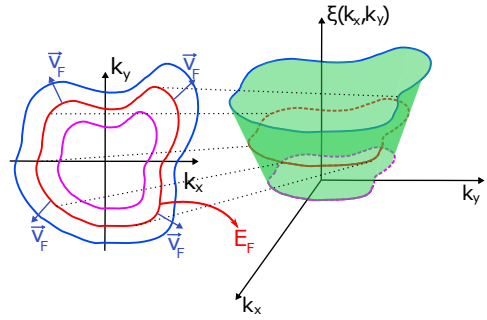

Figure 3.2: **Sketch of an arbitrary Fermi Contour. Right panel:** Sketch of the quasiparticle energy versus two dimensional momentum $\mathbf{k}$. The red curve, at $\xi = 0$, is the FC. **Left panel:** sketch of the FC on the (k_x, k_y) plane. The vector $\mathbf{v}_F$ is parallel to $\boldsymbol{\nabla}_\mathbf{k}\xi$ and hence points in the direction perpendicular to the curves of equal energy.

$$\xi(\mathbf{k}) \approx \mathbf{v_F}\cdot(\mathbf{k}-\mathbf{k_F}), \tag{3.7}$$

where the Fermi velocity, $\mathbf{v}_F \equiv \nabla_\mathbf{k}\xi\big|_{\mathbf{k_F}}$, points in the direction perpendicular to the constant energy contours [Fig. 3.2]. The integral over ξ goes from $-\mu$ to ∞. In metallic systems, μ is usually the largest energy scale. Hence, we take the limit $\mu \gg \Delta$ and integrate it using the residue theorem.

The philosophy of this parametrization of the integral is the same as followed in the isotropic FC case. All the information about the correlations of the quasiparticles is enclosed in a small energy window around the FC. Consequently, the direction perpendicular to the contour is "straightforward" to calculate, giving the exponential decay of the correlations. On the other hand, the integral around the FC depends on its shape, i.e., all information about the origin and distribution of the QPI is present in that integral. In the next section, we exemplify these by computing the integral (3.6) for inscribed regular polygons and discussing some cases.

3.2.3 Effect of the dimensionality and shape of FC on the YSR states spatial dependence

In a 2D superconductor with a circular FC, the decay of the GF, which determines the correlations, obeys $(k_F r)^{-1/2}e^{-r/\xi_s}$ [Eq. (A.9) in Appendix A.1]. Assuming that the FC can be approximated by an M-sided regular polygon, we can determine the GF without impurities (the bare GF of the superconductor) following the procedure described in the previous subsection. We start by separating the integral in M sections [Eq. (A.1)], on each polygon side. The integral for each side is given by a line integral

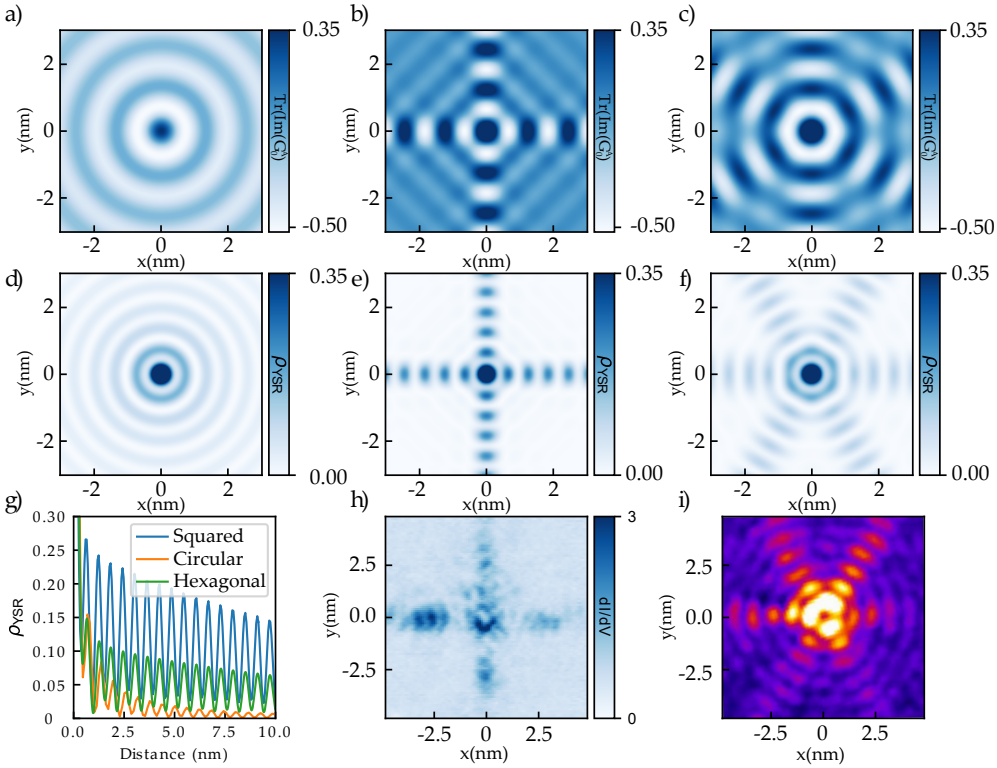

Figure 3.3: **The GF and YSR extension for different FC**. **(a)-(c)** The spatial dependence of the correlation function $\mathrm{Tr}\big[\mathrm{Im}[\check{G}_0(x,y;\omega+i\epsilon)]\big]$ evaluated at $\omega = 2\Delta$ and normalized with respect to its value at $(x,y) = (0,0)$: **(a)** for a circular , **(b)** for a square , and **(c)** for a hexagonal FC. **(d)-(f)** YSR calculated DoS for the three different FCs and normalized with respect to its value at $x = y = 0$. **(e)** Radial cut along the (100) direction of the LDoS of the YSR state in panels **(d)-(f)**. **(h)** Conductance map recorded by STS for one YSR state of an isolated V adatom deposited on $\beta-Bi_2Pd$ [1]. Parameters: I=250 pA, V=0.93 mV. **(i)** YSR spatial dependence measured for magnetic impurities on La(1000) films grown on a Re(1000) crystal, adapted from figure 1a in Ref. [33].

along the polygon plus the usual integral in energy (perpendicular direction to the FC) [Eq. (A.2)]. The unperturbed GF we obtain is the sum over the M integrals [*cf.* Eq. (A.3)]:

$$\check{G}_0(x,y) = \sum_{k=1}^{M} \frac{1}{(2\pi)^2} \int_{n^k/w^k - \tan\frac{\pi}{M}}^{n^k/w^k + \tan\frac{\pi}{M}} d\chi \int d\xi G_0(\xi) e^{-i\left(\frac{m\xi}{k'_F} + k'_F\right)\chi w^k} \,. \tag{3.8}$$

Here, $n^k = x\cos\left(\frac{2\pi k}{M}\right) + y\sin\left(\frac{2\pi k}{M}\right)$, $w^k = -x\sin\left(\frac{2\pi k}{M}\right) + y\cos\left(\frac{2\pi k}{M}\right)$, and $k'_F = k_F\cos\left(\frac{\pi}{M}\right)$, with $k = 1, 2, ..., M$. In the limit $M \to \infty$, we recover the result for the circular FC [Eq. (A.4) and (A.5)].

We focus on three particular examples – the square ($M = 4$), hexagon ($M = 6$), and circular ($M \to \infty$) FCs – and compare the spatial decay of the states bounded to the impurities in all cases. The exact expressions for the circular and square-shaped GF are given in the Appendix [Eq. (A.5) and (A.10)]. To illustrate the anisotropic spatial behavior of the GF, we compute G_0 in two directions: $y = 0$ [Eq. (A.12)] and $x = y$ [Eq. (A.13)]. These equations show decaying behaviors that differ from an isotropic 2D superconductor. The decay resembles a 3D superconductor along the diagonal direction, while, along the $y = 0$ direction, one obtains a 1D-like decay.

In Figs. 3.3(a)-(c) we show the correlation function, $\mathrm{Tr}[\mathrm{Im}\,\check{G}_0^A(\mathbf{r})]$ at an energy $\omega = 2\Delta$, for circular, square-shaped and hexagon-shaped FCs, respectively. The square- and hexagon-shaped FCs resemble the Fermi surface of the β-Bi_2Pd [31] and La(0001) [33] superconducting surface. We approximate both cases by a single, square- or hexagon-shaped FC. We observe a clear directionality in the correlation functions. The nesting arising from the FCs maximizes the correlations in the directions perpendicular to the parallel flat portions of the FC.

The correlation function can not be directly measured, as it is not an observable, but the DoS of the YSR states, which can be written in terms of the unperturbed Green's functions (G_0), encodes this information [see Eq. (2.31)]. The poles of the second term on the right-hand side of Eq. (2.31) determines the energy of the YSR bound states; all the spatial information is contained in the unperturbed GF, $\check{G}_0(\mathbf{r})$. We use the same set of parameters throughout this section to compare the results. Namely, for the superconducting gap $\Delta = 0.78$ mV, effective mass $m = 6.67\ \mathrm{m}_e$, Fermi momentum $k_F = 0.274/a_0$ ($a_0 = 3.3$ Å), and exchange coupling $\alpha^2 = (\pi\nu_0 JS)^2 = 0.156$.

Next, we focus on the spatial distribution of the YSR states for the same three examples. In Figs. 3.3(d)-(f), we show the spatial dependence of the DoS obtained from the full GF [Eqs. (2.14) and (2.31)] evaluated at the energy of the YSR bound state. Similar to Figs. 3.3(a)-(c), the shape of the FC is inscribed in the evolution of the YSR states; furthermore, we see that the extension of these in-gap states is focused even more than the bare GF along the crystallographic directions. This is because the YSR depends on G_0^2, making the focusing more extreme. In panel Fig. 3.3(g), we show cuts of the DoS along the (100) direction. The spatial decay of the circular FC is faster than the one along the symmetrical direction of the square-shaped FC, which behaves as a lower dimensional case. The hexagon-shaped case lies in between. As expected, the longer the parallel flat portions of the FC are, the slower the decay along the nesting direction is, i.e., the decay of a square-shaped FC is the slowest.

Finally, in Figs. 3.3(h) and 3.3(i) we show STM measurements. Fig. 3.3(h) shows the spatial dependence of a YSR state created by a V adatom on the surface of β−Bi_2Pd, which has square-shaped bands [Sec. 3.1]. Qualitatively, this is confirmed by comparing Fig. 3.3(h) and our predictions for a (single) square-shaped FC [Fig. 3.3(e)]. In Fig. 3.3(h), we show an example of a hexagon-shaped FC. Namely,

the spatial dependence of the YSR of magnetic impurities in the La(1000) films grown on Re(1000) [33].

The good agreement between theoretical [Figs. 3.2(e)-(f)] and experimental [Figs. 3.2(h)-(i)] results demonstrate the suitability of our model for a qualitative description of the $\rho(\mathbf{r},\omega)$ of superconductors with magnetic impurities. The results also demonstrate how the low-symmetric square- and hexagon-shaped FCs lead to a slower decay of the YSR states. Such a decay is similar to the 1D situation and suggests the use of superconductors with a square-shaped FC for the realization of one-dimensional Andreev crystals [134, 135] by placing chains of magnetic defects along the direction parallel to the symmetry axis of the square.

3.3 Hybridization of YSR bound states from neighbouring impurities

Atomic manipulation using the tip of an STM has demonstrated a large potential for fabricating atomic nanostructures of magnetic impurities on superconductor and exploring the hybridization of their YSR wavefunction [103, 116, 117, 121, 122, 136–140]. As predicted by Flatté and Reynolds [141], the hybridization between overlapping YSR states depends on the relative alignment of the impurities' spins. For the case of parallel aligned spins, YSR hybridization leads to splitting the sub-gap features into two new states with symmetric and antisymmetric spatial distribution. The splitting oscillates with the separation between impurities (d) with periods comparable with the Fermi wavelength of the substrate. In the presence of non-isotropic FCs, the spatial distribution of the YSR splitting shows intriguing orientation dependence for short inter-impurity distances [103, 141].

In this section, we combine the previously introduced theory and the experimental results measured in Mn adatoms on β-$Bi_2Pd$to explore the YSR hybridization and study the role of the YSR-focusing effect on the interaction between adatoms. We analyze YSR hybridization on ensembles of classical impurities on a surface with a squared FC as a function of their alignment on the substrate. In Sec. 3.3.1, we study the YSR hybridization in atomic dimers by forming them in different crystallographic orientations. We see that their relative spin orientations differ. In Sec. 3.3.2, we then exploit this information to simulate the effects on more complex ensembles of impurities.

3.3.1 Mn dimers on the β-Bi_2Pdsurface

We first assume that the impurities have a parallel spin and analyze the splitting of their YSR states as a function of their alignment. The GF of the dimer can be obtained by constructing the matrix in Eq. (3.5) with N=2. The resulting spectral function shows that the YSR states are split by an amount E representing the hybridization between YSR states. As shown in Fig. 3.4(a), the splitting energy oscillates as a function of the distance between impurities. In Fig. 3.4(b) and 3.4(c), we show that the oscillation amplitude of the YSR splitting is barely constant when the impurities

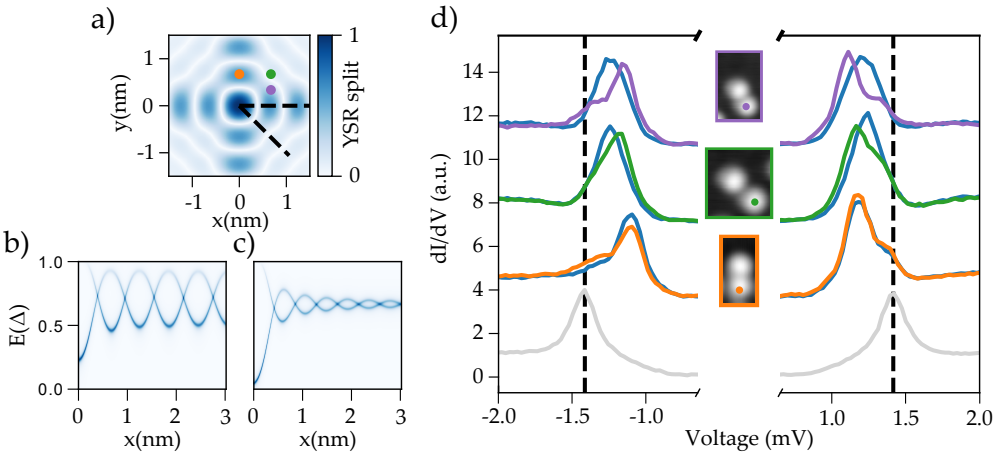

Figure 3.4: **The splitting of the YSR states on a dimer. (a)** The YSR splitting energy $E(\Delta)$, on an impurity as a function of the $x-$ and $y-$position of a second impurity on a 2D superconductor with a square-shaped FC. The anisotropy of the band determines certain directions along which the splitting is larger. **(b)-(c)** YSR subgap spectra on the impurity as a function of the position of the second impurity along the (1,0) and (1,-1) lines of high symmetry (indicated with dashed lines in **(a)**). **(d)** dI/dV STS measurements with a superconducting tip (coated with β-Bi_2Pd) on a Mn adatom on β-Bi_2Pd before (blue) and after (coloured) formation of a Mn_2 dimer by bringing a second Mn adatom into three different substrate positions, with respect to the probed adatom. From top to bottom: $(2a,a)$, $(2a,2a)$ and $(0,2a)$, with a being the lattice constant of β-Bi_2Pd (i.e. $d = \sqrt{5}a$, $2\sqrt{2}a$, and $2a$, respectively). These atomic sites are represented in panel **(a)** as colored dots. The bottom gray spectra is the reference spectra measured on a bare substrate region (the gap of the β-Bi_2Pd substrate is 0.78 meV and the tip's gap approaches close to this value).

are aligned along the (100) direction [Fig. 3.4(b)], while quickly decays along the (110) direction [Fig. 3.4(c)]. This proves that the focusing effect enhances the hybridization when the atoms are aligned parallel to the direction of the nesting vectors.

To correlate these simulations with real systems, we compare them with experimental results on pairs of manganese adatoms positioned with precision using atomic manipulation on the β-Bi_2Pdsuperconductor surface. The β-Bi_2Pdsurface is a squared lattice of Bismuth atoms with lattice parameter $a = 3,36$ Å. Adatoms in neighboring sites frequently collapse in Mn_2 dimers with no subgap features [137]. Therefore, we explore the possible next-neighbor distances, namely Mn dimers aligned along the (210), (110) and (100) crystallographic directions with spatial separation $\sqrt{5}a$, $2\sqrt{2}a$ and $2a$, respectively. In Fig. 3.4(c), we compare differential conductance spectra measured on a reference adatom before (blue) and after placing a second adatom at the position indicated in the insets. When the second adatom is located at the sites $(2a,a)$ or $(2a,2a)$ the YSR state appears split by $\sim$300 μeV and $\sim$200 μeV, respectively. The

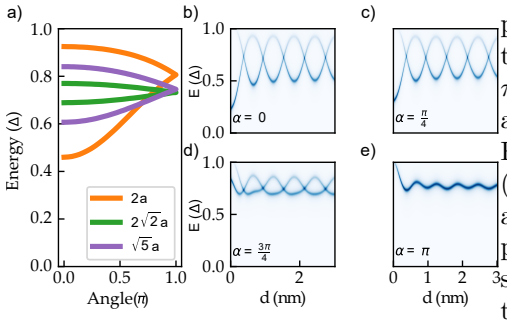

Figure 3.5: **Angle dependence of the YSR states splitting. (a)** Calculated dependence of the YSR splitting on the mutual spin orientation, from 0 (FM dimer) to π (AFM dimer). The two adatoms are on a 2D superconductor with a square-shaped FC, in three configurations along the (100), (110) and (210) directions, i.e., with interatomic distances $2a$, $2\sqrt{2}a$ and $\sqrt{5}a$, respectively. **(b)-(e)** Evolution of the YSR spectral function with the dimer's separation along the (100) direction for different spin angles.

larger splitting for the former, as well as the range of the splitting energy, are qualitatively reproduced by the theory, thus suggesting that these dimers have their spin with a close-to-parallel alignment.

For the third dimer, the YSR peaks are barely affected by the addition of a Mn adatom on the (0,2a) site, while our model in Fig. 3.4(a) predicts a larger splitting than in the previous cases due to the focusing effect. This suggests that in this configuration, the Mn dimers are antiferromagnetically (AFM) aligned. As observed in our previous results on this surface [137], the substrate-mediated exchange coupling between adatoms also depends on their relative orientation, with a preference for AF alignment along the high-symmetry (100) direction.

To account for different alignment between the classical spins, we apply our continuum model to obtain the spectral evolution of YSR states as a function of the relative angle between impurities, as in Ref. [103], where the angle dependence of the spins of a YSR dimer was studied using a tight-binding lattice. Figure 3.5(a) shows the angular dependence of the energy splitting of hybridized YSR states for the three Mn dimers of the experiment shown in Fig. 3.4(d). As mentioned above, the YSR splitting of a (2a,0) dimer is expected to be the largest for parallel spins but quickly reduces with the relative angle, vanishing for AFM spins. Figures 3.5(b) and 3.5(e) show the evolution of the YSR states with dimer separation along the (100) direction for different relative angles of the impurity spins. The oscillation amplitude of even and odd states decreases when they are non-collinear and merge into a single peak for AFM spins. These results suggest that Mn dimers built along (100) direction are antiferromagnetically aligned in contrast to the other dimers explored, whose YSR splitting is consistent with a close to ferromagnetic alignment of their relative spins. We suggest that, in addition to inducing a larger YSR wavefunction hybridization along the (100) direction, the anisotropic FC also leads to stronger exchange interaction (mediated by RKKY) between dimers [142], which at such close distances promotes their mutual AFM alignment.

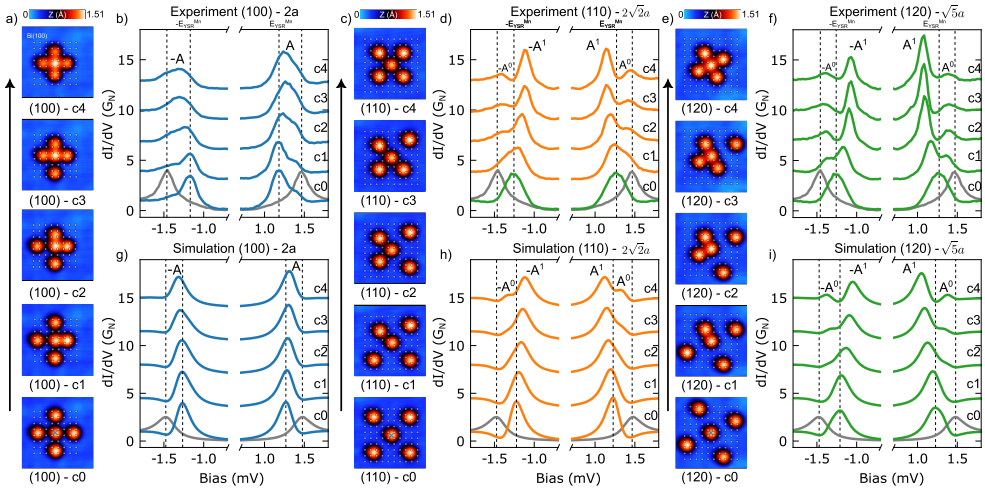

Figure 3.6: **Mn_5 structures along different directions. (a), (c), (e)** From bottom to top are the topography of the manipulation sequence to construct Mn_5 crosses along (100) from 3a to 2a, (110) from $4\sqrt{2}a$ to $2\sqrt{2}a$, and (120) from $2\sqrt{5}a$ to $\sqrt{5}a$ with a = 3.3 Å(V = -100 mV, I = 40 pA). **(b), (e), (h)** dI/dV spectra of the central atom of the Mn structures after moving each lateral Mn atom, offset vertically for clarity (V = 5 mV, I = 500 pA). In gray, the reference spectrum in β-Bi_2Pd. The spectrum for stage (110)-c0 is missing; we use the (120)-c0 as a reference. At $2\sqrt{5}a$ and $3\sqrt{2}a$ the Mn atom are not interacting. **(c), (f), (i)** Model simulation of the five impurity structures with the Green function approach. The spin orientation angle is 90° for 2a-(100) while 0° for the other two configurations (simulation parameters $k_F^{100} = 0.32/a_0$, $k_F^{110} = 0.21/a_0$, $k_F^{120} = 0.28/a_0$, $m^* = 5.85/m_e$, $\alpha = \pi\nu_0 JS/2 = 0.030$, $\beta = \pi\nu_0 U = 0.011$ where a_0 is the Bohr radius and ν_0 is the normal metal density of states). Figure adapted from Ref. [143].

3.3.2 More complex structures

Now that we understand the relative spin orientations that impurities adopt along different crystallographic directions, we can extend our simulations to more complex structures built following the atomic manipulation technique introduced earlier. Fig. 3.6(a), 3.6(c), and 3.6(e) illustrate the step-by-step formation of "atomic crosses" (cross-shaped atomic pentamers). These crosses are constructed along the same three directions used for dimers, allowing us to predict the relative spin orientations within these structures. It is important to note that we assume minimal to no interaction from next-nearest neighbor adatoms and no SOC. If significant interactions were present, the results from the dimers would not be applicable, as the interaction between next-nearest neighbors would alter the relative spin orientations between adatoms. This is due to the RKKY-like interaction between adatoms, which governs spin alignment

and oscillates between AFM and FM spin alignment depending on the distance. Extracting the relative spin orientation for such a complex system -although possible- would be very computationally demanding.

Figs. 3.6(a), 3.6(c), and 3.6(e) show the formation of the crosses. Starting from a dimer, c0, we add one Mn each step, from c1 to c4, and take spectroscopic measurements on top of the central adatom. Figs. 3.6(b), 3.6(d), and 3.6(f) present the measured data for the stars formed in the (100), (110) and (120) directions, respectively, while Figs. 3.6(g), 3.6(h), and 3.6(i) are their corresponding simulations. From c0 up to c4 we present the evolution of the spectra. We first notice that in the (100) direction [Fig. 3.6(b)], the YSR state does not split but shifts slightly towards the gap edge. In the other two directions, we see a clear split emerging in the YSR state as more adatoms are approached to the central one [Fig. 3.6(d) and 3.6(f)]. This agrees with our measurements on the dimers, the adatoms in the (100) direction are antiferromagnetically coupled while the other two are ferromagnetically coupled. The exchange coupling of the adatoms with the substrate used to perform the simulations was calculated from the YSR of a single impurity. For each crystallographic direction, we need to adjust the value of k_F to account for the roundness of the edges of the real β-Bi_2PdFC [Figs. 3.1(c) and 3.1(d)]. There is no further parameter change for the simulation in each direction to make them more robust.

Accounting for the roundness of the real FC, we can perfectly describe the evolution of the YSR states as we built the crosses [Figs. 3.6(h) and 3.6(i)]. Moreover, it is important to note that the strong SOC of the surface probably affects the colinearity of the adatom's spins, which we are not considering in our calculations. In the absence of SOC, the RKKY interaction favors the FM or AFM alignments but no other configurations. For a finite SOC, however, a perfect alignment is probably not the most realistic configuration. Any shift from a perfect alignment effectively decreases or increases the interaction between adatoms. This can be fixed by lowering or increasing k_F, which has the same effect. As we took realistic values of k_F, and the simulations calculated for AFM or FM configuration fit the spectrum of the multiimpurity systems well, we believe the spins are close to a perfect FM or AFM alignment.

In conclusion, the data for the starts in the (110) and (120) directions [Figs. 3.6(b) and 3.6(g)] indicate that these adatoms are ferromagnetically coupled, as when we add Mn to the structures, the YSR states further split. The simulation supports this [Figs. 3.6(h) and 3.6(i)], for which we assumed a FM coupling, and as we see, the simulations follow the same trend as the measured data. Moreover, note that all data and simulations show a single [Fig. 3.6(a)] or couple of YSR states [Figs. 3.6(b) and 3.6(g)]. This is due to the symmetry of the stars. As next-nearest-neighbor interaction is not considered, a single-valued interaction term is used (all adatoms interact with each other with the same RKKY interaction); furthermore, the exchange coupling of each adatom is also the same. This allows for a single YSR state in the AFM case and two YSR states (a split state) in the FM case.

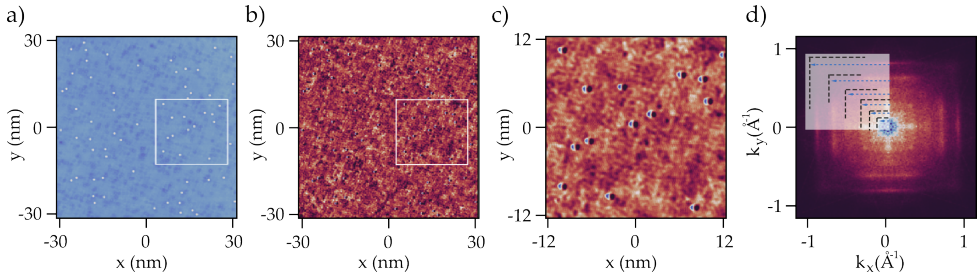

Figure 3.7: **QPI pattern from the intrinsic impurities of β-Bi_2Pd: (a)** 60 nm×60 nm topographic image of the bare β-Bi_2Pdsurface (V=50 mV, I=250p). **(b)** dI/dV map at V=50 mV. **(c)** a 24 nm×24 nm zoom-in of the dI/dV map. The oscillatory pattern arising from the impurities can be distinguished. **(d)** FFT of the QPI pattern showing a square-shaped dispersion taken from Ref. [1]

3.4 Multiband superconductivity and orbital selectivity

At the beginning of this chapter, we have introduced the β-Bi_2Pdas a multiband superconductor with two surface and bulk bands [Fig. 3.1(c)]. Still, throughout the chapter, we have omitted this fact and used a single band to explain the experimental results. In the following, using Quasiparticle Interference (QPI) measurements, we analyze how the extensions of the YSR states [Fig. 3.3(h)] can be used as a visualization tool for understanding the band structure of a material.

	Wavevec. (Å^{-1})	Scattering Bands
q_A	0.12 ± 0.03	S_1-B_1
q_B	0.2 ± 0.04	S_1-S_2
q_C	0.31 ± 0.03	S_2-B_1
q_D	0.50 ± 0.04	B_1-B_2
q_E	0.68 ± 0.03	S_1-B_2
q_F	0.90 ± 0.02	S_2-B_2

Table 3.1: **Scattering vectors.** A list of all scattering vectors measured from the FFT and their corresponding bands.

Before introducing the QPI pattern of in-gap states (arising from magnetic adatoms), it is essential to understand the out-gap QPI patterns we see in the bare β-Bi_2Pdsubstrate coming from intrinsic impurities (Bi adatoms and Pd vacancies). Figure 3.7 shows an 80 nm×80 nm scan of the bare superconducting surface [Fig. 3.7(a)] and its relative dI/dV map at V = 50 mV [Figs. 3.7(b) and 3.7(c)]. The dI/dV map gives information about the LDoS, which is proportional to the local charges. As the QPI are charge oscillations, the dI/dV is related to the electrons' scattering at the selected voltage. A FFT calculation of the image [Fig. 3.7(d)] represents the distribution of frequencies associated with said scatterings. Note that from Fig. 3.7(d), one can extract six prominent scattering vectors that form the FC's square shape. The value of these vectors is summarized in Table 3.1.

Comparing the vectors with the values taken from literature [30, 31], we can iden-

tify the different bands taking part in the scattering processes, see Fig. 3.1(c). There are no scattering vectors connecting the same band. The single band solution of the magnetic impurity on a superconductor produces oscillations in the extension of the YSR state due to scattering in the same band from k_F to $-k_F$. This produces, in analogy to the Friedel oscillations, a $2k_F$ oscillatory wavefunction, which can be seen in the $\sin^2(k_F r)$ term in Eq. (2.34).

To understand why intraband scattering terms do not appear in the FFT, we consider spin conservation in the scattering processes. ARPES [31] measurements and DFT calculations [30] demonstrated a strong Rashba spin-orbit coupling on the surface. Due to spin and momentum locking in a Rashba system, the direction of momentum fixes the spin of the electrons [Fig. 3.1(c)]. Then, due to time-reversal symmetry, spin is flipped for opposite momentum direction, e.g., if $(\mathbf{k}, \uparrow)$ are connected, $(-\mathbf{k}, -\uparrow)$ will be connected. Hence, the strong SOC turns the bands with a helical spin texture. In this scenario, as we show in our calculations in App. A.2, QPI oscillations vanish because backscattering is forbidden between states with different spin. The only possible source of the oscillatory behavior is the interband scattering.

Interband scattering, i.e., the interference of electrons from different bands induced by an impurity, could explain the scattering vectors. However, it is essential to note that if one takes two distinct bands, they are in two different Hilbert spaces, as the bands are eigenstates of the crystal's Hamiltonian. Although a single impurity can be responsible for the scattering from one band to another, the initial and final electronic states lie in two different subspaces. Note that the Friedel oscillations arise from the constructive interference between an incoming and an outgoing wave. If the two waves are in different Hilbert subspaces, the interference does not happen, as they are both in orthogonal states. In conclusion, a single impurity with an interband scattering term is not enough to ensure Fridel oscillations with the semi-sum of the two bands' Fermi vector; hybridization between different bands, which connects the different subspaces and breaks orthogonality, is needed for this. This statement is also proven in Appendix A.2.

In the following, we present the effects of magnetic impurities on the QPI pattern. We note that, below the superconducting gap, as the YSR states arise from the hybridization of the d-orbitals with a single band, some of the scattering vectors in Table 3.1 are suppressed. Moreover, an effective theoretical model that describes the scattering processes for the magnetic as well as the non-magnetic impurities is described. This model accounts for the polarization and hybridization of the bands.

3.4.1 QPI of V adatoms on β-Bi_2Pd

Figure 3.8 depicts the QPI measurements done on V adatoms on top of β-Bi_2Pd. The experimental results are taken from Ref. [1]. The electronic configuration of a free V atom is $[Ar]\ 3d^3\ 4s^2$, so its total spin is $S = 3/2$. Spectroscopic measurements on top of the adatoms indicate that the V adatom hosts three distinct YSR states: $\pm\alpha$, $\pm\beta$ and $\pm\gamma$, indicated by arrows in Fig. 3.8(a). The energies, extracted from Fig. 3.8(a), read $\omega_\alpha = \pm 0.22$ meV, $\omega_\beta = \pm 0.63$ meV and $\omega_\gamma = \pm 0.72$ meV (the tip's gap has been disregarded). This indicates that there are three distinct YSR channels

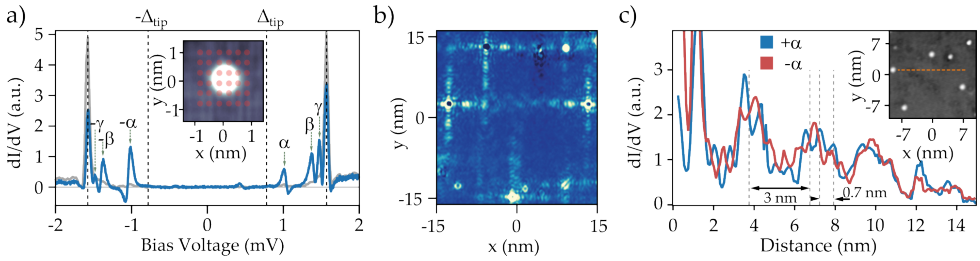

Figure 3.8: **Extension of the YSR states of V on β-Bi_2Pd. (a)** Spectroscopic measurement (setpoint V=2 mV, I=500 pA) on the top of the V adatom (blue) in the inset image compared to the spectra of the bare superconductor (grey). Three YSR states are indicated with arrows. **(b)** dI/dV map of a 15 nm×15 nm area containing several V adatoms at the α YSR energy. **(c)** Line spectra along the (100) crystallographic direction at the α YSR energy. Figure adapted from Ref. [1].

associated with the three electrons of the d-shell. Thus, the spin 3/2 persists on the surface.

A dI/dV map of a few V adatoms at the energy of peak α reveals the nesting of the YSR wavefunction along the crystallographic direction (100) and (010) [Fig. 3.8(b)], similar to Fig. 3.3(h). A cut along the (100) direction of peaks $\pm\alpha$ reveals a complex oscillatory pattern of the extension of the YSR state, depicted in Figure 3.8(c). The long extension of the YSR wavefunction (up to 15 nm) is measured, which is expected [see Sec. 3.2] due to the focusing effect of the square-shaped FC, resembling a 1D system.

To disentangle the possible effects responsible for the complex extensions of the YSR states, as we did for normal scatterers (previous paragraphs), we calculate the FFT of an ensemble of adatoms [1]. Fig. 3.9(a) shows a topographic image of an ensemble of adatoms in a 80 nm×80 nm region, and Fig. 3.9(b) the corresponding dI/dV map at $V = \omega_\alpha$. The calculated FFT from 3.9(b) is shown in 3.9(c). Two concentric squares can be spotted, each corresponding to a scattering vector. An average of the FFT signal in a region close to the (100) direction, white rectangle in Fig. 3.9(c), is plotted in Fig. 3.9(d) (cyan curve), along with the corresponding data for Fig. 3.7(d) (red curve) for comparison.

The two plots in Fig. 3.9(d) refer to the scattering at energies higher than the superconducting gap (red curve) and at the energy of the α peak (cyan curve). Consequently, the former is related to the normal scattering, while from the latter, we can extract information about the superconducting condensate. Comparing both curves, we observe that the cyan curve shows fewer scattering vectors. We can only see two vectors, which we named q_1 and q_4. The values for these vectors read $q_1 = 0.20 \pm 0.02$ Å^{-1} and $q_4 = 0.90 \pm 0.04$ Å^{-1}, which coincide with q_A and q_F in Table 3.1. These two vectors correspond to scattering processes connecting the surface bands S_2 with other bands, namely to S_1 and B_2. In contrast, we do not see any scattering vector connecting (for example) S_1 with B_1. The involvement of only those scattering pro-

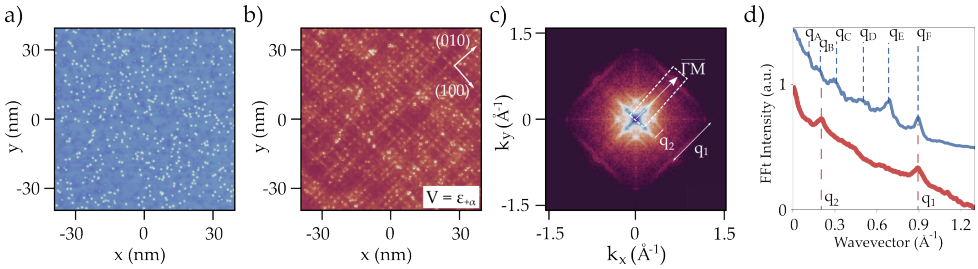

Figure 3.9: **QPI measurements of V adatoms on β-Bi_2Pd. (a)** 80 nm×80 nm topographic image of the β-Bi_2Pdsurface with 1% coverage of V adatoms (V=100 mV, I=100 pA). **(b)** dI/dV map of the same region at the voltage of the α YSR state. **(c)** FFT of panel **(b)**, showing two main scattering square shaped contours depected by q_1 and q_2. **(d)** Cut of the FFT along the $\overline{\Gamma M}$ direction (k_x) compared to the QPI of the normal scatterers measured at V=50 mV. Only two of the six scattering vectors appear in the extension of the YSR state. Figure adapted from Ref. [1].

cesses related to one of the bands, namely S_2, is a fingerprint of this band being part of the YSR channel. This indicates that the d-orbitals of V are hybridized with the S_2 surface band.

In the following subsection, we present an effective theory demonstrating the crucial role of interband pairing in the superconducting state, the formation of the YSR states, and how it modulates the QPI of single impurities. We start by describing a general two-band Hamiltonian with spin-orbit coupling and slowly go through the approximations that allow us to describe the QPI pattern with simple spin and band index conservation rules.

3.4.2 Helical Spin-Polarized Bands

Since the β-Bi_2Pdsubstrate has a square-shaped FC, the extension of the YSR states in the (100) and (010) directions resemble that of a 1D crystal due to the focusing effect [Sec. 3.2]. As these are the directions where the maximal dI/dV signal is, and they are essentially independent of each other[1], we can center our attention on one of the directions. Moreover, as the solution for a square-shaped FC is almost the same as that from a 1D system, we implement an effective 1D Hamiltonian, simplifying solving a multiband problem by removing the angle integral in App. A.1.

We define a general multiband 1D Hamiltonian with Rashba SOC to describe the

[1]Appendix A.2 shows the exact calculations of the GF for a square-shaped FC. From there, we can extract that the extension in the (100) direction ((010) direction) is due to the FC sides that are parallel to the k_x (k_y) axis, i.e., these two extension can be calculated independently.

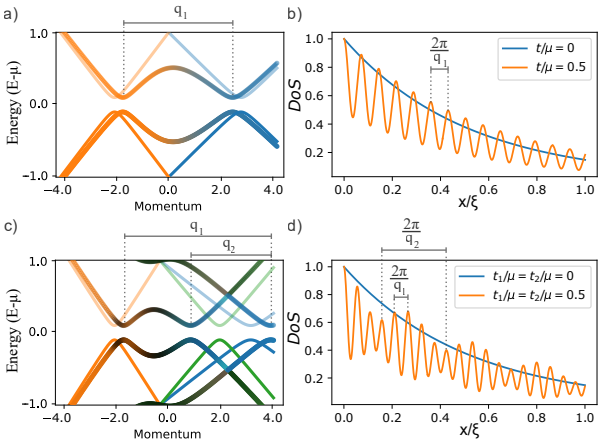

Figure 3.10: **QPI in multi-band systems. (a)** and **(c)** 1D band structure for a two-band (three-band) model. We plot the original bands and the hybridized ones. **(b)** and **(d)** Decay of the DoS at the YSR energy for the two-band (three-band) model without (blue) and with (orange) interband hopping. The vectors corresponding to the observed oscillations are marked as q_1 and q_2.

system:

$$\begin{aligned}\check{H} = &\left[(\frac{k^2}{2m_1} + \lambda_1\sigma_3 k - \mu)\tau_3 + \Delta\tau_1\right]\frac{(1+\eta_3)}{2} \\ &+ \left[(\frac{k^2}{2m_2} + \lambda_2\sigma_3 k - \mu)\tau_3 + \Delta\tau_1\right]\frac{(1-\eta_3)}{2} + t\eta_1 \ .\end{aligned} \tag{3.9}$$

Here, the σ, τ, and η are Pauli matrices that describe spin, particle-hole, and band degrees of freedom, respectively, m_1 and m_2 describe the effective mass of the bands, and λ_1 and λ_2 their corresponding Rashba spin-orbit coupling. These two can be positive or negative, depending on the relative spin orientation of the bands. As the β-Bi_2Pdhas an absolute superconducting gap, so we assume the two bands to have the same superconducting coupling parameter Δ. Finally, the chemical potential is described as μ, and we added the simplest interband coupling term as t. This interband coupling is a constant, not spin-independent, hopping term. We disregarded any anomalous interband coupling term as the coupling strength would be small compared to a direct hopping term ($\Delta \ll \mu$).

As mentioned above and demonstrated in App. A.2, a single impurity with an interband scattering term does not host an oscillatory behavior in the extensions of the YSR state. In contrast, when a hopping term, t, is added to hybridize the bands, the interference of incoming and outgoing waves in different bands emerges. With finite t, the incoming and outgoing waves are no longer in different bands but in new bonding- and antibonding-like bands [Figs. 3.10(a) and 3.10(c)]. The hybridization term mixes the original bands (S_1, S_2, B_1, and B_2) forming a new set hybridized bands (S_1^*, S_2^*, B_1^* and B_2^*), with renormalized wavevectors ($k_{Fi}^* = \sqrt{2m_i^*\mu_i^*}$) distinct to the original ones ($k_{Fi} = \sqrt{2m_i\mu_i}$).

Figure 3.9 shows the QPI patterns for a two-band and a three-band model with their respective band dispersion. Figure 3.10(b) shows the extension of the YSR DoS, which oscillates with a period related to the renormalized Fermi momentum

of the system [q_1 in Fig. 3.10(a)]. In order to host two oscillations, the same as measured in the V adatoms, we add a third band to the Hamiltonian [App. (A.21)]. In Sec. 3.4.1, we deduced that the d-orbitals of V are hybridized to a single band, S_2; therefore, when the adatom is added to the Hamiltonian, we assume the YSR channel is only hybridized to one of the bands existing before turning on t. The colors in the bands plotted in Figs. 3.10(a) and 3.10(c) represent the overlap between the original bands and the hybridized ones. The YSR is connected to the blue band, which has a maximal overlap with the normalized bands at the furthermost positive momenta. See Fig. 3.10(c). The oscillatory pattern from a three-band Hamiltonian is depicted in Fig. 3.10(d). A double oscillation is observed in the extension of the YSR state. The period is connected to the renormalized Fermi momenta of the bands, q_1 and q_2 in Fig. 3.10(c), and their relative intensity to t_{12}/t_{13}: the hopping term between each band. See App. A.2.

The renormalization of the Fermi momenta complicates comparing the observed scattering vectors in Fig. 3.9(c) with ARPES measurements [31] and their respective DFT calculations [30, 31]. If the hopping term is not an intrinsic property of the substrate (it arises from our experimental setup), we can not compare it with the ARPES measurements. Still, the DFT calculations [31] suggest that these bands are connected at higher energies, thus providing the origin of the hybridization. Consequently, as the bands are originally connected, the Fermi momenta obtained by DFT and ARPES are related to the normalized momenta described previously. From our analysis, we conclude that the β-Bi_2Pdshould not be described with four unconnected surface bands but with hybridized bands.

3.5 Conclusions

We have presented an analytical method to compute the GFs and the spectrum of a two-dimensional superconductor with an arbitrary FC. We applied the technique to FCs with the shape of a regular polygon. In the presence of magnetic impurities, we found that the spatial dependence of the YSR subgap states reflects the symmetry of the FC and that the characteristic decay length of such states strongly depends on the spatial direction. Namely, Fermi surface nesting in low symmetry cases leads to a focusing effect of the YSR spectrum. We contrasted our model with STM measurements on materials with different FC shapes and found a good agreement. The applicability of the theory to multi-impurity structures was proven. This and the relation between the extension of YSR states and FC opens the doors to finding materials where the focusing effect can help build atomic structures where the interaction between atoms is maximized.

Furthermore, these quasi-1D decaying wave functions were used to analyze the QPI of V adatoms on the surface of β-Bi_2Pd. We found that the QPI patterns can be used to extract information about the intricate multiband structure of the material and to understand the formation of the Cooper Pair condensate. The analysis of the QPI pattern proved the β-$Bi_2Pd$is formed from several bands with a square-shaped FC. Moreover, we found that the hybridization between bands and the strong Rashba-

type SOC is needed to describe the system, as seen by ARPES measurements and DFT calculations [30, 31]. Finally, we proved that the formation of the YSR states is closely linked to the hybridization of the magnetic impurity's orbitals with a single band.

4

Quantum Impurities in proximitized Superconductors

In the previous Chapter, we used a classical approximation of the spin [19, 23, 81] to understand the STM measurements done on V and Mn adatoms on the β-Bi_2Pdsuperconducting surface. The advantage of this approximation is that the problem is analytically solvable, which allowed us to calculate the spatial extension of the YSR states. Moreover, any system of interacting impurities can be exactly described, without the need of employing effective Hamiltonians. However, this approximation does not take into account the quantum nature of the impurity's spin, which can give rise to many-particle effects such as the Kondo effect [21] and it is determinant when, e.g., describing the spin carried by the YSR excitations [144].

A fully quantum-mechanical treatment of the problem can provide a comprehensive description of experiments [107] but often requires the use of sophisticated but numerically costly methods such as the numerical renormalization group (NRG) [37, 38] or continuous time Montecarlo simulations [39]. Several models have emerged that treat the quantum many-body aspects of YSR states that even allow the incorporation of higher spin and anisotropic impurities into the problem with affordable computational efforts. These models use drastic approximations, representing the superconductor by a single site [36, 145, 146] or considering an infinite gap superconductor [147, 148] and have already been successfully used to explain some spectral features observed in recent experiments [3, 34, 149, 150].

In this chapter, we study the interaction of single magnetic impurities with a thin metallic film proximitized by a superconductor. Proximitized systems have been studied mainly in the diffusive limit using the Usadel formalism [151]. This approach predicts the decay of the proximity effect in the limit of electron mean free paths much smaller than the superconducting coherence length and successfully describes spectroscopic features such as the closing of the gap and the formation of a minigap in the proximitized material [152, 153]. Experiments with diffusive systems [153–156] have clearly confirmed those predictions. However, the systems studied in this context are mesoscopic in size, and the experimental probes employed cannot resolve the behavior at local scales caused by, for example, a single magnetic impurity. On the other hand, thanks to currently available molecular beam epitaxy techniques, it is possible to grow epitaxial metallic overlayers with controlled thicknesses of just a few atomic layers on top of superconductors [2, 3, 157, 158]. These novel hybrid systems open the door to act as a host of complex molecular spin architectures engineered by on-surface synthesis [159–163], not occurring naturally on bulk superconductors due to their large reactivity, and explore the interaction of collective spin modes with pairing correlations. Such thin crystalline layers are not within the diffusive limit; instead, they must be described using a ballistic approach.

In this chapter, we introduce an experimental system comprising a magnetic molecule on top of a proximitized superconductor [Sec. 4.1]. This system, reported in Refs. [4] and [3], motivates us to introduce a single-site model for the superconductor that captures the quantum nature of a spin on top of a proximitized superconductor and proves that it is a good approximation to treat the YSR problem [164] [Sec. 4.2]. In Sec. 4.3, this model is used to interpret the results obtained on magnetic molecules on top of a proximitized superconductor [3]. Finally, in Sec. 4.4, we apply the single-site model to predict the many-body spectrum of a molecular spin chain on a superconductor. This system is proposed as a prototype of a spin-singlet-based qubit that could potentially enhance the lifetime of modern spin qubits.

4.1 Magnetic molecules on the proximitized Au/V(100) surface.

The theoretical model introduced in Sec. 4.2 is motivated by experimental results on Iron chlorinated-porphyrin (FeTPPCl) molecules on top of the novel Au/V(100) surface [2, 3], which is extensively described in Refs. [4] and [3]. The molecule is a $S = 5/2$ magnetic impurity with easy axis magnetic anisotropy, $D = 0.75$ meV [2, 165, 166]. The Au/V(100) substrate is formed by depositing a few layers of Au on top of V(100) in UHV conditions. Vanadium is a s-type superconductor with a gap $\Delta = 0.76$ meV. Here, it proximitizes the epitaxial gold film grown on top, converting it into an ideal platform to measure the interplay between molecular physics and superconductibity [2, 3].

Although the interaction of similar molecules with superconducting surfaces has already been studied [165, 166], the interaction with proximitized superconductors is unknown. When a thin metallic layer proximitized by a superconductor is analyzed in the ballistic limit, subgap bound states appear in the normal region and extend into the superconductor over distances of the order of the coherence length. These states arise from Andreev reflection (AR) processes at the superconductor/normal metal interface and the vacuum side of the layer. Since they were predicted by de Gennes and Saint James for the first time [167, 168], we named them de Gennes-Saint James (dGSJ) states.

Figure 4.1(a) illustrates the Au/V(100) surface, with a constant height image showing the atomic resolution of Au in the lower left inset. The surface appears flat and has a square lattice. Figure 4.1(b) compares spectroscopic measurements on bare Vanadium and the proximitized system. The bare Vanadium gap appears on the metal film as narrow subgap resonances separated from the continuum of states [Fig. 4.1(b)]. These are dGSJ states. Due to their protection, the lifetime of spin excitations in these molecules is increased [2]. The energy of these states can be controlled with the thickness of the normal metal layer [2, 35, 169].

Deposition of FeTPPCl molecules onto the Au/V(100) surface results in four types of molecular species: 4-fold FeTPPCl, 2-fold FeTPPCl, 4-fold FeTPP, and 2-fold FeTPP, illustrated in Fig. 4.1(c). Some molecules lose their Cl during evaporation, and the observed 2-fold or 4-fold symmetries result from distinct adsorption sites.

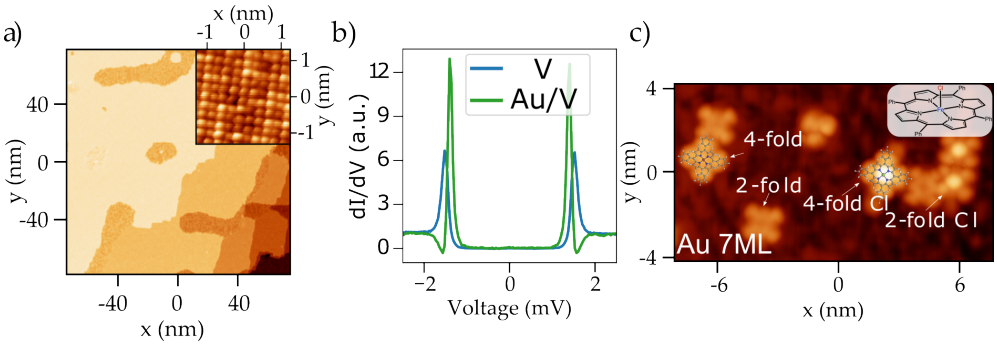

Figure 4.1: **Description of the experimental system. (a)** Topographic STM measurement of the Au/V(100) surface (V=10 mV, I=100 pA). The inset shows the atomic resolution of Au (V=10 mV). **(b)** Comparison between the dI/dV in a seven monolayer Au/V(100) surface and bare Vanadium. **(c)** STM image showing different FeTPP and FeTPPCl species on the same substrate (V=300 mV, I=30 pA). Inset: chemical structure of FeTPPCl

Notably, only one type of chlorinated species exhibits distinct spectral fingerprints, revealing their magnetic state. The 2-fold FeTPPCl shows a single in-gap state with two out-gap spin excitations [2], attributed to inelastic spin excitation. The 4-fold FeTPPCl has multiple in-gap and out-gap excitations.

The protection derived from the dGSJ states, separated from the continuum of states, on the YSR excitations measured on this system makes the classical approximation of the spin [Sec. (2.4.1)] obsolete. For this reason, in Sec. 4.2, we present a single-site model that captures the quantum nature of a single spin-1/2 magnetic impurity on a thin metallic film in proximity to a superconductor. Then, in Sec. 4.3, we extend the single-site model to account for a higher spin and magnetic anisotropy, which we use to understand the complex spectra measured on the FeTPPCl molecules on Au/V(100).

4.2 Quantum Spin Impurities on Proximitized Metals

The studied system is sketched in Fig. 4.2(a): a magnetic impurity exchange coupled to a thin metallic layer proximitized by a bulk superconductor. In Sec. 4.2.1, we first study the system treating the magnetic impurity as a classical spin in the ballistic limit when a single dGSJ bound state exists in the gap [Fig. 4.2(b)]. Within this approximation, we find that a YSR state is formed by redistributing the spectral weight of the dGSJ bound state, i.e., a large overlap exists between the Bogoliubov-de Gennes spinors of the dGSJ and YSR states [Sec. 4.2.2].

Motivated by this result, we propose that a single-site description is a relevant simplified model for the complex system consisting of the magnetic impurity on the proximitized thin film [Sec. 4.2.3]. This model can be solved exactly and provides a

computationally cheap way to treat the many-body effects associated with the quantum spin of the impurity. The adequacy of the single-site model is then assessed by employing a "poor man's" scaling analysis [Sec. 4.2.4]. To this end, we introduce a Hamiltonian consisting of a single-site model perturbed by an impurity-mediated coupling to the continuum of other excitations. Under certain conditions, we find that, as the high-energy continuum states are integrated out, the impurity remains most strongly coupled to the single site describing the dGSJ state. These results are published in Ref. [164], and the most technical details have been relegated to Appendix B.4.

4.2.1 System and Model

Figure 4.2(a) shows a schematic picture of the system studied in this section, which is motivated by experiments reported in Sec. 4.3 and Refs. [2, 3, 158, 170]. The system consists of a magnetic impurity on top of a thin, normal metal film (N) in proximity to a superconductor (S). The superconductor occupies the half-space $x > 0$, while the N film corresponds to $-a < x < 0$. The system is translationally invariant in the (y, z)-plane, so it is convenient to describe the electron wave function as $\psi(x, \mathbf{k}_\parallel)$, where $\mathbf{k}_\parallel$ is the component of the momentum vector parallel to the S/N interface at $x = 0$. We assume a perfect S/N interface with no Fermi-level mismatch or potential barrier. The effect of a Fermi-level mismatch is to change the effective thickness of the metallic layer for different momentum directions, thus modifying the energy of the bound dGSJ state. See Ref. [22] and Sec. B.2 for an extended discussion. This would mainly affect the non-normal propagation direction, which is disregarded due to the

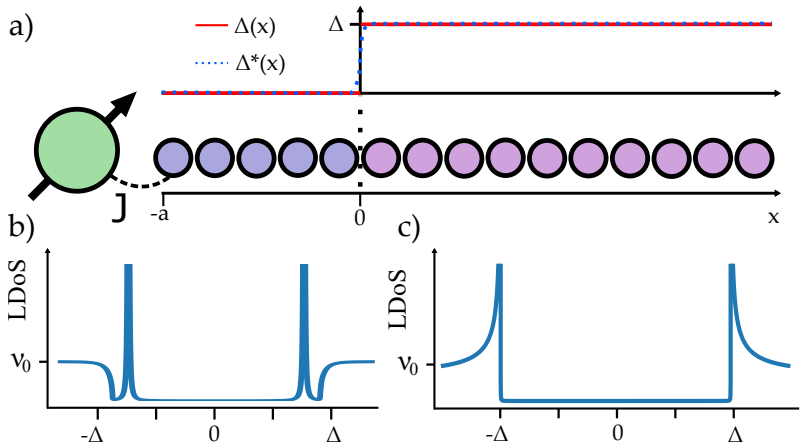

Figure 4.2: **Representation of a magnetic impurity on a proximitized superconductor. (a)** Representation of an impurity on a normal metal layer (darker) on a superconductor (lighter) atoms. **(b)** and **(c)** LDoS in the thin proximitized metallic film and the bulk of the superconductor, respectively. ν_0 is the normal state DoS.

geometry and nature of the analyzed system (see below).

In the absence of mismatch, the N region acts as a cavity for electrons with energy $E < \Delta$: they undergo Andreev retro-reflections at the S/N interface and normal, specular reflections at the interface with the vacuum. According to the Bohr-Sommerfeld quantization rule, the phase accumulated along a closed classical trajectory must be a multiple of 2π. A closed trajectory in the N/S system under consideration consists of two Andreev retro-reflections at the S/N interface and two normal reflections at $x = -a$. Thus,

$$\frac{2a}{\xi \cos\varphi}\frac{E}{\Delta} - \cos^{-1}\left(\frac{E}{\Delta}\right) = n\pi \tag{4.1}$$

where $\cos^{-1}(E/\Delta)$ is the phase shift associated to each AR, $\xi = \frac{v_F}{\Delta}$ is the coherence length of the superconductor and $\cos\varphi = k_\parallel/k_F$. Equation (4.1), determines the subgap dGSJ bound states [167].[1] This solution is valid for clean N-layers with a mean free path larger than its thickness a. When considering all angles of non-specular directions, Eq. (4.1) describes a continuum of subgap states [167, 172].

In STM experiments [2, 3], this continuum is not observed, and the dGSJ states appear as sharps subgap peaks. This happens for several reasons. The tunneling in STM experiments is mainly specular [173], and the decay of the wavefunction of these substrate excitations into vacuum is maximized for zero $\mathbf{k}_\parallel$. Then, in the tunneling regime, excitations with large $|\mathbf{k}_\parallel|$ are filtered out [173–175], and dGSJ states are observed as narrow subgap resonances made of dGSJ quasiparticles with $\mathbf{k}_\parallel \approx 0$ [2, 3]. See Figs. 4.2(c) and 4.1(b).

Additionally, small amounts of disorder tend to randomize trajectories, particularly suppressing the coherence of non-specular directions. A magnetic impurity on top of the proximitized film has compact and anisotropic orbitals that typically couple to several scattering channels from the substrate. However, since the dGSJ quasiparticles with $\mathbf{k}_\parallel \simeq 0$ penetrate farther into the vacuum, they are also expected to contribute substantially to the most strongly coupled scattering channel. Thus, one can effectively approximate the tunneling problem using a one-dimensional model which neglects the motion parallel to the surface:

$$\hat{H} = \hat{H}_0 + \hat{H}_J \ , \tag{4.2}$$

where

$$\begin{aligned}\hat{H}_0 = &\sum_\sigma \int_{-a}^{\infty} dx\, \hat{\psi}^\dagger_\sigma(x)\left[-\frac{\hbar^2}{2m^*}\partial_x^2 - E_F\right]\hat{\psi}_\sigma(x') \\ &+ \int_0^\infty dx\, \Delta\, \hat{\psi}^\dagger_\uparrow(x)\hat{\psi}_\downarrow(x) + \text{h.c.}\ ,\end{aligned} \tag{4.3}$$

[1] The dGSJ states in S/N structures arise from the same phenomenon as the Andreev bound states in SNS junctions, precisely the Andreev reflection at an S/N interface. This has been discussed, for example, in Ref. [171] Equation (4.1), which describes the dGSJ states in an S/N structure, coincides with the equation for the Andreev bound states in an SNS junction when the length of the normal region N is twice the value of the film thickness a. The phase difference between the superconductors is zero.

and

$$\hat{H}_J = \sum_{\sigma\sigma'} J\hat{\psi}^\dagger_{0\sigma}\hat{\mathbf{S}}\cdot\mathbf{s}_{\sigma\sigma'}\hat{\psi}_{0\sigma'}\ . \tag{4.4}$$

Here, $\hat{\psi}_\sigma(x)$ ($\hat{\psi}^\dagger_\sigma(x)$) represents the annihilation (creation) operator for an electron with spin $\sigma =\uparrow,\downarrow$ in the metal-superconductor substrate. $\hat{H}_0$ describes a proximitized thin film of thickness $a > 0$. The first term contains the kinetic energy and chemical potential E_F, and the second is the s-wave pairing potential. The pairing potential is not self-consistently calculated. Corrections due to self-consistency result in a spatially non-uniform pairing potential, $\Delta(x)$, but they have only a small effect on the spectral properties of the dGSJ states [174, 175], see Fig. 4.2(a). The magnetic exchange with the impurity is described by $\hat{H}_J$, with $\mathbf{s}$ denoting the electron-spin Pauli matrices and $\hat{\mathbf{S}}$ denoting the impurity spin operator. The operators $\hat{\psi}_{0\sigma}$ ($\hat{\psi}^\dagger_{0\sigma}$) annihilate (create) electrons at the position of the impurity. For the one-dimensional model introduced above, $\hat{\psi}_{0\sigma} = \hat{\psi}_\sigma(x = -a)$. In the following section, we analyze this model using the classical approximation approach, i.e., the impurity spin, $\hat{\mathbf{S}}$, is treated as a classical vector.

4.2.2 YSR in Proximitized Thin Films

In the previous section, we have derived the equation that determines the spectrum of subgap states [cf. Eq. (4.1)] using the Bohr-Sommerfeld semiclassical approximation. As explained above, we focus on the one-dimensional case, i.e., $\cos\varphi = 1$ in Eq. (4.1). To deal with the coupling to the magnetic impurity, we solve the model described by Eqs. (4.2)-(4.4). To this end, we use Green's Functions (GFs) and follow the approach outlined in Ref. [175], from which we can get the LDoS. The technical details of the calculation are described in Sec. B.1.

Figure 4.3(a) shows the LDoS on the surface as a function of film thickness. As we increase the thickness, new dGSJ states enter the gap. The GF also has poles with a finite imaginary part outside the superconducting gap which correspond to states in the continuum (i.e. above the superconductor gap), and give rise to McMillan-Rowell-Tomasch oscillations [176, 177]. From here on, we focus our discussion on thin films with a single subgap bound state, and we tackle the coupling to the magnetic impurity.

Using the GFs obtained for the proximitized thin film in the Dyson equation, Eq. (2.31), we get the YSR GFs:

$$\check{G}_{YSR}(x,x') = \check{G}(x,x') + \check{G}(x,-a)\check{V}(\check{\mathbb{1}} - \check{V}\check{G}(-a,-a))^{-1}\check{G}(-a,x')\ . \tag{4.5}$$

Figure 4.3(b) and 4.3(c) shows the evolution of the YSR state (for $a = 0$ and $a \sim 0.2\xi$, respectively) as a function of the exchange coupling $\alpha = \nu_0\pi JS$ [Eq. (2.33)], with ν_0 being the normal metal DoS. Note that the exchange coupling splits the dGSJ state into two states (spin up and down), one of which shifts to higher energy while the other shifts to lower energy, see Fig. 4.3(c). As J increases beyond a certain value, the higher energy state disappears into the continuum. From this point on, the energy of the remaining subgap state behaves similarly to a YSR in a bulk superconductor

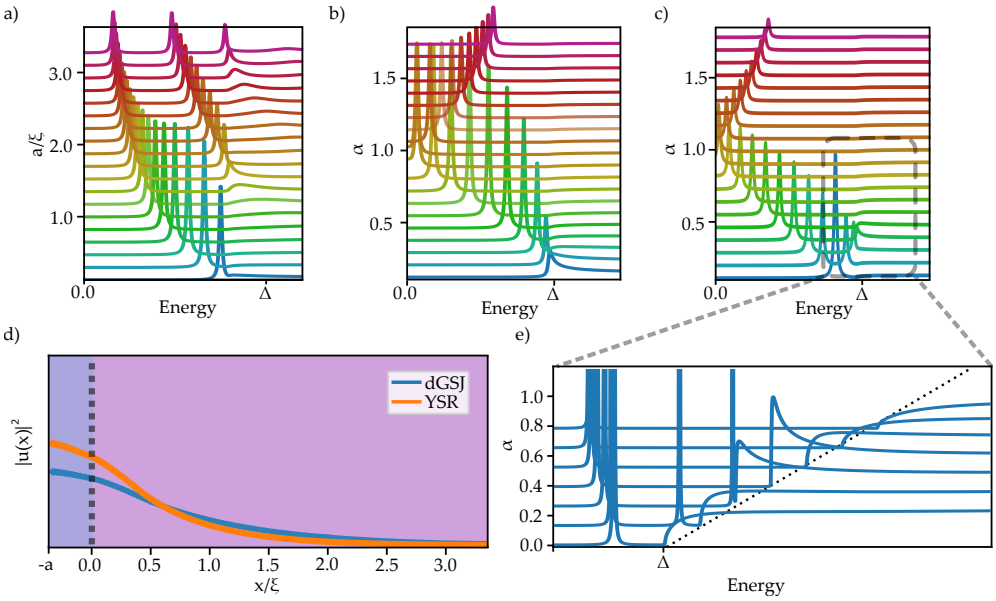

Figure 4.3: **The YSR states on a proximitized superconductor. (a)** Evolution of the dGSJ states as a function of the thickness in units of the coherence length ($\xi = v_F/\Delta$) of the metallic layer. **(b)-(c)** Evolution of a YSR spectral density on a pure superconductor (i.e., $a = 0$) and a proximitized superconductor for a fixed metallic layer thickness ($a \sim 0.2\xi$) as a function of the exchange coupling, respectively. **(d)** Particle component of the amplitude of the dGSJ and YSR states, as calculated from the residue of the GF, averaged over distances $\gg k_F^{-1}$. **(e)** Zoom-in of the evolution of the YSR state spectral density.

[19, 23, 81]. For thicker films with more than one dGSJ state, the behavior is similar: each bound state splits in two, shifting in opposite directions depending on their spin projection, with more excited states eventually merging in the continuum and disappearing.

The transmutation of the dGSJ into the YSR state can be regarded as a result of a spectral reorganization around $|\omega| = \Delta$ caused by ARs [Fig. 4.2(c)]. Using an analogy to semiconductor physics, YSR states appear in a superconductor because of the coherence "peak" behavior $\sim (\omega^2 - \Delta^2)^{-1/2}$ [Fig. 4.2(b)] resembles that of a van Hove singularity at the bottom (top) of the conduction (valence) band of a one-dimensional insulator. Bound states appear due to the infinitesimal attraction provided by the magnetic impurity Dirac-delta potential. However, in a proximitized film, AR reorganizes the spectral weight by removing the van Hove-like singularity while shifting most of its spectral weight to the dGSJ state [Fig. 4.2(c)]. The localization of the dGSJ states at the surface enables the transmutation of one of the dGSJ states per spin into a YSR. Thus, a large overlap of the wavefunctions of YSR and dGSJ states

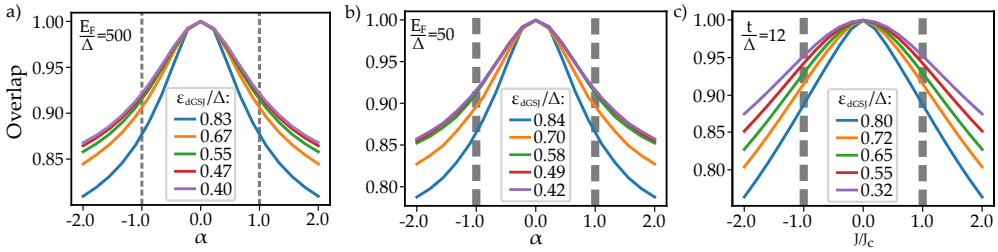

Figure 4.4: **Overlap between the YSR wavefunction and the dGSJ wavefunction. (a), (b)** Calculation done from the continuous model for different dGSJ bound state energies and values of E_F/Δ. **(c)** The same calculation done with a tight-binding model [see Sec B.2 for details about the latter].

is expected.

In the following, we compute the overlap of the YSR and the dGSJ states as a function of the exchange coupling J. This can be achieved by using the GF obtained from the scattering solution of the problem with and without magnetic impurity [Eq. (B.10)]. The square of the overlap is computed from the following integral involving the residue of the two GFs:

$$\begin{aligned} |\Theta|^2 &= \int dx \left[u_{dGSJ}(x) u^*_{YSR}(x) + v_{dGSJ}(x) v^*_{YSR}(x)\right] \\ &= \int dx dx' \,\mathrm{Tr}\left\{\mathrm{Res}\ \check{G}(x,x'))\,\mathrm{Res}\ \check{G}_{YSR}(x',x)\right\}. \end{aligned} \tag{4.6}$$

Here $\mathrm{Res}\,\check{G}_{YRS}$ ($\mathrm{Res}\,\check{G}$) is the residue of the Nambu GF matrix at the YSR (dGSJ) pole with spin up, related to the Nambu spinor amplitudes u_{YSR} and v_{YSR} (u_{dGSJ} and v_{dGSJ}) [Sec. B.1].

In Fig. 4.4(a) and 4.4(b), we show the behavior of the overlap Θ as a function of exchange coupling J for different values of film thickness, which determines the dGSJ state energy. To check our results beyond the leading order in Δ/E_F, we also compute the overlap by solving the Bogoliubov-de Gennes equations for a one-dimensional tight-biding chain containing up to 1500 sites. The results are shown in Fig. 4.4(c) as a function of J normalized to the critical value J_c where the system undergoes the parity-changing QPT [19, 23, 42, 81]. The overlap between the YSR and dGSJ states decreases as the exchange coupling increases, but it remains close to unity even across the QPT. It is worth noting that the energy of the YSR excitation shifts away from that of the dGSJ state as the exchange coupling is increased. The significant overlap between the two states suggests that the YSR state primarily descends from the dGSJ state, with a minor contribution from the continuum states of the proximitized film. Therefore, in a first approximation, the coupling with the magnetic impurity can be described by replacing the proximitized film with a single level representing the dGSJ state.

4.2.3 Single-site Model

From the previous section, we obtain that the YSR is mainly formed from the dGSJ. Motivated by the results depicted in Fig. 4.4, we introduce a simplified model that replaces the entire proximitized film with a single site representing the dGSJ state. This model is useful for analyzing the coupling between the dGSJ state and a quantum spin. The Hamiltonian of the single site is given by:

$$\hat{H}_0 = \sum_\sigma E_s \left(\hat{\gamma}_\sigma^\dagger \hat{\gamma}_\sigma - \frac{1}{2} \right), \tag{4.7}$$

where $\hat{\gamma}_\sigma$ ($\hat{\gamma}_\sigma^\dagger$) are the annihilation (creation) operators for a dGSJ quasiparticle with spin $\sigma = \uparrow, \downarrow$, and E_s is the eigenvalue of the Bogoliubov-de Gennes Hamiltonian (in the absence of magnetic impurity). As explained in Sec. B.3, this Hamiltonian can be recast in terms of electron operators $\hat{d}_\sigma, \hat{d}_\sigma^\dagger$ as follows:

$$\hat{H}_0 = U \sum_\sigma \hat{n}_\sigma + \left[\Delta_s \hat{d}_\downarrow \hat{d}_\uparrow + \text{h.c.} \right], \tag{4.8}$$

where $\hat{n}_\sigma = \hat{d}_\sigma^\dagger \hat{d}_\sigma$; U and Δ_s are effective scattering and pairing potentials, respectively. In terms of U and Δ_s, $E_s = \sqrt{U^2 + \Delta_s^2}$. Without loss of generality, below we discuss the particle-hole (ph) symmetric case where $U = 0$ and therefore $E_s = \Delta_s$.

Next, we introduce the coupling to the impurity. To make contact with the classical description employed in the previous section, we first discuss the Ising limit of the exchange coupling, i.e.

$$\hat{H}_J^{\text{Ising}} = J_{dd}^{\parallel} \hat{S}^z \left(\hat{n}_\uparrow - \hat{n}_\downarrow \right), \tag{4.9}$$

where $J_{dd}^{\parallel} > 0$ is the exchange coupling with the dGSJ quasiparticle. This model reproduces the most salient features of the YSR states described above. To begin with, note that, besides the fermion parity $\hat{P} = \prod_\sigma (-1)^{\hat{n}_\sigma} = \pm 1$, the impurity spin operator S^z is also conserved in this limit, i.e. $\left[\hat{S}^z, \hat{H}_0 + \hat{H}_J^{\text{Ising}} \right] = 0$. Thus, the ground state is doubly degenerate, corresponding to the two possible orientations of the classical vector $\mathbf{S} = \pm S \hat{z}$.

For $J_{dd} < J_c = 2\Delta_s$ the ground state is one of the two following states $\{|BCS\rangle \otimes |\pm \tfrac{1}{2}\rangle\}$ with $P = +1$ and $\hat{\gamma}_\sigma |BCS\rangle = 0$ [Eq. (2.36)]. For $J_{dd} > J_c$, the ground state is one in $\{|\uparrow\rangle \otimes |-\tfrac{1}{2}\rangle, |\downarrow\rangle \otimes |+\tfrac{1}{2}\rangle\}$ with $P = -1$ and $|\sigma\rangle = \hat{d}_\sigma^\dagger |BCS\rangle$. The YSR excitation is a transition between these two ground states of opposite parity with excitation energy [3, 36] $|\Delta_s - J_{dd}/2|$. In addition, the odd parity sector of the Hilbert space also contains the following two states: $\{|\uparrow\rangle \otimes |+\tfrac{1}{2}\rangle, |\downarrow\rangle \otimes |-\tfrac{1}{2}\rangle\}$ with excitation energy equal to $\Delta_s + J_{dd}/2$. For small J_{dd}, a transition from the ground state with $P = +1$ to these states corresponds to the second subgap peak in the LDoS of the classical approach that shifts up in energy with increasing exchange and eventually disappears into the continuum [Fig. 4.3(e)]

Next, we generalize Eq. (4.9) by adding the spin-flip term, which allows the impurity spin to fluctuate:

$$\hat{H}_J^d = J_{dd}^{\parallel} \hat{S}^z \left(\hat{n}_\uparrow - \hat{n}_\downarrow \right) + J_{dd}^{\perp} (\hat{S}^+ \hat{d}_\downarrow^\dagger \hat{d}_\uparrow + \text{h.c.}) \tag{4.10}$$

As argued in Refs. [36, 146], the single-site model provides an economical and fully quantum-mechanical description of YSR spectra in superconductors, which compares well with the results obtained using sophisticated but computationally expensive methods like the Numerical Renormalization Group (NRG) [38]. The accuracy of this description in the present system is addressed in the following subsection.

The spin-flip term, $\propto J_{dd}^{\perp} > 0$, has important consequences for the spectrum of the model. In the weak coupling limit, i.e., for $J_{dd}^{\parallel} + 2J_{dd}^{\perp} < 2\Delta_s$, (assuming an unbiased preparation of the system) the following density matrix describes the ground state:

$$\hat{\rho}_{GS} = \frac{1}{2}\left[|BCS,+\tfrac{1}{2}\rangle\langle+\tfrac{1}{2},BCS| + |BCS,-\tfrac{1}{2}\rangle\langle-\tfrac{1}{2},BCS|\right], \tag{4.11}$$

On the other hand, in the strong coupling limit where $J_{dd}^{\parallel} + 2J_{dd}^{\perp} > 2\Delta_s$, the ground state is a singlet:

$$|GS\rangle = \frac{1}{\sqrt{2}}\left(|\uparrow\rangle \otimes |+\tfrac{1}{2}\rangle - |\downarrow\rangle \otimes |-\tfrac{1}{2}\rangle\right). \tag{4.12}$$

That is a pure state resulting from the quantum superposition of the two ground states of the Ising limit of the model. In weak and strong-coupling regimes, unlike the conventional classical approach of YSR [19, 23, 81], the quantum model predicts that YSR excitations carry no spin polarization [144].

Finally, since in the original model [Eq. (4.4)] the energy of the YSR does not grow without bound as the exchange with the magnetic impurity J becomes arbitrarily large, the couplings $J_{dd}^{\perp}, J_{dd}^{\parallel}$ cannot be much larger than Δ_s in the single-site model. Note that, for large $J_{dd}^{\perp}, J_{dd}^{\parallel}$ the energy of the YSR grows like $\max\{J_{dd}^{\perp}, J_{dd}^{\parallel}\}$. Thus, for the energy of the YSR to remain within the gap, the exchange couplings of the single-site model must saturate to an upper bound so that $\max\{J_{dd}^{\perp}, J_{dd}^{\parallel}\} \lesssim \Delta_s$. Therefore, they must be regarded as renormalized exchange interactions, which are also the result of the spectral reorganization and localization of excitations with energy $\sim \Delta_s$ caused by AR at the S/N interface.

4.2.4 Scaling Approach

To investigate the accuracy of the single-site model, we reintroduce the coupling to the continuum of excitations as a perturbation. Whether this perturbation changes the low-energy spectrum substantially or not can be assessed using the poor man's scaling method [40], as we describe in the following.

In the single-site model, the effective exchange coupling of the impurity and dGSJ quasiparticle is $J_{dd} = J_{dd}^{\perp} = J_{dd}^{\parallel}$, where, for the sake of simplicity, we assume an isotropic coupling. Our conclusions also apply to the anisotropic case with minor modifications. Through the exchange interaction with the magnetic impurity, the dGSJ quasiparticles can also couple to the continuum of excitations of the proximitized film. Let us introduce the following modified exchange coupling, which, besides the coupling to the dGSJ, describes an impurity-mediated coupling of the dGSJ-site to

the continuum and is treated below as a perturbation:

$$\begin{aligned}\hat{H}_J^{dc} = \sum_{\sigma\sigma'} \Big(J_{dd}\, \hat{d}_\sigma^\dagger \mathbf{s}_{\sigma\sigma'} \hat{d}_{\sigma'} + J_{\Phi\Phi}\, \hat{\Phi}_{0\sigma}^\dagger \mathbf{s}_{\sigma\sigma'} \hat{\Phi}_{0\sigma'} \Big) \cdot \hat{\mathbf{S}} \\ + J_{d\Phi} \sum_{\sigma\sigma'} \Big(\hat{d}_\sigma^\dagger \mathbf{s}_{\sigma\sigma'} \hat{\Phi}_{0\sigma'} + \hat{\Phi}_{0\sigma}^\dagger \mathbf{s}_{\sigma\sigma'} \hat{d}_{\sigma'} \Big) \cdot \hat{\mathbf{S}}.\end{aligned} \tag{4.13}$$

The operators $\hat{\Phi}_{0\sigma}, \hat{\Phi}_{0\sigma}^\dagger$ are the annihilation and creation operators for electrons in the continuum at the position of the magnetic impurity. Phenomenologically, we have assumed different couplings for the various processes involving the scattering of the dGSJ and the continuum excitations by the impurity. These couplings can be calculated from first principles. However, they depend on microscopic details of the matrix elements of the impurity orbitals and the continuum of both subgap and outer-gap excitations, which are challenging to model. For this reason, we treat their bare values as free parameters in the analysis below.

We carry out the poor man's scaling analysis [40] of the model (4.13) by integrating out the high energy degrees of freedom from the continuum with energies of the order of the bandwidth $D \sim E_F$. Since these band-edge modes exhibit vanishing superconducting correlations because their energies are well above the gap, the calculations do not differ much from those of the standard Kondo scaling of a magnetic impurity [40]. Some details are provided in App. B.4. In what follows, we focus on the discussion of the solutions to the scaling equations, which read

$$\frac{dg_{\Phi\Phi}}{d\ell} = g_{\Phi\Phi}^2, \tag{4.14}$$

$$\frac{dg_{d\Phi}}{d\ell} = g_{d\Phi} g_{\Phi\Phi}, \tag{4.15}$$

$$\frac{dg_{dd}}{d\ell} = g_{d\Phi}^2. \tag{4.16}$$

Here $g_{dd} = 2\nu_0 J_{dd}$, $g_{d\Phi} = 2\nu_0 J_{d\Phi}$, and $g_{\Phi\Phi} = 2\nu_0 J_{\Phi\Phi}$ are dimensionless couplings, $\nu_0 \sim 1/D$ being the mean density of continuum states. The scaling variable ℓ is defined such that the bandwidth is reduced according to $D(\ell) = De^{-\ell} \to 0$ as $\ell \to +\infty$, where $D \sim E_F$.

As the bandwidth of the system is reduced, the above scaling equations imply that the renormalization of g_{dd} and $g_{d\Phi}$ is driven by the growth of $g_{\Phi\Phi}$. Indeed, Eq. (4.14) for $g_{\Phi\Phi}$ is mathematically identical to the scaling equation for the exchange coupling of a magnetic impurity in a normal metal (Kondo scaling). The equations can be readily solved by the ansatz $g_{\Phi\Phi}(\ell) = (\ell^* - \ell)^{-1}$, where $\ell^* = 1/g_{\Phi\Phi}(0)$. Like the ordinary Kondo scaling, ℓ^* corresponds to the logarithmic scale where $g_{\Phi\Phi}(\ell)$ diverges and the perturbative renormalization breaks down. This happens when the bandwidth becomes of the order of a "Kondo temperature", T_K^Φ, i.e. for $\ell^* = \log\big(D/T_K^\Phi\big)$. Hence, $g_{\Phi\Phi}(\ell^*) \sim 1$ leads to $T_K^\Phi = De^{1/(2\nu_0 J_{\Phi\Phi})}$. Note that $T_K^\Phi \gg \Delta_s$ would imply that the continuum states at energies much higher than the superconducting gap are strongly coupled to the magnetic impurity. In this situation, the single-site description, as

introduced above, breaks down. In the classical approach, such a strong coupling to the continuum should result in substantial suppression of the overlap between the YSR and dSGJ states.

Indeed, the wavefunction overlap Θ, Fig. 4.4, can be used to obtain a rough estimate of the ratios of the bare couplings $g_{d\Phi}(0)/g_{dd}(0)$, and $g_{\Phi\Phi}(0)/g_{dd}(0)$. To this end, we first notice that $g_{dd} \sim J_{dd}$, $g_{d\Phi} \sim J_{d\Phi}$, and $g_{\Phi\Phi}(0) \sim J_{\Phi\Phi}$ contain matrix elements with zero, one, and two powers of the continuum orbitals, respectively. Recall that the exchange couplings are second order in the matrix element describing the tunneling between the impurity magnetic orbital and the metallic host states. Let $\gamma = 1 - |\Theta|$ measure the degree of admixture of the YSR state with the continuum; γ is enhanced by quantum fluctuations relative to the estimates provided by the classical approach [Sec. 4.2.2]. Nonetheless, we expect γ to remain much smaller than one. Thus, $g_{dd}(0) \sim \gamma^0$, $g_{d\Phi} \sim \gamma$ and $g_{\Phi\Phi} \sim \gamma^2$, to leading order in γ. Furthermore, $g_{dd}(0) = 2\nu_0 J_{dd} \sim \Delta_s/D \sim \Delta/D \ll 1$ according to the discussion at the end of the previous subsection.

Next, we proceed to obtain solutions to the scaling equations using the above estimates for the initial conditions of the flow. Concerning the solutions of Eqs. (4.15) and (4.16), we notice that Eq. (4.15) is solved by the ansatz $g_{d\Phi}(\ell) = r_{d\Phi}/(\ell^* - \ell)$ with $r_{d\Phi} = g_{d\Phi}(0)/g_{\Phi\Phi}(0)$. Introducing this result into Eq. (4.14) and integrating, we obtain the following renormalized coupling between the impurity and the dSGJ:

$$g_{dd}(\ell) = g_{dd}(0) + \frac{g_{d\Phi}^2(0)}{g_{\Phi\Phi}(0)} \frac{(\ell/\ell^*)}{1-(\ell/\ell^*)} \tag{4.17}$$

Using $g_{d\Phi}^2(0)/g_{\Phi\Phi}(0) = \gamma^2 g_{dd}^2(0)/[\gamma^2 g_{dd}(0)] \simeq \gamma^0 g_{dd}(0)$, the above expression simplifies to:

$$g_{dd}(\ell) \simeq \frac{g_{dd}(0)}{1-(\ell/\ell^*)}. \tag{4.18}$$

which needs to be compared with the behavior of the renormalized coupling to the continuum after setting $g_{\Phi\Phi}(0) \simeq \gamma^2 g_{dd}(0)$:

$$g_{\Phi\Phi}(\ell) \simeq \frac{\gamma^2 g_{dd}(0)}{1-(\ell/\ell^*)}. \tag{4.19}$$

Note that both couplings diverge at $\ell^* = \log\big(D/T_K^\Phi\big)$ with $T_K^\Phi \simeq De^{-1/2(\nu_0\gamma^2 J_{dd})} \ll \Delta$ if $\gamma \ll 1$, which is consistent with what was discussed above. For instance, if we choose $\gamma \approx 0.2$ (corresponding to $\Theta \approx 0.8$), then

$$\frac{g_{\Phi\Phi}(\ell)}{g_{dd}(\ell)} \simeq \gamma^2 \ll 1. \tag{4.20}$$

Thus, as the continuum states are integrated out, the impurity remains most strongly coupled to the single site describing the dGSJ quasiparticle and therefore the single-site model remains an accurate description of the magnetic impurity on the proximitized thin film.

Let us close this section by pointing out some potential problems with the scaling analysis described above. First of all, like the original poor man's scaling [40], the equations are obtained perturbatively. Therefore, the solutions to the scaling equations are valid, provided the couplings remain small compared to unity. This is not a problem under the above assumptions because the scale where the couplings diverge ℓ^* is much smaller than the superconductor gap, and the scaling must be stopped at the scale of Δ. As we get closer to the gap scale, the superconducting correlations cannot be neglected, and taking them into account modifies the flows of the renormalized couplings. Nevertheless, we should interpret the above analysis as providing information on the tendency of the high-energy continuum states to couple to the impurity in the presence of the coupling to the dGSJ state.

4.3 Magnetic molecules on Au films proximitized by V

We now focus on the 4-fold FeTPPCl molecules on the Au/V(100) superconducting surface described in Sec. 4.1, whose spectroscopic features are presented in Fig. 4.5, indicating three in-gap states and two out-gap peaks. The outer peak, A, lies at the same energy as the spin-flip excitation measured for the 2-fold FeTPPCl molecules [2].

The three sub-gap excitations are YSR states arising from the interaction between molecular orbitals and the itinerant electrons. The asymmetry between positive and negative peaks is due to a finite scattering potential on the molecule [107]. Moreover, $\pm\gamma^*$ is a thermal peak, only visible due to the tunneling between a superconducting tip and sample at finite temperatures.

The coexistence of the multiple subgap and out-gap features, as well as the high spin and magnetic anisotropy of the molecule, makes it difficult to assign each peak a certain excitation. To interpret the complex spectrum observed in STM measurements, in the upcoming section, we introduce an extended single-site Hamiltonian with a high spin ($S = 5/2$) and an anisotropy term. This model for a quantum spin with

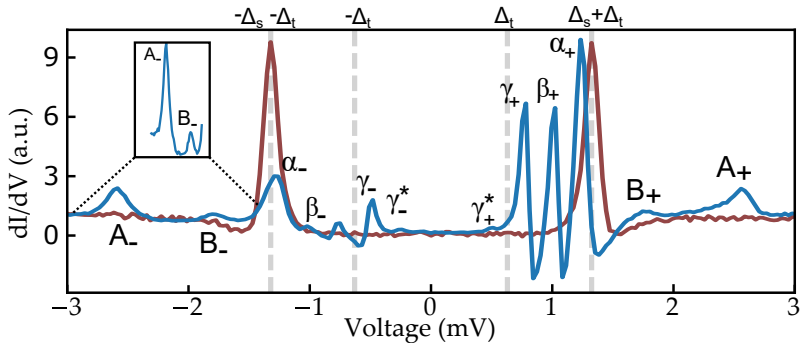

Figure 4.5: **Spectra of a 4-fold FeTTP-Cl molecule.** Three sub-gap states named α, β, and γ and two out-gap peaks, A and B (zoom-in in the inset), can be distinguished. In red, the spectrum of the bare surface is shown for comparison.

anisotropy finds that every subgap state in Fig. 4.5 arises from the excitation of an entangled molecular spin with an electronic state in the substrate. We also show that peak A arises from a spin-flip tunneling process, whereas peak B relates to a novel two-particle or Cooper Pair Excitation (CPE), which is not observable in most single-particle tunneling experiments.

4.3.1 Extended Single-Site Model

The full Hamiltonian, taking into account the tip, sample, and tunneling between both, is written as

$$\hat{H}_{\text{model}} = \hat{H}_s + \hat{H}_t + \hat{H}_{ts} \,, \tag{4.21}$$

where $\hat{H}_s$ and $\hat{H}_t$ describe sample and tip, respectively, and $\hat{H}_{ts}$ is the tunneling Hamiltonian; $\hat{H}_s$ is a single-site superconductor coupled to a quantum impurity with spin $S = 5/2$:

$$\begin{aligned}
\hat{H}_s &= \hat{H}_0 + \hat{H}_M + \hat{H}_J \\
\hat{H}_0 &= \Delta_s \hat{c}^\dagger_\uparrow \hat{c}^\dagger_\downarrow + \text{h.c.} \\
\hat{H}_M &= D\hat{S}_z^2 + E(\hat{S}_x^2 - \hat{S}_y^2) \\
\hat{H}_J &= \sum_{\sigma\sigma'} \hat{c}^\dagger_\sigma \left[U\delta_{\sigma\sigma'} + J_z \hat{S}_z s^z_{\sigma,\sigma'} + J_\perp \left(\hat{S}_+ s^-_{\sigma\sigma'} + \hat{S}_- s^+_{\sigma\sigma'} \right) \right] \hat{c}_{\sigma'} .
\end{aligned} \tag{4.22}$$

Here Δ_s is the strength of the superconducting pairing in the substrate. As introduced in Sec. 4.2.3, in a proximitized superconductor, Δ_s corresponds to the energy of the dGSJ state, D and E are the axial and transverse magnetic anisotropy of the molecule, J_z and $J_\perp$ are the axial and transverse magnetic exchange couplings, and U is the impurity scattering potential, which, without loss of generality, we assume to be $U = 0$. Applying Ockham's razor, the Hamiltonian (4.22) has a single exchange coupling channel with magnetic anisotropy, presenting a simpler framework for capturing the full range of excitations compared to a multi-channel model.

We also treat the Hamiltonian describing the superconducting tip, H_t, as a single-site superconductor:

$$H_t = \Delta_t c^\dagger_{t\uparrow} c^\dagger_{t\downarrow} + \text{h.c.} \,. \tag{4.23}$$

Finally, the tunneling between the tip and sample is described by

$$\hat{H}_{ts} = \sum_\sigma \hat{\mathcal{T}}_{\sigma\sigma'} \hat{c}^\dagger_{t\sigma} \hat{c}_{\sigma'} + \text{h.c.} \,, \tag{4.24}$$

with $\hat{\mathcal{T}}_{\sigma\sigma'} = \mathcal{T}_0 + \mathcal{T}_1 \hat{\boldsymbol{S}} \cdot \boldsymbol{s}_{\sigma\sigma'}$, where $\mathcal{T}_0$ is related to the normal tunneling and $\mathcal{T}_1$ to the spin-flip tunneling. As expected in the tunneling regime, we assume no Josephson current or multiple Andreev reflections between the tip and the sample.

The complete analysis of the Hamiltonian is transferred to App. B.5, where the different parameters are switched on independently to understand their effects. Here, we discuss the combined effect of all terms in the model, i.e., the superconducting gap

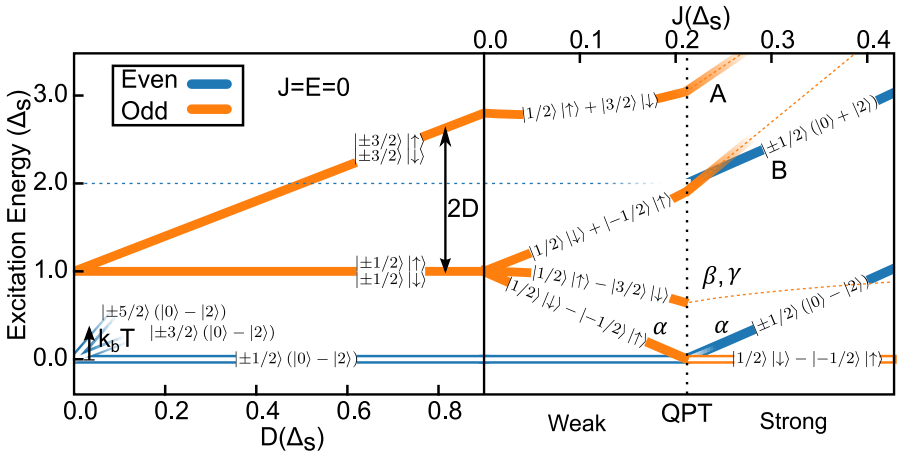

Figure 4.6: **Energy of the eigenstates as a function of D and J.** For the left square $J = 0$, so the effects of the magnetic anisotropy can be observed. In the right one J is switched off. The transverse magnetic anisotropy, E, is zero. Blue and orange represent the parity of the state: even or odd, respectively. The solid lines are the states accessible with tunneling electrons.

Δ_s, the magnetic anisotropies, D and E, and the exchange coupling J. In Fig. 4.6, we show the evolution of the eigenstates of Eq. (4.22) as the values of the different couplings are turned on up to values compatible with the experimental ones.

The superconducting pairing separates the even and odd sample parity eigenstates by $2\Delta_s$, as introduced in Sec. 2.4.2. This is represented by the blue (even) and orange (odd) lines in the figure. When a tunneling electron excites the system, the parity of the sample changes, which forbids tunneling between states with the same parity; e.g., if the sample's ground state is even in parity (blue), only odd states (orange) are accessible via tunneling.

On top of the parity change, we assume that spin-flip tunneling paths are available, proportional to $|\mathcal{T}_1|^2$. This means that a tunneling electron can change the total spin of the impurity/sample system by ± 1. For example, the spin excitation measured in the 2-fold molecules [2] is a transition from the lowest-lying $|\pm 1/2\rangle$ state to $|\pm 3/2\rangle$, which are split. Similarly, in the 4-fold molecules, the axial magnetic anisotropy splits the states by spin-z projections. This is represented in the first square of Fig. 4.6.

The solid lines in the figure are the levels reachable by tunneling electrons considering the change of parity and the maximum total spin change of ± 1. These are calculated at 0th order in transverse magnetic anisotropy, E. The resulting terms are of order $|\mathcal{T}_0|^2$ and $|\mathcal{T}_1|^2$ in the tunneling current.[2]

The right square of Fig. 4.6 illustrates the evolution of the eigenstates when the exchange coupling is considered. Three YSR states form from the combination of

[2]There is no term proportional to $\mathcal{T}_0\mathcal{T}_1^*$ if TRS is preserved.

the molecule's spin, and the superconductor's Bogoliubov states. These states read: $|1/2\rangle|\uparrow\rangle - |-1/2\rangle|\downarrow\rangle$, $|1/2\rangle|\uparrow\rangle - |3/2\rangle|\downarrow\rangle$ and $|-1/2\rangle|\downarrow\rangle - |-3/2\rangle|\uparrow\rangle$. The first state corresponds to the lowest-lying YSR state, α, a spin-0 state. When a critical value of the exchange coupling, J_c, is surpassed, marked with a dotted line in Fig. 4.6, the parity of the ground state changes, and state α becomes the ground state. The other two states are the β and γ excitations, which are degenerate for $E = 0$, and have a total spin 1.

Finally, we consider the effect of a small transverse magnetic anisotropy E, which the molecules can host due to the distortion of their 4-fold symmetry from the surface. Unlike anisotropic exchange, transverse anisotropy breaks the Z_2 symmetry. This does not affect even-parity states, where Kramers' degeneracy keeps states with opposite total spin z-projection degenerate. The Z_2 breaking splits odd-parity states whose degeneracy is not protected by TRS. This causes a separation between peaks γ and β.[3]

4.3.2 The Cooper Pair Excitation

We attributed the three subgap states to molecular and electronic spin entangled states split by the axial and transverse magnetic anisotropies. To understand the origin of the out-gap peaks A and B, Fig. 4.7 shows spectroscopic measurements of three molecules on different regimes of the QPT. From top to bottom, these molecules are in the weak coupling regime, QPT, and strong coupling regime. In the weak coupling regime, i.e., $J < J_c$, we see three YSR states (α, β, and γ), representing excitations from the even ground states to the previously introduced odd states. Moreover, the two out-gap states, A and B, are observed. Peak A has a larger intensity than peak B.

The middle curve in Fig. 4.7 illustrates the spectra measured on a molecule on the QPT. At this point, peak α appears at zero energy, representing the crossover between the even and odd ground states. The relative height of the out-gap peaks changes at the QPT. Peak B appears more prominent, while peak A's intensity seems unchanged.

The ground state is odd in the strong coupling regime ($J > J_c$), so tunneling electrons cannot excite other odd states. The lowest curve in Fig. 4.7 shows the spectrum of a molecule in this regime. Peaks β and γ are absent, as they are not accessible anymore. Moreover, the intensities of peaks A and B have reversed compared to the weak coupling regime. Peak A is barely visible in this curve.

This analysis demonstrates that peak A, mainly observed in the weak coupling regime, arises from the excitation of an odd state. On the other hand, peak B, observed

[3] The value of E used here is small (0.044 meV), so a minor splitting is expected. A first-order perturbation calculation for degenerate states $\left|\frac{1}{2},\uparrow\right\rangle - \left|\frac{3}{2},\downarrow\right\rangle$ and $\left|-\frac{1}{2},\downarrow\right\rangle - \left|-\frac{3}{2},\uparrow\right\rangle$ yields $\Delta E \sim 3\sqrt{2}E$, accounting for a separation of ~ 0.2 meV. Other states' splittings are negligible in this approximation. Additionally, transverse anisotropy induces only slight mixing of states with different $S_{z,T}$, which should not significantly alter the above analysis. Although a two-channel model could explain the observed splitting, it would increase complexity and fitting parameters, validating our simpler one-channel model choice.

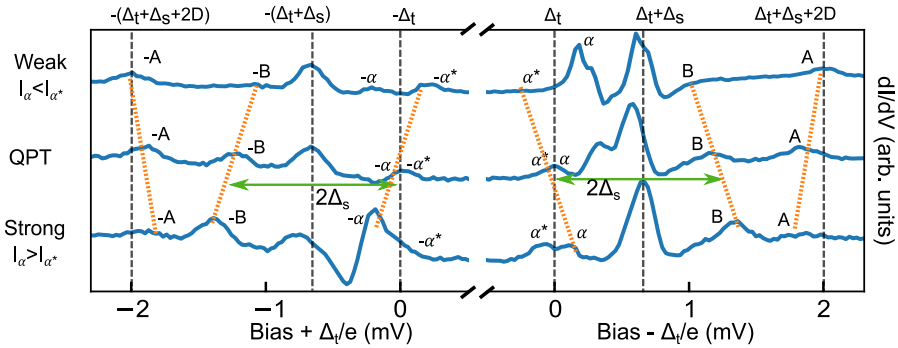

Figure 4.7: **Spectra on molecules with different exchange coupling with the surface.** Spectroscopic measurement of three different molecules in three different positions of the diagram in Fig. 4.6. From top to bottom, the molecules are in the weak coupling regime ($J < J_c$), in the QPT ($J = J_c$), and in the strong coupling regime ($J > J_c$).

in the strong coupling regime, forms due to the transition to an even state. In the QPT, both peaks can be observed because the two distinct parity ground states cross. Moreover, a reminiscence of peak A (B) can be seen in the strong (weak) coupling regime due to the finite thermal population of the even (odd) ground state.

As introduced earlier, peak A lies at the same energy of the spin excitations observed in the 2-fold molecules [2]; moreover, the energy diagram in Fig. (4.6) shows an odd state at the energies measured for peak A, namely the state $|1/2\rangle|\uparrow\rangle + |3/2\rangle|\downarrow\rangle$. We conclude that peak A is an excitation from the BCS even ground state to this state, a spin excitation. On the other hand, peak B is an excitation from the odd ground state, formed by the spin-0 α state, to an even state. Following the energy diagram in Fig. (4.6), the even state at the corresponding energy is $(|0\rangle - |2\rangle)|\pm 1/2\rangle$, which we defined as a CPE in Sec. 2.4.2, an excitations that is not accessible with single-particle tunneling in bulk superconductors.

To further prove that this is indeed a CPE, we note that moving through the QPT in Fig. 4.7 not only changes the relative intensities of peaks A and B, but also their excitation voltage. The orange dashed lines represent the evolution of these peaks. We observe that peak B follows the same dispersion as α, and the separation between both amounts to $2\Delta_s$, pointing out that B is indeed a CPE.

The energy of the dGSJ state, Δ_s, is controlled with the thickness of the Au layer on top of the superconductor. Consequently, to further corroborate the identification of peak B as a pair excitation, we study the evolution of peaks A and B on 15 molecules lying on different regions and film thicknesses. Figure 4.8(a) shows the value of Δ_s in the surroundings of 15 molecules. For each one, we measure E_A and E_B, i.e., the energy separation between the α peak and peaks A and B, respectively. Plotting these values against the energy of the dGSJ states, we see a clear correlation between Δ_s and E_B [Fig. 4.8(c)], demonstrating that peak B arises from a CPE. On the other

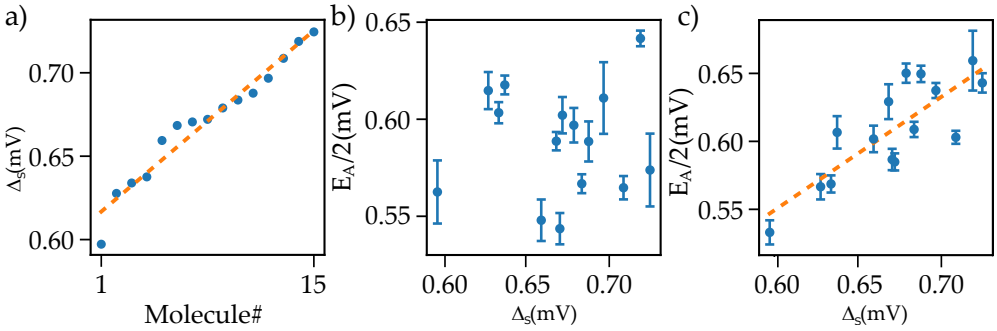

Figure 4.8: Δ_S **dependence of peak A and B (a)** Measured superconducting gap for 15 molecules in different preparations. **(b)** Energy difference between the YSR state and peak A for the 15 molecules. No clear correlation with Δ_s can be seen. **(c)** Energy difference between the YSR state and peak B. A clear correlation with the superconducting gap can be observed, it is almost a one-to-one correlation ($E_B/2 \sim \Delta_s$)

hand, there is no correlation between Δ_s and E_A [Fig. 4.8(b)], this is expected for a spin excitation. The separation between α and A depends on D, which can vary slightly due to the adsorption site.

Usually, pair excited states [8] are measured from adsorption of microwaves [178, 179] photons or Andreev pairs [180]. Parity conservation forbids a single tunneling electron from exciting a pair of Bogoliubov quasiparticles in a superconductor. Due to the magnetic molecule and our setup's capability to control the ground state parity, we could observe a CPE as peak B [Fig. 4.8]. Even if this resonance appears outside the spectral gap, the pair state in the proximitized film is a double population of a subgap state. Hence, it is expected to have a larger lifetime, facilitating its detection. Moreover, the measurement of peak B is a smoking gun to assess the local parity of the system, which usually can not be determined due to the symmetry involved in the QPT spectrum.

4.4 Spin-singlet based Qubit

To conclude this chapter, we apply the single-site model to describe a novel spin-qubit platform based on a spin-1 chain. The on-surface synthesis technique [159, 181] offers precise engineering of carbon-based molecules, making it possible to engineer their magnetic properties. The spin state of several nanographene structures can be controlled with this method [182–184]. The authors in Ref. [162] show that a complex spin-1 chain can be built using triangulenes (a triangular nanographene) as building block [Fig. 4.9(a)]. These chains host topologically protected spin-1/2 fractional edge states [162, 185], with the chain length controlling the exchange coupling between the edge states. We start this section by presenting a single-site model that describes

the interacting spin-1/2 fractional edge states of a Heisenberg spin-1 chain. We show that this system's ground and excited states are singlet states and that it is possible to implement a novel qubit platform, based on these singlet states, that is protected against Spin-Orbit and Hyperfine interactions. We will finish proposing a device that can be used as a singlet-based SQ.

Figures 4.9(a) and 4.9(b) show the sketch of a triangulene spin-1 chain on top of a superconducting surface. These chains have been produced on Au(111) crystals, and ongoing experiments show that they can also be formed on proximitized Ag(111) and Au(111) films, which can be proximitized if grown on top of a superconductor [2, 3, 35, 169]. The fractional states of the chains are unpaired end spin-1/2 states. This can be visualized by describing each spin-1 triangulene as composed of two strongly interacting spin-1/2 [185], as shown in Fig. 4.9(b). The inner spins form a valence bond solid, and the unpaired spins in the edges form the fractional end states. For shorter chains, they interact [Fig. 4.9(a)], and their relative orientation depends on the parity of the chain, i.e., even or odd amount of triangulenes. The strength of this interaction decays exponentially with the length of the chain.

On a superconductor, these edge states can couple with the condensate via Kondo coupling. This gives rise to in-gap YSR states at both end sites. Due to the finite overlap between wave functions, there is a non-zero exchange coupling between the

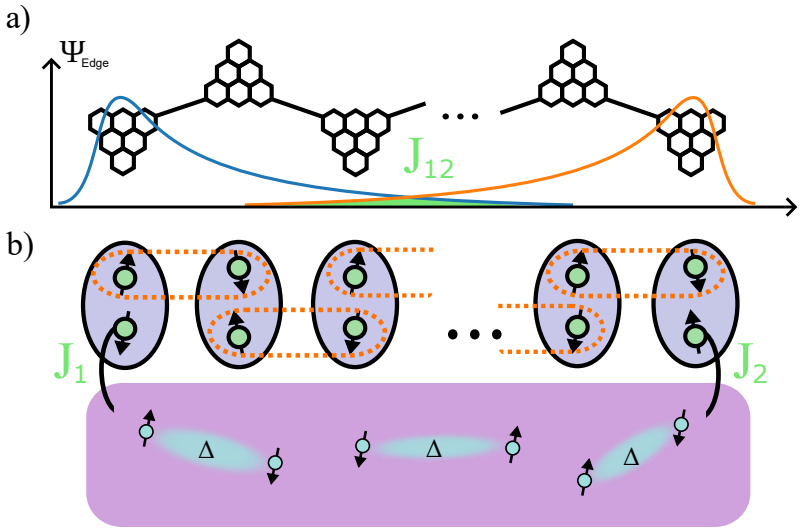

Figure 4.9: **Spin-1 chain on a superconductor (a)** Sketch of the triangulene chain and the wave function of the fractional edge states. An exchange coupling J_{12} describes the overlap between wave functions. **(b)** Formation of the end states. Each spin-1 in the chain can be described by two spin-1/2. These spins form a valence bond solid, leaving two spins free in the edges, which interact with the itinerant electrons via the exchange coupling.

state	(S, P)	
Antiferromagnetic singlet(S_0)	(0, 1)	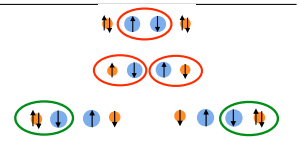
Kondo quartet(S_2)	(0,1)	
Doublets(D_1, D_2)	(1/2, -1)	

Table 4.1: **Possible ground state for the zero hopping limit.** Red and green solid circles represent singlets and doublets formed at two sites, respectively. Blue(orange) circles are impurity(conduction electron) sites. Parity 1 and -1 stand for even and odd, respectively.

end spins, as shown in Fig. 4.9(a). The Hamiltonian describing the spin-1 chain plus the superconducting bath reads

$$\hat{H} = \hat{H}_{\mathrm{SC}} + \hat{H}_{\mathrm{QD}}. \tag{4.25}$$

$$\hat{H}_{\mathrm{QD}} = \sum_{\sigma,\sigma'} \sum_{i=1,2} J_i \hat{\psi}^\dagger_\sigma(x_i) \hat{\mathbf{S}}_i \cdot \mathbf{s}_{\sigma\sigma'} \hat{\psi}_{\sigma'}(x_i) + J_{12} \hat{\mathbf{S}}_1 \cdot \hat{\mathbf{S}}_2 \tag{4.26}$$

$$\hat{H}_{\mathrm{SC}} = \sum_{\mathbf{k}\sigma} \xi_{\mathbf{k}} \hat{c}^\dagger_{\mathbf{k}\sigma} \hat{c}_{\mathbf{k}\sigma} + \Delta \sum_k \left[\hat{c}^\dagger_{\mathbf{k}\downarrow} \hat{c}^\dagger_{-\mathbf{k}\uparrow i} + \hat{c}_{\mathbf{k}\downarrow} \hat{c}_{-\mathbf{k}\uparrow} \right], \tag{4.27}$$

where $\hat{\psi}^\dagger_\sigma(x_i)$ ($\hat{\psi}_\sigma(x_i)$) is the creation (annihilation) operator of an electron with spin σ in the position x_i, $\hat{\mathbf{S}}_i$ and J_i are the spin-1/2 operator and the exchange coupling with the substrate of the ith edge state, and J_{12} is the exchange coupling between edge states.

This Hamiltonian has no interaction between the spins in the bulk of the chain and the superconductor but considers that only the edges are exchange-coupled to the superconductor. We assume that the exchange coupling between the spins forming the valence bond solid is the largest energy scale of the system, so the inner spins are in a spin-0 state and no exchange coupling is present.

4.4.1 Single-site model for the spin chain

In the following, we simplify Eq. (4.25) into a single-site model. The simplest approach is to describe two S=1/2 impurities exchange coupled between them (J_{12}) and, each, also exchange coupled to two independent single-site superconductors:

$$\hat{H}_0 = \sum_{i\sigma\sigma'} \sum_i J_i \hat{c}^\dagger_{i\sigma} \hat{\mathbf{S}}_i \cdot \mathbf{s}_{\sigma\sigma'} \hat{c}_{i\sigma'} + \Delta \hat{c}^\dagger_{i\uparrow} \hat{c}^\dagger_{i\downarrow} + \Delta \hat{c}_{i\downarrow} \hat{c}_{i\uparrow} + J_{12} \hat{\mathbf{S}}_1 \cdot \hat{\mathbf{S}}_2, \tag{4.28}$$

where $\hat{c}^\dagger_{i\sigma}$ ($\hat{c}_{i\sigma}$) is the creation (annihilation) operator of an electron with spin σ in the ith site.

This Hamiltonian has a 4×4×2×2=64-dimensional Hilbert space, so exact diagonalization is possible. The system's parity and total spin are good quantum numbers,

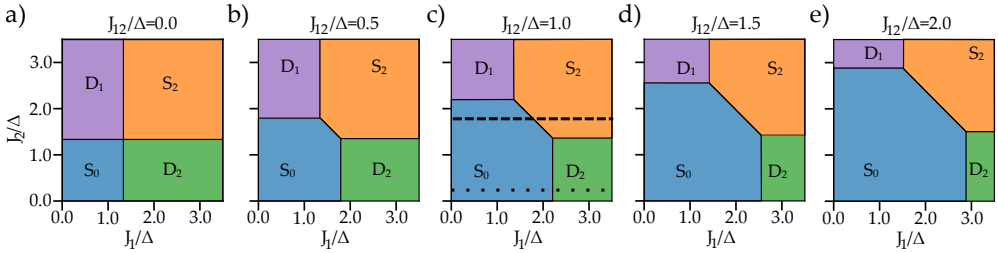

Figure 4.10: **Phase diagram of the two impurity system for t=0. (a)-(e)** Phase diagram for $J_{12}/\Delta = 0, 0.5, 1, 1.5, 2$, respectively. The dashed and dotted lines in **(c)** represent the non-local QPT and the common parity changing QPT, respectively.

as well as the local parity. Table 4.1 shows the four possible ground states of the system for an antiferromagnetic coupling between the impurities, with their respective total spin, S, and parity, P. Two distinct singlet states are possible to form. The first one, S_0, is the ground state of the weak coupling regime. It is formed by the antiferromagnetic singlet between the two impurities, with both superconducting sites in the even (BCS) ground state. The other singlet, S_2, is also even in total parity but has a trapped quasiparticle in each site. This singlet is formed by the antiferromagnetic interaction between the spins of the trapped superconducting quasiparticle and the end states. In addition, there are two doublet states, D_1 and D_2, which are the low-lying states accessible with tunneling electrons because they have opposite parity than the ground state. These doublets have one of the two superconducting sites in an even state and one trapped quasiparticle on the other, so the global parity is odd.

Figures. 4.10(a)-(e) show the phase diagram of the system in the J_1, J_2 space for different values of J_{12} from 0 to 2Δ, i.e., for various values of spin-1 chain length. For $J_{12} = 0$, we find that changing the exchanges J_1 or J_2 drives the system through the QPT from the S_0 to D_1 or D_2. These are similar to the QPT described for a single impurity. The corresponding site traps a quasiparticle, and the parity of the system changes from even to odd. To reach S_2, both exchange constants have to be changed across their respective QPT.

On the other hand, for $J_{12} > 0$, a new transition is present, namely the $S_0 \rightarrow S_2$ transition, marked with a black dashed line in Fig. 4.10(c). The evolution of the four states in this line-cut is illustrated in Fig. 4.12(a), which shows the transition between the S_0 and the S_2 state. The parity changing QPT, $S_0 \rightarrow D_i$ can also be performed, as marked by the dotted line in Fig. 4.10(c). The evolution of the states through the dotted line is shown in Fig. 4.12(a), which illustrates the transition from S_0 to D_2.

The $S_0 \rightarrow S_2$ transition represents the simultaneous trapping of a quasiparticle in each superconducting site, i.e., the parity of both sites changes; hence, the total parity remains even. This transition happens similarly by fixing one of the exchange couplings, J_1 or J_2, and increasing the other, as shown by the dashed line in Fig. 4.10(c) for constant J_2. As the two sites are spatially separated and the transition can be performed by acting in only one impurity, this is a Non-Local Quantum Phase

Transition (NLQPT), i.e., an example of quantum teleportation.

Up to this point, we have considered that the two superconducting sites are independent. However, the real system we simulate is a macroscopic superconductor so it is inexact to treat the two sites as independent. This means that due to the long-range order of the superconductor, a coupling term between superconducting sites must be considered to describe the system adequately. Following Ref. [186], we add a tunneling term between the superconducting sites so that the total Hamiltonian now reads

$$\hat{H} = \hat{H}_0 + \hat{H}_T \tag{4.29}$$

with,

$$\hat{H}_T = \sum_{\sigma} t\hat{c}^{\dagger}_{1\sigma}\hat{c}_{2\sigma} + \text{h.c.}\,, \tag{4.30}$$

where t is the hopping amplitude between the sites. A discussion on the adequacy of this Hamiltonian is given in App. B.6.

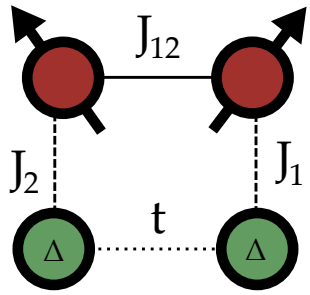

Figure 4.11: **Representation of the spin Hamiltonian.** Two magnetic impurities exchange coupled between each (J_{12}) other and a superconducting site (J_i). The superconducting sites are coupled via hopping, t.

This new term couples the two superconductors, as illustrated in Fig. 4.11, generating a finite matrix element between S_0 and S_2, so that two new states that are a linear combination of S_0 and S_2 become the new eigenstates, namely S and S'. As a consequence, the NLQPT is no longer accessible. Instead, an anticrossing is created at the boundary of the NLQPT. This is depicted in Fig. 4.12(c), where a comparison between the ground states of the Hamiltonian with and without the tunneling term is shown.

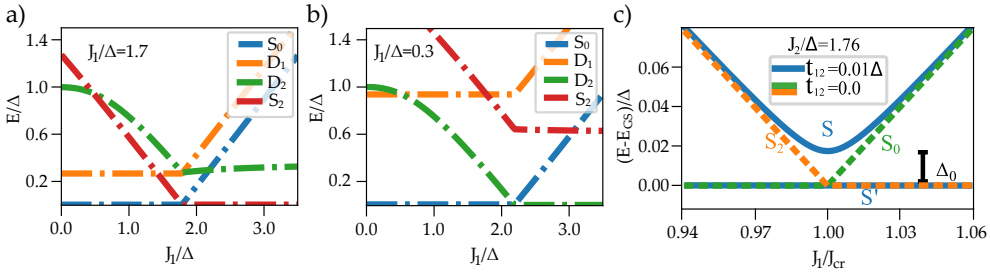

Figure 4.12: **Excitations of the spin-singlet based Qubit. (a)** and **(b)** Excitation spectrum of the two impurity systems with $t = 0$ for the two black lines in Fig. 4.10(a). In panel **(a)**, the NLQPT is shown, with the states D_1 and D_2 lying at higher energies. In panel **(b)**, the QPT between S_0 and D_2 is represented. States D_1 and S_0 appear at higher energies. **(c)** Comparison between the Hamiltonian without and with tunneling. An anticrossing between the two lowest-lying levels develops.

Fine-tuning the system around the critical value of the exchange coupling for the NLQPT, J_{cr}, states S and S' can be used as the orthogonal states forming a qubit. As the two states are a linear combination of two singlets, S_0 and S_2, themselves are singlets. We finish the section by introducing a spin qubit based on these two states. We also introduce the design of a plausible device to host this singlet-based spin qubit.

4.4.2 A Spin-singlet Qubit

Since the first proposal by Loss and DiVincenzo [187], numerous spin qubit platforms have been proposed with increasingly better performance in terms of quantum coherence and addressability [188–193]. The main decoherence effects of these qubits are the spin-orbit interaction (SOI) with the itinerant electronic cloud [194, 195] and the hyperfine coupling (HC) with the nuclei in the quantum dot [196, 197]. The two spin-singlet states hosted at the end of the spin chains are protected against decoherence arising from SOI and HI due to their spin-0 nature.

Coupling a microwave with STM to induce the resonant state between the two singlets can be a suitable proof-of-principle setup to check the validity of this spin qubit [198]. However, beyond the proof of concept, the difficulty of a single-molecule device will be part of any multiscale device. Therefore, we propose a nanofabricated device with an engineered electromagnetic environment where the different parameters of the system can be precisely controlled. Figure 4.13 shows a scheme of a possible device structure enabling the implementation of the proposed singlet-qubit. This mesoscopic system is built from two quantum dots (QD) connected to two distinct superconducting baths [44], connected among them via tunneling; for example, two parallel superconducting nanowires. The energy of the QD levels can be controlled with gate voltages V_{G1} and V_{G2}, which is equivalent to changing the exchange coupling of an impurity [79]. Moreover, another gate, V_{G12}, would control the tunneling between QD, which we effectively represent as an exchange coupling [148, 199]. Finally, the hopping term between superconductors can be controlled with a thin oxide layer, which would be fixed by details of the device nanofabrications, e.g., the width of the oxide layer or its composition.

The qubit could be manipulated by adding an AC electrostatic potential to one of the QD gates, effectively controlling the exchange coupling of one of the impurities.

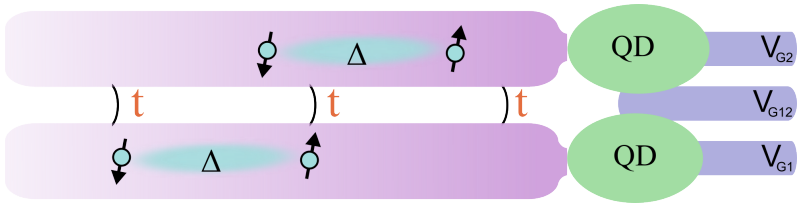

Figure 4.13: **Device for a spin-single qubit.** Schematic proposal of a device based on two coupled Quantum Dots, each on top of a superconducting wire. The wires are coupled via tunneling, with a strength tunable through a gate potential.

This perturbation can be used to control the qubit's state coherently. The readout mechanism could be performed by measuring the reflectance or absorption of the AC signal in the gate line [178, 179]. Another control mechanism could be achieved by putting the qubit in a superconducting cavity, similar to Ref. [44].[4]

4.5 Conclusions

We have studied the YSR excitations in a thin metal film proximitized by a superconductor. This has been carried out by introducing a one-dimensional model of the metal film/superconductor substrate [Sec. 4.2.1]. The spectrum of this model, which consists of the dGSJ subgap bound states, arises from the Andreev reflection at the metal/superconductor interface, leading to a substantial spectral reorganization around and below the gap energy. Treating the impurity spin as a classical vector, we have found a substantial overlap of the wavefunctions of the YSR and the dGSJ states, which motivated us to use a single-site model [Sec. 4.2.3]. We have addressed the accuracy of the single-site model by phenomenologically re-introducing the coupling to the continuum of excitations of the proximitized film as a perturbation and using the poor man's scaling method [Sec. 4.2.4]. We have shown that the exchange coupling with the site that describes the dGSJ quasiparticle excitation remains the dominant coupling under scaling. Thus, the continuum of excitations of the proximitized film can be neglected in a first approximation, and the YSR states can be regarded as resulting from the exchange interaction of the magnetic (quantum) impurity with the dGSJ quasiparticles.

This model replaces the complexity of the proximitized film with a single site with a single level that represents the dGSJ quasiparticle excitation and is coupled to the impurity with an effective exchange coupling. The single-site model is exactly solvable and allows us to go beyond the classical description of the impurity by treating its spin quantum mechanically.

This approach has been afterward generalized to treat impurities with higher spin and account for magnetic exchange anisotropies [Sec. 4.3.1]. With this, we were able to rationalize the complex spectral features of the FeTPPCl molecules (S=5/2) on top of the Au/V(100) proximitized surface [3]. Our findings properly describe the formation of entangled states formed from the molecular and quasiparticle spins on the system and reveal that in the strong coupling regime, a Cooper pair excitationcould be measured: a smoking gun to detect the local parity of the system [Sec. 4.3.2].

Moreover, our findings are also relevant to superconductor/quantum dots [200–202] hybrid systems. In particular, similar single-site models applied to describe the spectroscopic properties of quantum dot systems [147, 203–205], which can find potential uses as qubits [Sec. 4.4.1]. As an example, after extending the model to describe a system built from two coupled spin-1/2 impurities, we described a singlet-based qubit [44] that is not affected by SOC or HC, increasing its coherence time [Sec. 4.4.2].

[4] The details regarding the exact manipulation technique and NRG calculations of the qubit will be published in a future work.

5

Interplay between Coulomb blockade and superconductivity

In the following two chapters, we investigate how confinement and size influence superconductivity. Specifically, we examine electron tunneling into small Pb islands suspended on graphene (Gr). When a metallic grain with dimensions smaller than the electron's screening length ($\lambda \sim 100$ nm) is connected to two electrodes, an additional energy must be supplied to allow an electron to tunnel. This energy, known as the Coulomb energy, E_C, arises from the Coulomb repulsion created by the tunneling electron: within the confined grain, the electron lacks sufficient space to move freely and screen the added charge. Consequently, excess energy is required to initiate tunneling, compelling electrons to tunnel sequentially, one at a time.

This sequential electron tunneling mechanism, or single-electron tunneling, is harnessed by Single Electron Transistors (SETs) [73, 206]. SETs play a crucial role in the miniaturization of electronic devices, enhancing energy efficiency and sensitivity, particularly in applications like quantum metrology [207, 208].

Contrary to the Coulomb interactions, superconducting correlations create an attractive force between electrons and, hence, favor the formation of a ground state made from Cooper Pairs [45, 46, 52, 208–210]. The competition between these two energy scales modifies the usual response of the SET to an external gate potential. The e-periodic system transforms into a 2e-periodic one [46, 47, 52, 211], where the ratio E_C/Δ describes the accessibility of the odd parity state of the island [46, 209]. Similarly, size and Coulomb interactions modify superconductivity, reducing the superconducting gap and changing the response of the superconductor to magnetic fields.

In this chapter, we perform STM measurements on Lead (Pb) islands on Gr with distinct sizes. We find that the spectral gap obtained from STS measurements is a combination of the effects of superconductivity and Coulomb Blockade (CB). By utilizing an effective theory based on single electron tunneling and the analysis of the evolution of the spectral gap under an external magnetic field, we are able to disentangle the contributions of each effect. The localized measurements enabled by STM make this experimental approach ideal for exploring the relationship between island size and superconductivity.

We start the chapter by introducing the experimental system under study and commenting on the main findings, mainly the spectroscopic measurements on top of small-sized islands [Sec. 5.1]. We then propose a theoretical approach to explain the spectroscopic measurements [Sec. 5.2, extended in App. C]. This theory, based on a master equation approach, extends the theory of single-electron tunneling in a SET [45], by including superconductivity. Next, we disentangle the combined effects of superconductivity and CB by measuring the evolution of the islands' spectra under a magnetic field up to 2.5T [Sec. 5.3]. The different impact of the magnetic field on

the superconducting condensate and the electron-electron interactions is discussed and exploited to obtain information about the values of Δ *and* E_C*. Finally, we present a methodology to control the residual charge state of Pb islands with an STM setup [Sec. 5.4], using high voltage pulses we realize an effective gating.*

5.1 Pb islands on Graphene

The Pb islands are evaporated on Graphene (Gr) grown on the Si side of SiC(0001). Silicon Carbide is a bipolar wide gap semiconducting crystal that can host Gr layers in both terminations [213, 214] (Si and C). The C-terminated face hosts multilayer, polycrystalline Gr. In contrast, the Si-terminated side hosts a monolayer or a bilayer of monocrystalline Gr [Fig. 5.1(a)]. In both cases, the Gr is created by heating the samples (either by resistive heating or e-beam heating), which makes the Si atoms evaporate in the crystal, leaving the C atoms that produce the Gr. In this experiment, we use the Si-terminated face, prepared by resistive heating of a SiC crystal up to 1400ºC in UHV conditions. The Gr formed on the SiC is flat and clean, as shown in STM images like in Fig. 5.1(b).

In the Si-terminated face, the Gr layer lies on top of a buffer layer formed from the collapse of the first two Gr layers [20, 215], which acts as a decoupling layer between the SiC and graphene. The top Gr is closer to a freestanding Gr but still has some n-doping [216, 217] that we detect from differential conductance spectra like in Fig. 5.1(c). This figure shows an STS measurement of bare Gr from -0.6 to 0.6 mV. The main spectroscopic features of the Gr on SiC(0001) can be observed:

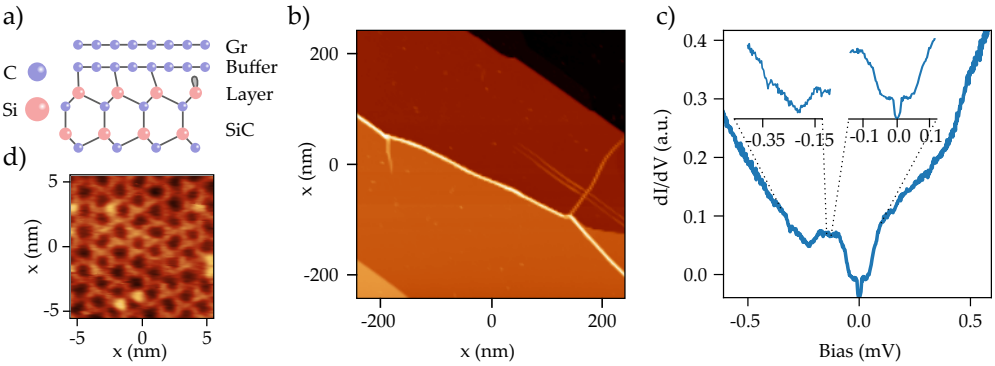

Figure 5.1: **Gr on SiC(0001). (a)** Sketch of the microscopic structure of the system. A buffer layer made of C atoms separates the Si surface of SiC from a monolayer of Gr. **(b)** 500 nm×500 nm scan of the bare Gr surface. Some step edges and a few impurities can be recognized (V=1 V, I=30 pA). **(c)** STS measurement of bare Gr, the insets depict the Dirac Point (left inset) and the phononic gap (right inset) of Gr [212] (V=1 V, I=500 pA). **(d)** Atomic resolution image of Gr (V=50 mV, I=1 nA). Panel **(b)** and **(c)** are adapted from Ref. [4].

the insets show the phononic gap of Gr [212] as a U-shaped minima (right) and the Dirac point at around $V = -0.25$ mV (left), consistent with n-doping. Moreover, the superconducting gap of the tip can also be observed in a small energy window around $V = 0$ as a V-shaped minima. The atomic resolution of the Gr is depicted in Fig. 5.1(d), exhibiting its well-known hexagonal pattern.[1]

To form the superconducting clusters used in this experiment, we evaporated lead on top of the SiC(0001) substrate at room temperature with a rate of ∼0.1 A/s for 30s. In Fig. 5.2(a), we show an STM image of a Pb-covered graphene region. The islands are generally 3-fold symmetric [218], with lateral sizes ranging from 10 to 200 nm and height from 3 to 12 nm. Using the STM tip, these islands can be manipulated, and they always align within the last Gr layer's crystallographic direction [4, 219].

Effects due to the size of the grains start appearing for islands with vol.$^{1/3} \lesssim 35$ nm. Differential conductance spectra of larger islands show an absolute superconducting gap of $\Delta/e \sim 1.35$ mV, the same as the bulk Pb. See the blue curve in Fig. 5.2(b) (top). Compared to bulk Pb spectra, the red curve in Fig. 5.2(b) (top), the coherence peaks in the Pb islands appear wider. We can exclude thermal broadening since, as in bulk lead, a SC tip is used here. Several factors can affect the broadening of the spectra, among them the inverse proximity effect and the effects on the environmental modes.

The former is a consequence of Gr having a finite DoS at the voltages around the island's coherence peaks, broadening the spectra. On the other hand, the latter is due to the change of the circuit. As introduced in Sec. 2.2 and extended in App. D.1, the effects of environmental modes have to be considered when we calculate the tunneling current, which is related to the impedance of the electrical circuit of the STM [45, 54, 156, 220, 221]. The difference between bulk Pb and Pb islands is that the double tunneling junction changes the circuit, mainly the capacitance, adjusting the environmental modes and increasing the spectral broadening [see App. D.1].

To characterize the double tunneling barrier, Fig. 5.2(d) plots the change in resistance as we approach the STM tip onto an island on a logarithmic scale. A change in the slope of the curve can be detected around the -50 pm relative distance point. This represents a transition from the tunneling exponential current dependence ($I \propto e^{-z}$) to the contact regime. Once the tip touches the sample, the current no longer has an exponential dependence on the distance. Previous reports show that break-junctions between Pb tips and Pb surfaces exhibit a broad distribution of contact conductances between G_0 and $5G_0$ [222], i.e., resistances between 2.58 and 12.9 kΩ. As we measure $R \sim 12$ kΩ for the point contact resistance, the resistance between the island and Gr should range between 0 and 10 kΩ.

In the following, we present a theoretical framework to understand the STS measurements on the Pb islands. We apply the double tunneling barrier tunneling formalism presented in Sec. 2.3 and add superconductivity to describe the tunneling to Pb island on Gr.

[1] Technically, the dark spots in the atomic resolution are six-member carbon rings.

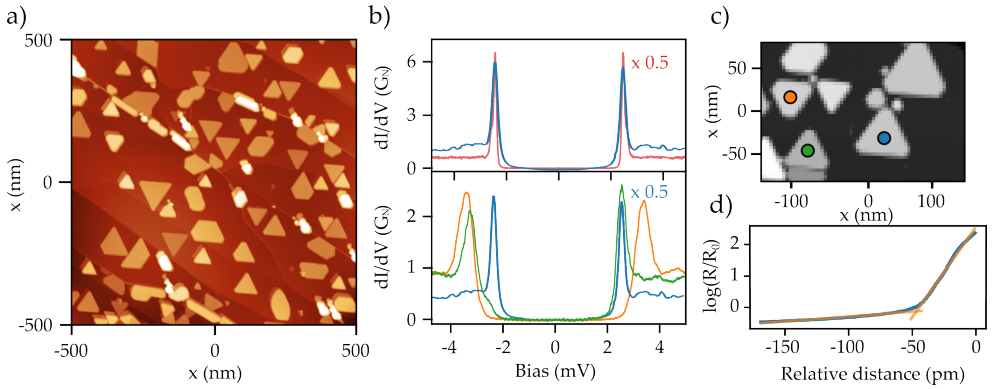

Figure 5.2: **Pb islands on Gr. (a)** 1μm×1μm image of the sample formed by Pb islands on top of Gr (I=20 pA, V=200 mV). **(b)** Comparison between STS on a big island (vol.$^{1/3}$ ∼38 nm) and bulk Pb (top), and between a small island (vol.$^{1/3}$ ∼20 nm) and the same big island (bottom). Some spectra are scaled by a factor of 0.5 (V=5 mV, I=500 pA). **(c)** STM image of the three islands measured in panel **(b)** (V=500 mV, I=30 pA). **(d)** Measurement of the resistance resistance approaching the STM tip to a Pb island (V=50 mV), $R_{=} \sim 13$ kΩ. The fitting lines are the best-fitting linear regression of the resistance.

5.2 Interplay between superconductivity and Coulomb interactions on Pb islands

We now focus on the spectroscopic features of smaller islands (vol.$^{1/3}$ $\lesssim$35 nm). The lower panel in Fig. 5.2(b) shows the spectra of two small islands (orange and green curves) with vol.$^{1/3}$=20 nm compared to that of the large island discussed above (blue curve). We observe a larger spectral gap in the dI/dV of the smaller islands.[2]

To explain the origin of the bigger gap, we note that the onset energy of single-particle excitations on a superconductor is Δ [Sec. 2.1.1]. As introduced before, when a metallic grain is small enough, extra energy must be paid when adding an electron to overcome the Coulomb interactions. The measurements are performed at T=1.3 K< T_C^{Pb}, so the islands should still be superconducting, even if the size of the islands can decrease the critical temperature [50, 218, 225, 226], see Sec. 5.3. Consequently, we attribute the larger spectral gap of the small islands to the combined effect of superconductivity and the CB in the islands.

To describe the competition of Coulomb correlations and superconducting correlations deduced from STS spectra of smaller islands, we describe the possible single-particle excitations the superconducting grains can host. The simplest approach is

[2]For higher voltages, after the coherence peaks, we measure a flat conductance corresponding to the normal metal one [App. C.3]. Small wiggling or peaks that are not reproducible can be observed, but not a clear peak corresponding to the charging of the island [45, 223, 224].

to start with the orthodox model for the Double Tunneling Junction (DBTJ) [45, 208, 210], introduced in Sec. 2.3, which describes the single-electron tunneling, and incorporate superconducting correlations into it. The orthodox model considers the Coulomb interactions by adding a Coulomb energy, E_C, to the single-particle excitations.

Equal to Sec. 2.3, we describe the DBTJ with an equivalent lumped circuit, see Fig. 5.3(a) [45, 54, 156, 220]. The circuit comprises two junctions characterized by a resistor and a capacitor in parallel: the Pb island is connected to the tip (substrate) by a resistor R_1 (R_2) and a capacitor C_1 (C_2). A potential from a third terminal (the gate) is added (described by a bias voltage V_G and a capacitor C_G). The gate potential breaks particle-hole symmetry (ph symmetry), which is essential to understand the asymmetric spectra we measure [green plot in Fig. 5.2(b)]. The gate electrode causes the gain of a residual fractional charge $q_0 = en_0$ in the island [cf. Eq. (5.3)], as already reported in similar systems [120, 218, 224, 227–229]. A justification for the origin of the excess charge on the island is given in Sec. 5.4

To describe our system, we must also consider superconducting correlations in the islands. Although adding superconductivity can be as easy as splitting the system into even and odd parity states separated by an energy Δ (superconducting gap), we must take a small hiatus to discuss size effects on superconductors.

The BCS ground state [8] is a $\mathcal{U}(1)$ gauge breaking wavefunction [50, 79]. This means that, as the theory is built on a grand canonical ensemble, this ground state does not conserve particle number, i.e., it is formed from a product of states containing different particle numbers. As the size of a superconductor shrinks and Coulomb interactions grow, fluctuations in particle number are reduced. In this scenario, the BCS formulation of the ground state starts to be inadequate, as fluctuations from the mean-field approximation have to be considered. A possible fix for this problem is to project the BCS ground state into a particle-conserving state [50, 79, 230], equivalent to the BCS ground state in the bulk limit [see Sec. 2.1].

A more sophisticated method to calculate the wavefunction of a superconducting grain was introduced by Richardson [231, 232], who found a method to calculate the wavefunction exactly. Other methods to do this calculation exist, such as the Density Matrix Renormalization Group [233, 234], the parity projected BCS method [235–237], *etc.* Reference [50] provides a comprehensive review of all these methods.

The main conclusion from these methods is that the BCS approach breaks down when the mean level separation, δ, of the superconducting nanoparticle is comparable to the superconducting gap. Consequently, the usual methodology (BCS approximation) can be used for $\delta/\Delta \lesssim 0.5$ [50, 230], with the exact distribution of the energy levels of the grains not being too important [238]. The mean energy separation in a grain is give by [50, 226, 239]

$$\delta = \frac{2\pi^2\hbar^2}{mk_F\text{vol.}} \sim \frac{179}{\text{vol}}\text{meV nm}^{-3}, \frac{103}{\text{vol}}\text{meV nm}^{-3} . \tag{5.1}$$

The two solutions correspond to the Fermi momentum of each band forming the superconducting condensate in bulk Pb [226, 240] (Pb is a multiband superconductor).

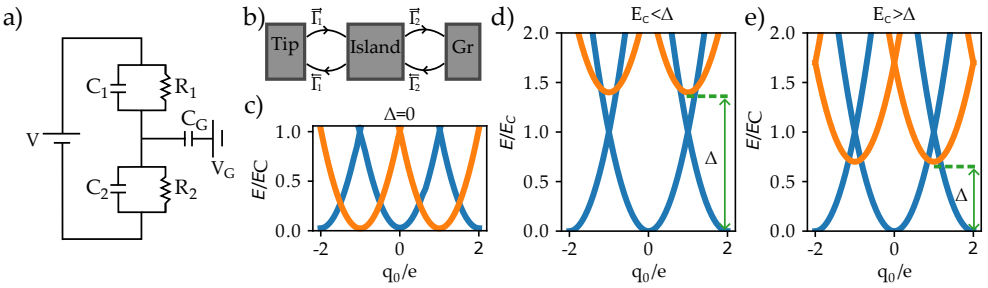

Figure 5.3: **Theoretical description of the system. (a)** Equivalent lumped circuit of the system. **(b)** Sketch of the tunneling rates. **(c)** Energy levels of the system for $\Delta = 0$. **(d)**, **(e)** Energy levels for $E_C > \Delta$ and $E_C < \Delta$, respectively.

For the smallest islands measured in our samples (vol$\sim$1000 nm^3), the level separation is $\delta/\Delta \lesssim 0.1$. With these sizes, we can apply the BCS formalism with minimal corrections due to the level spacing.[3] Then, the tunneling rates can be calculated using the BCS DoS.

With these considerations in mind, we can write the Hamiltonian of the system,

$$\hat{H} = \hat{H}_0 + \hat{H}_S \tag{5.2}$$

with the charging energy as [45, 208, 210]

$$\hat{H}_0 = \frac{(\hat{n} - q_0/e)^2}{2(C_1 + C_2)} e^2 = E_C(\hat{n} - q_0/e)^2 \,. \tag{5.3}$$

$\hat{n}$ is the excess charge in the island, defined as $\hat{n} = \hat{n}_1 - \hat{n}_2$, where $\hat{n}_i$ is the charge in the ith junction, and $q_0 = V_G/C_G$ is an effective fractional charge arising from the electrostatic potential of a gate electrode. The charging energy is $E_C = \frac{e^2}{2C}$, with $C = C_1 + C_2$. This Hamiltonian describes parabolic bands separated by an island's charge e [Fig. 5.3 (c)]. We add the superconducting correlations by breaking the even-odd symmetry [47, 52, 206, 211, 241, 242]:

$$\hat{H}_S = \frac{(1 - (-1)^{\hat{n}})}{2} \Delta \,. \tag{5.4}$$

The periodicity of the bands change from e to $2e$. Moreover, we can now distinguish two distinct regions: $E_C < \Delta$ [Fig. 5.3(d)] and $E_C > \Delta$ [Fig. 5.3(e)]. Notice that for $T = 0$, the population of the odd states is always zero for $E_C < \Delta$, while for $E_C > \Delta$, a gate potential (or excess charge) can change the ground state from even to

[3] The Δ used for the calculation is $\Delta = 1.35$ meV, which is the value for the bulk superconducting gap. Next section [Sec. 5.3] shows that the gap decreases up to 0.5 meV for the smallest islands. Even in this scenario, $\delta/\Delta < 0.5$, i.e., the BCS formalism can still be applied.

odd, populating the odd states. As we measure at T=1.3 K, we must consider a finite population of the excited states [50, 211], which we do following the master equation described in App. C.1 [see Eq. (C.3)]. The only functions to be calculated are the tunneling rates:

$$\begin{aligned}\overrightarrow{\Gamma}_1(V,q) &= \frac{e}{R_1}\int d\omega \rho_{\text{tip}}(\omega) f(\omega) \rho_{\text{isl},n}(\omega + E_1(V,q)) f(-\omega - E_1(V,q)) \\ \overrightarrow{\Gamma}_2(V,q) &= \frac{e}{R_2}\int d\omega \rho_{\text{isl},n}(\omega) f(\omega) \rho_{\text{Gr}}(\omega + E_2(V,q)) f(-\omega - E_2(V,q))\end{aligned} \tag{5.5}$$

where ρ_i are the DoS of the tip, island, and sample, f is the Fermi-Dirac distribution, and E_i/e is the voltage drop from a single electron tunneling in the ith junction, defined in Eq. (C.1), and ρ_i (i = tip, isl, Gr) are the DoS. The island's DoS reads

$$\rho_{\text{isl},n}(\omega) = \begin{cases} N_0 \,\text{Im}\, \dfrac{\omega + i\epsilon}{\sqrt{\Delta^2 - (\omega + i\epsilon)^2}} & \text{, if n is even} \\ N_0 & \text{, if n is odd.} \end{cases} \tag{5.6}$$

Equation Eq. (5.5) does not consider the minimum required energy to add an electron into a superconductor: Δ. This is considered by the DoS, which has a spectral gap for the even parity states. Furthermore, the DoS has no gap for the odd states, as adding an electron to a superconductor that already has one is a gapless excitation. When $\Gamma_1 \ll \Gamma_2$, we consider we are in the tunneling limit [see Sec. 2.3], greatly simplifying the problem. For our system, one can verify that solving the full Master equation [Eq. C.3] or applying the tunneling limit [Sec. 2.3] has the same outcome.[4] The current in the tunneling limit reads

$$\begin{aligned} I &= \sum_n p_n \left[\overrightarrow{\Gamma}_1(V,q) - \overleftarrow{\Gamma}_1(V,q)\right] \\ &= \sum_n \frac{e^{-\beta E_n(q_0)}}{\mathcal{Z}} \left[\overrightarrow{\Gamma}_1(V, ne - q_0) - \overrightarrow{\Gamma}_1(-V, -ne + q_0)\right] , \end{aligned} \tag{5.7}$$

where $\mathcal{Z} = \sum_i \exp\{-\beta E_i\}$ is the partition function and $E_i(q_0)$ are the eigenvalues of $\hat{H} = \hat{H}_0 + \hat{H}_S$.[5] In the rest of the chapter, we use Eq. (5.7) to simulate and fit the measurements. In the next section, this model is used to extract E_C and Δ for several islands by fitting dI/dV spectra using an external magnetic field. On the other hand, in Sec. 5.4, we study theoretically the effect of changing the residual charge on the islands, simulating the effects of a gating potential. This is then compared with experiments where the excess charge is controlled with the STM.

[4] The solution of the full master equation changes the shape of the spectra and the positions of the peaks a little, but this change is smaller than the resolution of our experiments.

[5] This approximation is valid only if $C_1 \ll C_2$, i.e., we do not consider the charging peaks on the current. Within this approximation, $E_C \sim e^2/2C_2$, so the Coulomn gap is given by $2E_C$.

5.3 Disentangling the effects of Superconductivity and Coulomb Blockade: Magnetic field dependence

The interplay between superconductivity and Coulomb interactions can be complex to disentangle from measured spectra since both effects produce gaps around zero bias. Furthermore, the measurements are done using superconducting tips. The tunneling spectra only resolve a spectral gap that is the combination of E_C, and the superconducting gap of the tip, Δ_{tip}, and island, Δ_{isl}. The superconducting gap of the islands is unknown, as it can differ from the bulk Pb gap due to its reduced dimensions [50, 218, 225, 226]. On the other hand, the Coulomb interactions follow the opposite trend: the smaller the island, the bigger the energy cost to add an electron into it. Moreover, the fractional charge measured in most islands makes the calculation more complex, as the gap is not equal for all charge states. This is a well-studied phenomenon: the dependence of the spectral gap on the excess charge follows a shape known as Coulomb Diamonds [45]. See Sec. 2.3.

Consequently, although Eq. (5.7) can fit the data, it requires too many parameters. Therefore a single measurement on an island can not disentangle the relative contributions from CB and superconductivity. To this end, we present a method to disentangle these two contributions based on the evolution of the spectroscopy with an external out-of-plane magnetic field up to 2.5T. With this method, we extract the values of the zero-field Coulomb and superconducting gaps by fitting the evolution of the total spectral gap for different fields. The effects of varying temperatures, which can also be used for the same end, are discussed elsewhere [App. C.2].

Although the consequence of a magnetic field on s-wave bulk superconductors is well known [243–245], magnetic field effects on granular superconductivity are more complex. Not only does the critical magnetic field increase considerably [172, 239, 246] (the magnetic flux enclosed by the islands is smaller), but the evolution for odd and even parity states is different [50, 246], meaning that knowing the ground state of the island is necessary for the analysis. Moreover, one needs to consider the reduction of the superconducting gap due to size effects [50, 218, 225, 226]. On top of these, the effect of the B-field on the superconducting state of the tip needs to be considered.

Similar to small-sized superconductors, which have a higher critical field than the bulk, the Pb-coated W tips we use also have a higher critical field with respect to the bulk [99]. The same superconducting tip is used for all measurements, the apex can vary from island to island, which does not affect the tip gap. We can obtain its characteristic behavior with a magnetic field by measuring spectra on Gr at various fields. An example of such behavior is plotted in Fig. 5.4(a) (blue dots). The values of the superconducting gaps for each field shown in Fig. 5.4(b) (blue and green dots) were extracted by fitting the data with a convolution between two BCS DoS with a changing Dynes parameter [244, 247], ϵ, in Eq. (5.6). The obtained evolution of the spectral gap is the one expected for a bulk superconductor with a critical field of B_C=750 mT with some slight variation at low fields. These are probably caused by the fast-closing proximitized gap of graphene with small fields

Once the evolution of the tip's gap with the field is characterized, we use it to

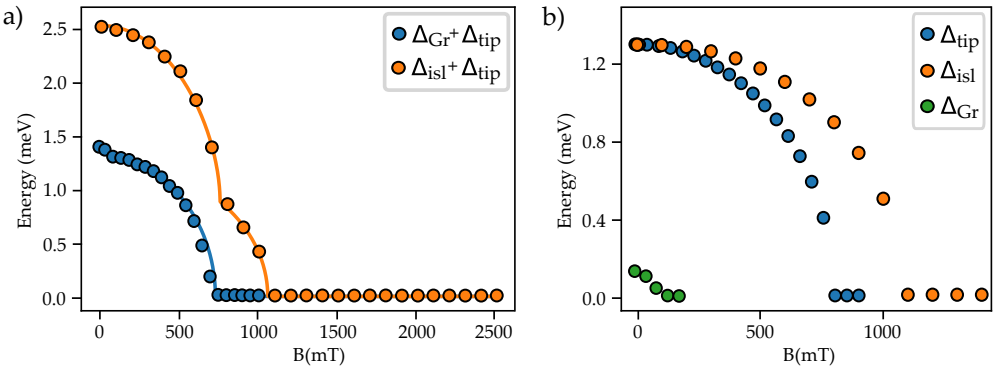

Figure 5.4: **Evolution of the superconducting gap under a magnetic field.** **(a)** Fitted evolution of the Gr plus tip (blue) and big island plus tip (orange) superconducting gaps. The fit was done using Eq. (C.5) ($B_C^{\text{tip}} = 750$ mT, $B_C^{\text{isl}} = 1$ T). **(b)** Values of the superconducting gap of the tip (blue), a big island (orange), and Gr (green). Extracted from panel **(a)**.

extract the critical field of the islands. For a big island (i.e., negligible Coulomb gap), the measured gaps show a non-monotonous evolution with the B field, depicted in Fig. 5.5(a) and as the orange dots in Fig. 5.4(a). Subtracting from these data the values of the tip's gap results in the evolution of the island's superconducting gap, shown in Fig. 5.4(b) (orange dots). Fitting the evolutions [solid lines in Fig. 5.5(a)] with the expression $\Delta(B) = \Delta_0(1 - B^2/B_C^2)^{1/2}$ [43], we extract a critical field of B_C=1 T for the big island. This is an order of magnitude larger than the critical field of the bulk crystal (B_C^{bulk}=80 mT). The spectral gap of the large island closes at the critical field, consistent with its negligible Coulomb energy.

For smaller islands, the spectral map in Fig. 5.5(b) reveals a dependence on the magnetic field that can not be explained with the previous formula. In this case, we use the Orthodox model [Sec. 5.2] to study the evolution of the spectral gap. This model requires seven fitting parameters: R_1, R_2, C_1, C_2, Δ_{tip}, Δ_{isl} and q_0 (a Dynes parameter is also used to account for the width of the coherence peaks). To simplify the fitting procedure, we note that in an STM junction $C_1 \ll C_2$ [156] and, in the tunneling regime, $R_1 \gg R_2$, which simplifies the fitting [Sec. 5.2].

Since the evolution of the superconducting gap of the tip is extracted as detailed above, we are left with three parameters: C_2, Δ_{isl}, and q_0. Focusing on islands with a symmetric (or close to symmetric) spectrum, q_0 has a small effect on the spectra, simplifying the fitting process.

The fitting process is as follows: we first start by fitting a global gap for each magnetic field value to obtain a plot similar to the one in Fig. 5.5(c) (blue dots). Then, the following equation is used to fit the evolution of the spectral gap [see App. C.3]:

$$\Delta E/2 = \Delta_{tip}(B) + \Delta_{\text{isl}}(B) + E_C - E_Z(B)\ , \tag{5.8}$$

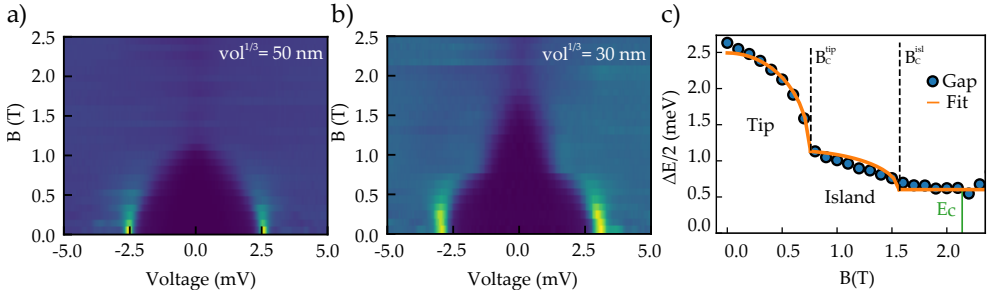

Figure 5.5: **Magnetic field dependence of the spectra on the Pb islands. (a)** Evolution of the dI/dV on a big island (vol^1/3=50 nm) as a function of the applied magnetic field. **(b)** Same evolution for a small island (vol^1/3=30 nm). **(c)** Spectral gap extracted from **(b)** as a function of the applied magnetic field. The fit using Eq. (5.8) is superposed ($B_C^{\text{tip}} = 750$ mT, $B_C^{\text{isl}} = 1.6$ T, $E_C = 0.6$ meV).

This equation has four different contributions. The first is the evolution of the tip's gap. The second is the evolution of the superconducting gap of the island, which is supposed to follow the same evolution as an s-wave superconductor but with a higher critical field [50, 172, 239]. We assume no change in E_C and add an extra Zeeman splitting term, which in our case gives a small 80 μeV correction [see App C.3].

Assuming that the island's superconducting gap is closed for the highest magnetic field values, we obtain E_C (C_2). The asymmetry of the spectra is also extracted to find the value of $q_0 \sim 0$. This fit is similar to that of Fig. 5.5(c) (solid orange curve).

We use the parameters obtained from fitting the spectral evolution with Eq. (5.8) as the starting values to fit each STS measurement with Eq. (5.7) and extract the best fitting values for Δ_{isl}, C_2, and q_0 [see Fig. C.2 in the appendix]. Finally, we plot $\Delta_{\text{tip}} + \Delta_{\text{isl}} + E_C$ [blue dots in Fig. 5.5(c)], obtained from the fit, which ignores the effects of any asymmetry arising from a fractional charge, and fit it one last time with Eq. (5.8). Figure 5.5(c) shows the fitting of the evolution of the gap following Eq. (5.8). As expected, for small islands, the gap of the tip is the first to close at $B_c^{\text{tip}} \sim 0.75$ T, and then the one of the island at $B_c^{\text{isl}} = 1.6 \pm 0.1$ T. For larger B, the spectral gap remains equal to $E_C = 0.6 \pm 0.1$ meV.

We repeat this procedure for several islands with different sizes. Figure 5.6(a) shows the dependence of the superconducting gap of the islands and the Coulomb energy as a function of the size of the islands, depicted by the parameter vol.$^{1/3}$. We find that $\Delta = E_C$ at vol.$^{1/3}$=15 nm. Above this size, superconductivity and CB coexist, the former being larger and susceptible to acquiring residual charges [see Sec. 5.4]. Below this size, Coulomb effects dominate, and odd states become accessible [Fig. 5.3(d) and 5.3(e)]. In this regime, we find that the reduction of the island's superconducting gap with size is more pronounced than in previously reported systems [225, 226], and theoretical calculations [50, 248]. We theorize that this effect is due to the graphene. The previous reports (and theoretical calculations) do not consider any

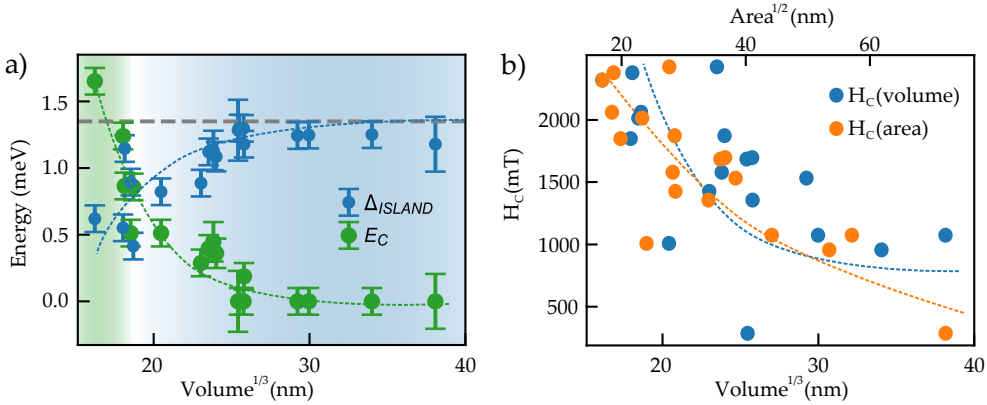

Figure 5.6: **Δ_{isl}, E_C and B_C as a function of island size. (a)** Δ_{isl} and E_C as a function of vol.$^{1/3}$. A crossover between energy scales can be spotted at vol.$^{1/3}$=15 nm. **(b)** Critical field as a function of vol.$^{1/3}$ (blue dots) and area.$^{1/3}$(orange dots). The dashed lines in both panels do not represent a fitting of the data, they are hand-made curves to help better visualize the trend the data follows.

interaction between substrate and islands, as they used insulating layers as substrates. In our case, we use graphene as the substrate, which has electronic states within the energy windows of interest ($|E| \lesssim 3$ meV), so the inverse proximity effect might be contributing to closing the island's superconducting gap.[6]

This fitting procedure also allowed us to obtain the critical magnetic field of each island, shown in Fig. 5.6(b). The blue dots represent the critical field as a function of the island's volume (vol.$^{1/3}$). Surprisingly, the dependence of B_c with size does not follow a clear trend: the points are very dispersed. This is probably caused by the different shapes of the islands in terms of volume, i.e., their volume/area ratio. The main factor defining the critical field is the enclosed magnetic flux in the island, which is proportional to the area rather than the volume. In fact, in Fig. 5.6(b), we plot instead, as orange dots, the same critical fields as a function of the island's area (area$^{1/2}$). The critical field increases as island sizes become smaller. B_C can get up to a few Teslas for the smallest islands, 30 times larger than the bulk's critical field [249, 250].

In this section, we have analyzed the spectra of several islands with an excess charge close to $q_0 = 0$ and described the evolution of the spectral gap with the magnetic field with Eq. (5.8). The evolution under a magnetic field for $q_0 = e$ can differ greatly depending on the ratio E_C/Δ. For the smallest islands ($E_C > \Delta$), the odd states can be accessed at $q_0 = e$, for which the evolution of the spectral gap under a magnetic

[6] Kim et al. [225] showed that for vol.$^{1/3} \sim 15$ nm, the gap was 80% of the original. We calculate 50% in our system. Then, the metallic substrate is responsible for a little more than half of the measured lowering.

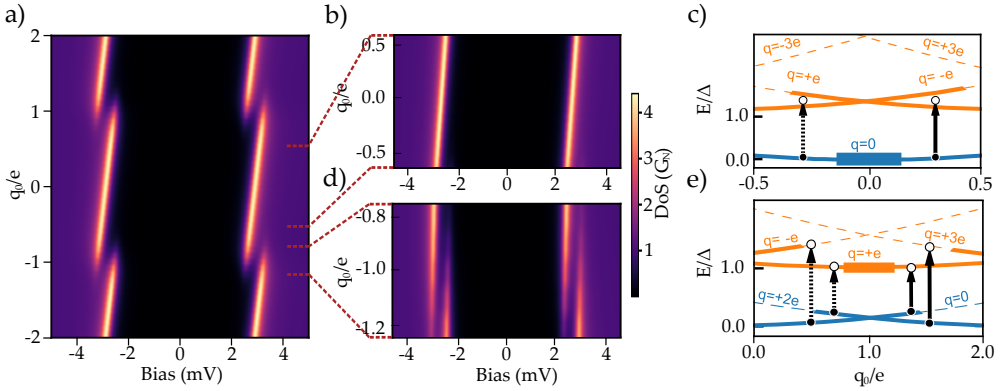

Figure 5.7: **dI/dV dependence on the excess charge. (a)** Contour plot of the dI/dV calculated theoretically for an island ($C_1 << C_2$=480 aF) as a function of the excess charge. **(b)**, **(d)** Zoom in of panel **(a)** around $q_0 \in [-0.6, 0.6]$ e and $q_0 \in [-1.2, 0.8]$ e, respectively. **(c)**, **(e)** Sketch of the transitions forming the dI/dV in the previous regions. Panel **(c)** is centered around q=0; it illustrates two possible excitations with the vertical lines. The dashed line depicts negative voltage transitions, and the solid line is the positive one. Panel **(e)** is centered around q=e,so four transitions are possible, depicted by the vertical lines.

field is different from Eq. (5.8) [246]. Instead of lowering the spectral gap, it increases. This is easy to rationalize by looking at Fig. 5.3(e). The energy of the odd states lowers with the magnetic field (Δ_{isl} decreases), so the transition between the state $n = 1$ and $n = 0, 2$ increases, increasing the gap. The odd state cannot be accessed for bigger islands ($E_C < \Delta$); in these cases, when $q_0 = e$, the spectral gap is much smaller than the one expected for an island that size. As the evolution for $q_0 = e$ is more complex, we only measured islands with $q_0 = 0$. In the following section, we focus on islands with an asymmetric dI/dV, i.e., finite excess charge, and present a method to control q_0.

5.4 Controlling the Ground State properties of the Pb islands

Controlling any system's electronic properties is vital for possible future applications. Although the local assessment of every island is possible in the STM, three-terminal geometries, where the excess charge of the island can be controlled with a gate potential, are challenging to implement. In the following, we present a mechanism to modify the spectral properties of the superconducting islands by controlling their residual charge. Combining this capability with the locality of our measurements and the possible determination of the islands' superconducting and Coulomb gaps, we demonstrate that this system is an ideal platform for characterizing future electronic applications of granular superconductors.

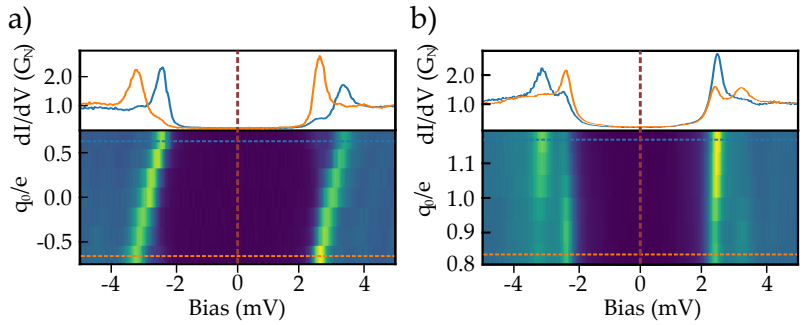

Figure 5.8: **Evolution of the island's fractional charge.(a)** Stacked dI/dV spectra after tip pulses (bottom) and two characteristic spectra (at the limits) of the evolution (top) for an island gated between -0.6e to 0.6e. **(b)** Same measurements for an island gated between 0.8e and 1.2e. For both islands, vol.$^{1/3}$ ∼28 nm (V=5 mV, I=500 pA). The approximate values of q_0 in the y-axis are calculated from the position of the coherence peaks.

The spectrum of a large BCS superconductor is particle-hole symmetric. Coulomb blockade frequently shows asymmetries in the dI/dV owing to electrostatic potentials of the confining nanoparticle [45, 218, 226], generating the typical Coulomb diamond structure. In Fig. 5.7(a), we use the orthodox model introduced in Sec. 5.2 to calculate the dI/dV of a double tunneling junction with $C_1 << C_2 = 480$ aF varying the excess charge q_0 for a finite temperature ($T = 1.3$ K). The coherence peaks shift linearly with q_0, and the dI/dV shows the expected 2e periodicity in q_0 [45]. In the central region, illustrated in Fig. 5.7(b) and sketched in Fig. 5.7(c), the ground state is mainly the parabola q=0 and the model predicts two excitations, namely the 0→e transition at positive bias and the 0→-e at negative bias. Away from q=0, spectra is asymmetric, as we frequently observe for islands with lateral sizes between 20 and 50 nm. Figure 5.8(a) (top) is an example of an island with asymmetric dI/dV. The blue and orange dI/dV measurements show the opposite symmetry. In both cases, one of the coherence peaks appears more intense than the other.

We noticed that the shape of the STS taken on a single island can be changed by applying bias pulses of a few milliseconds with values ±3 V [229]. This process always keeps almost the same gap width but changes the position of the peaks and their intensity accordingly, what is interpreted as a changing the excess charge of the islands. Applying a sequence of pulses with increasing magnitude allows us to modify the excess charge gradually in $q_0 \in [-0.6, 0.6]$e. In Fig. 5.8(a), we show a stack of sequential spectra obtained after bias pulses of increasing voltage showing a continuous shift of the 0→e and 0→-e transitions, which are reminiscent of the coherent peaks of the bare superconductor [see Fig. 5.7(c)].

Focusing on a region close to $q = \pm e$, Figure 5.7(d) shows four quasiparticle peaks. For residual charge close to e, both q=0 and q=2e have a finite population due to thermal effects, and the single-particle excitations are duplicated, namely 2e→e and

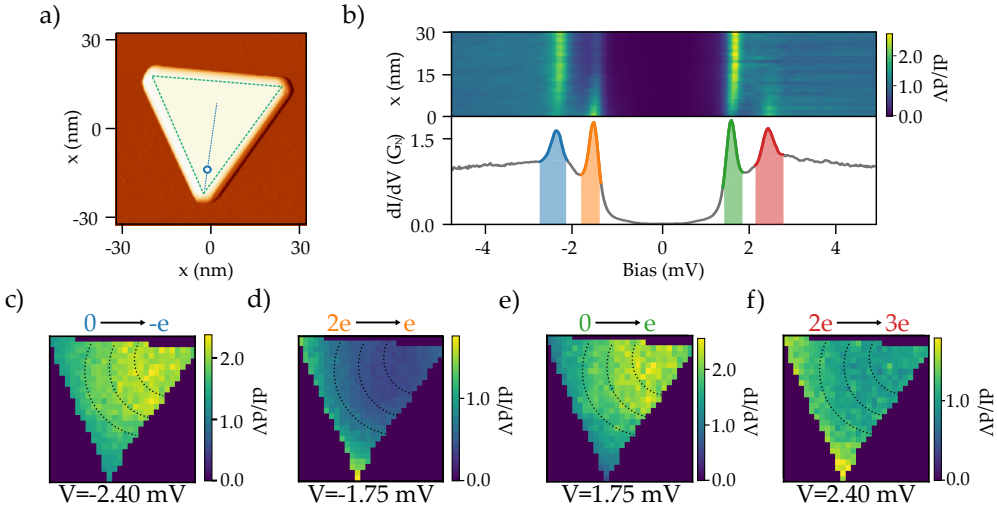

Figure 5.9: **Excess charge fluctuation within an island. (a)** Topographic image of the 45 nm lateral-sized island. **(b)** Contour plot (upper plot) of the dI/dV taken in the dashed blue line in panel **(a)**, and the spectra (lower plot) taken in the blue dot of panel **(a)**. The spectra show four peaks highlighted with colors. **(c)-(f)** Evolution of a triangular dI/dV grid at the voltages of the four peaks, representing four distinct transitions. The dashed black lines are a visual representation of the evolution of the peaks.

2e→3e [Fig. 5.7(e)]. Crossing the q_0=e point, the ground state population shifts from 0e to 2e; therefore, the q=0 ground state excitations vanish, and the q=2e ground state excitations intensify. In Fig. 5.8(b), we present data for a Pb island with excess charge around $q = \pm e$. We observe the presence of the four excitations described above, symmetric in energy but with asymmetric intensity. Increasing the excess charge by voltage pulses as described above, we indeed observe variations in the intensity of the peaks while their energy is slightly shifted, as predicted by the model [Sec. 5.2].

5.4.1 The origin of the gate

A direct measurement of the element responsible for the gating effect that provides some hint of its microscopic origin is complex in the STM geometry. Still, our experiments suggest that local variations of the work function on Gr can explain the variations in residual charge caused, for example, by charged paddles induced at the interface with the bulk SiC crystal. Note that moving islands with the help of the STM tip around the Gr surface can also change the symmetry of the dI/dV [4, 219]. It is known that these charge puddles exist in graphene on insulating substrates (e.g., BN [251]) and that they can be created, removed, or reversed by applying voltage

pulses with an STM, similarly as we do here. These charge puddles are static in the insulating substrate and induce local work function variation. A gate potential is nothing more than an electrostatic field applied to the central region of the double tunneling barrier, which changes its work function and gives rise to the ph asymmetry. This is probably the effect caused by a charged puddle close to an island.

To corroborate the previous assumption with the measurements, Fig. 5.9(a) shows an island with 1333 nm^2 area and size around $vol.^{1/3}$ ∼28 nm. Spectra taken on the island [Fig. 5.9(b) bottom] shows two peaks at positive and negative bias, indicating that its residual charge is q_0 ∼e, as in Fig. 5.7(d) and (e). Probing the dI/dV along the line on top of the island shown in Fig. 5.9(a), we note that the intensity and energy of the peaks gradually changes [Fig. 5.9(b) top], resembling the spectral evolution with changes of residual charge plotted in Fig. 5.8(b), i.e., from 0.8e to 1.2e. Here, no voltage pulse was applied.

To understand the mechanism for this, we plot in Figs. 5.9(c)-(f) distribution of the four spectral peaks [Fig. 5.9(b) bottom] obtained by measuring STS on a triangular grid of points on top of the island. We note the transitions $0 \rightarrow e$ and $0 \rightarrow -e$ [Fig. 5.9(c) and 5.9(e)] have their maxima in the upper right corner of the island and slowly decay towards the left. The opposite behavior is measured for the $2e \rightarrow e$ and $2e \rightarrow 3e$ transitions [Fig. 5.9(d) and 5.9(f)], which are weaker on the right corner but stronger around the left edge of the island. We conclude that the q=0 state is mainly populated in the upper right corner. Its population decays towards the left side of the island. *Vice versa* for the q=2e state.

The circular dashed lines added to Figs. 5.9(c)-(f) represent contours of the progression of the transitions. The circular shape of these contours suggests that an intrinsic charged puddle is the most probable cause of the spectra distortion. We believe that when bias pulses are applied to the islands, the charge of one or a few puddles is perturbed, modifying the electrostatic environment beneath the island and perturbing the spectra. The localized puddles gradually change the effective excess charge of the islands as an effective gating (or electrostatic potential) with the shape depicted by the dashed lines. For this island, a positively charged puddles in the upper left corner explains the experimental results.

5.5 Conclusions

We observed that small Pb islands exhibit an energy gap larger than the intrinsic superconducting gap, arising from the interplay between superconducting and Coulomb effects [Sec. 5.2]. By applying a magnetic field to sequentially suppress superconductivity in the STM tip and Pb island, we determined the Coulomb energy, E_C, and its dependence on island size. Using a double tunneling barrier model, we further disentangled the superconducting gap Δ_{isl} and critical field B_C, revealing a size threshold around $vol^{1/3} = 15\,nm$, below which Coulomb interactions dominate over superconducting pairing [Sec. 5.3].

Our measurements revealed that the Coulomb gap increases as island volume decreases, consistent with enhanced Coulomb interactions in smaller islands where elec-

trons have limited space to screen incoming charges. Additionally, we observed a reduction in the superconducting gap by up to 50% from the bulk value, which we attribute to the inverse proximity effect from graphene.

We also observed spectral asymmetries in many islands, indicative of fractional excess charges, which we were able to control through bias pulses applied with the STM tip, similar to a gate electrode in a three-terminal device [Sec. 5.4]. We linked this gating effect to charged impurities between the graphene and insulating substrate, allowing for fine-tuning of the electronic properties of small islands even without a conventional three-terminal geometry.

Furthermore, we found an increase in the critical magnetic field of Pb islands up to 2.5 T—over 30 times the bulk value. The stability and flatness of these islands, as shown in STM topographic images, make them ideal candidates for qubit characterization, as they can host single adatoms or molecules for use as qubits. This platform's ability to sustain high out-of-plane magnetic fields while preserving the superconducting gap presents a novel environment for qubit studies.

6

The Cooper Pair Diode

Non-reciprocity is a general property of nature that appears when the symmetry of a system is broken. In electronic circuits, non-reciprocal current and the consequent rectification are essential for computational purposes. In conventional diodes, in a p-n junction, the non-reciprocal current comes from a combined break of the inversion (or parity) and charge symmetries, i.e., a CP symmetry break [252]. These devices have low resistances in one current direction and a larger resistance in the other, so they are essential components in modern electronics, used as rectifiers and photodetectors [253].

A current goal in modern low-temperature electronics is the use of superconducting materials for low-power electronics; for this purpose, mechanisms that create a non-reciprocal response or diode effect on superconducting devices are important. Like classical diodes, a broken symmetry is needed for the superconducting or Josephson diode effect to arise. For the superconducting case, inversion and Time-Reversal Symmetry (TRS) must be broken (PT-symmetry break) [254, 255] to create finite momentum Cooper pairs [254], which have a non-reciprocal response to an applied current. Once PT symmetry is broken, the superconductor's positive and negative critical currents differ: $I_c^+ \neq I_c^-$. Most proposals of Josephson diodes [256–259] focus on non-centrosymmetric superconductors or superconducting structures, which show a nonreciprocal current upon applying an external magnetic field due to the magnetochiral effect. Others exploit asymmetric Josephson Junction (JJ) structures [260, 261]. The main inconvenience for device applications is that these methods need an external magnetic field to break the time-reversal symmetry, which is problematic for fast computation and memory recording.

In this chapter, we explore a superconducting structure that exhibits a non-reciprocal (diode) effect in the tunneling of Cooper pairs based on the system described previously (small Pb islands on Gr). In this platform, we investigate the effects of Coulomb correlations when we shift from the tunneling regime to the Josephson regime, i.e., from $R_T \sim 1$ MΩ to $R_T < 100$ kΩ. The Coulomb correlations split the conventional Josephson zero bias peak into two peaks in the I-V Characteristics (IVC) measurements, which we associate with a Resonant Cooper pair Tunneling (RCT) mechanism. The RCT voltage depends on the island's size, and its relative position can be controlled by gating the excess charge on the island, following the process described in Chapter 5. This asymmetry induces non-reciprocal transport in the V-I Characteristics (VIC), resulting in a diode effect. The interaction with the environment modulates the RCT peaks, i.e., they arise from an incoherent transport mechanism, which we simulate considering the environmental modes in calculating the current. On the other hand, although we consider that the charge of each junction is not well defined, the charge of the island is, which we exploit to describe the VIC within the theory of Bloch oscillation in JJs [262]. Finally, we demonstrate that this effect can be used in typical diode

applications, such as tunable rectification of Cooper pairs current and photodetection of microwave radiation.

The Chapter starts with the description of the two measurement modes used in our experiments: voltage-bias and current-bias [Sec. 6.1]. We first use measurements on bulk Pb(111) crystal as an example of the different modes and explain the relation between them. Then, we describe the Josephson regime in the Pb/Gr system. Next, we show the main results of the voltage-biased measurements on small islands and rationalize them with an effective theory [Sec. 6.2] extended in App. D. We continue by presenting the VIC, which we interpret following the Bloch oscillation theory for JJs [Sec. 6.3]. Finally, we introduce the Cooper Pair Diode [Sec. 6.4] - a superconducting-based diode arising from the combined inversion and ph symmetry break- and provide examples of a diode's two main applications: rectification [Sec. 6.4.1] and photodetection [Sec. 6.4.2].

6.1 Voltage and Current biasing in STS

In the tunneling regime, i.e., the most common regime in STM, we measure the current through a system under an applied bias voltage, so the circuit comprises a voltage source and an amperometer, see Fig. 6.1(a). A divider is added to the voltage input to improve resolution around the superconducting gap in the mV range. Moreover, RC or LC filters in the voltage line are added to block external radiation and further enhance the energy precision of the biasing voltage. In this setup, differential conductance measurements at the bias voltage value are obtained using a lock-in amplifier: a low frequency (< 1 kΩ) AC signal is added to the DC voltage, and the output current in response to the bias modulation is measured.

In this chapter, we use a current-biased setup to characterize our system further, inspired by the approach in Ref. [55]. This circuit, illustrated in Fig. 6.1(b), includes a 1 MΩ resistor at room temperature, connected in series with the voltage source. Rather than measuring the current directly, we record the voltage drop across the STM junction with a voltmeter in parallel. When the added resistor significantly exceeds the tunneling resistance, the combined resistor and voltage source function as an effective current source. The current for an applied voltage V reads

$$I = \frac{V}{R + r + R_T} = \frac{V}{R}\frac{1}{1 + (r + R_T)/R} \sim \frac{V}{R} + \mathcal{O}\left(\frac{R_T}{R}\right) . \tag{6.1}$$

R is the 1 MΩ resistor added in series with the voltage source, R_T is the tunneling resistance, and r is the resistance of the rest of the circuit, which is small compared to the other two: $r \sim 100\ \Omega \ll R, R_T$. An ideal current source is obtained when $R_T \to 0$. This value is controlled by the tip-sample distance. The current-bias measurements were mainly done in the 20 to 100 kΩ tunneling resistance regime, i.e., a 2 to 10% shift from the ideal current source is expected. We simultaneously measure the voltage drop and the current across the STM junction with the voltmeter and amperometer in Fig. 6.1(b). Comparing the expected current, $I = VR$, with the measured one, we calculate the shift from the ideal current source and fix any errors in the posterior analysis.

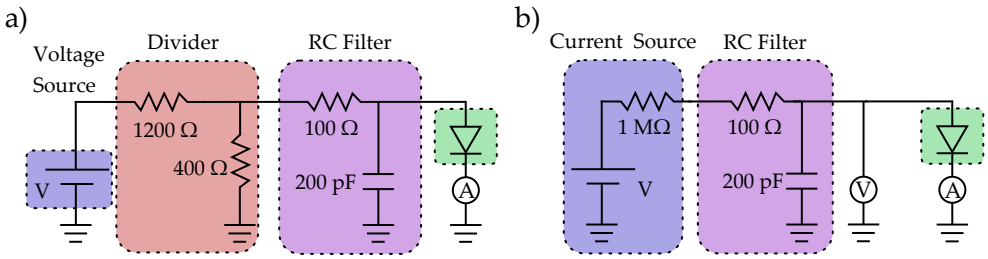

Figure 6.1: **Voltage- and Current-biased setups (a)** Sketch of the electrical circuit used for the IVC. It comprises a voltage source, a divider (1/100), an RC filter ($f_{\text{cutoff}} \sim$ 44 kHz), the junction, and an amperometer. **(b)** Sketch of the electrical circuit used for the VIC. It comprises a voltage source in series with a big resistor (1 MΩ), which we use as a current source, an RC filter ($f_{\text{cutoff}} \sim 50$ Hz), the junction and an amperometer and voltmeter. The voltmeter is in parallel to the STM junction.

The simplicity of the current source has a major throwback. The added resistor generates a larger noise source than more complex setups where operational amplifiers are used [263]. The thermal noise arising from a resistor is known as the Johnson-Nyquist noise, which amounts to 12.5 $\mu V/\sqrt{Hz}$ for our 1 MΩ room-temperature resistor. For this reason, no larger resistors are used in the current-bias setup, as the noise would become too big. A second problem of this setup is that the extra resistor lowers the cutoff frequency of the RC filter in the current-bias mode, forcing this mode to be very slow and impeding that we perform differential resistance measurements with a locking. To solve this, we select an RC filter that works in both measuring modes. The capacitance of the RC filter is $C_{\text{RC}} = 3$ nF, with a 100 Ω resistor in the line. With this value, the voltage-bias circuit has a cutoff frequency at $f_{\text{cutoff}} \sim 44$ kHz, which suppresses higher frequency noise, while the current-bias setup has a $f_{\text{cutoff}} \sim 50$ Hz cutoff frequency. This is large enough to meet our measurements.

As the two modes are complementary for the measurements, we add a solid-state relay to switch between measuring modes while maintaining the tip-sample distance constant. Controlling the STM tip in a static position is essential to compare the IVC and VIC at the same setpoint. The STM tip must be left stabilizing for around two hours to reduce the creep to a minimum. Following Ref. [55], we also perform the Josephson spectroscopy on Pb adatoms, this offers improved stability compared to performing the measuremnt directly on Pb.

6.1.1 Comparing voltage and current biased measurements in bulk Pb

In the following, we introduce measurements in the Josephson regime ($R < 100$ kΩ) in bulk Pb. Figure 6.2(b) shows the dI/dV measured in a junction between a Pb-coated tip and a Pb(100) sample at $R_T = 20$ kΩ. The red arrow points to five characteristic

peaks, introduced in Sec. 2.5.

This section focuses on the sharp peak around $V = 0$: the Josephson peak [45, 51, 71, 72, 86, 90, 91]. In a voltage-biased STM circuit, the phase difference between superconductors in the tunneling junction is not fixed. With no phase difference, the DC component of the Josephson current is zero [264, 265]; nevertheless, we observe a peak in conductance and a net current around zero in the corresponding I-V curve, depicted in Fig. 6.2(b). Ivanchenko and Zil'Berman [266] (see also Ref. [70]) were the first to explain the origin of the zero-bias peak observed in tunneling junctions. By introducing a fluctuating voltage, modeled as a thermal, frequency-independent white noise from a resistor, they showed that this noise causes a fluctuating phase difference that adds to the static phase. This fluctuating phase results in a DC component of the supercurrent, with a characteristic width of $k_B T R(2e)^2$, which diminishes at higher applied voltages. For a more advanced noise model, see, e.g., Ref. [56].

A more sophisticated approach, considering the effects of the circuit on the tunneling current, was given by Averin *et al.* [71], who considered that due to the effects of the environment, incoherent tunneling of Cooper pairs is possible [45, 51, 71, 72]. This calculation is shown in Sec. D.1.2. The main result of Refs. [45, 51, 71, 72] can be summarized in the following expression for the incoherent current of Cooper pairs

$$I_S = \pi e E_J^2 \left(P'(2eV) - P'(-2eV)\right) \tag{6.2}$$

The function $P'(\omega)$ is defined in Eq. (2.26). The $P'(\omega)$ is a distribution function named PoE function that describes the effects of the environment on the tunneling Cooper pairs [45, 51, 71, 72]. The current is proportional to the square Josephson energy, E_J^2, which indicates that this formula corresponds to a second-order tunneling transport mechanism. The current is zero when the interaction with the environment is not considered, i.e., it arises from tunneling assisted by the bosonic modes of the environment, similar to the Tien-Gordon theory introduced in Sec. 2.1.1. In this case, we say that Eq. (6.2) describes an incoherent tunneling of Cooper pairs. This approach does not consider the JJ as a part of the circuit when the PoE is calculated, i.e., the inductance of the JJ is not considered [267]. When the JJ is considered, a divergence is generated close to $V = 0$. Still, this approach is valid for small environmental interactions and away from the strict $V = 0$.[1]

We now introduce the current biased measurements in bulk Pb. The setup is switched from voltage- to current-bias while the sample-tip distance is kept constant at a specific tunneling resistance R_T=20 kΩ. With this, we measure the junction's response to an applied current and voltage under the same conditions. Figure 6.2(c) shows the voltage drop through the Pb-Pb junction when a bias current is applied in forward (blue) and backward (orange) directions. We observe a hysteretic behavior in the voltage response, characteristic of an underdamped JJ [56, 265], whose origin we describe in the following with the Resistively and Capacitively Shunted Junction (RCSJ) theory [43, 265].

[1] For a low impedance circuit, this approach is valid as long as $E_J \ll E_C$, while, for a high impedance circuit, $E_J \ll E_C(R_K/Z)^{1/2}$ has to be fulfilled [45]. In both cases, the approach breaks down at $V = 0$.

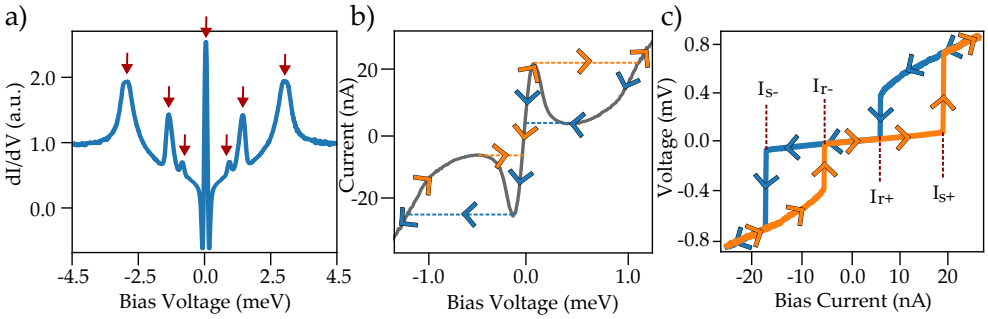

Figure 6.2: **Comparison between IVC and VIC. (a)** dI/dV measurement between a Pb-coated tip and a Pb(100) sample. **(b)** IVC of the same junction in a small window around V=0. **(c)** VIC at the same setpoint. All measurements are done at a constant resistance that amounts to $R = 20$ kΩ.

In the RCSJ theory, the voltage response of a Josephson junction, in parallel with a resistor and a capacitor, illustrated in Fig. 6.3(a), maps to an analogous classical dynamic system. This system models a particle, called the "phase particle," moving in a washboard potential $U(\phi)$, illustrated in Fig. 6.3(a) and 6.3(c). The particle's position is given by the phase difference ϕ between the superconductors, creating a periodic potential. When a current is applied, an additional term, $I\phi$, tilts the potential. The voltage drop across the junction follows from the second Josephson relation [Eq. (2.23)].

As the current is ramped from negative to positive, a plateau emerges at positive currents, as shown by the blue curve in Fig. 6.2(c). This plateau corresponds to the phase-particle trapped in the potential, as indicated in the shaded sketch in Fig. 6.3(b). The measured finite voltage arises from thermal quasiparticle tunneling [265], represented by the resistor parallel to the junction. Upon reaching a threshold current $I_{s+} = 18$ nA, the tilt in the potential allows the phase particle to escape, illustrated in Fig. 6.3(b). The phase change, related to the voltage via the second Josephson relation, results in a voltage jump at this threshold.

During the downward ramp, the current required to retrap the phase particle is lower, $I_{r+} = 6$ nA$< I_{s+}$, depicted in Fig. 6.3(c). This phenomenon is attributed to the inertia of the phase particle, characteristic of an underdumped JJ [56, 265]. It results in a retrapping current that depends on the measurement's ramping speed. We minimize variations in retrapping current by selecting a slow ramping speed, effectively fixing it to thermal fluctuations.

In Fig. 6.2(b), we show the IV curve in a small voltage range around V=0. The arrows represent the response of the junction when a monotonously increasing bias current is applied. The incoherent tunneling of Copper pairs rises linearly with a very small voltage change until it reaches the cusp of the current peak. At this point, the current switches to the quasiparticle regime, with a sudden increase in the voltage

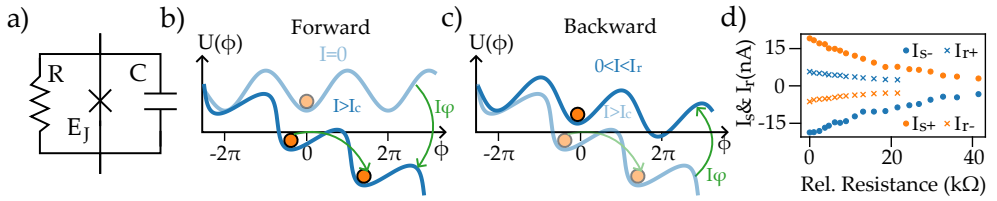

Figure 6.3: **The RCSJ model (a)** Sketch of the circuit representing the Josephson junction. **(b)** and **(c)** Drawings of the phase-particle in the potential well, $U(\phi)$, as a function of the applied current in the forward and backward directions, respectively. **(d)** Switching and retrapping currents as a function of the junction resistance, controlled with the distance between tip and sample.

drop across the JJ, represented by an orange dashed line in Fig. 6.2(b). Note that, contrary to an ideal system, this jump is not to the continuum of normal states, i.e., the voltage we measure in Fig. 6.2(c) for $I > I_{s+}$ (and $I < -I_{s-}$) is not arising from the normal conduction of electron but from Andreev reflections.

As the current is lowered back, we observe bistability, marked by a dashed blue line, where the current switches from the Andreev reflection branch back to the superconducting branch, causing a voltage drop back to $V = 0$ at the retrapping current. The response for negative current can be explained similarly. In differential conductance measurements, these bistabilities appear as regions of negative differential conductance, as observed in Fig. 6.2(a). Thus, any measured negative differential conductance corresponds to a hysteretic behavior in the VIC.

Both I_s and I_r are modified by the environment. As a consequence, the value of the switching current is always smaller than the theoretical critical current, given by [51, 70]

$$I_C = \frac{\pi\Delta}{2eR} \tanh \frac{\Delta}{2k_B T} \,. \tag{6.3}$$

According to Eq. (6.3), the critical current for the measured Pb-Pb junction is $I_C = 85$ nA. However, in our experiments, the measured switching current only reaches $I_s = 18$ nA, see Fig. 6.2(c). The switching current is influenced by the height of the incoherent Copper pair tunneling peaks in Fig. 6.2(b), which depends on the PoE function [Eq. (6.2)]. When environmental effects lower the Josephson peak height below the normal conduction onset, $\sim \frac{\Delta}{2eR}$, there is no transition to the normal conduction branch but rather to the Andreev reflection branch. Consequently, the switching current relates to Andreev reflections instead of normal quasiparticle tunneling, meaning that $I_s < I_C$.

Figure 6.3(d) shows the dependence of the switching and retrapping currents on the relative resistance of the junction, starting from $R_T = 25$ kΩ. The switching current follows a $1/R$ trend, expected from Eq. (6.3).

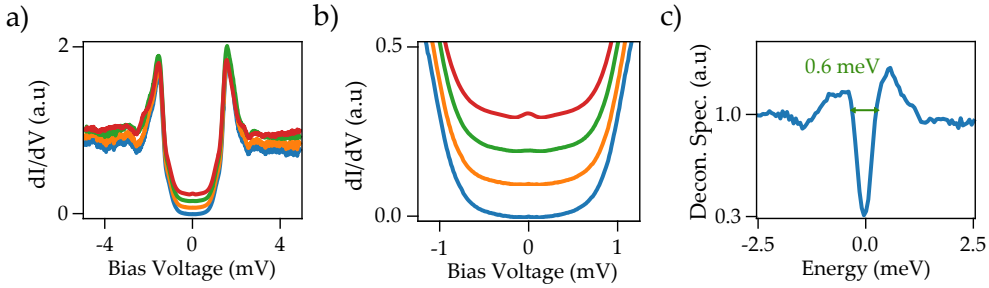

Figure 6.4: **Proximity effect on Graphene. (a)** dI/dV measurements in the tip-Gr junction for resistances from 1 MΩ (blue) to 125 kΩ. **(b)** The same measurements in a small voltage window around V=0. The Josephson peak at V=0 starts to develop. **(c)** Deconvolution of the blue spectrum in panel **(a)**. A pseudogap that amounts to 600 μeV is observed, arising from a proximitized gap of $\Delta_{Gr} \sim 300$ μeV

6.2 Interplay between Cooper Pair tunneling and Coulomb blockade.

In the Pb tip-Pb island-Gr system, the junction between the tip and the Pb island can be described with the circuit depicted in Fig. 6.3(a). However, now we also need to describe the junction between the Pb island and Gr junction. Graphene is a normal metal, but as discussed in the previous chapter [Sec. 5.3], Gr becomes superconducting due to the proximity effect induced by the ensemble of Pb islands. This is further proved by observing a zero-bias peak in the low-resistance tunneling between the Pb tip and Gr. Figure 6.4 shows the differential conductance recorded as we approach the tip to the sample, up to $R_T = 125$ kΩ. At zero bias, a peak starts to develop in the IVC, which we attribute to the onset of a Josephson peak. In fact, our measurements on this system find that Gr develops a superconducting gap that amounts to $\Delta_{\mathrm{Gr}} \sim 300$ μeV [4], as illustrated in the deconvoluted spectrum in Fig. 6.4(c).

The measured proximitized gap is much smaller than the Pb bulk gap, $\Delta_{\mathrm{Gr}} \sim 0.25\Delta_{\mathrm{Pb}}$, a consequence of the finite resistance between the Pb islands and Gr, which can get up to several kΩ [Sec. 5.1]. As the proximitized gap is much smaller than the Pb bulk gap, the extension of the proximity effect, which depends inversely on the energy,[2] is more significant. As the extension of the proximity effect is larger than the average separation between Pb islands, we observe a homogeneous gap in Gr. See Ref. [3] for a detailed discussion. In the following, we introduce the possible tunneling mechanism in a DBTJ made of superconductors, acknowledging the interplay between the tunneling of Cooper pairs and the Coulomb blockade.

First, we present the IVC in the double junction. A comparison between the dI/dV of a big (blue) and a small (orange) island in a narrow voltage range around

[2]The coherence length related to a proximitized gap of energy Δ_p reads $\xi_p = \sqrt{D/\Delta_p}$, where D is the diffusion coefficient of the proximitized material.

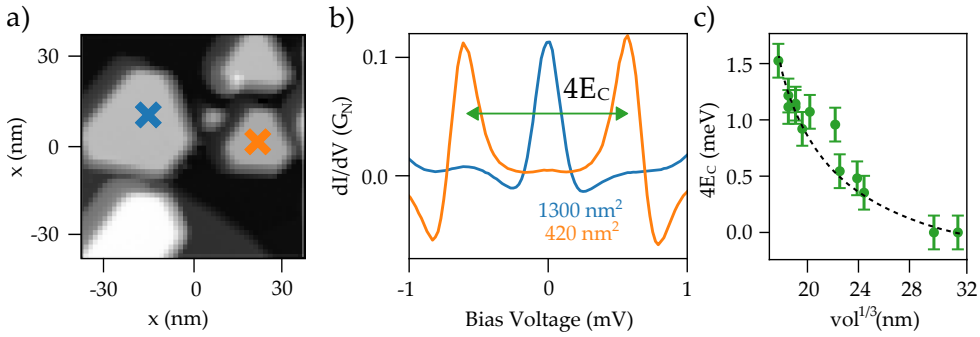

Figure 6.5: **Resonant Cooper Pair Tunneling (RCT) in small islands. (a)** Topographic image of some islands (V=200 mV, I=20 pA) **(b)** dI/dV measurement of a small voltage range at $R_n = 25$ kΩ of the two islands depicted in panel **(a)** and a third asymmetric dI/dV spectra on a different island. **(c)** Island size dependence of the separation between the RCT peaks (measured in several islands).

V=0 at $R = 25$ kΩ is plotted in Fig. 6.5(b). The blue and orange crosses in Fig. 6.5(a) represent the island on which the measurements were taken. For the large island, at zero energy, we detect the conventional Josephson peak due to the inelastic tunneling of Cooper pairs mediated by the environment [45, 51, 71, 72], similar to that in Fig. 6.2(a). In contrast, on the small island, this peak is split into two. This is a general trend for the smaller islands where the energy separation between peaks decreases with island size, as shown in Fig. 6.5(c). This plot resembles Fig. 5.6(a), where the charging energy of several islands is depicted. Note that the separation between peaks has been identified as $4E_C = 2e^2/(C_1 + C_2)$. This is proven in the following text.

In the next section, we explore a model that explains how the peaks move as we change the gate and what defines the separation between peaks.

6.2.1 Resonant Cooper Pair Tunneling

Transport mechanisms between superconductors with a strong Coulomb blockade energy have been studied in several works [45, 47, 52, 53, 211, 268]. In Chapter 5, we have only considered sequential single-particle tunneling events [Sec. 5.2], consistent with large resistances. Once the Josephson coupling between the two junctions is substantial, the simple scheme depicted in Fig. 5.3 breaks down, and coupling between bands with different particle numbers has to be considered. Adding this new energy scale, E_J, the Hamiltonian of the system reads;

$$\hat{H} = \frac{\hat{Q}_1^2}{2C_1} + \frac{\hat{Q}_2^2}{2C_2} + E_{j1}\cos\hat{\phi}_1 + E_{j2}\cos\hat{\phi}_2 \,, \tag{6.4}$$

where $\hat{Q}_i$, $\hat{\phi}_i$, C_i, and E_{Ji} are the excess charge, phase difference, capacitance, and Josephson coupling energy of the ith junction, respectively. In the following discussion,

we assume that the excess charge of each junction is quantified by the amount of Cooper pairs tunneling: $\hat{Q}_i = 2e\hat{n}_i$. We will discard odd parity levels, as we only work with islands with $E_C \lesssim \Delta$. We add the following voltage drop to each junction: $V_i = \kappa_i V$, with $\kappa_1 = C_2/C$ and $\kappa_2 = C_1/C$, where $C = C_1 + C_2$. Then, the Hamiltonian reads,

$$\hat{H} = E_{C1}\hat{n}_1^2 + E_{C2}\hat{n}_2^2 + E_{J1}\cos\hat{\phi}_1 + E_{J2}\cos\hat{\phi}_2 - 2e(\kappa_1\hat{n}_1 + \kappa_2\hat{n}_2)V \ . \tag{6.5}$$

The voltage drop of the junction shifts the energy as a function of the total charge tunneling $e(\kappa_1\hat{n}_1 + \kappa_2\hat{n}_2)$. The phase and number operator commute $[\hat{n}_k, \hat{\phi}_j] = 2i\delta_{kj}$, so the two cosine terms can be understood as translation operators. Taking $2\hat{k} = \hat{n}_1 + \hat{n}_2$ and $2\hat{n} - 2n_0 = \hat{n}_1 - \hat{n}_2$, Eq. (6.4) reads [see Sec. 2.2.2]

$$\begin{aligned}\hat{H} =& E_{C1}(\hat{k} + \hat{n} + n_0)^2 + E_{C2}(\hat{k} - \hat{n} - n_0)^2 - 2e(\kappa_1(\hat{n} + \hat{k} + n_0) + \kappa_2(\hat{k} - \hat{n} - n_0)V \\ &+ \frac{1}{2}E_{J1}\sum_{n,k}|n+1,k+1\rangle\langle n,k| + \text{h.c.} + \frac{1}{2}E_{J2}\sum_{n,k}|n+1,k-1\rangle\langle n,k| + \text{h.c.} \ .\end{aligned} \tag{6.6}$$

k and n are now the number of Cooper pairs tunneling through the junctions and the excess Cooper pairs in the island, respectively, and $n_0 \in [-1, 1]$. The Josephson couplings connect the states $|n,k\rangle$ with $|n \pm 1, k \pm 1\rangle$. Starting from $n = k = 0$ (the ground state for zero voltage), for $E_{J1} = E_{J2} = 0$, the crossing between levels $|n,k\rangle$ with $|n \pm 1, k \pm 1\rangle$ happens when

$$\begin{aligned}&(0,0) \leftrightarrow (1,1);\ eV = (E_{C1} + E_{C2})(1 + n_0) \\ &(0,0) \leftrightarrow (-1,-1);\ eV = (E_{C1} + E_{C2})(n_0 - 1) \\ &(0,0) \leftrightarrow (1,-1);\ eV = (E_{C1} + E_{C2})(n_0 - 1) \\ &(0,0) \leftrightarrow (-1,1);\ eV = (E_{C1} + E_{C2})(1 + n_0) \ .\end{aligned} \tag{6.7}$$

When the E_{Ji} are turned on, an anticrossing between levels is generated. As an example, we take the doublet $|0,0\rangle$ and $|1,1\rangle$ close to the resonant voltage point,

$$\begin{aligned}&\check{H}_{\{0,0\},\{1,1\}} = \\ &= \begin{pmatrix} E_{C1}(2+n_0)^2 + E_{C2}n_0^2 - \frac{2eV(C_2(2+n_0) - C_1 n_0)}{C_1+C_2} & \frac{E_{J1}}{2} \\ \frac{E_{J1}}{2} & E_{C1}n_0^2 + E_{C2}n_0^2 - \frac{2eV(C_2 - C_1)n_0}{C_1+C_2} \end{pmatrix}\end{aligned} \tag{6.8}$$

The energy separation between the doublets reads $\omega_{01} = \sqrt{4((E_{C1} + E_{C2})(1 + n_0) - eV)^2 + E_{J1}^2}$. Fermi golden rule dictates that the intra-doublet transition rate is (see Ref. [52])

$$\Gamma_{ij} = |\langle j|\hat{I}|i\rangle|^2 \frac{S_V(\omega_{ij})}{(\omega_{ij})^2} \ , \tag{6.9}$$

where S_V is the spectrum density of the fluctuations of the applied voltage and ω_{ij} is the energy separation between levels. The current operator reads

$$\hat{I} = 2ei\frac{E_{J1}}{4}\sum_{n,k}|n+1,k+1\rangle\langle n,k| - \text{h.c.} + 2ei\frac{E_{J2}}{4}\sum_{n,k}|n+1,k-1\rangle\langle n,k| - \text{h.c.}\,, \tag{6.10}$$

so the rates of such Resonant Cooper Pair Tunneling (RCT) mechanism, according to Eq. (6.9), are second order in E_J. As they are second order in E_J and activated by the environment, they are an incoherent tunneling mechanism. Consequently, the width of the resonance peaks is related to the environment via a fluctuation spectrum density function, S_V, which is directly associated with the PoE function [52, 267]. Note that when the voltage is added to the Hamiltonian [Eq. (6.6)], the spectrum becomes unbounded; the larger the k value, the lower the energy. Therefore, for large enough values of Josephson coupling, a cascade of transition to lower energy doublets occurs [52], which appear at lower energies than the first RCT, defined in Eq. (6.7).

In Eq. (6.5), we assumed each junction's excess charge to be well-defined and found an expression for the intra-doublet transitions. These transitions depend on both junctions' charging energy and the island's excess charge.[3] Moreover, we discussed the existence of inter-doublet cascade transitions, which lay at lower voltages than the intra-doublet transitions and can have high transition rates [52], i.e., this mechanism can not be discarded in our system. The experimental measurements in Fig. 6.5(b) only show two peaks, one at positive and one at negative voltages, with a thickness comparable (but wider) to the bulk Pb Josephson peak in Fig. 6.2(b).

As no extra peak connected to inter-doublet transitions is observed, we conclude that the charge of each junction is not well defined due to the environmental effects. Then, the Hamiltonian (6.5) can not be applied to our double JJ.

In the following, and extended in App. D.2, we present an effective theory that considers all possible transitions within the PoE theory. For this, we will consider that the island's excess charge is well defined, which is possible because the island is isolated from the tip and Gr, but not the excess charge for each junction, which fluctuates due to the applied voltage. Taking $\tilde{k} = \kappa_1 q_1 + \kappa_2 q_2$, equation (6.4) reads

$$\hat{H} = E_C(\hat{n}+n_0)^2 + \tilde{E}_C\hat{\tilde{k}}^2 + E_{J1}\cos\left(\hat{\psi}+\kappa_2\hat{\phi}\right) + E_{J2}\cos\left(\hat{\psi}+\kappa_1\hat{\phi}\right) - 2e\hat{\tilde{k}}V\,, \tag{6.11}$$

with $\tilde{E}_C = e^2\frac{C_1+C_2}{C_1C_2}$, $\psi = \kappa_2\hat{\phi}_1 - \kappa_1\hat{\phi}_2$, $\hat{\phi} = \hat{\phi}_1 + \hat{\phi}_2$, and the commutators $[\hat{\tilde{k}},\hat{\phi}] = [\hat{n},\hat{\phi}] = 2i$ are fulfilled. Assuming that n is well defined but not $\tilde{k}$, we follow the approach of Refs. [71, 72] and find that the current in the ith junction can be written as [Eq. (D.35)]

$$I_j = \frac{e}{2}E_{Jj}^2\,\text{Im}\left\{\int d\tau\langle e^{i\kappa_j(\phi(\tau)-\phi(\tau'))}\rangle\langle e^{i(\psi(\tau)-\psi(\tau'))}\rangle\right\}\,. \tag{6.12}$$

[3] Note that, due to the tip's geometry, $C_1 \ll C_2$, i.e, $E_{C1} \gg E_{C2}$. Consequently, the intra-doublet transition energy can reach high voltages $V > \Delta/e$.

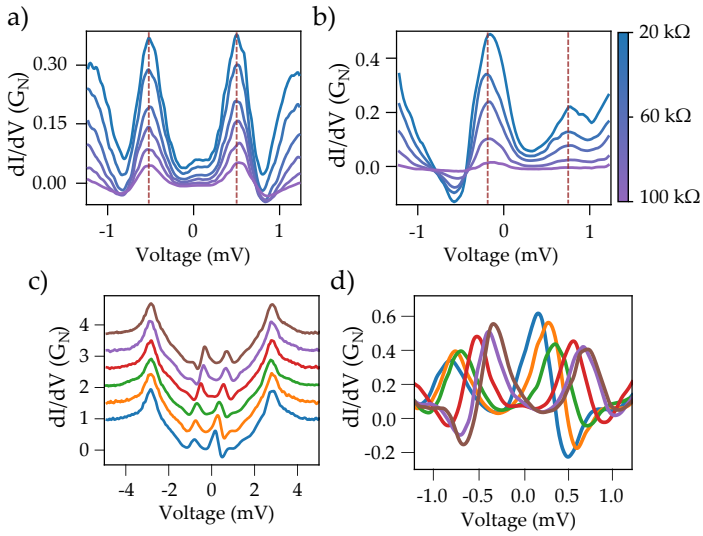

Figure 6.6: **Evolution of the RCT peaks.** **(a)** and **(b)** dI/dV measurement of a small voltage range (-1 to 1 mV) from 100 to 20 kΩ in two islands. **(a)** shows the evolution of symmetric RCT peaks, and **(b)** shows the same evolution for asymmetric RCT peaks. **(c)** Evolution of the RCT peaks on the same islands as we change the excess charge with pulses (R=25 kΩ). **(d)** Same evolution in a shorter voltage range.

The two factors in the integral have the shape of the average of a translation operator, e.g., $e^{i\psi(\tau)}$ is the imaginary time function related to the translation operator of one Cooper pair in the island. Whereas the first term is the PoE function, which describes the effects of the environment on the tunneling of Cooper pairs, the second term considers the energy needed to add (or subtract) a CP into the island. The latter can be straightforwardly calculated in the limit of $E_J \ll E_C$, the limit we consider here [see Eq. (D.36)]. For T=0, the second term adds an energy shift to the PoE function, so the current reads

$$I_i = \pi e E_{Ji}^2 \left[P_i'(2eV - 4E_c(1+n_0)) - P_i'(-2eV + 4E_c(n_0-1))\right] \tag{6.13}$$

We do not expect the P' to change drastically for the smallest island compared to the big one presented in the blue curve in Fig. 6.5(b). The differential conductance of the big island, similar to bulk Pb, can be described with two Gaussian-shaped functions, as described in Fig. D.2. Consequently, Eq. (6.13) describes two Gaussian-shaped peaks separated by a voltage $4E_C$. We are not considering the effects of the Coulomb Blockade and environment on the value of E_{Ji}, which would make it a function of E_C and n_0. E_{Ji} is maximized when $n_0 \sim \pm 1$ and for larger E_C (see Ref. [52, 211]), then, we expect the peaks to maximize when they are closer to zero voltage, i.e., $n_0 \sim \pm 1$. Once the transition rates for each junction are known, a master equation considering both junctions should be developed to calculate the

current flowing through the two junctions. When $E_{J1} \ll E_{J2}$, the current can be approximated to I_1, given by Eq. (6.13), which is the tunneling limit we employed in Sec. 5.2.

To prove that in our system $E_{J1} \ll E_{J2}$, Fig. 6.6(a) and 6.6(b) show the evolution of the RCT peaks as we approach the tip to an island in a symmetric and asymmetric charge configuration. The intensity of the peaks increases as the tip approaches the island, rising E_{J1}, proving the dependence between the transition rate and the Josephson coupling. We assume no change in the second junction's coupling. Moreover, neither the voltage of the peaks nor their shape changes. If the relative change between E_{J1} and E_{J2} in the approach was significant, we would expect an evolution in the position and shape of the peaks. The absence of any evolution proves that similar to Sec. 5.2, the current is fixed by the junction with the lowest rate.

On the other hand, Fig. 6.6(c) and 6.6(d) show the evolution of the RCT peaks as a function of the island's excess charge, controlled with pulses [Sec. 5.4]. The voltage of each peak is extracted in Fig. 6.8(b) (dots). We observe two peaks with a constant valued separation $\Delta V = 1.5 \pm 0.03$ meV. The variance is around 0.03 meV$\sim \Delta/40e$. The small variance indicates that the separation between peaks is constant as a function of the excess charge, which proves that the position of the positive and negative RCT should have the opposite trend. In Eq. (6.13), we proposed that the peak voltage is given by $eV_{\pm} = 2E_C(n_0 \pm 1)$. This function fulfills the requirements measured in the experiments.

Summarizing, we proposed an effective theory where the charge tunneling through the junctions fluctuates and interacts with the environment. This led us to Eq. (6.13). This formula describes two RCT peaks at $eV_{\pm} = 2E_c(n_0 \pm 1)$ with a thickness defined by the PoE function, i.e., by the environmental fluctuations.

6.3 VIC of small Pb islands.

Using the two measuring modes of STS, we can compare the response of a double JJ to an applied voltage and current at the same setpoint. Fig. 6.7(a) illustrates the VIC corresponding measurements in Fig. 6.5(b). The blue curve depicts the VIC on the big island. The switching from Cooper pair tunneling to Andreev tunneling and retrapping back to the former regime is present at symmetric positive and negative current values. The orange curve, measured in the small island, also shows symmetric switching and retrapping currents at values similar to the large island but with a smaller hysteresis. Nevertheless, close to the zero applied current, two finite voltage jumps can be detected, indicated as V_c in Fig. 6.7(a) with red dashed lines. These voltage steps are larger than the voltage expected from thermal quasiparticle tunneling. Since the only change between voltage- and current-bias circuits is the addition of a resistor in series to the voltage source, the voltage step in the current-bias plot should be related to the two peaks observed in the voltage-biased dI/dV plot.

In the tunneling between the tip and bulk Pb, we measure no voltage drop when a finite current is applied. On the other hand, the circuit instantly causes a voltage increase with a small current in the small islands because the RCT peaks lie at finite

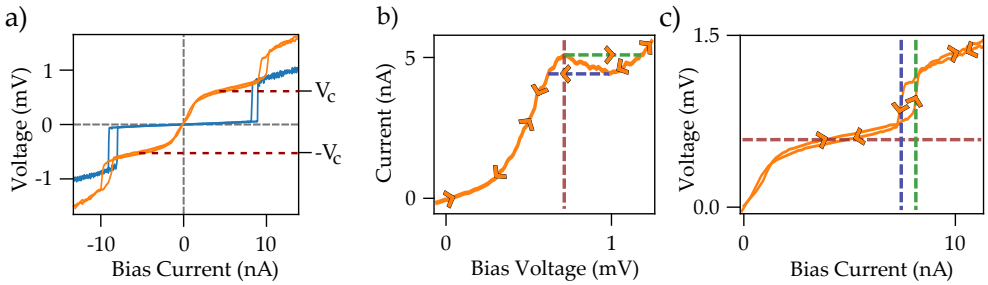

Figure 6.7: **VIC vs IVC (a)** VIC measured on a big island (blue) and a small island (orange and green). The measurements are taken at R=20 kΩ in the same islands as Fig. 6.5. **(b)** IVC of the orange curve in **(a)** in a short voltage range from 0 to 1.2 mV. The dashed lines represent some of the main features of the curve. The RCT peak's position is pointed out in red, and the bistability points are in blue and green. **(c)** VIC corresponding to **(b)**. The dashed lines are added to compare both curves, and the arrows represent the directionality of the applied current.

voltages. Figures 6.7(b) and 6.7(c) show a comparison between both measuring modes. The red dashed lines lie at the RCT peak voltage. When the current corresponding to the maximum value of the RCT peak is reached, depicted by a green dashed line in Fig. 6.7(b), the junction switches to a different conduction mechanism, causing a voltage jump. This is represented by the green dashed line in Fig. 6.7(c). In the backward direction, the IVC has another bistability. This is connected to the retrapping, which happens at a different value ($I_s \neq I_r$), depicted with a purple dashed line in Fig. 6.7(c). This is consistent with the negative differential conductance measured in the orange curve of Fig. 6.5(b).

The evolution of the VIC depending on the excess charge of the island is shown in Fig. 6.8(a). The VICs are measured at the same setpoint as the IVCs at $R = 25$ kΩ. They are shifted in current as we gradually change the island's excess charge. We observe that the hysteretic behavior shifts from the positive bias current (blue curve) to the negative one (brown curve). Moreover, the voltage jumps arising from the RCT also evolve. In the blue curve, the negative voltage jump is the largest, the red curve is symmetric, and in the brown curve, the positive voltage jump is the most prominent. Figure 6.8(b) illustrates the position of the voltage jumps (starts) compared to the position of the RCT peaks in the IVC corresponding to each measurement (dots). The excess charge corresponding to each curve was calculated from Eq. (6.13). As expected, the voltages coincide for all gatings. This confirms that the RTC is the mechanism generating the voltage jumps in the VIC.

6.3.1 Bloch oscillations in double JJs

In the following, we further rationalize the VIC by returning to Hamiltonian (6.4). In this case, we are interested in the response of the junctions to an applied current,

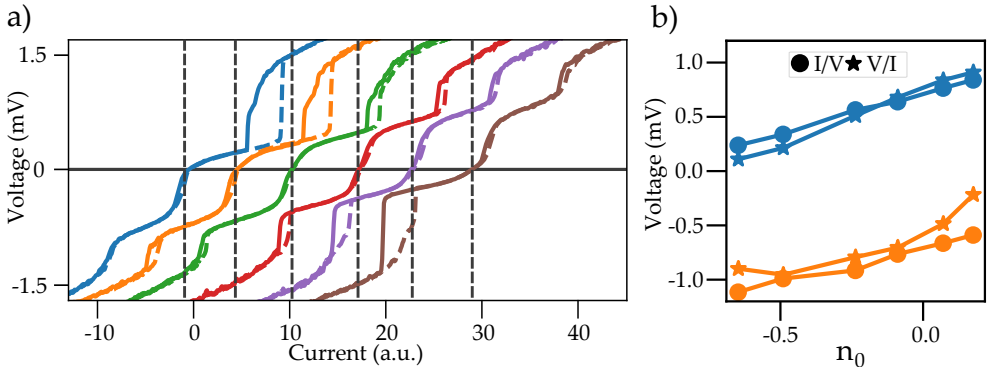

Figure 6.8: **VIC dependence on the excess charge. (a)** Evolution of the VI characteristics as we apply bias pulses (R=20 kΩ). **(b)** Data extracted from **(a)** and Fig. 6.6(d). The colors represent the polarity of the RCT (blue for positive and orange for negative). The dots are the energy of the RCT peaks in the IV curves, and the stars are the value of the voltage jumps in **(a)**.

which we assume to be smaller than the switching current: $I < I_s$. For $I = 0$, Hamiltonian (6.5) is periodic with respect to $\phi_i \to \phi_i + 2\pi$. This periodicity makes it possible to describe the eigenvector following Bloch's theorem [262], analogous to a 2D crystal. The eigenvectors read,

$$\psi(\phi_1, \phi_2) = \sum_{N,M} \int_{-\infty}^{\infty} dk_1 dk_2 \mathcal{C}(k_1 + N, k_2 + N) u(\phi_1, \phi_2) e^{i(k_1+N)\phi_1 + i(k_2+M)\phi_2} \ , \quad (6.14)$$

where the $\mathcal{C}$ are constants, $u(\phi_1 + 2\pi, \phi_2 + 2\pi) = u(\phi_1, \phi_2)$ and k_i is defined inside the first Brillouin zone, with $q_1 = 2ek_1$ and $q_2 = 2ek_2$. These two can be regarded as a quasicharge, analogous to the quasimomentum in a crystal. The energy dispersion, $E(k_1, k_2)$, is defined with the following equation:

$$\begin{aligned} &\left(\frac{(q_1 + 2en)^2}{2C1} + \frac{(q_2 + 2em)^2}{2C1} - E \right) C(q_1 + 2en, q_2 + 2em) \\ &+ \sum_{n,m} U_{n,m} C(q1 + 2en, q_2 + 2em) = 0 \ , \end{aligned} \quad (6.15)$$

with $n, m = 0, 1, 2, 3...$ and $U_{n,m} = -\frac{E_{J1}}{2}\delta_{n,m+1} - \frac{E_{J2}}{2}\delta_{n,m-1}$. In the following, we solve Eq. (6.15) in the case of symmetric and asymmetric junctions.

Symmetric Junctions

The gating fixes the difference between junction charges as $Q_1 - Q_2 = q_0$. This transforms the problem from 2D to 1D. Taking $q_0 \in [-1, 1]$e, we truncate Eq. (6.15) to nine states: {n,m}={0,0}, {1,0}, {0,1}, {-1,0}, {0,-1}, {1,1}, {-1,1}, {1,-1} and

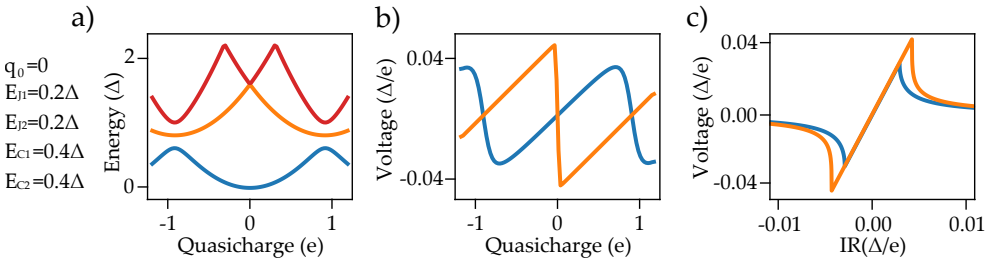

Figure 6.9: **Bloch Oscillations in a symmetric double JJ. (a)** Dispersion of the lowest lying four bands. The second and third bands are degenerate. **(b)** Derivative of the first two bands.**(c)** Voltage response of a double JJ when the charge-particle is in the first (blue) and second (orange) bands.

{-1,-1}. In the following, we solve the matrix equation (6.15) for a symmetric system; we get nine bands, $E^s(k)$. The first four are depicted in Fig. 6.9(a), and the derivative of the first two bands, $\frac{dE^{(s)}}{dq}$, in Fig. 6.9(b). The derivatives have the same absolute maximum and minimum slope $|\max\{\frac{dE^{(s)}}{dq}\}| = |\min\{\frac{dE^{(s)}}{dq}\}|$.

At $T = 0$, the basic equation defining the response of the double JJ to an applied current is similar to that of a periodic crystal with an applied electrostatic field [262]. Hence, it is described by

$$\frac{dq}{dt} = I(t) - G\frac{dE^{(0)}}{dq} - \tilde{I}(t)\,. \qquad (6.16)$$

Here, $\tilde{I}(t)$ is the current arising from noise and fluctuations, and G is the conductance of the resistor parallel to the JJ. The derivative of the band respect to the quasicharge is related to the voltage.

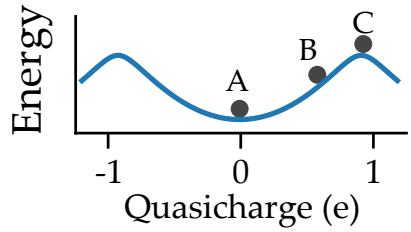

Figure 6.10: **Diagram of the charge-particle on the first energy band.** Point A represents the equilibrium position for no applied current. For small applied currents the particle evolves to B. The system has an ohmic response here. C is the critical point for the supercurrent to flow.

In what follows, we assume no current fluctuations $\tilde{I}(t) = 0$.[4] Figure 6.10 illustrates the charge-particle in the 0th band. When the applied current is zero, the charge-particle is in position A, and as the current is increased, it slowly moves towards point B and later to C. If the current is ramped slowly, and there is no AC component, the derivative of the quasicharge is zero, $\frac{dq}{dt} = 0$, for any current $I < |\max\{\frac{dE^{(s)}}{dq}\}|/R$. This is the value of the current needed to move the charge-particle to C.

[4]The analysis made from this point on is a work in progress and will be published in the future considering non-zero temperatures and fluctuations.

This can be understood from Eq. (6.16). For small values of the current and $\tilde{I} = 0$, there is always a value of q where $I - G\frac{dE^{(s)}}{dq} = 0 = \frac{dq}{dt}$, i.e., a static solution of the problem exists. For these currents, the response of the system is ohmnic:

$$V = \frac{dE^{(0)}}{dq} = IR \tag{6.17}$$

When the current surpasses this critical value, the charge-particle gains enough energy to continuously transition from the position C to equivalent positions in higher Brillouin zones. Moving to a higher Brillouin zone is equivalent to tunneling one Cooper pair through the two junctions, as the system's reciprocal lattice constant is $q = 2e$. Consequently, the time derivative of the quasicharge now oscillates, corresponding to the charging and discharging of the capacitor in parallel with the JJ.

This process reopens the channel for Cooper pair tunneling, which had previously been blocked. As a result, the junction's response changes dramatically from ohmic to shunted. The response of a symmetric junction with the charge-particle initially in the first band is shown in Fig. 6.9(c) (blue). To calculate the response of the second band, we substitute $\frac{dE^{(0)}}{dq}$ with $\frac{dE^{(1)}}{dq}$ in Eq. (6.16). This is also illustrated in Fig. 6.9(c) (orange). For both cureves, at low applied current, the response of the system is linear until the crtical value of the current is applied. Then the voltage response drops to zero. Note that the critical current differs from the 0th to the 1st band. It is larger in the 1st band.

Asymmetric Junctions

We now consider an asymmetric junction with a finite excess charge in the island, breaking inversion and ph symmetries. The first four bands for such a system are shown in Fig. 6.11(a). Due to the breaking of the two symmetries, the bands are no longer symmetric with respect to quasicharge inversion. Additionally, the derivatives of the first two bands, depicted in Fig. 6.11(b), show different maximum and minimum values, i.e., $|\max\{\frac{dE^{(s)}}{dq}\}| \neq |\min\{\frac{dE^{(s)}}{dq}\}|$.

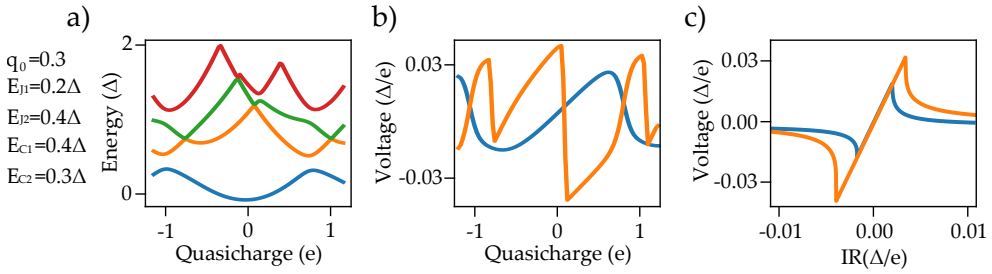

Figure 6.11: **Bloch Oscillations in a asymmetric double JJ. (a)** Dispersion of the lowest lying four bands. **(b)** Derivative of the first two bands.**(c)** Voltage response of a double JJ when the charge-particle is in the first (blue) and second (orange) bands.

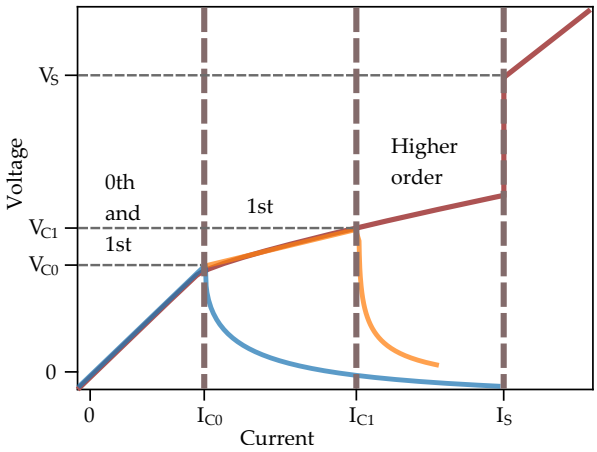

Figure 6.12: **Representation of the voltage response of a double JJ.** We connect the sketch of the measured response (sketched as the red curve) with different contributions of the charge-particle in several bands. In blue is the contribution of the 0th band, and in orange, the 1st.

Following a similar reasoning as for the symmetric case, we now distinguish between positive and negative applied currents. For positive current, the system responds ohmically until $I < |\max\{\frac{dE^{(s)}}{dq}\}|/R$ is reached. However, for negative current, the ohmic response lasts while $I > |\min\{\frac{dE^{(s)}}{dq}\}|/R$. This disparity means that Cooper pair tunneling has different onset currents for positive and negative bias currents, as illustrated in Fig. 6.11(c) for the first (blue) and second (orange) bands. Thus, non-reciprocity emerges from the system's ohmic response. Similar to the symmetric case, the critical current onset of the tunneling of Cooper pair is larger in the 1st band than in the 0th band.

To understand the voltage response to an applied bias current, we conclude by discussing the influence of temperature.

Effects of temperature and comparison with the experiments

Figure 6.12 is a sketch of the different contributions that can add up to describe the voltage response of the system to an applied current. When the temperature is considered, two new effects emerge: the finite population of higher-order bands and the Landau-Zener tunneling between bands. The former depends on the energy of the bands, and the latter depends on the applied current, i.e., the position of the charged particle, and on the separation between bands [262]. We suggest that the system's response to a small applied current arises from the combined effect of the first two thermally populated bands. This is represented by the linear section for $I < I_{C0}$ in Fig. 6.12. Once the critical current of the first band is surpassed, the tunneling of Cooper pairs starts to flow. This changes the slope at $I = I_{C0}$. At this point, the particle in the first band is shunted, so it makes no contribution to the voltage. The voltage in this region is mainly given by the second band, which has a higher critical current $I_{C1} > I_{C2}$. At this point, the Zener tunneling is large enough to populate higher energy bands. High Zener tunneling rates change the system's response close

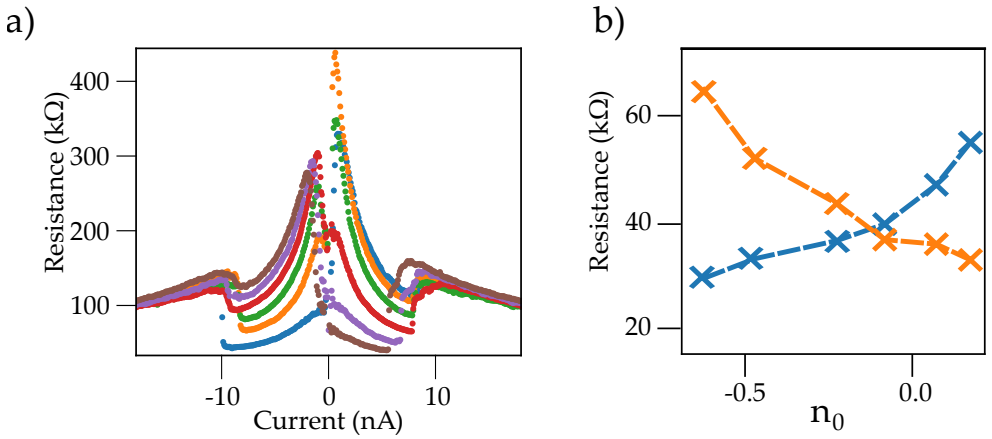

Figure 6.13: **Resistance of the double JJ as a function of the excess charge in the island. (a)** R-I characteristic of an island for distinct values of the excess charge. The colors refer to the VIC in Fig. 6.8(a). **(b)** Extracted resistance values for the voltage jumps in the VIC.

to ohmic as the highest energy bands start to be populated. At $I = I_S$, we reach the switching current of the system, and the approach we use breaks down.

The previous discussion was primarily focused on positive currents. For negative currents, as shown in Figs. 6.11, non-reciprocity emerges due to a direction-dependent ohmic response when inversion and ph symmetry are broken. The same analysis applies, but the voltage jump values differ, which explains the non-reciprocal response observed in the VIC.

The exact resistance of the slope between I_{C0} and I_s varies depending on the relative population of the bands. The resistance measured in a small island depending on the excess charge is depicted in Fig. 6.13(a). From these curves, we extract the resistance on the voltage jumps, depicted in Fig. 6.13(b). We observe that the higher the energy of the voltage jump, the larger the resistance. These values change as the excess charge of the island is controlled. This is because Zener tunneling and band population depend on the system's response to the applied current, which differs between positive and negative currents when an excess charge is present in the islands.

In summary, the combined effects of several bands must be considered to understand the shape of the measured VIC fully. Nevertheless, a single-band analysis suffices to explain the non-reciprocal response in the double Josephson junction. Future works will address the effects of temperature and fluctuations in the current source.

6.4 The Cooper Pair Diode

Throughout this chapter, we have proved that the RCT is a transport mechanism severely modulated by the environment that can be controlled with a gate electrode.

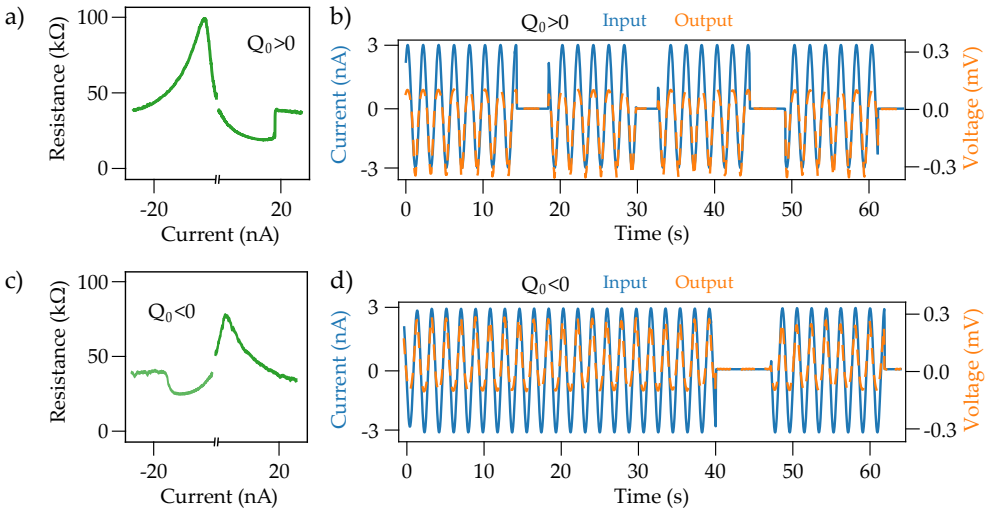

Figure 6.14: **Rectification of the current.** **(a)** and **(c)** RI characteristics of an island in (almost) opposite charge states (R=25 kΩ). **(b)** and **(d)** rectification of an applied $I_{pp} = 6$ nA and $f = 1$Hz current for the two charge states. The output voltage (orange) is superposed on top of the input current (blue).

Although we do not have a three-terminal geometry, as introduced in Sec 5.4 and further used in the previous section, pulses applied with the tip can effectively be used as a gate potential.

The control of the islands' charge state has been proven useful in modifying the transport reciprocity in the IVC and VIC. The tip pulses are used to change the intensity and directionality of the asymmetries measured in the system. The system's non-reciprocal response is an example of a diode. As the diode is based on the tunneling of Cooper pairs, we name it Cooper Pair Diode (CPD). In the following, we exploit the system for the main two applications of a diode: the rectification of an AC current and the photodetection of microwave radiation.

6.4.1 Rectification

When the position of an RCT is close to zero ($q_0 \to \pm e$), we find a high asymmetry in the R-I characteristics. These extremes show a high resistance peak above or below zero current, a typical characteristic of oppositely polarized diodes. Figs. 6.14(b) and 6.14(d) show the rectification of a sinusoidal current input with f=1 Hz, I_{pp}=6 nA (peak to peak current) for an island gated into distinct charge states illustrated by Figs. 6.14(a) and 6.14(c). They show oppositely signed rectification in the voltage output, which can be expected from the R-I curves. Moreover, the effectiveness of the rectification depends on the applied signal, with a maximum at $I_{pp} \sim \pm 6$ nA, corresponding to the maxima of resistance in Fig. 6.14(a) and (c).

In Josephson diodes, the TSR breaking induces an asymmetry in the positive and negative switching currents ($I_{s+} \neq I_{s-}$) so that it can only rectify signals for values of the current between I_{s+} and I_{s-}. The CPD conserves TRS, so $I_{s+} = I_{s-}$, but breaks the ph symmetry instead. This generates a non-reciprocal current before the switching currents; consequently, arbitrarily small signals can be rectified. A diode always presents a finite leakage current that, in our system, manifests as a finite voltage drop on the low resistance side. A gate electrode can fine-tune one of the RCT peaks close to zero bias and the other far away, reducing the diode's leakage current.

6.4.2 Photodetection

In a second application, we analyze the effect of a microwave field on the tunneling current through the CPD. The most direct method to calculate such an effect is assuming that the microwave field can be simplified to a classical oscillating electric field. This method, known as Tien-Gordon theory [68], assumes that microwave radiation affects the junction by shifting the chemical potential in an oscillatory manner, with the same frequency as the field; i.e., it assumes an instantaneous (no inertia) response of the electron in the source and drains to the applied field. This has been explained in the introduction [Sec. 2.1], where the photon-assisted current is split into the effect of different photon-number processes.

$$I(V) = \sum_n (J_n(V_{RF}/\Omega))^2 I_0(V + n\Omega) \,, \tag{6.18}$$

where $J_n(x)$ is the n-th Bessel function, V_{RF} is the potential related to the intensity of the field (see below), $\Omega = 2e/\omega_{RF}$ and $I_0(V)$ stands for the current without any applied microwave field. This model has successfully been used in several STM measurements with microwaves, see Refs. [269–271].

Note that, in the definition of Ω we have used the charge of a Cooper pair, 2e [269–271], because in the voltage range we are working in, the main contribution to the current is the tunneling of Cooper pairs. Finally, V_{RF} is the magnitude of the AC field created in the junction related to the microwave field. This is an effective value that accounts for the coupling of the applied field and the junction.

The fraction of the applied microwave power absorbed by the tip-sample junction is not possible to calculate, as many circuit variables are unknown. For this reason, we assume that the tip-substrate junction detects an unknown field, which changes the IVC following Eq. (6.18), then we progressively change the input power of the field for several radiation frequencies. We record the evolution of the IVC upon these changes and fit it with the best potential, V_{RF}, for each power and frequency. From this calculation, we estimate the transfer function of the system: a function that connects the input power and frequency with a potential drop, V_{RF}, in the tip-sample junction.

The dotted lines in Fig. 6.15(a) are the IVC of an island in two distinct almost opposite charge states in a narrow bias voltage range around V=0. The finite excess charge induces an asymmetric I-V curve. The solid lines are the theoretical evolution of these two curves under a microwave field as calculated from Eq. (6.18) for different potential, V_{RF}. Due to the IV curve's non-reciprocity, a finite current at zero voltage

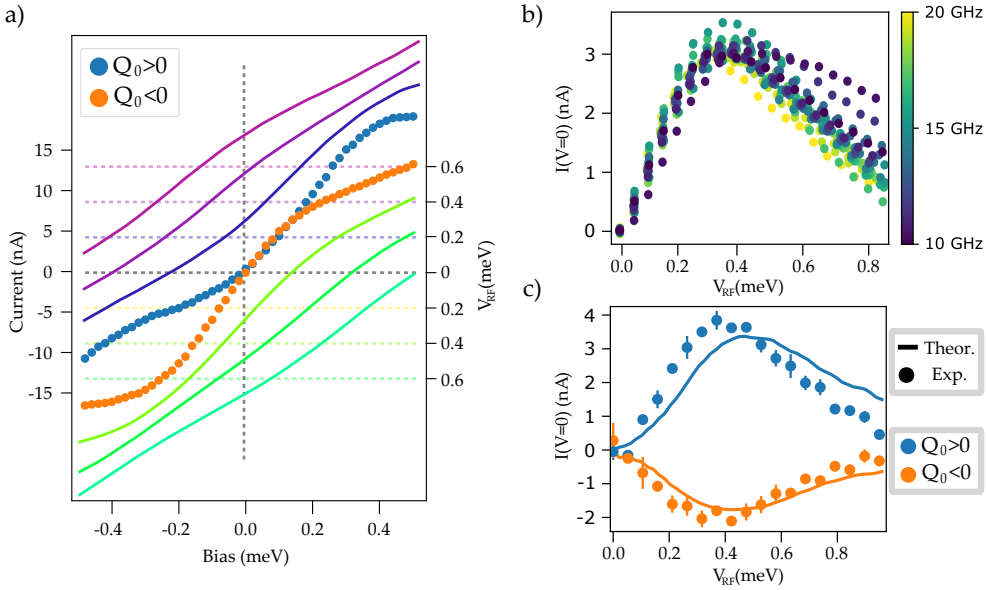

Figure 6.15: **Detection of a microwave signal. (a)** IV characteristics of an island in two (almost) opposite charge states (orange and blue dots) in a small voltage range at $R = 20$ kΩ. The solid lines, shifted with respect to the experimental measurement to better see the evolution, are the theoretical calculations of the system's response to an increasing intensity external microwave field. **(b)** Photon-assisted current at zero applied voltage for an island with positive charging for several microwave frequencies. **(c)** Theoretical calculation (solid lines) and experimental measurement (dots) of the photon-assisted current at zero applied voltage for an island in two distinct charge states (blue and orange). Same states as in panel **(a)**.

develops. At this voltage range, the current due to the radiation arises from Cooper pair tunneling. Then, the calculations suggest that a photon-assisted tunneling current develops a zero bias from the tunneling of Cooper pairs. This is a supercurrent that develops without any external magnetic field to fix the phase.

Figure 6.15(b) shows the measured current with no applied voltage when the sample is irradiated with a radiofrequency signal with a varying frequency from 10GHz to 20GHz as a function of V_{RF}. We observe that the detected supercurrent on the CPD weakly depends on the frequency of the input radiation. The maxima is always around $V_{RF} = 0.5$ meV, which defines the maximum efficiency point. The signal decays afterward. This current can be calculated from the following equation [Eq. (6.18) for $V = 0$]:

$$I(V=0) = \sum_{n>0} (J_n(V_{RF}/\Omega))^2 \left[I(n\Omega) + I(-n\Omega) \right] \ . \tag{6.19}$$

Figure 6.15(c) shows the zero bias current as a function of applied microwave voltage

for two gatings (blue and orange) for $f = 10$ GHz. The theoretically calculated current (solid lines) is superposed, which shows almost the same distribution. Similar to Fig. 6.8(b), the maximum efficiency point is around V_{RF}=0.4 meV; after that, the VI characteristic flattens, and the zero bias signal is suppressed.[5] These results suggest that the diode can detect photons, and its directionality can be controlled with the effective gating mechanism introduced in Sec. 5.4. Moreover, this detection is given without any externally applied voltage, meaning the CPD is a passive device. Only a gate electrode is needed. Moreover, the signal arises from a supercurrent, i.e., there is no dissipation.

6.5 Conclusions

In this chapter, we have proved that the control of the excess charge can manipulate the reciprocity of the current of Cooper pairs. In the IVC, we noted that the Josephson peak splits into two RCT peaks, which energy we could manipulate [Sec. 6.2]. Moreover, the VIC showed that the asymmetric position of these peaks generates a non-reciprocal response to the applied bias current [Sec. 6.3]. Summarizing, the Pb islands deposited on Gr have proven to be an ideal platform for studying the interaction between superconductivity and Coulomb interactions. Utilizing the STM, the excess charge of the islands and the Josephson coupling can be controlled. Moreover, islands of different sizes can be measured, which helps us understanding the system's response to an applied voltage or current [Sec. 6.1].

By approaching the superconducting tip to the small Pb islands, we measured the split of the Josephson peak due to the Coulomb interactions, which we described as a resonant tunneling of Cooper pairs [Sec. 6.2]. We proved that the position of these peaks can be changed with the excess charge and developed an effective theory based on the PoE function to describe this transport mechanism [Sec. 6.2.1]. Simultaneously, exploiting the dual STM modes, we measured the response of the double JJ to a current bias. We explained the results within the Bloch oscillations theory for JJs [Sec. 6.3] and proved that the system's output is non-reciprocal due to the break of inversion and ph symmetry.

This non-reciprocity is controlled with the gate and can be exploited to use the system as a diode, which we named Cooper Pair Diode [Sec. 6.4]. This diode, similar to a classical p-n diode, has a non-reciprocal resistance, which we exploit to implement the two main applications of the diode: rectification [Sec. 6.4.1] and photodetection [Sec. 6.4.2]. We first proved that the rectification of the current can be controlled with the gating so that with fine-tuning, one could always look for the most effective rectification. Moreover, the double junction was used as a microwave detector for frequencies from 10 to 20 GHz.

[5] We do not measure at higher power for two reasons. The first is that the STM chamber starts to heat up for high powers, making these measurements complex to perform. The second is that if we want to ensure the zero-bias current is a Cooper pair current, we can not have a large potential in the junction. At high enough powers, we start having photon-assisted single-electron tunneling from the coherence peaks.

7

Conclusions

In this thesis, we have investigated novel superconducting phenomena arising from interactions between magnetic nanostructures and superconductors, as well as the effects of reducing superconductor size to nanoscale dimensions. We used UHV growth techniques to fabricate atomic and molecular magnetic systems on superconducting surfaces and Scanning Tunneling Microscopy (STM) methods to investigate and manipulate their properties, enabling precise control and exploration of subgap states like YSR states. Moreover, we have grown small-sized superconductors to understand how Coulomb interactions influence superconductivity. Additionally, we developed theoretical models to simulate and interpret the behavior of complex superconducting states under various conditions. By bridging theory and experiment, this thesis reveals new insights into superconductivity.

In Chapter 3, we studied the "focusing" along certain surface directions of the Yu-Shiba-Rusinov (YSR) state decay with STM measurements on V adatoms on β-Bi_2Pd. We introduced an analytical method to calculate the Green's Functions (GFs) and spectral properties of a two-dimensional superconductor with an arbitrary Fermi Contour (FC). By examining superconductors with polygonal-shaped FCs, our study reveals that the spatial characteristics of the YSR Density of States (DoS) reflect the FC symmetry and reproduce the direction-dependent decay lengths along the directions with flat FC edges. The extension of YSR states hosted by single V impurities agrees with the theoretical prediction on square-shaped FCs. The model is further exploited to analyze QPI from V adatoms on the β-Bi_2Pdsurface. QPI analysis shows the need for band hybridization and strong Rashba-type spin-orbit coupling to describe this material accurately, explaining the formation of the multiband BCS ground state of β-Bi_2Pd. The GF approach is also applied to simulate the DOS of structures formed by multiple Mn impurities fabricated by atomically precise manipulation with the STM tip, suggesting ways to optimize atomic interactions through focused YSR state extensions.

Motivated by the observation of complex spectroscopic features on the magnetic FeTPP-Cl molecules on the proximitized Au/V(100) surface, in Chapter 4, we studied the origin of YSR excitations in a thin metal film proximitized by a superconductor. We found a significant overlap between the wavefunction of YSR states formed on the proximitized metal and dGSJ states formed from the Andreev reflections on the thin, normal metal. This led to a simplified, exactly solvable single-site model that captures the quantum nature of the magnetic impurity. We extended the model for high spins and magnetic anisotropies to understand the STS measurements on FeTPP-Cl molecules on the proximitized Au/V(100) surface. Utilizing the tip-molecule interaction to modify the exchange coupling between FeTPP-Cl and surface, we move the system through the parity-changing quantum phase transition and find that the two-particle excitation, elusive in the even parity ground state is now accessible, thus being

a measure of the local parity of the system.

Extending the single-site model to account for two impurity systems, we proved that two magnetic impurities exchange coupled with each other and the surface generate an ideal platform for a singlet-based qubit. This configuration is robust against decoherence from spin-orbit and hyperfine interactions. Additionally, we proposed a more realistic device model featuring two superconducting rods and two quantum dots, offering potential applications for quantum computing in future technologies.

In the second part of this thesis, we investigated nanoscale superconducting Pd islands grown on graphene and the interplay between the Coulomb blockade and superconducting phenomena.

In Chapter 5, we have shown that small Pb islands exhibit an energy gap larger than the intrinsic superconducting gap due to the interplay between superconductivity and Coulomb effects. We determined the Coulomb energy and its dependence on island size by applying a magnetic field. We identified a size threshold around $\mathrm{vol}^{1/3}$=15 nm, below which Coulomb interactions dominate over the superconducting pairing. The Coulomb gap increases as island volume decreases, while the superconducting gap reduces by up to 50% from the bulk value, a result of the larger electronic level separation on the small islands and the inverse proximity effect from graphene.

We also found that the islands exhibit spectral asymmetries linked to fractional excess charge on the Pb grains. Interstingly, STM bias pulses can control the excess charge, mimicking the effect of a gate voltage on a tree-terminal device. We described this effect with charged paddles between graphene and the SiC, which we charge or discharge by bias pulsing. This was simulated with a double tunneling junction theory containing the effects of the superconducting pairing and the Coulomb blockade.

In Chapter 6, we studied the effect of Coulomb charging in Josephson junctions. The zero voltage Josephson peak, appearing in the I-V characteristics of STM tunneling junctions between bulk superconductors, splits into two peaks in small islands. Varying the excess charge of the islands with bias pulses with the STM tip, we found that although the separation between peaks is constant, their position depends on the excess charge of the island. We described the process generating these peaks as resonant tunneling of Cooper pairs mediated by the interaction with the environment, i.e., an incoherent tunneling mechanism. The developed effective theory corroborates the experimentally measured dependence of the peaks with the excess charge of the islands.

The experiments in the Josephson regime justified the change to a different measurement strategy based on biasing the current rather than the voltage. The implemented current-biased setup is based on a switchable resistor in series with the voltage supply. We measured the effect of the Coulomb blockade on the V-I characteristics. In the islands, the Coulomb blockade appeared as finite voltage steps around zero current, which is a direct consequence of the resonant tunneling of Cooper pairs. Based on the theory of Bloch oscillation of a JJ, we explain the finite voltage jumps with the evolution of the charge-particle. We found that the combined break of inversion and charge-conjugation symmetries generates a non-reciprocal response of the charge-particle to the applied current.

For finite excess charge in the grain, a non-reciprocal response to the applied current is measured: a diode effect. We introduced the concept of a Cooper Pair Diode, which can be used for rectification and photodetection and has potential applications as a microwave detector. The gate-controlled non-reciprocity in this system opens up possibilities for controlling current rectification and fine-tuning diode performance.

The experimental results of this thesis, combined with the theoretical models, provide new insights into nanoscale phenomena related to superconductivity utilizing various experimental and theoretical tools. A better understanding of the interplay between superconductivity and magnetic impurities, classical and quantum, and the Coulomb blockade is developed. I believe that the experimental results and their corresponding theoretical description will promote further investigation into nanoscale superconducting phenomena, an exciting field with many potential applications in future technologies.

A

Calculation of the exact GF

A.1 Integration of several FCs.

In this appendix, we present the result of the integral Eq. (3.6) for a M-sided regular polygon. We then use the solution to calculate the integral for the square-shaped contour and the $M \to \infty$ limit which corresponds to the circular case.

We define the basis vectors $(\hat{\mathbf{u}}_x, \hat{\mathbf{u}}_y) \to (\hat{\mathbf{n}}, \hat{\mathbf{w}})$, where $\hat{\mathbf{n}}$ is a vector normal to a polygon's side and $\hat{\mathbf{w}}$ its perpendicular vector. The vertices of the polygon are at the points

$$V_i : (\cos\left(\frac{2i-1}{M}\pi\right), \sin\left(\frac{2i-1}{M}\pi\right)) \,. \tag{A.1}$$

It is also convenient to define $k'_F = k_F \cos\left(\frac{\pi}{M}\right)$, where k_F if the Fermi momentum of the inscribing circumference, i.e, the momentum in the vertices of the polygon. The integral along one of the polygon sides can be written as

$$\begin{aligned} &\frac{1}{(2\pi)^2}\int \frac{d\xi}{k_n}\check{G}_0(\xi,\omega)e^{-i(\frac{m\xi}{k'_F}+k'_F)n^k}\int_{-k_u^k\tan\frac{\pi}{M}}^{k_n^k\tan\frac{\pi}{M}} e^{-iqw^k}dq \\ &= \frac{1}{(2\pi)^2}\int_{n^k/w^k-\tan\frac{\pi}{M}}^{u^k/w^k-\tan\frac{\pi}{M}} d\chi \int d\xi \check{G}_0(\xi,\omega)e^{-i(\frac{m\xi}{k'_F}+k'_F)\chi w^k} \,, \end{aligned} \tag{A.2}$$

where we defined, $n^k = x\cos\left(\frac{2\pi k}{M}\right) + y\sin\left(\frac{2\pi k}{M}\right)$, $k_n^k = k_x\cos\left(\frac{2\pi k}{M}\right) + k_y\sin\left(\frac{2\pi k}{M}\right)$, $w^k = -x\sin\left(\frac{2\pi k}{M}\right) + y\cos\left(\frac{2\pi k}{M}\right)$ and $k_w^k = -k_x\sin\left(\frac{2\pi k}{M}\right) + k_y\cos\left(\frac{2\pi k}{M}\right)$. Thus, the GF reads

$$\check{G}_0(\mathbf{r},\omega) = \sum_{k=1}^{M}\frac{1}{(2\pi)^2}\int_{n^k/w^k-\tan\frac{\pi}{M}}^{n^k/w^k+\tan\frac{\pi}{M}} d\chi\int d\xi\check{G}_0(\xi,\omega)e^{-i(\frac{m\xi}{k'_F}+k'_F)\chi w_k} \,. \tag{A.3}$$

Defining $\theta_p = \frac{2\pi k}{M}$, in the limit $M \to \infty$ we get that

$$\begin{aligned} \check{G}_0(\mathbf{r},\omega) &= \sum_{k=1}^{N}\frac{1}{(2\pi)^2}\int_{n(\theta_p)/w(\theta_p)-\frac{d\theta}{2}}^{n(\theta_p)/w(\theta_p)+\frac{d\theta}{2}} d\chi\int d\xi\check{G}_0(\xi,\omega)e^{-i(\frac{m\xi}{k_F}+k_F)\chi w(\theta_p)} \\ &= \int_0^{2\pi}\frac{d\theta}{(2\pi)^2}\int d\xi\check{G}_0(\xi,\omega)e^{-i(\frac{m\xi}{k_F}+k_F)u(\theta_p)} \,. \end{aligned} \tag{A.4}$$

Note that $u(\theta_p) = x\cos(\theta_p) + y\sin(\theta_p) = r[\cos(\theta_p)\cos(\theta_r) + \sin(\theta_p)\sin(\theta_r)] = r\cos(\theta_p - \theta_r)$, so;

$$\check{G}_0(\mathbf{x},\omega) = \int_0^{2\pi}\frac{d\theta_p}{(2\pi)^2}\int d\xi\check{G}_0(\xi,\omega)e^{-i(\frac{m\xi}{k_F}+k_F)r\cos(\theta_p-\theta_r)} \tag{A.5}$$

Integral (A.5) corresponds to the circular FC, which can be analytically solved.

$$\begin{aligned}\check{G}_0(\mathbf{r},\omega) &= \frac{m}{(2\pi)^2}\int_0^{2\pi} d\theta_p e^{ik_F r\cos(\theta_p-\theta_r)}\int_{-\infty}^{\infty} d\xi \frac{\omega\tau_0+\Delta\tau_1+\xi\tau_3}{\xi^2+\Omega^2} e^{i\frac{m}{k_F}\xi r\cos(\theta_p-\theta_r)} \\ &= \frac{m}{4\pi}\int_0^{2\pi} d\theta_p[\rho_{BCS}(\omega)+i\text{sign}(\cos(\theta_p-\theta_r))\tau_3]e^{-\frac{m}{k_F}\Omega r|\cos(\theta_p-\theta_r)|+ik_F r\cos(\theta_p-\theta_r)} ,\end{aligned} \tag{A.6}$$

where $\check{\rho}_{BCS}(\omega) = \frac{\omega\tau_0+\Delta\tau_1}{\Omega}$, with $\Omega = \sqrt{\Delta^2-\epsilon^2}$. The integral is easier to evaluate after making the change $\theta' = \theta_p - \theta_r$. Noticing that

$$\int_{-\frac{\pi}{2}}^{\frac{\pi}{2}} d\theta e^{iu\cos(\theta)} = \pi\left(J_0(u)+iH_0(u)\right) , \tag{A.7}$$

where $J_0(x)$ is the zero Bessel function of the first type and $H_0(x)$ is the zero Struve function, we finally obtain:

$$\check{G}_0(\mathbf{r}) = \pi N_0\left\{\check{\rho}_{BCS}(\omega)\left[\text{Re}\{J_0(u)+iH_0(u)\}\right]+i\tau_3\left[\text{Im}\{J_0(u)+iH_0(u)\}\right]\right\} , \tag{A.8}$$

where $u = (k_F + i\frac{m}{k_F}\Omega)r = (k_F + i\xi_s^{-1})r$ and N_0 is the normal metal DoS. In the limit $r \to 0$ this expression reduces to the BCS Green's function. In the asymptotic limit $k_F r \gg 1$ we obtain [272]:

$$\begin{aligned}\check{G}_0(\mathbf{r},\omega) =& \pi N_0 i\tau_3\left[\sqrt{\frac{2}{\pi k_F r}}\sin\left(k_F r-\frac{\pi}{4}\right)e^{-r/\xi_s}\right. \\ &\left.+\frac{2}{\pi k_F r}+\pi N_0\check{\rho}_{BCS}(\omega)\sqrt{\frac{2}{\pi k_F r}}\cos\left(k_F r-\frac{\pi}{4}\right)e^{-r/\xi_s}\right.\end{aligned} \tag{A.9}$$

We now calculate the integral for a square-shaped FC. Taking $M = 4$ in Eq. (A.3) one can straightforwardly check that:

$$\begin{aligned}\check{G}_0(\mathbf{r},\omega) = &\frac{m}{2\pi y}\int_{x-y}^{x+y} dv(\check{\rho}_{BCS}(\omega)\cos(k_F v)-\sin(k_F|v|)\tau_3)e^{-\frac{m}{k_F}\Omega|v|} \\ &+\frac{m}{2\pi x}\int_{y-x}^{x+y} dv(\check{\rho}_{BCS}(\omega)\cos(k_F v)-\sin(k_F|v|)\tau_3)e^{-\frac{m}{k_F}\Omega|v|}\end{aligned} \tag{A.10}$$

All these integrals are analytically solvable. We focus here on the region $x+y>0$ and $x-y>0$ (due to the symmetry of the system, results for the other regions are obtained similarly). In leading order in $m\Omega/k_F^2 \ll 1$ we obtain

$$\begin{aligned}\check{G}_0(\mathbf{x},\omega) =& \pi\frac{N_0}{4}\frac{\check{\rho}_{BCS}(\omega)}{k_F^2}\left\{e^{-\frac{m}{k_F}\Omega(x+y)}\left(\frac{1}{x}+\frac{1}{y}\right)k_F\sin(k_F(x+y))\right. \\ &\left.+e^{-\frac{m}{k_F}\Omega(x-y)}\left(\frac{1}{x}-\frac{1}{y}\right)k_F\sin(k_F(x-y))\right\} \\ &-\pi\frac{N_0}{4}\frac{\tau_3}{k_F^2}\left\{e^{-\frac{m}{k_F}\Omega(x+y)}\left(\frac{1}{x}+\frac{1}{y}\right)k_F\cos(k_F(x+y))\right. \\ &\left.+e^{-\frac{m}{k_F}\Omega(x-y)}\left(\frac{1}{x}-\frac{1}{y}\right)k_F\cos(k_F(x-y))-\frac{2k_F}{x}\right\}+\mathcal{O}\left(\frac{m\Omega}{k_F}\right) .\end{aligned} \tag{A.11}$$

In the main text we discuss the GF over the lines $y = 0$ and $x = y$:

$$\begin{aligned}\check{G}_0(x, y = 0) =& \pi N_0 \check{\rho}_{BCS}(\omega) \left\{ e^{-|x|/\xi_s} \left[\frac{1}{k_F x} \sin(k_F x) + \cos(k_F x) \right] \right\} \\ & - \pi N_0 \tau_3 \left\{ e^{-|x|/\xi_s} \left[\frac{1}{k_F x} \cos(k_F x) - \sin(k_F x) \right] - \frac{1}{k_F x} \right\}\end{aligned} \tag{A.12}$$

$$\begin{aligned}\check{G}_0(x = y) =& \frac{m}{\pi} \check{\rho}_{BCS}(\omega) \left\{ e^{-2x/\xi_s} \frac{1}{k_F x} \sin(2k_F x) \right\} \\ & - \frac{m}{\pi} \tau_3 \left\{ e^{-2x/\xi_s} \frac{1}{k_F x} \cos(2k_F x) - \frac{1}{k_F x} \right\}\end{aligned} \tag{A.13}$$

A.2 Helical multi-band superconductor

This section is used to get the GF of Eq. (3.9). We will start by adding the different terms contributing to the full Hamiltonian and understanding their effects. We start by considering two independent bands (so that it is enough to solve for one), and we will take the Rashba coupling to be strong to take helical band approximation, i.e., $t = 0$ and $\lambda_i \gg 1$. In the following, we solve for one of the spin directions (taking $v_F \to -v_F$ flips the spin):

$$\check{H}_k = (v_F k - \mu)\tau_3 + \Delta\tau_1 \tag{A.14}$$

then,

$$\check{G}(\omega, k) = [\omega \mathbb{1} - \check{H}_k]^{-1} = \frac{1}{(\Delta^2 - \omega^2) + (v_F - \mu)^2} (\omega + (v_F k - \mu)\tau_3 + \omega + \Delta\tau_1) \tag{A.15}$$

we get the real space GF from the FT of this equation. In a 1D system, one can always solve the integral by finding the poles in the positive or negative imaginary plane. The poles read $k v_F = \pm i\Omega + \mu$. For $x > 0$, we look in the positive plane, and for $x < 0$, in the negative. The real space GF reads:

$$\check{G}(x) = \frac{-1}{v_F} (\frac{\omega}{\Omega} + i \text{sign}(x)\tau_3 + \frac{\Delta}{\Omega}\tau_1) e^{-ix\mu/v_F - \Omega|x|/v_F} \ , \tag{A.16}$$

with $\Omega = \sqrt{\Delta^2 - \omega^2}$. The GF describing the YSR state can be found using the same formula as in Eq. (2.31). Note that as the YSR potential (in the classical limit) does not connect bands with different spin indexes, there will be no oscillatory behavior in the extension of the YSR states.[1]

Let us add a second independent band and assume that the impurity responsible for the YSR state has an interband scattering term:

$$\check{H} = \begin{pmatrix} \check{H}_1 & 0 \\ 0 & \check{H}_2 \end{pmatrix} \qquad \check{V} = \begin{pmatrix} 0 & \check{V}_{12} \\ \check{V}_{21} & 0 \end{pmatrix} . \tag{A.17}$$

[1] $\check{G}_{YSR}(x) = \check{G}(0) + \check{G}(x)[\check{\mathbb{1}} - \check{G}(0) \cdot \check{V}]\check{G}(-x)$. Then, $\check{G}(x)\check{G}(-x)$ cancels out the oscillations.

The GF of the bare superconductor will be block diagonal, and each block will have the same form as Eq. (A.15), where v_F is exchanged by v_i. Taking the Dyson equation for one of the bands, we get

$$\begin{aligned}\check{G}_{ii}(x,x) =&\check{G}_{ii}(0) + \check{G}_{ij}(x)[\check{\mathbb{1}} - G(0)V]_{jk}\check{G}_{ki}(-x)\\ =&\check{G}_{ii}(0) + \check{G}_{ii}(x)[\check{\mathbb{1}} - G(0)V]_{ii}\check{G}_{ii}(-x)\ ,\end{aligned} \tag{A.18}$$

where we used $\check{G}_{ij} = \check{G}_{ii}\delta_{ij}$. We again note that the only terms that will oscillate are the nondiagonal terms of $\check{G}_{ij}$, but these terms do not contribute to the LDoS, defined as $\rho \propto \mathrm{Tr}\,\check{G}(x)$. Then, a single impurity - even with an interband scattering term - will not produce any oscillatory behavior in a multiband helical system.

Finally, we will solve the full Hamiltonian, adding the hopping term t. The poles of the GF now read,

$$k = \frac{-\tilde{v}(\mu \pm i\Omega\pm)\sqrt{t^2(\tilde{v}^2 - v^2) + (\mu \pm i\Omega)^2}}{\tilde{v}^2 - v^2} \tag{A.19}$$

with $\tilde{v} = v_1 + v_2$ and $v = v_1 - v_2$. Depending on the relative spin orientation of the bands, $\tilde{v}$ and v can be either positive or negative. We notice that the GF coming from these poles reads

$$G_{11}(x) \sim e^{(i\mu - \Omega|x|)/v_1}\frac{\omega}{v_1\Omega} + e^{(i\mu-\Omega|x|)/v_2}\frac{\omega}{\Omega}\frac{t^2 v_2}{(v_1^2 - v_2^2)\mu^2} \tag{A.20}$$

We note that, when the Dyson equation is applied, checking the diagonal terms, we will have an oscillation arising from the scattering between the two original bands: $\exp\{ix\mu(1/v_1 + 1/v_2 + \mathcal{O}(t/\mu))\} = \exp\{ix(k_{F1} + k_{F2} + \mathcal{O}(t/\mu))\}$. The intensity of these oscillations is $\mathcal{O}(t/\mu)^2$. As the oscillations have a significant contribution to the DoS, $t \sim \mu$. This results in the renormalization of the Fermi momenta and of the bands [Sec. 3.4.1].

A third band has to be added to Hamiltonian (3.9) to reproduce the two oscillations measured in the extension of the YSR states hosted by the V adatoms. This Hamiltonian reads;

$$\check{H}_{3\text{ bands}} = \begin{pmatrix} v_{F1}k - \mu & \Delta & t_{12} & 0 & t_{13} & 0\\ \Delta & -v_{F1}k + \mu & 0 & -t_{12} & 0 & -t_{13}\\ t_{12} & 0 & v_{F2}k - \mu & \Delta & 0 & 0\\ 0 & -t_{12} & \Delta & -v_{F2}k + \mu & 0 & 0\\ t_{13} & 0 & 0 & 0 & v_{F3}k - \mu & \Delta\\ 0 & -t_{13} & 0 & 0 & \Delta & -v_{F3}k + \mu \end{pmatrix}, \tag{A.21}$$

where v_{Fi} is the Fermi velocity of the ith band and t_{12} and t_{13} are the hopping terms between the 1st and 2nd and 1st and 3rd bands, respectively. No hopping term is added between the 2nd and 3rd bands. We only couple the impurity to the 1st band. In this case, hybridizing the other two bands only renormalizes the oscillations, but no new scattering vector would appear. The results obtained from this Hamiltonian (solved numerically) are summarized in Fig. 3.10(c) and 3.10(d).

B

Single-Site model

B.1 Two-layer Green's Functions

As discussed in Ref. [273], the GFs of a composite system (4.3) can be obtained from the GFs of the constituent subsystems. We denote the GFs of each subsystem as $\check{g}_i(x,x')$, with $i = N, S$. Next, we impose the following boundary conditions:

$$\frac{d\check{g}_i(x,x')}{dx}\Big|_{x=0} = 0, \qquad \frac{d\check{g}_i(x,x')}{dx'}\Big|_{x'=0} = 0, \tag{B.1}$$

$$\frac{d\check{g}_N(x,x')}{dx}\Big|_{x=-a} = 0, \qquad \frac{d\check{g}_N(x,x')}{dx'}\Big|_{x'=-a} = 0, \tag{B.2}$$

$$\check{g}_S(x\to+\infty,x') = 0, \qquad \check{g}_S(x,x'\to+\infty) = 0, \tag{B.3}$$

$$\lim_{\delta\to 0^+}\tau_3\frac{d\check{g}_i(x,x')}{dx}\Big|_{x=x'-\delta}^{x=x'+\delta} = 2m, \qquad \lim_{\delta\to 0^+}\tau_3\frac{d\check{g}_i(x,x')}{dx'}\Big|_{x'=x-\delta}^{x'=x+\delta} = 2m. \tag{B.4}$$

We assume a zero derivative at the vacuum interface, except for the semi-infinite superconductor at $x, x' \to \infty$, for which the GFs are assumed to vanish.

Using the above boundary conditions and assuming continuity of the full GF and its derivative at the N/S interface, we obtain the following relations:

$$\check{G}(x,x') = \begin{cases} \check{g}_S(x,x')\theta(x') \mp \check{g}_S(x,0)[\check{g}_S(0,0)+\check{g}_N(0,0)]^{-1}\check{g}_{S,N}(0,x') : x>0, x' \gtrless 0 \\ \check{g}_N(x,x')\theta(-x') \mp \check{g}_N(x,0)[\check{g}_S(0,0)+\check{g}_N(0,0)]^{-1}\check{g}_{S,N}(0,x') : x<0, x \gtrless 0 \end{cases} \tag{B.5}$$

The GFs for the isolated system are easy to calculate from the Bogoliubov-de Gennes equation [173]. After that, one can get the dressed GF from Eq. (B.5), see Ref. [175]. The GF shows a pole with the following energy distribution:

$$\frac{\omega}{\sqrt{\Delta^2-\omega^2}}\tan\left(\frac{2ma}{k_F}\omega\right) = 1 \tag{B.6}$$

Note that by expanding the tangent around zero to the first order, we arrive at the same solution as obtained from a semi-classical argument Eq. (4.1).

From the knowledge of the GFs we can calculate the Nambu spinors from the residue of the corresponding pole, as follows from the spectral representation of the GFs:

$$\check{G}^R(x,x',\omega) = \sum_n \frac{\check{\phi}_n(x)\check{\phi}_n^\dagger(x')}{\omega-\xi_n+i\epsilon} \tag{B.7}$$

In the case of a continuum eigenbasis, we have:

$$\begin{aligned}\check{G}^R(x,x',\omega) &= L\int \frac{dk}{2\pi}\frac{\check{\phi}_k(x)\check{\phi}_k^\dagger(x')}{\omega-\xi_k+i\epsilon} = \frac{L}{2\pi}\int dE_k|\frac{dk}{dE_k}|\frac{\check{\phi}(E_k,x)\check{\phi}^\dagger(E_k,x')}{\omega-\xi_k+i\epsilon}\\ &\sim iL|\frac{dk}{dE_k}|_{k_F}\check{\phi}(\omega,x)\check{\phi}^\dagger(\omega,x') + L\mathcal{P}\int dk\frac{\check{\phi}_k(x)\check{\phi}_k^\dagger(x')}{\omega-\xi_k}\\ &=\sim iLN_0\check{\phi}(\omega,x)\check{\phi}^\dagger(\omega,x') + L\mathcal{P}\int dk\frac{\check{\phi}_k(x)\check{\phi}_k^\dagger(x')}{\omega-\xi_k}.\end{aligned} \tag{B.8}$$

However, in our case, the eigenbasis can be divided into a continuum part ($\omega > \Delta$) and a discrete part corresponding to the dGSJ or YSR states (for $\omega < \Delta$). Thus,

$$\check{G}^R(x,x',\omega) = \begin{cases} iLN_0\check{\phi}(\omega,x)\check{\phi}^\dagger(\omega,x') + L\mathcal{P}\int da\dfrac{\check{\phi}(a,x)\check{\phi}^\dagger(a,x')}{\omega-\xi_k} & \text{for } \omega>\Delta,\\ \displaystyle\sum_n \frac{\check{\phi}_n(x)\check{\phi}_n^\dagger(x')}{\omega-\xi_n+i\epsilon} & \text{for } \omega<\Delta.\end{cases} \tag{B.9}$$

Hence,

$$\mathrm{Res}_{\omega\to E_n}\,\check{G}^R(x,x',\omega<\Delta) = \check{\phi}_n(x)\check{\phi}_n^\dagger(x') = \begin{pmatrix} u(x)u(x') & u(x)v(x')\\ v(x)u(x') & v(x)v(x')\end{pmatrix}. \tag{B.10}$$

B.2 Tight-binding model

To carry out some of the calculations of Sec. 4.2.2 beyond the leading order in Δ/E_F and to investigate the effect of a mismatch in the Fermi level, we use a one-dimensional tight-binding model which describes a short normal chain coupled to a longer superconducting chain. The exchange potential describing a classical magnetic impurity acts on the first site of the (normal) chain. The Hamiltonian reads:

$$\hat{H}_{TB} = \hat{H}_0 + \hat{H}_J, \tag{B.11}$$

where

$$\hat{H}_0 = \sum_{\langle i,j\rangle\sigma} t_i\hat{c}_{i\sigma}^\dagger\hat{c}_{j\sigma} + \sum_i \mu_i\hat{c}_{i\sigma}^\dagger\hat{c}_{i\sigma} + \sum_i \Delta_i\hat{c}_{i\sigma}^\dagger\hat{c}_{j\bar{\sigma}}^\dagger + \text{h.c}\,. \tag{B.12}$$

Here, $t_i = t_{metal}\theta(N_{metal}-i) + t_{SC}\theta(i-N_{metal})$, $\mu_i = \mu_{metal}\theta(N_{metal}-i) + \mu_{SC}\theta(i-N_{metal})$ and $\Delta_i = \Delta\theta(i-N_{metal})$. The interaction the chain and the magnetic impurity is described by

$$\hat{H}_J = J(\hat{c}_{0\uparrow}^\dagger\hat{c}_{0\uparrow} - \hat{c}_{0\downarrow}^\dagger\hat{c}_{0\downarrow}) \tag{B.13}$$

We diagonalize this Hamiltonian for a chain of 1500 sites and calculate the overlap between the Nambu spinors of the lowest-lying level of $\hat{H}_0$ and $\hat{H}_{TB}$ for different values of J. The results are shown in Fig. 4.4, where the calculation was performed for $\mu_{metal} = \mu_{SC}$, i.e., no Fermi-level mismatch at the interface. Fig. B.1 shows the

overlap between the dGSJ and YSR states for a larger parameter space of the tight-binding model. Some particular values of Fermi-level mismatch, such as, $\mu_{SC}/\mu_{metal} = 20\Delta, 40\Delta$ are shown. Comparing this figure with Fig. 4.4(c), we note a small reduction of the overlap due to the mismatch. Nevertheless, the values of the overlap are still fairly close to unity, and in line with what was discussed in Sec. 4.2.2 we do not expect substantial modifications to our results concerning the applicability of the single-site model.

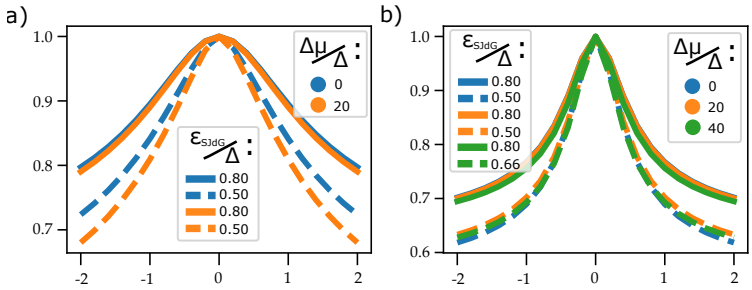

Figure B.1: **Exploration of the overlap between dGSJ and YSR eigenstates for varying exchange coupling on a larger parameter space of the tight-binding model.** **(a)** and **(b)** Calculation of the overlap for $t = 1.0$ and $t = 2.5$, respectively. We set the hopping between superconducting sites to $t_{SC} = 1$ and the superconducting gap to $\Delta = 0.05$ and change the hopping in the normal metal and the Fermi-level mismatch. The two panels show the overlap for different values of the mismatch of the Fermi energy and two different dGSJ energies, one closer to Fermi energy and the other closer to the superconducting gap.

B.3 Single site Hamiltonian for a proximitized superconductor

By solving the Bogoliubov-de Gennes equations for the proximitized thin film, the electron field operator at the position of the magnetic impurity,$\hat{\phi}_{0\sigma}$, can be written as follows:

$$\hat{\psi}_{0\sigma} = u_0\hat{\gamma}_\sigma + \sigma v_0^*\hat{\gamma}_{-\sigma}^\dagger + \sqrt{1-Z}\,\hat{\phi}_{o\sigma}. \tag{B.14}$$

We start by changing the basis on the unperturbed Hamiltonian (4.3), where first two terms described the dGSJ quasi-particle and $\check{\phi}_{0\sigma}$ describes the modes in the continuum. We now introduce a rotation for the operators creating the discrete state:

$$\begin{pmatrix} \hat{d}_\sigma \\ \hat{d}_{-\sigma}^\dagger \end{pmatrix} = \begin{pmatrix} \cos\theta & -\sin\theta \\ \sin\theta & \cos\theta \end{pmatrix} \begin{pmatrix} \hat{\gamma}_{0\sigma} \\ \hat{\gamma}_{0-\sigma}^\dagger \end{pmatrix} . \tag{B.15}$$

This rotation leads to (4.8), where $U = E_s\cos 2\theta$ and $\Delta_s = E_s \sin 2\theta$. Furthermore, requiring that

$$\hat{\psi}_\uparrow = \sqrt{Z}\hat{d}_\uparrow + \sqrt{1-Z}\hat{\phi}_{0\uparrow} = u_0\hat{\gamma}_\sigma + \sigma v_0^*\hat{\gamma}_{-\sigma}^\dagger + \sqrt{1-Z}\hat{\phi}_{0\uparrow}\,. \tag{B.16}$$

Hence, $\tan\theta = -v_0/u_0$ and $Z = u_0^2 + v_0^2$, where $U = E_s(u_0^2 - v_0^2)$ and $\Delta_s = 2E_s u_0 v_0$.

B.4 Calculation of the scaling equations

In order to perturbatively obtain the scaling equations of the model introduced in Sec. 4.2.4, we consider an expansion of the partition function of the system, i.e.

$$Z(D) = Z_0(D)\langle \mathcal{T} \exp\left[-\int_0^\beta \hat{H}_J^{dc}(\tau)\right]\rangle_0, \tag{B.17}$$

in powers of the couplings $J_{dd}, J_{d\phi}$ and $J_{\check{\phi}\check{\phi}}$. In the above expression for $Z(D)$ $Z_0(D) = \mathrm{Tr}\, e^{\beta \hat{H}_0}$ is the partition function of the system without magnetic impurity at inverse absolute temperature $\beta = (k_B T)^{-1}$; $\langle \ldots \rangle_0$ is the expectation value over the non-interacting grand canonical ensemble defined by $\hat{H}_0$. The operator $\hat{H}_J(\tau) = e^{\hat{H}_0 \tau} \hat{H}_J e^{-\hat{H}_0 \tau}$, where $\hat{H}_J$ is given in Eq. (4.13), describes the magnetic exchange with the impurity in the interaction representation and $\mathcal{T}$ is the imaginary time-ordering symbol. We have also introduced a parameter, D_F, which is the bandwidth of the composite thin film and superconductor system.

Following Anderson [40], we shall use perturbation theory to obtain a map onto a system with smaller bandwidth $D' = D - \delta D < D$. Associated with the bandwidths D and D', there are also the following characteristic (imaginary) time scale (in units where $\hbar = 1$) $\tau_c = D^{-1}$ and $\tau_c' = (D')^{-1} > \tau_c$. The lowest order terms of the perturbation series for the system with bandwidth D read:

$$\begin{aligned} Z(D) = Z_0(D)\,\{1 - \int d\tau\, \langle \hat{H}_J^{dc}(\tau)\rangle_0 \\ + \frac{1}{2!} \int_{|\tau-\tau'|>\tau_c = D^{-1}} d\tau d\tau'\, \langle \mathcal{T}\left[\hat{H}_J^{dc}(\tau)\hat{H}_J^{dc}(\tau')\right]\rangle_0 + \cdots \Big\}, \end{aligned} \tag{B.18}$$

where we have made explicit the constraints on τ imposed by the finite bandwidth of the continuum of states described by $\hat{\phi}_\sigma$ and $\hat{\phi}_\sigma^\dagger$.

Next, let us integrate out the high energy degrees of freedom contained $\hat{\phi}_{0\sigma}$ and $\hat{\phi}_{0\sigma}^\dagger$ (recall that the $\hat{d}_\sigma$, $\hat{d}_\sigma^\dagger$ describe a low-energy subgap state and it cannot be integrated out). Such degrees of freedom involve excitations with energies $\sim D$ above the ground state and, therefore, determine the short imaginary time behavior of the Green's functions for $\hat{\phi}_\sigma$. Note that, since at excitation energies $\sim D$ Bogoliubov quasiparticles either behave as electrons or holes (in other words, either $u \to 0$ or $v \to 0$), the anomalous GFs involving the operator $\hat{\phi}_0$, i.e., $\langle \mathcal{T}\left[\hat{\phi}_{0\uparrow}(\tau)\hat{\phi}_{0\downarrow}(\tau')\right]\rangle_0$, etc, vanish for $|\tau - \tau'| \simeq \tau_c^{-1}$. Thus, in the above perturbation series, for $|\tau - \tau'| \sim \tau_c$, we need to consider only normal correlations, which take the familiar Fermi liquid form:

$$\langle \mathcal{T}\left[\hat{\phi}_{0\sigma}(\tau)\hat{\phi}_{0\sigma'}^\dagger(\tau')\right]\rangle_0 \simeq \frac{\nu_0 \delta_{\sigma\sigma'}}{(\tau - \tau')} \tag{B.19}$$

for $|\tau' - \tau| \simeq \tau_c^{-1}$, where ν_0 is the (mean) density of states of the normal state. Thus, the first non-constant contribution to the scaling of the couplings stems from

the second-order term. We first split the integrals over τ, τ' according to:

$$\int\limits_{|\tau-\tau'|>\tau_c=D^{-1}} d\tau d\tau' \ldots = \int\limits_{|\tau-\tau'|>\tau_c'=(D')^{-1}} d\tau d\tau' \ldots + \int\limits_{\tau_c'=(D')^{-1}>|\tau-\tau'|>\tau_c=D^{-1}} d\tau d\tau' \ldots \tag{B.20}$$

and consider the terms in the second term for which $\tau_c' > |\tau - \tau'| > \tau_c$. Expanding the second order term in powers, corrections to the couplings contained in the first order term are generated at $O(J_{d\phi}^2)$, $O(J_{d\phi}J_{\phi\phi})$ and $O(J_{\phi\phi}^2)$. We explicity evaluate below the $O(J_{d\phi}^2)$ term. The calculations for the remaining terms are similar and not reproduced here. Einstein's convention of repeated index summation is used throughout:

$$\begin{aligned}
O(J_{d\phi}^2) = \frac{J_{d\phi}^2(D)}{2!} \int\limits_{\tau_c'>|\tau-\tau'|>\tau_c} d\tau d\tau' \Big\{ &\langle \mathcal{T}\left[\hat{S}^a(\tau)\hat{S}^b(\tau')\right]\rangle_0 \left(s^a_{\sigma\sigma'}s^b_{\lambda\lambda'}\right) \\
&\times \langle \mathcal{T}\left[\hat{d}^\dagger_\sigma(\tau)\hat{\phi}_{0\sigma'}(\tau)\hat{\phi}^\dagger_{0\lambda}(\tau')\hat{d}_{\lambda'}(\tau')\right]\rangle_0 \\
+ \langle \mathcal{T}\left[\hat{S}^a(\tau)\hat{S}^b(\tau')\right]\rangle_0 &\left(s^a_{\sigma\sigma'}s^b_{\lambda\lambda'}\right) \langle \mathcal{T}\left[\hat{\phi}^\dagger_{0\sigma}(\tau)\hat{d}_{\sigma'}(\tau)\hat{d}^\dagger_\lambda(\tau')\hat{\phi}_{0\lambda'}(\tau')\right]\rangle_0 \\
= \frac{J_{d\phi}^2(D)\nu_0}{2!} \int\limits_{\tau_c'>|\tau-\tau'|>\tau_c} d\tau d\tau' \Big\{ &\langle \mathcal{T}\left[\hat{S}^a(\tau)\hat{S}^b(\tau')\right]\rangle_0 \frac{\left(s^a_{\sigma\lambda}s^b_{\lambda\lambda'}\right)}{(\tau-\tau')} \langle \mathcal{T}\left[\hat{d}^\dagger_\sigma(\tau)\hat{d}_{\lambda'}(\tau')\right]\rangle_0 \\
&+ \langle \mathcal{T}\left[\hat{S}^a(\tau)\hat{S}^b(\tau')\right]\rangle_0 \frac{\left(s^b_{\lambda\sigma}s^a_{\sigma\sigma'}\right)}{(\tau-\tau')} \langle \mathcal{T}\left[\hat{d}_{\sigma'}(\tau)\hat{d}^\dagger_\lambda(\tau')\right]\rangle_0 \\
= -\frac{J_{d\phi}^2(D)\nu_0}{4} \int\limits_{\tau_c'>|\tau-\tau'|>\tau_c} d\tau d\tau' &\frac{i\epsilon^{abc}\left[s^a, s^b\right]_{\sigma\sigma'}}{|\tau-\tau'|} \langle T\left[\hat{S}^c(\tau)\right]\rangle_0 \langle \mathcal{T}\left[\hat{d}^\dagger_\sigma(\tau)\hat{d}_{\sigma'}(\tau')\right]\rangle_0 \\
= -\frac{J_{d\phi}^2(D)\nu_0}{2} \int\limits_{\tau_c'>|\tau-\tau'|>\tau_c} d\tau d\tau' &\frac{\left(\epsilon^{abc}\epsilon^{abf}s^f_{\sigma\sigma'}\right)}{|\tau-\tau'|} \langle T\left[\hat{S}^c(\tau)\right]\rangle_0 \langle \mathcal{T}\left[\hat{d}^\dagger_\sigma(\tau)\hat{d}_{\sigma'}(\tau')\right]\rangle_0 \\
= -\frac{J_{d\phi}^2(D)\nu_0}{2} \int\limits_{\tau_c'>|\tau-\tau'|>\tau_c} d\tau d\tau' &\frac{1}{|\tau-\tau'|} \langle \mathcal{T}\left[\hat{d}^\dagger_\sigma(\tau)\hat{S}^c(\tau)s^c_{\sigma\sigma'}\hat{d}_{\sigma'}(\tau')\right]\rangle_0
\end{aligned} \tag{B.21}$$

In the above derivation we have used the following results: $\epsilon^{abc}\epsilon^{abd} = 2\delta_{cd}$ and

$$\begin{aligned}
\mathcal{T}\left[\hat{S}^a(\tau)\hat{S}^b(\tau')\right] &= \theta(\tau-\tau')\hat{S}^a\hat{S}^b + \theta(\tau'-\tau)\hat{S}^b\hat{S}^a \\
&= \frac{1}{2}(\hat{S}^a\hat{S}^b - \hat{S}^b\hat{S}^a)\left[\theta(\tau-\tau') - \theta(\tau'-\tau)\right] + \frac{1}{2}(\hat{S}^a\hat{S}^b + \hat{S}^b\hat{S}^a) \\
&= \frac{i}{2}\epsilon^{abc}\hat{S}^c \mathrm{sgn}(\tau-\tau') + \left\{\hat{S}^a, \hat{S}^b\right\}
\end{aligned} \tag{B.22}$$

because $\hat{S}^a(\tau) = e^{\hat{H}_0\tau}\hat{S}^a e^{-\hat{H}_0\tau} = \hat{S}^a$. As noted above, the operators describing the dGSJ quasi-particle have time dynamics varying on the scale of $\Delta^{-1} \ll \tau_c'$, which is very slow compared to the fast degrees of freedom being integrated out from $\hat{\phi}_{0c}$ and $\hat{\phi}_c^\dagger$. Introducing $\tau_- = \tau - \tau'$ and $\tau_+ = (\tau + \tau')/2$. Thus, the term proportional to $\{\hat{S}^a, \hat{S}^b\}$ drops because it is multiplied by τ_-^{-1} rather than $|\tau_-|^{-1}$ and the integral over τ_- of former vanishes to leading order. Thus, to leading order in τ_-, we are left with

$$\begin{aligned} O(J_{d\phi}^2) &= -J_{d\phi}^2(D)\nu_0 \int d\tau_+ \, \langle \mathcal{T}\left[\hat{d}_\sigma^\dagger(\tau_+)\hat{\mathbf{S}}(\tau_+)\cdot \mathbf{s}_{\sigma\sigma'}(\tau_+)\hat{d}_\sigma(\tau_+)\right]\rangle_0 \int\limits_{\tau_c'>|\tau_-|>\tau_c} \frac{d\tau_-}{|\tau_-|} \\ &= -2\nu_0 \frac{\delta D}{D} J_{d\phi}^2(D) \int d\tau \, \langle \mathcal{T}\left[\hat{d}_\sigma^\dagger(\tau)\hat{\mathbf{S}}(\tau_+)\cdot \mathbf{s}_{\sigma\sigma'}(\tau)\hat{d}_\sigma(\tau)\right]\rangle_0. \end{aligned} \tag{B.23}$$

In the last expression, we have evaluated the integral over τ_- using

$$\int\limits_{\tau_c'>|\tau_-|>\tau_c} \frac{d\tau_-}{|\tau_-|} = 2\log\left(\frac{\tau_c'}{\tau_c}\right) = 2\log\left(\frac{D}{D'}\right) = -2\log\left(\frac{D-\delta D}{D}\right) \simeq \frac{2\delta D}{D}, \tag{B.24}$$

and replaced $\tau_+ \to \tau$. Notice that the resulting expression in Eq. (B.23) takes the same form as the contribution $\propto J_{dd}$ in the first order term of (B.18). This leads to the following recursion relation:

$$J_{dd}(D-\delta D) = J_{dd}(D) + 2\nu_0 J_{d\phi}^2(D)\frac{\delta D}{D} \tag{B.25}$$

(B.26)

Assuming the couplings are continuous functions of the cut-off D, the recursion relation becomes a differential equation:

$$D\frac{dJ_{dd}(D)}{dD} = -2\nu_0 J_{d\phi}^2, \tag{B.27}$$

which implies that J_{cc} increases with decreasing bandwdith D.

Similarly, we can tackle the terms at $O(J_{d\phi}J_{\phi\phi})$ and $O(J_{\phi\phi})$ (note the latter one is the only one present in the standard poor man's scaling treatment of the Kondo model). From those terms, the following differential equations are obtained:

$$D\frac{dJ_{d\phi}(D)}{dD} = -2\nu_0 J_{d\phi}J_{\phi\phi}, \tag{B.28}$$

$$D\frac{dJ_{dd}(D)}{dD} = -2\nu_0 J_{\phi\phi}^2. \tag{B.29}$$

It is convenient to introduce a new scaling variable defined by the differential equation:

$$\frac{dD}{D} = d\ell \Rightarrow D(\ell) = D_0 e^{-\ell}. \tag{B.30}$$

Thus, as $\ell \to +\infty$ $D(\ell) \to 0$. Furthermore, if we define the dimensionless couplings $\check{g}_{dd} = 2\nu_0 J_{dd}$, $\check{g}_{d\phi} = 2\nu_0 J_{d\phi}$, and $\check{g}_{\phi\phi} = 2\nu_0 J_{\phi\phi}$, we finally arrive at the scaling equations (4.14) to (4.16) discussed in Sec. 4.2.4.

B.5 S=5/2 Single-Site model

In the upcoming, we will introduce the different terms in Eq. (4.22) gradually. The first term, $\hat{H}_0$, is introduced in Sec. 2.4.2. Let us consider now the tunneling between the tip and the sample at zero temperature when both the tip and the sample are in their respective ground states: $|GS\rangle = \frac{1}{2}(|2\rangle_t + |0\rangle_t)(|2\rangle_s + |0\rangle_s) = |BCS\rangle_t|BCS\rangle_s$. When e.g. a spin-up electron tunnels from sample to tip [see Fig. B.2 (a)], we have

$$\hat{c}^\dagger_{t\uparrow}\hat{c}_\uparrow |GS\rangle = \frac{1}{2}|\uparrow\rangle_t |\downarrow\rangle_s \ . \tag{B.31}$$

This corresponds to a transition of energy $\Delta_s + \Delta_t$, whilst the process in the opposite direction (from tip to sample) involves an energy $-(\Delta_t + \Delta_s)$. This translates into two peaks at $\pm(\Delta_t + \Delta_s)$ in the tunneling spectrum, which mimic the coherence peaks observed in the tunneling between two s-wave superconductors.

Spin-5/2 impurity with zero exchange coupling

The Hamiltonian (4.21) is invariant under time-reversal symmetry (TRS) and commutes with the parity operator of combined the tip+sample system, $\hat{P}_T = (-1)^{\hat{N}_T}$, where $\hat{N}_T = \hat{N}_t + \hat{N}_s$ is the total electron number operator. Notice that the tunneling Hamiltonian $\hat{H}_{ts}$ does not commute with the sample (tip) parity operator $\hat{P}_s = (-1)^{\hat{N}_s}$ ($\hat{P}_t = (-1)^{\hat{N}_t}$). However, $\hat{P}_s$ is still a good quantum number when considering the diagonalization of $\hat{H}$ alone, as we shall do below. Thus, the Hilbert space of the sample can be separated into two parity sectors: even parity with $P_s = 1$ and odd parity with $P_s = -1$. In addition to TRS and parity, Eq.(4.21) exhibits other symmetries in certain limiting cases. For example, in the limit where the transverse magnetic anisotropic E vanishes, the Hamiltonian is invariant under the Z_2 symmetry that maps $\hat{S}_{T,z} \to -\hat{S}_{T,z}$ and interchanges $\hat{S}_{T,x} \leftrightarrow \hat{S}_{T,y}$, where $\hat{\boldsymbol{S}}_T = \hat{\boldsymbol{S}} + \frac{1}{2}\hat{c}^\dagger_\sigma \boldsymbol{s}_{\sigma\sigma'}\hat{c}_{\sigma'}$ is the total spin operator. This symmetry is generated by the rotation $\hat{\mathcal{U}} = e^{i\pi\hat{S}_{T,y}}e^{i\pi\hat{S}_{T,z}/2}$. In addition, we neglect the scattering potential V in Eq. (4.22). This potential breaks particle-hole symmetry (PHS) and would modify the spectral weights of the peaks, as mentioned in the main text. However, it does not modify the overall structure of the spectrum. Therefore, for the sake of simplicity, it can be taken to be zero, which renders the model invariant under PHS. Next, we consider how the excitation of the molecular spin reflects on the tunneling spectra. Since D is a large energy scale, we will first neglect the exchange coupling and set $J_z = J_\perp = 0$. This limit is expected to capture some of the physics on the weak coupling side of the quantum phase transition (QPT, see below) [105, 274]. Now the Hamiltonian of the sample is $\hat{H}_s = \hat{H}_0 + \hat{H}_M$, where the spin Hamiltonian $\hat{H}_M$ accounts for the intrinsic magnetic anisotropy of the molecular spin:

$$\hat{H}_M = D\hat{S}_z^2 \tag{B.32}$$

We assume easy-plane anisotropy ($D > 0$) and, for the sake of simplicity, zero transverse magnetic anisotropy $E = 0$. The effect of the latter will be discussed in the last subsection, where the spectrum of full Hamiltonian is described.

Since in this limit there is no exchange coupling, the Hilbert space of the sample is the tensor product of the Hilbert space of the superconducting site and the molecular spin (see Supplementary Fig. B.2 (b)). We use the basis $\{(|2\rangle, |0\rangle, |\uparrow\rangle, |\downarrow\rangle)\,|M\rangle\}$, where M is the eigenvalue of z-projection of the impurity spin, S_z. In the even parity sector $S_{T,z} = S_z = M$, which is half-integer (recall that $S = 5/2$) and therefore, by TRS the eigenstates $\{|BCS\rangle\,|M\rangle\ (|\overline{BCS}\rangle\,|M\rangle\})$ with the $S_{T,z} = \pm M$ are Kramers pairs and therefore degenerate in energy. In the odd parity sector, the Z_2 discussed above ensures the same for the eigenstates $|\sigma\rangle\,|M\rangle$. Since $D > 0$, the ground state is the doublet $S_{T,z}$ in the even parity sector, i.e. $|GS\rangle = |BCS\rangle\,|\pm\frac{1}{2}\rangle$. The eigenstates in the odd parity sector, describe a single (quasi-) particle excitations and, in this limit, have higher energy (see Supplementary Fig. B.2).

Let us consider the tunneling of a single electron between the tip and the sample in this limit. The tunneling Hamiltonian, Eq. (4.24), contains spin-independent and spin-dependent terms with amplitude T_0 and T_1, respectively. Since the tunneling current is second order in the tunneling amplitude, there are three different contributions. The term of order $|T_0|^2$ yields a spectrum identical to the one described in the previous subsection. The term of order $T_0 T_1^*$ and its complex conjugate vanish due to TRS (but they would not in an external magnetic field that breaks TRS). Finally, the term of order $|T_1|^2$ accounts for the spin-flip processes which we discuss in the following. One of the possible tunneling processes is:

$$\hat{c}^\dagger_{t\downarrow}\hat{c}_{s\uparrow}\hat{S}_+\,|GS\rangle = \hat{c}^\dagger_{t\downarrow}\hat{c}_{s\uparrow}\hat{S}_+\left[|BCS\rangle_t\,|BCS\rangle_s\,\left|\tfrac{1}{2}\right\rangle\right] \propto |\downarrow\rangle_t\,|\downarrow\rangle_s\,\left|\tfrac{3}{2}\right\rangle\ . \tag{B.33}$$

This process involves an excitation of the molecular spin and costs an energy $\pm(\Delta_s + \Delta_t + 2D)$, the minus sign corresponding to tunneling in the opposite direction (i.e. from tip to sample). Transitions (Fig. B.2 (b)) to higher spin states are enabled by spin pumping [165].

Spin-5/2 impurity with finite exchange coupling

Next, we account for the exchange coupling between the impurity and the substrate in the single-site approximation and explain how the parity-changing QPT takes place. The sample Hamiltonian is given in Eq. (4.22), where H_J is the exchange term. We begin by investigating the isotropic limit where $J_z = J_\perp = J$ and $D = E = 0$, i.e. $\hat{H}_M = 0$. The situation is not quite realistic but makes the discussion of the QPT particularly clear.

Given the significant molecular axial anisotropy D, in the main text, we assume an anisotropic exchange coupling, $J_z \neq J_\perp$, with an optimized ratio $p = J_\perp/J_z = 3$. This value is close to that found by projecting an $S = 5/2$ spin onto an $S = 1/2$ pseudo-spin representing the lowest-energy doublet in a quantum impurity with $D > 0$ [275]. However, the anisotropic exchange may generally result from several different mechanisms [275].

In the isotropic limit, the total spin of the superconductor plus impurity $\hat{\boldsymbol{S}}_T$ is conserved. Therefore, the eigenstates are organized into multiplets of $0 \otimes \frac{5}{2} = \frac{5}{2}$, for the even parity sector with $P_s = +1$, and $\frac{1}{2} \otimes \frac{5}{2} = 2 \oplus 3$, for the odd parity sector with

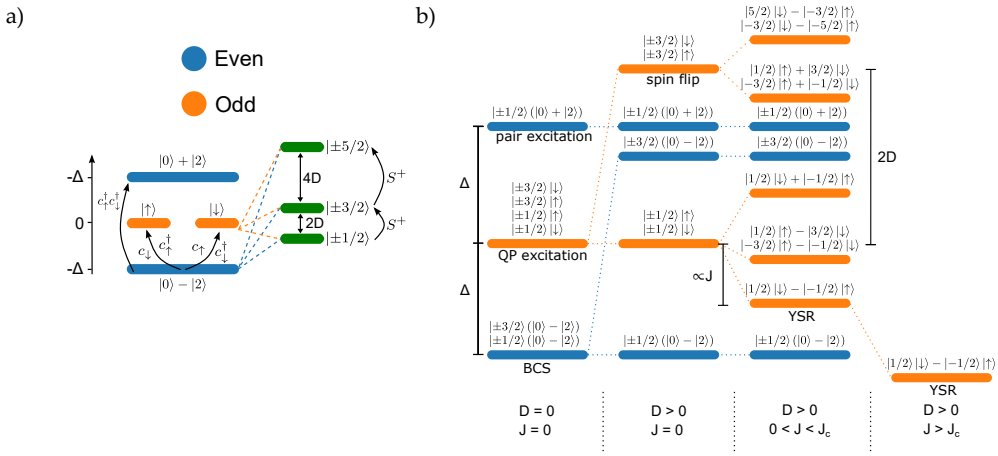

Figure B.2: **Eigenstates dependence on the different parameters. (a)** Spectrum of a single-site superconductor with states labeled by fermion parity: even (blue) and odd (orange) parity. When adding a spin $S = 5/2$ quantum impurity with easy-axis magnetic anisotropy D but negligible exchange each eigenvalue is split into three components. **(b)** Effect of a finite exchange coupling together with axial magnetic anisotropy on eigenvalues and eigenvectors. The parity changing QPT occurs for exchange greater than a critical value. To simplify the notation, the coefficients of the linear combinations have been suppressed.

$P_s = -1$. In the latter sector, the lowest energy state belongs to the multiplet with the smallest total spin, i.e., $S_T = 2$. Note that, by introducing a new energy scale $J > 0$, the ground state is no longer uniquely determined by Δ_s [see Fig. B.2 (c)]. In particular, the parity eigenvalue P_s of the ground state can change from even to odd by tuning J, resulting in a QPT [42, 276]. The transition occurs when the energies of the lowest energy states in the even and odd parity sectors cross as J increases. For a $S = 5/2$ quantum impurity in the isotropic exchange limit, the critical value is $J_C = 4\Delta/7$.

Regarding the overall structure of the spectrum, in the even parity sector, the spin of the single-site superconductor is zero; therefore, the exchange coupling has no effect. The eigenstates take the form $\{|BCS\rangle |M\rangle, |\overline{BCS}\rangle |M\rangle\}$, i.e, there are two eigenstates per impurity spin $S_z = M$ projection. The states with the same superconductor component are Kramers pairs for $S_z = \pm M$ and, therefore, degenerate in energy.

On the other hand, in the odd parity sector, the exchange coupling is effective, and the total spin of the eigenstates is an integer, as discussed above. In the multiplet with $S_T = 2$, the eigenstate $(|\frac{1}{2}\rangle |\downarrow\rangle - |-\frac{1}{2}\rangle |\uparrow\rangle)/\sqrt{2}$ with zero $S_{T,z}$ eigenvalue becomes the lowest energy state. Indeed, for $D > 0$ both multiplets of $\hat{\boldsymbol{S}}_T$ split, resulting in the states with the smallest $S_{T,z}$ eigenvalue from both multiplets having the smallest energy. The Z_2 symmetry implies that the eigenstates with the opposite $S_{T,z}$

	Symmetries of the system	Nº of non-degenerate states. Weak Coupling $J < J_C$	Strong Coupling $J > J_C$
$D = E = 0$ $J = 0$	TRS, Z_2, FSR_{sub}, FSR_{mol}	2	1
$D > 0$, $E = J = 0$	TRS, Z_2, FSR_{sub}	6	3
$D, J > 0$, $E = 0$	TRS, Z_2	6	7
$D, J, E > 0$	TRS	6	12

Table B.1: Symmetries of the model in various limiting cases. The acronyms and symbols stand for TRS = time-reversal symmetry, FSR_{sub} = full spin rotation symmetry for substrate electrons, FSR_{mol} = full spin rotation symmetry for molecular spin, Z_2= 180º rotation around the y-axis followed by a 90º rotation around the z-axis, .

eigenvalue are degenerate.

B.6 Two impurity single site model

In this section, we will describe how to form the single-site model used for the calculation of the singlet-based qubit. For this, we will follow Ref. [277], where the full calculation is properly done. The starting point is Eq. (4.25). We introduce the following operators:

$$\hat{a}_{i\sigma} = \frac{1}{\sqrt{\rho(\xi)}} \int \frac{d\mathbf{k}}{(2\pi)^3} e^{i\mathbf{k}\mathbf{R}_i} \hat{c}_{\mathbf{k}\sigma} \delta(\xi - \xi_{\hat{k}}) \,, \tag{B.34}$$

where $\mathbf{R}_i$ is the position of the$i$th impurity and $\{\hat{a}^\dagger_{i\sigma}, \hat{a}_{i\sigma'}\} = \delta_{\sigma\sigma'}\delta(\xi - \xi')$ and $\{\hat{a}^\dagger_{1\sigma}, \hat{a}_{2\sigma'}\} = \mathcal{S}(\xi)\delta_{\sigma\sigma'}\delta(\xi - \xi')$. $\mathcal{S}(\xi)$ is an overlap function, showing that the $\hat{c}_{\vec{k}\sigma}$ operators all lie within the same superconductor. If each impurity was in a different superconductor $\{\hat{a}^\dagger_{1\sigma}, \hat{a}_{2\sigma'}\} = 0$. As these two do not commute, the authors in Ref. [277] define a new set of operators $\hat{c}_{e/o} = (\hat{a}_1 + \hat{a}_2)/\sqrt{2(1 \pm \mathcal{S})}$. After mapping to a Wilson chain, the authors prove that the system has the structure shown in Fig. B.3(a).[1]

This structure differs from that proposed in Sec. 4.4. The Hamiltonian described in Eq. (4.29) couples two superconducting sites in distinct Hilbert spaces, generating a coupled state where Cooper pairs are formed with an electron on each site. Suppose the coherence length of the superconductor (ξ) is larger than the separation between the edge states. In that case, the non-locality of the BCS condensate should be considered, i.e., Cooper pairs have a spatial extension, so they can be formed from electrons in different positions. This is represented by the Wilson chain in Fig. B.3(b).

[1] This is an original idea of Chen-How Huang

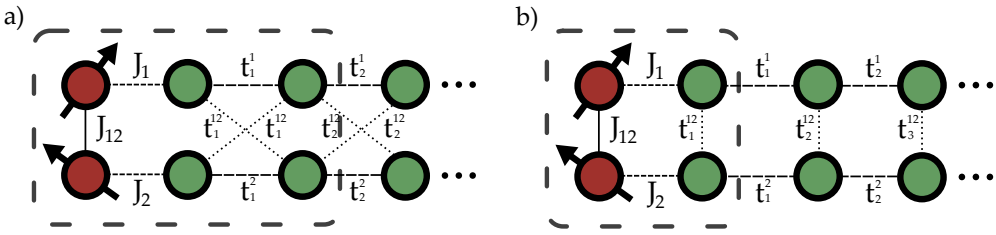

Figure B.3: **Structure of the Wilson chain, visualization of the logarithmic discretization of the band. (a)** For two impurities in the same superconductor and **(b)**, for two impurities on different superconductors with a tunneling Hamiltonian. The Dashed squares show the minimal single-site model for each case.

This reasoning presents a problem. The tunneling term would only be valid if each impurity's superconductor were independent; however, these impurities lie within the same superconductor, so the simple tunneling term is insufficient. The minimal single-site Hamiltonian for Fig. B.3(b), depicted by the dashed square, reads

$$\begin{aligned}\hat{H} = &\sum_{i\sigma\sigma'}\sum_{i=1,2} J_i \hat{c}^\dagger_{i\sigma}\hat{\mathbf{S}}_i\cdot\mathbf{s}_{\sigma\sigma'}\hat{c}_{i\sigma'} + \Delta\hat{c}^\dagger_{i\uparrow}\hat{c}^\dagger_{i\downarrow} + J_{12}\hat{\mathbf{S}}_1\cdot\hat{\mathbf{S}}_2 \\ &+ \sum_\sigma t_1\hat{c}^\dagger_{1\sigma}\hat{c}_{3\sigma'} + t_1\hat{c}^\dagger_{2\sigma}\hat{c}_{4\sigma'} + t_{12}\hat{c}^\dagger_{1\sigma}\hat{c}_{4\sigma'} + t_{12}\hat{c}^\dagger_{2\sigma}\hat{c}_{3\sigma'} + \text{h.c.}\,.\end{aligned} \tag{B.35}$$

Contrary to two independent superconductors with an added tunneling Hamiltonian, we need four sites in the superconductor to generate the single-site model. Using the proper single-site Hamiltonian for the two-impurity system states S_0 and S_2 are not mixed, and the NLQPT survives. In this case, parity and particle-hole symmetry have to be broken to mix the two singlets [277]. Once this happens, Eq. (4.28) and (4.30) can be used to describe the system. Parity symmetry is straightforward to break by fixing $J_1 \neq J_2$. Particle-hole symmetry, on the other hand, is usually broken due to a finite scattering potential on the impurities in STM experiments. For a device, it can be controlled by the gate potential. Then, Eq. (4.29) is adequate for the description of our system.

C Granular superconductivity

C.1 Rate equations for a DBTJ

This section introduces the model we use to do the fittings in Chapter 5. Most of the calculations were done in Refs. [45, 223, 224], so we will only summarize the results and add superconductivity to the model, which the previous works do not do. We describe the system as the lumped circuit depicted in Fig. 5.3(a). Solving the circuit's electrostatics (Kirchhoff's law) we get the energy change arising from a tunneling electron in the ith junction

$$\begin{aligned} E_1(V,q) &= \kappa_1 V + e\frac{(ne - q_0 - e/2)}{C} \\ E_2(V,q) &= \kappa_2 V - e\frac{(ne + q_0 + e/2)}{C} \end{aligned} \tag{C.1}$$

with $\kappa_1 = C2/C$ and $\kappa_2 = C1/C$. The tunneling rates for each junction read[45]

$$\overrightarrow{\Gamma}_{1(2)}(V,q) = \frac{e}{R_{1(2)}} \int d\omega \rho_{L(c)}(\omega) f(\omega) \rho_{c(R)}(\omega + E_{1(2)}(V,q)) f(-\omega' - E_{1(2)}(V,q)). \tag{C.2}$$

Here, $f(\omega)$ is the Fermi-Dirac distribution and ρ_i is the DoS for L=tip, c=Pb island, and R=Gr. The effects arising from the environmental modes have been disregarded as they can be considered with a Dynes parameter in the DoS of the superconductor[247]. We are only interested in the position of the peaks in the dI/dV measurements, so we do not use the PoE function here.

Using these rates, one can define the following master equation for the population of each charge state p_n:

$$\begin{aligned} \dot{p}_n(V) = &[\overrightarrow{\Gamma}_1(V, ne + e - q_0) + \overleftarrow{\Gamma}_2(V, ne + e - q_0) p_{n+1} \\ &+ [\overleftarrow{\Gamma}_1(V, ne - e - q_0) + \overrightarrow{\Gamma}_2(V, ne - e - q_0) p_{n-1} \\ &- [\overrightarrow{\Gamma}_1(V, ne - q_0) + \overleftarrow{\Gamma}_2(V, ne - q_0) \\ &+ \overleftarrow{\Gamma}_1(V, ne - q_0) + \overrightarrow{\Gamma}_2(V, ne - q_0) p_n \ . \end{aligned} \tag{C.3}$$

The first term on the right-hand side describes the tunneling from the (n+1) to the n state through the two junctions. The second, from the (n-1) to the n. The last term describes the tunneling from n to (n-1) and (n+1), so it has a negative contribution. Taking $\dot{p}_n(V) = 0$, one can solve for the stationary population of each state (p_n).

Once the population of each junction is known, the current reads

$$I = \sum_n p_n \left[\overrightarrow{\Gamma}_1(V, ne - q_0) - \overleftarrow{\Gamma}_1(V, ne - q_0) \right] \\ \sum_n p_n \left[\overrightarrow{\Gamma}_2(V, ne - q_0) - \overleftarrow{\Gamma}_2(V, ne - q_0) \right] . \tag{C.4}$$

This equation was used to obtain Figs. 2.3 and 2.4 considering a normal metal for the left and right electrode and the central grain.

C.2 Temperature dependence of small islands

The temperature dependence (from 1.3 K to 8 K) of three islands with varying sizes is plotted in Fig. C.1(a)-(c). We selected islands with a close to symmetric dI/dV, i.e., $q_0 = \sim$. Increasing the temperature, the spectra broaden, and the gaps slowly close. When we use the model introduced in Sec. 5.2 to fit these spectra for several islands, we obtain Fig. C.1(d). This figure shows the calculated charging energy for each island using the data taken at T=7 K and T=8 K. The critical temperature of bulk Pb is T_C =7.19 K, so we expect no contribution from either the tip's or sample's gap. We note that the values obtained for the two temperatures are not equal; the values of E_C for the lower temperature appear to be shifted downwards by around 1 meV.

Even if at 7 K, there was a small contribution from the not fully closed superconducting gap, it can not be 1 meV, which is almost as big as the bulk superconducting gap. As the charging energy that we measure changes with temperature, we conclude that either (1) the charging energy has a temperature dependence that we do not know

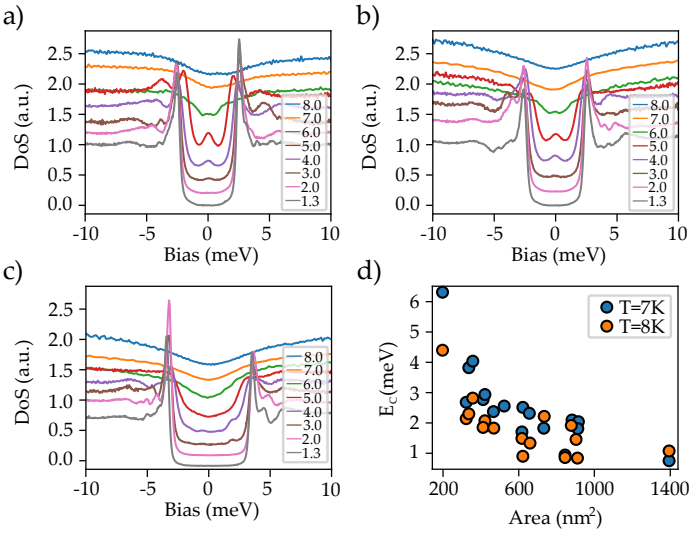

Figure C.1: **Temperature dependence of the island's spectra. (a)-(c)** Evolution of the dI/dV of three different islands from T=1.3 K to T=8 K. All islands are close to $q_0 = 0$. **(d)** Calculation of the charging energy of several islands using the model introduced in Sec. D.1 for $T = 7K$ and $T = 8K$

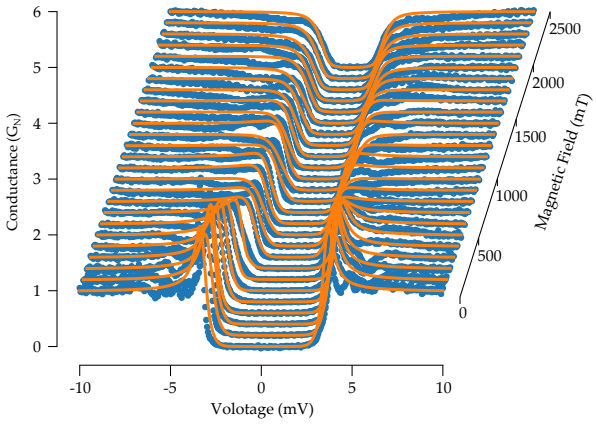

Figure C.2: **Fitted magnetic field dependent spectral evolution** The blue dots represent the measured data for magnetic fields from 0 to 2.5T. The orange solid lines are the fitted spectra following the model presented in Sec. 5.2. The dI/dV measurements have been shifted in conductance and voltage for increasing magnetic field to be able to visualize it better.

or (2) the charging energy does not change with temperature, but our fitting model has two big of an error when temperature increases. It is known that quasiparticle tunneling (which depends on temperature) can change the effective capacitance of a junction [67]; on the other hand, we are not considering any effect of the environment when we calculate the current because we could always assimilate this effect in the Dynes parameter of the superconducting DoS. Once superconductivity is broken, the effects of the environment should be considered as a temperature-dependent factor [218]. Consequently, we can not use the temperature dependence as a probe to calculate E_C and Δ.

C.3 Magnetic field dependence of small islands

Figure C.2 shows all the spectra measured (blue dots) in an island with an applied out-of-plane magnetic field up to 2.5 T. On top of the measured conductance, we plot a fitted curve using the model introduced in Sec. 5.2. The fitting is precise for all spectra from 0 to 2.5 T, and from it, we can extract the values of E_C and Δ for each magnetic field and do a plot similar to Fig. 5.5(c). This plot is later fitted applying Eq. (5.8).

In the following, we discuss the formulas used for each term in Eq. (5.8). The first term refers to the evolution of the tip's gap. As stated in Sec. 5.3,

$$\Delta_{\text{tip}}(B) = \Delta_0\sqrt{1-\left(\frac{B^2}{B_C}\right)^2} \;:\; \Delta_0 = 1.35 \text{ meV, and } B_C = 750 \text{ mT}. \tag{C.5}$$

As the tip's apex can vary from island to island, we assume that the critical field's error is $\delta B_C \sim 100$ mT, which we adjust to get the best fit. The second term is the charging energy (E_C), which we assume to be field-independent. The last is a Zeeman term that considers the split of the odd states in up and down spin states

$$E_z = -\frac{g_{\text{isl}}}{2}\mu_B B\,, \tag{C.6}$$

where μ_B is the Bohr magneton and g_{isl} is the island's g-factor, which can differ from the single-electron value. This term is small; it gives a correction smaller than 100 μeV at 2.5. We take $g_{\mathbf{isl}} = 2$ for the calculations.

The second term, $\Delta_{\text{isl}}(B)$, considers the evolution of the island's superconducting gap. When the islands are tiny, the trapped flux by the islands starts to be insignificant, and the superconducting state is broken due to the spin paramagnetism (Pauli limit) [43, 50, 248, 278]. Our islands are not that small, so the superconductivity is suppressed due to the more common orbital paramagnetism. We simulate the gap of the islands following Ref. [239]. The authors claim that for small islands where the superconductivity is broken due to the orbital paramagnetism, the same formula as in Eq. (C.5) can be used with a slight change. The gap is independent of the magnetic field until the field $B_1 = 2\Delta_0/\mu_B p_F d$ is reached, where d is the effective diameter of the island. This value is a few hundred mT in our islands:

$$\Delta_{\text{isl}}(B) = \begin{cases} \Delta_0 & \text{if } B \leq B_1 \\ \Delta_0 \sqrt{1 - \left(\dfrac{(B - B_1)^2}{B_C} \right)^2} & \text{if } B > B_1 \end{cases} . \tag{C.7}$$

More sophisticated evolution functions could be used (such as Ref. [279]), but we find Eq. (C.7) to work well for the evolutions we measure.

D

PoE calculation

This appendix extends the discussion started in Chapter 5 and calculates the effects of the environment in normal and Cooper Pair tunneling. We begin by solving the problem of a single junction with the interaction of an environment; we will end up with a tunneling formula for normal and Cooper pair currents with environmental effect. Next, the double junction problem will be solved. Again, we will get a normal and Cooper Pair tunneling formula and present a master equation that considers every possible charge state of the central region.

D.1 Junction between superconductor with environment

The circuit for which we have to calculate the current is depicted in Fig. D.1(a), which represents a single JJ. The impedance (Z) considers the effects of the environment [280]. The Hamiltonian of the system without environment is given by Eqs. (2.2), (2.16) and (2.17).

$$\hat{H} = \hat{H}_L + \hat{H}_R + \hat{H}_T + \hat{H}_C \tag{D.1}$$

$$\hat{H}_i = \sum_{\mathbf{k}\sigma} \xi_{i\mathbf{k}} \hat{c}^\dagger_{i\mathbf{k}\sigma} \hat{c}_{i\mathbf{k}\sigma} - \frac{\gamma_i}{V} \sum_{\mathbf{k}\mathbf{k}'} \hat{c}^\dagger_{i\mathbf{k}\uparrow} \hat{c}^\dagger_{i-\mathbf{k}\downarrow} \hat{c}_{i-\mathbf{k}'\downarrow} \hat{c}_{i\mathbf{k}\uparrow} \tag{D.2}$$

$$\hat{H}_T = \sum_{\mathbf{k}\mathbf{q}} \mathcal{T}_{\mathbf{k}\mathbf{q}} \hat{c}^\dagger_{L\mathbf{k}\sigma} \hat{c}_{R\mathbf{q}\sigma} + \text{h.c.} \tag{D.3}$$

$$\hat{H}_C = \frac{1}{2C} \left(\sum_{\mathbf{k}} \frac{\hat{c}^\dagger_{L\mathbf{k}\sigma} \hat{c}_{L\mathbf{k}\sigma} - \hat{c}^\dagger_{R\mathbf{k}\sigma} \hat{c}_{R\mathbf{k}\sigma}}{2} \right)^2 \tag{D.4}$$

H_i describes both the superconducting source and drain: $\xi_{i\mathbf{k}} = \epsilon_{i\mathbf{k}} - \mu_i$ is the energy dispersion and γ_i is the superconducting coupling, V the volume, C the capacitance of the junction and $\hat{c}^\dagger_{i\mathbf{k}\sigma}$ ($\hat{c}_{i\mathbf{k}\sigma}$) the creation (annihilation) operator of an electron with momentum $\mathbf{k}$ and spin σ in the ith electrode. H_T is the tunneling Hamiltonian, where $\mathcal{T}$ is tuhe tunneling amplitude [Eq. (2.16)], and H_C is the charging energy of the junction [Eq. (2.17)]. The partition function of the system reads

$$\mathcal{Z} = \int \mathcal{D}[\overline{c}_L, c_L] \mathcal{D}[\overline{c}_R, c_R] e^{-S[\overline{c}_L, c_L, \overline{c}_R, c_R]} \, . \tag{D.5}$$

where c_i and $\overline{c}_i$ are the Grassman fields related to the annihilation and creation operators of electrons in the ith electrode, which we take in imaginary times. To integrate the electronic degrees of freedom, we perform three Hubbard-Stratonovich decouplings. Two are for the superconducting correlations of each lead. The other one (see Ref. [67]) for the charging energy: $V_i = e \sum_{\mathbf{k}\sigma} \langle \hat{c}^\dagger_{i\mathbf{k}\sigma} \hat{c}_{i\mathbf{k}\sigma} \rangle / C$. These two fields are

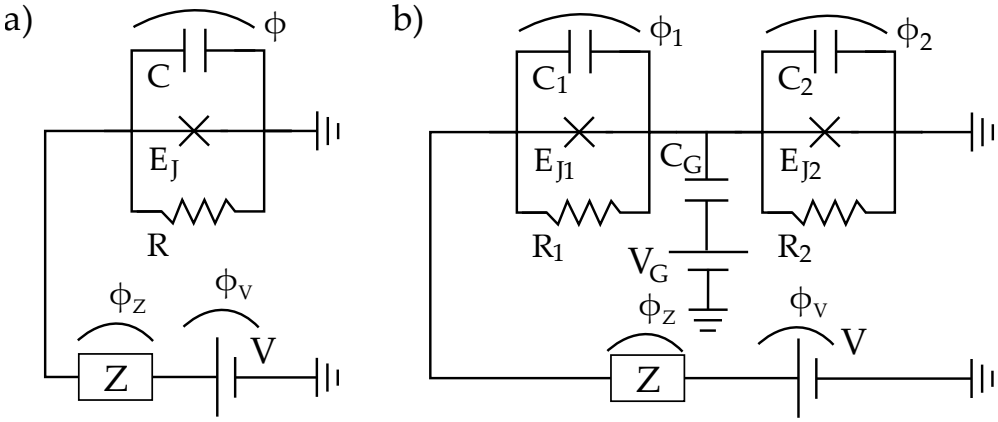

Figure D.1: **Equivalent lumped circuits. (a)** Circuit for a single JJ. **(b)** Circuit for a double JJ. The Z refers to the impedance of the circuit.

connected to the applied voltage as $V_L - V_R = V_x$. Where V_x is the voltage drop in the junction.

Using these fields, the electronic degrees of freedom can be integrated out, leaving the following partition function;

$$\mathcal{Z} = \int \mathcal{D}[\overline{\Delta}_L, \Delta_L]\mathcal{D}[\overline{\Delta}_R, \Delta_R]\mathcal{D}[V] e^{-\mathcal{G}[\overline{\Delta}_L, \Delta_R, \overline{\Delta}_R, \Delta_L, V_x]} \tag{D.6}$$

with, $-\mathcal{G}[\overline{\Delta}_L, \Delta_R, \overline{\Delta}_R, \Delta_L, V_x] = \sum_{\mathbf{k}} \mathrm{Tr}\left\{\ln G^{-1}_{\mathbf{k},\mathbf{k}}\right\} - \sum_{i\mathbf{k}} \frac{|\Delta_i|^2}{\gamma_i} - \int_0^\beta d\tau \frac{CV_x^2}{2\hbar}$, where,

$$\begin{aligned} \check{G}^{-1}_{\mathbf{k},\mathbf{k}'} &= \begin{pmatrix} \check{G}^{-1}_{L\mathbf{k},\mathbf{k}'} & -\check{\mathcal{T}}_{\mathbf{k},\mathbf{k}'} \\ -\check{\mathcal{T}}^{\dagger}_{\mathbf{k},\mathbf{k}'} & \check{G}^{-1}_{R\mathbf{k},\mathbf{k}'} \end{pmatrix}, \text{ with} \\ \check{G}^{-1}_{L(R),\mathbf{k}\mathbf{k}'} &= \left\{-\partial_\tau + \left(\xi_{L(R)} - (+)\frac{ieV_X}{2}\right)\tau_3 - \check{\Delta}_{L(R)}\right\}\delta_{\mathbf{k}\mathbf{k}'}\delta(\tau - \tau') \end{aligned} \tag{D.7}$$

and

$$\check{\Delta}_{L,R} = \begin{pmatrix} 0 & |\Delta_{L,R}|e^{i\phi_{L,R}} \\ |\Delta_{L,R}|e^{-i\phi_{L,R}} & 0 \end{pmatrix} \qquad \check{\mathcal{T}} = \begin{pmatrix} \check{\mathcal{T}}_{\mathbf{k},\mathbf{k}'} & 0 \\ 0 & -\check{\mathcal{T}}^*_{\mathbf{k},\mathbf{k}'} \end{pmatrix}.$$

$\check{G}_{L(R),\mathbf{k}\mathbf{k}}$, are the bare superconducting GFs as defined in Eq. (2.10) with a slight difference. The energy dispersion is shifted by $eV_X/2$, resulting from the potential drop in the junction.

We neglect any fluctuations from the average values for Δ_i, so only the integral over V_x has to be performed in Eq. (D.6). We also assume no k-dependence on the tunneling term, $\mathcal{T}_{\mathbf{k}\mathbf{k}'} = \mathcal{T}$. Applying the following gauge, $\check{U} = \mathrm{diag}\left\{e^{i\phi_L\tau_3/2}, e^{i\phi_R\tau_3/2}\right\}$, we

get rid of the ϕ dependence on the superconducting gap. The GF after the transformation reads

$$\check{G}^{-1}_{L(R),\mathbf{k}\mathbf{k}'} = \left\{ -\partial_\tau + \left(\xi_{L,R} \pm i \left[\frac{\partial_\tau \phi_{L(R)}}{2} \mp \frac{eV_X}{2} \right] \right) \tau_3 - |\Delta_{L(R)}| \tau_1 \right\} \delta_{\mathbf{k}\mathbf{k}'} \delta(\tau - \tau') \tag{D.8}$$

and

$$\check{\mathcal{T}} = \mathcal{T} \tau_3 e^{i\phi\tau_3/2}, \text{ with } \phi = \phi_L - \phi_R \, . \tag{D.9}$$

Without a loss of generality, we assumed $\mathcal{T}$ to be real. The action-minimizing path respect to the phase reads

$$\partial_\tau \phi = 2eV_X \, . \tag{D.10}$$

This is known as Josephson's second relation [69]. Considering this, the partition function can be written as

$$\mathcal{Z} = \int \mathcal{D}[\phi] e^{-\mathcal{G}[\phi]} \, . \tag{D.11}$$

We expand the GF on the exponent to first order in tunneling: $-\mathcal{G}[\phi] = \mathrm{Tr}\{\ln \check{G}\} \sim \mathrm{Tr}\{\ln \check{G}_0\} + \frac{1}{2}\mathrm{Tr}\{\check{G}_0 \check{T} \check{G}_0 \check{T}\}$. We sumed over momentum, so $\check{G}$ and $\check{G}_0$ are the dressed and bare GF of the system projected into the position of the tunneling, respectively. The partition function reads,

$$\begin{aligned} \mathcal{Z} = \int \mathcal{D}[\phi] \exp\left\{ \int\int \alpha(\tau - \tau') \cos\left(\frac{\phi(\tau) - \phi(\tau')}{2} \right) - \beta(\tau - \tau') \cos\left(\frac{\phi(\tau) + \phi(\tau')}{2} \right) \right\} \\ + \int d\tau \frac{C}{8e^2} (\partial_\tau \phi)^2 \, . \end{aligned} \tag{D.12}$$

with

$$\alpha(\tau) = -2|T|^2 g_L(\tau) g_R(-\tau)]/2 \qquad \beta(\tau) = -|T|^2 f_L(\tau) f_R(-\tau)]/2 \, , \tag{D.13}$$

where $g_i(\tau)\tau_3 + f_i(\tau)\tau_1 = \sum_{\mathbf{k}} G_{i\mathbf{k}}$. In imaginary times, the current reads,

$$I = e \, \mathrm{Im}\left\{ \int d\tau' \alpha(\tau - \tau') \langle e^{i\phi(\tau)/2} e^{-i\phi(\tau')/2} \rangle + \int d\tau' \beta(\tau - \tau') \langle e^{i\phi(\tau)/2} e^{i\phi(\tau')/2} \rangle \right\} \tag{D.14}$$

We need to calculate the averages $\langle e^{i\phi(\tau)/2} e^{\pm i\phi(\tau')/2} \rangle$ over phase fluctuations. To consider the effect of the circuit modes, one adds an environment made of harmonic oscillators that interact with the tunneling electrons. The action attributed to these oscillators can be encoded in a new phase with an effective action (see Ref. [280])

$$S_z[\phi_z] = \frac{1}{2\beta} \sum_\omega \frac{|\omega|}{4e^2} Z(-i|\omega|) \phi_z(\omega) \phi_z(-\omega) \, . \tag{D.15}$$

We add this new phase to the partition function (D.12) and calculate the averages. From energy conservation, we get that $\phi + \phi_z + \phi_V = 0$ [Fig. D.1], with $\partial_\tau \phi_V = 2eV$. We assume that the partition function can be written as

$$\mathcal{Z} = \int \mathcal{D}[\phi] \exp\left\{ - \int d\tau E_J \cos(\phi(\tau)) + \int\int d\tau d\tau' \alpha(\tau - \tau') \cos\left(\frac{\phi(\tau) - \phi(\tau')}{2}\right)\right\} + \int d\tau \frac{C}{8e^2} (\partial_\tau \phi)^2 S_z[\phi_z];. \tag{D.16}$$

Seemingly, the current can be simplified to

$$\langle I \rangle = E_J \langle \sin \phi(\tau) \rangle + \int \alpha(\tau - \tau') \langle \sin \frac{\phi(\tau) - \phi(\tau')}{2} \rangle \, . \tag{D.17}$$

In these steps, we have disregarded the term in the supercurrent with a $\tau + \tau'$ dependence ($\exp\{\phi(\tau) + \phi(\tau)\}$). A discussion about the implications of this term can be found in Ref. [267].

When the phase-phase correlation is calculated, we will assume that $E_J, \alpha \gg Z^{-1}$. This disregards any crossed interaction between the environment and tunneling current: the environment affects the tunneling current but not *vice versa*. Within this approximation, we get

$$\langle e^{i\phi(\tau)} e^{-i\phi(\tau')} \rangle = \mathcal{Z}^{-1} \int \mathcal{D}[\phi] \exp\left\{ \frac{i}{2\beta} \sum_\omega \phi(\omega)(e^{i\omega\tau} - e^{i\omega\tau'}) - \sum_\omega \frac{C\omega^2}{8\beta e^2} \phi(\omega)\phi(-\omega) \right. \\ \left. \sum_\omega \frac{|\omega|}{8e^2 \beta Z(-i|\omega|)} (\phi(\omega) + \phi_V(\omega))(\phi(-\omega) + \phi_V(-\omega)) \right\} \tag{D.18}$$

This is a Gaussian integral, hence, it can be performed exactly. After integration, we get

$$\langle e^{i\phi(\tau)/2} e^{-i\phi(\tau')/2} \rangle \\ = \exp\left\{ - \sum_\omega \frac{1 - \cos(\omega(\tau - \tau'))}{\beta} D_\omega^{-1} + i \sum_\omega \frac{|\omega|}{8e^2 \beta Z(-i|\omega|)} D_\omega^{-1} \phi_V(\omega)(e^{-i\omega\tau} - e^{-i\omega'\tau'}) \right\} \tag{D.19}$$

with

$$D^{-1}_{\omega\omega'} = D^{-1}_\omega \delta_{\omega,-\omega'} = \frac{8e^2 \beta \delta_{\omega,-\omega'}}{-C\omega^2 + |\omega| Z^{-1}(-i|\omega|)} \tag{D.20}$$

This equation can be written in a more familiar way by calculating $\langle \phi(\tau)\phi(\tau') \rangle_{\text{eq}}$,

where, eq means equilibrium, i.e., no applied voltage ($\phi_V = 0$),

$$\begin{aligned}\langle\phi(\omega)\phi(\omega')\rangle &= \mathcal{Z}^{-1}\int \mathcal{D}[\phi]\phi(\omega)\phi(\omega')e^{-\sum_{\nu\nu'}\phi(\nu)D_{\nu\nu'}\phi(\nu')} \\ &= \lim_{\eta,\lambda\to 0}\mathcal{Z}^{-1}\partial_\eta\partial_\lambda\int\mathcal{D}[\phi]e^{-\sum_{\nu\nu'}\phi(\nu)D_{\nu\nu'}\phi(\nu')+\eta\phi(\omega)+\lambda\phi(\omega')} \\ &= \lim_{\eta,\lambda\to 0}\partial_\mu\partial_\lambda\exp\{\eta D_\omega^{-1}\lambda\delta_{\omega,-\omega'}\} = D_\omega^{-1}\delta_{\omega,-\omega'} = \frac{8e^2\beta\delta_{\omega,-\omega'}}{-C\omega^2+|\omega|Z^{-1}(-i|\omega|)}\end{aligned} \tag{D.21}$$

then, $\langle\phi(\tau)\phi(\tau')\rangle_{\rm eq} = \langle\phi(\tau-\tau')\phi(0)\rangle_{\rm eq} = \sum_\omega e^{-i\omega(\tau-\tau')}\frac{8e^2\beta}{-C\omega^2+|\omega|Z^{-1}(-i|\omega|)}$. With this, we can rewrite the second term in Eq. (D.17) as

$$\begin{aligned}\langle\sin\frac{\phi(\tau)-\phi(\tau')}{2}\rangle_{\rm eq} = &\sin\left\{\sum_\omega\frac{|\omega|}{Z^{-1}(-i\omega)(-C\omega^2+|\omega|Z^{-1}(-i\omega))}\left(e^{i\omega\tau}-e^{i\omega\tau'}\right)\phi_V(\omega)\right\} \\ &\times\exp\left\{-\frac{1}{8}\langle[\phi(\tau)-\phi(\tau')]^2\rangle_{\rm eq}\right\}\end{aligned} \tag{D.22}$$

Finally, we note that $Z(\omega)V_z(\omega) = I(\omega) \Rightarrow I(\omega) = -\frac{Z(\omega)}{i\omega}(\phi(\omega)+\phi_V(\omega)) = \frac{Z_c(\omega)}{i\omega}\phi(\omega)$, with $Z_c(\omega) = 1/(C\omega + Z^{-1}(\omega))$, so that $\phi_V(\omega) = -\frac{Z_c}{Z}(1+\phi(\omega))$. Then,

$$\langle\sin\frac{\phi(\tau)-\phi(\tau')}{2}\rangle = \sin\left\{\int_{\tau'}^{\tau}eV(s)ds\right\}\exp\left\{-\frac{1}{8}\langle[\phi(\tau)-\phi(\tau')]^2\rangle_{\rm eq}\right\} \tag{D.23}$$

Here the second Josephson relation have been applied to write $\phi_V(\tau) = \int^\tau dseV(s)$

D.1.1 The single particle tunneling

The single-particle tunneling for a DC applied voltage reads [see Eq. (D.14)]

$$I = e\int d\tau'\alpha(\tau-\tau')\sin\left(eV(\tau-\tau')\right)\exp\left\{-\frac{1}{8}\langle[\phi(\tau)-\phi(\tau')]^2\rangle_{\rm eq}\right\} \tag{D.24}$$

The analytical continuation of this equation brings the tunneling current modified by the PoE function [45, 54, 71, 72, 156], which reads,

$$I = 4e\int_{-\infty}^{t}dt'\sin(eV(t-t'))\,{\rm Im}\left(\alpha^{>}(t-t')e^{J(t-t')}\right), \tag{D.25}$$

with

$$\begin{aligned}J(t) &= \frac{1}{4}\langle[\phi(t)-\phi(0)]\phi(t)\rangle_{\rm eq} \\ &= \frac{e^2}{\pi}\int_0^\infty d\omega\frac{{\rm Re}\,Z_c(\omega)}{\omega}\left[\coth(\beta\omega/2)(\cos(\omega t)-1)-i\sin(\omega t)\right]\end{aligned} \tag{D.26}$$

the $>$ sign means that we are taking the 'greater' term of $\alpha(t)$ in the Keldish contour [63]. By noting that $J^*(t-t') = J(t'-t)$, the current simplifies to (see Ref. [45])

$$\begin{aligned} I &= 4|\mathcal{T}^2|e\int d\omega d\omega' g_L^>(\omega)g_R^<(\omega')P(\omega'-\omega-eV) - g_L^<(\omega)g_R^>(\omega')P(\omega-\omega'+eV) \\ &= 4|\mathcal{T}^2|\pi^2 e\int d\omega d\omega' \rho_L(\omega)\rho_R(\omega')f(\omega)f(-\omega)P(\omega'-\omega-eV) \\ &\qquad -\rho_L(\omega)\rho_R(\omega')f(-\omega)f(\omega')P(\omega-\omega'+eV)\,. \end{aligned} \tag{D.27}$$

$g^<$ and $g^>$ are the 'lesser' and 'greater' GFs, which we connect with the DoS via fluctuation-dissipation theorem: $g^<(\omega) = 2i\pi\rho(\omega)f(\omega)$ and $g^>(\omega) = -2i\pi\rho(\omega)f(-\omega)$. Moreover, $P(\omega) = \int \exp(J(t)+i\omega t)$ is the PoE function. For no environmental effects, we take $P(\omega) = \delta(\omega)$ and obtain Eq. (2.20).

D.1.2 The Cooper Pair (Josephson) tunneling

We now focus on the tunneling of Cooper pairs. In Sec. 2.2, we deduced a formula for the Josephson current in a tunneling junction and found that for an applied DC voltage, only an AC current develops. Moreover, if the phase between the superconductors is not fixed, there is no Josephson current for zero voltage. In the following, we prove that when the effects of the environment are considered, there is a nonzero current response of Cooper pair to a DC applied voltage that is second order in transmittance. For this, we must calculate the average in the first term in Eq. (D.17): $\langle\sin\phi(\tau)\rangle$. Assuming a small applied voltage ($V \lesssim \Delta/e$) $\alpha << E_J, Z^{-1}$, and expanding the partition function to first order in E_J,

$$\begin{aligned} -E_J\langle\sin\phi(\tau)\rangle &= \mathcal{Z}^{-1}\int d\tau' \int \mathcal{D}\sin\phi(\tau)\cos\phi(\tau')e^{-S_0[\phi_V,\phi]} \\ &\sim \frac{E_J^2}{2}\int d\tau'\langle\sin(\phi(\tau)-\phi(\tau'))\rangle \end{aligned} \tag{D.28}$$

from eq. (D.23) we easily get that

$$I_S = -E_J\langle\sin\phi(\tau)\rangle = \int d\tau' \sin\left\{\int_{\tau'}^{\tau} 2eV(s)ds\right\}\exp\left\{-\frac{1}{2}\langle[\phi(\tau)-\phi(\tau')]^2\rangle_{\text{eq}}\right\} \tag{D.29}$$

The analytical continuation reveals the solution obtained in Refs. [45, 46, 72].

$$I = \pi e E_J^2\left(P'(2eV) - P'(-2eV)\right), \text{ with } P'(\omega) = \int dt e^{4J(t)+i\omega t} \tag{D.30}$$

Using this equation, we can extract the PoE of our system from the IVC in a small window around $V = 0$, as the one shown in Fig. D.2(a). Applying Eq. (D.30) to fit the measurements of the incoherent current or Cooper pair in an atomic-scale junction, we can extract the shape of the PoE function for our circuit [51]. This is shown

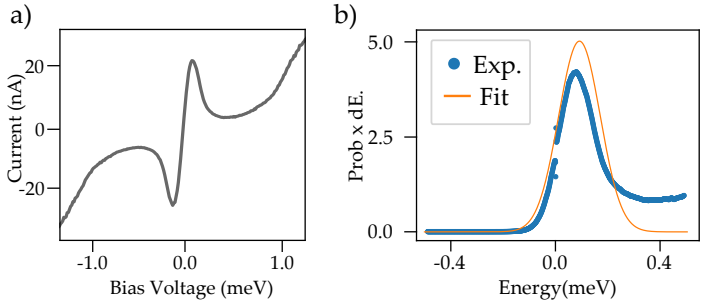

Figure D.2: **PoE of the STM circuit. (a)**IVC in a small window around V=0 at $R = 20$ kΩ. **(b)** Extracted PoE and a fir with a Gaussian distribution.

in Fig. D.2(b). The PoE has a Gaussian shape peaked at 0.15 meV and a thickness of ~ 100 μeV. In the limit of low environmental coupling, the PoE function approaches $P(\omega) \to \delta(\omega)$. For strong coupling, it becomes $P(\omega) \to \exp\left[-C\frac{(\omega - e^2/2C)^2}{2k_BT}\right]$, representing a Gaussian centered at $e^2/2C$. Our extracted distribution is shifted to 0.15 meV, indicating that we are not in the very weak coupling limit. Moreover, a Gaussian fit (orange curve) is not perfect, as the distribution if nos completelly simmetric around the maxima. The tip-sample capacitance is generally low [156], so we expect $E_C \gg 0.15$ meV. The obtained distribution suggests we are in an intermediate regime between weak and strong coupling.

D.2 Double Josephson Junction with environment

The approach to a double tunneling barrier it similar to the single tunneling barrier case. The action has now a new variable, connected to the island's degrees of freedom. In this case, the Josephson relation (D.10) is a little more complex,

$$\begin{aligned} \partial_\tau \phi_L(x) &= eV_1 \\ \partial_\tau \phi_C(x) &= eV_2 - eV_1(+eV_G) \\ \partial_\tau \phi_R(x) &= -eV_2, \end{aligned} \tag{D.31}$$

where V_i is the voltage drop in the ith junction, ϕ_j is the phase in $j = L$, $j = C$ and $j = R$, and V_G is the gate voltage, see Fig. D.1(b). We will omit the gate voltage for now. To get the proper Josephson relation, one has to apply a gauge to the potential: $\lambda = \frac{V_1 - V_2}{2a}xt + \frac{V_1 - V_2}{2}t$, where $2a$ is the thickness of the island. With this gauge, we get the following;

$$\begin{aligned} \partial_\tau(\phi_L(-a) - \phi_C(-a)) &= \partial_\tau \phi_1 = 2eV_1 \\ \partial_\tau(\phi_C(a) - \phi_R(a)) &= \partial_\tau \phi_2 = 2eV_2 \end{aligned} \tag{D.32}$$

where $\pm a$ are the positions of the junctions. After the mean field is applied to the charging of each junction, the following effective action is obtained from the charging

Hamiltonian Eq. (2.27);

$$\begin{aligned} S_0 &= \int d\tau \frac{C_1 V_1^2}{2} + \frac{C_2 V_2^2}{2} = \int d\tau \frac{C_1}{8e^2}(\partial_\tau \phi_1)^2 + \frac{C_2}{8e^2}(\partial_\tau \phi_2)^2 \\ &= \int d\tau \frac{C_\Sigma}{8e^2}(\partial_\tau \phi)^2 + \frac{C}{8e^2}(\partial_\tau \psi)^2 \ , \end{aligned} \tag{D.33}$$

where two new phases were defined: $\phi = \phi_1 + \phi_2$ and $\psi = \kappa_2 \phi_1 - \kappa_1 \phi_2$, with $\kappa_1 = C_2/C_\Sigma$, $\kappa_2 = C_1/C_\Sigma$, $C = C_1 + C_2$ and $C_\Sigma = C_1 C_2/C$. These are the same as the ones used in Eq. (2.27). ϕ is related to the charge transfer through the whole system, while ψ is related to the charge of the island, i.e., $[\hat{\phi}, \hat{Q}] = ie$ and $[\hat{\psi}, \hat{q}] = ie$. We can now write the total action in the tunneling limit as

$$\begin{aligned} S = &\sum_{i=1,2} \int d\tau d\tau' \alpha_i(\tau - \tau') \cos\left(\frac{\phi_i(\tau) - \phi_i(\tau')}{2}\right) + \sum_{i=1,2} E_{Ji} \int d\tau \cos \phi_i(\tau') \\ &+ \int d\tau \frac{C_\Sigma}{8e^2}(\partial_\tau \phi)^2 + \frac{C}{8e^2}(\partial_\tau \psi)^2 + S_z[\phi_z] \ , \end{aligned} \tag{D.34}$$

where E_{Ji} is the Josephson couplin of the ith junction and $\alpha_i(\tau)$ is defined as in Eq. (D.13) for each junction. We again neglected any term that is a function of $\tau + \tau'$. Calculating the tunneling of Cooper pairs in each junction separately reads

$$I_S^1 = 2eE_{J1} \langle \sin \phi_1(\tau) \rangle \sim 2eE_{J1}^2 \int d\tau \, \mathrm{Im}\Big\{ \langle e^{i\kappa_1(\phi(\tau) - \phi(\tau'))} e^{i(\psi(\tau) - \psi(\tau'))} \rangle \Big\} \ . \tag{D.35}$$

Here, we applied the same expansion in E_J as in Eq. (D.28). Note that at first order in the E_J, a term connecting the two junctions would also appear, proportional to $E_{J1}E_{J2}$. We disregard this term for now. For small voltages and $\alpha \ll E_J \ll Z^{-1}$, both ϕ and ψ are separated in the action, so we can calculate their averages independently. The $e^{i\psi}$ is the 2e translator operator for the charge of the island. Then, its average reads

$$\langle e^{i(\psi(\tau) - \psi(\tau'))} \rangle = \sum_{n,n'} p_n \langle n | \, e^{i\psi(\tau)} \, | n' \rangle \langle n' | \, e^{-i\psi(\tau')} \, | n \rangle = \sum_n p_n e^{i(E_n - E_{n-2})(\tau - \tau')} \tag{D.36}$$

The p_n should be calculated using a rate equation (see below), as we are looking at a dynamic problem. To get to Eq. (D.36), we have assumed that n, the charge state of the island, is a good quantum number. This is only true for $E_J \ll E_C$. Within this approximation, it is straightforward to solve the remaining problem, as we can follow the same steps we took in the single junction case. The current for the first junction

in real times for a DC drive reads

$$\begin{aligned} I_S^1 =& {}^2_{J1} \int dt \left(\sum_n p_n e^{2ieVt} e^{i(E_n - E_{n-2})t} \langle e^{i\kappa_1(\phi(t)-\phi(0))} \rangle \right. \\ & \left. - \sum_n p_n^{-2ieVt} e^{i(E_n - E_{n+2})t} \langle e^{i\kappa_1(\phi(t)-\phi(0))} \rangle \right) \\ =& \pi e E_{J1}^2 \sum_n p_n [\tilde{P}_1(2eV + E_n - E_{n-2}) - \tilde{P}_1(-2eV + E_n - E_{n+2})], \end{aligned} \tag{D.37}$$

with $\tilde{P}_i(\omega) = \int dt \exp(4\kappa_i J(t) + i\omega t)$. To properly calculate the populations p_n, a master equation should be employed. For this, we define the rate of tunneling as

$$\begin{aligned} \overrightarrow{\Gamma}_{1,n} &= \pi e E_{J1}^2 \tilde{P}_1(2eV - 4E_c(n + 1 - q_0/e)) \\ \overleftarrow{\Gamma}_{1,n} &= \pi e E_{J1}^2 \tilde{P}_1(2eV - 4E_c(1 - n - q_0/e)). \end{aligned} \tag{D.38}$$

The rates for the second junction are similar. Then Eq. (C.3) is used with the defined rates to calculate p_n, with even n. For the limit where $\Gamma_1 \ll \Gamma_2$, equal to the single-particle tunneling case in Chp. 5, the Cooper pair tunneling will be fixed by the rates of the first junction. Note that E_{Ji} depend on E_C and q_0 [47], so a more careful calculation should be done.

E

A few facts to enliven your reading

1. Few people being remembered for the works of many does not apply only to science but to any history-related event and has been discussed by historians and philosophers. An example of this fact that I very much like is the concept of "intrahistoria," coined by Miguel de Unamuno.

2. Both Alhazen (Ibn Al-Haytham) and Avicenna (Ibn Sina) were intellectuals in the Islamic golden era. Alhazen is regarded as the creator of the scientific method as well as the first to propose that light always follows an extremal path (also known as the Fermat law). Both proposed the inertia law, and Avicenna even proposed an idea similar to Newton's second law, which was more than 500 years before Newton's era. Galileo gave credit to these two intellectuals in his work proposing the inertia law. The inertia law has had a long trip before current days. Even in ancient China, in the Warring States period ($\sim$ 300 BC), Mozi, a philosopher and founder of Mohism, wrote, 'The cessation of motion is due to the opposing force... If there is no opposing force... the motion will never stop. This is as true as that an ox is not a horse.'

3. Leiden University was founded as a gift for the city of Leiden because they helped in the independence war against Spain. It has always had a remarkable independence related to their teaching. Due to this special regime, it is one of the three universities that defined for the first time the concept of Academic Liberty: the idea that the universities should be able to select their teaching independently to any social or political change in their countries. Thus, this university has been at the center of many scientific discoveries, including superconductivity.

4. Note that Superconductivity was found in 1911, only a decade after Drude proposed his model for electrical conductivity. From Drude's formula one concludes that conductivity should fall down to zero at $T = 0$, something that was highly believed (William Thomson was a defender of this idea) and only theoretically disproven with the rise of quantum theory (Pauli's exclusion principle)

5. How is a superconductor different from a perfect metal due to the Meissner effect? Let us take a metal in a magnetic field and suddenly make the metal to be perfect. The field inside the metal will remain the same before maki it perfect. This does not happen with superconductivity. Independently to the field the metal had before becoming a superconductor, the field inside the metal will always be zero when it transitions into a superconductor.

6. Gor'kov was one of the most important scientists to unite Soviet and Western research in this area. Two years after the BCS discovery, he published a paper in Russian and English, proving that one can derive the Ginzburg-Landau free

energy from the newborn microscopic theory. This and Abrikosov's finding on the vortices in type II superconductors were the two main findings that gave popularity to the theory.

7. Interestingly, the original Bogoliuvob paper defining his transformation[64] -later known as the bogoliubov transformation- was submitted a few months before the BCS theory was published[8]. In this work, Bogoliuvob cites Frölich's paper on superconductivity[13] and a short letter published by Bardeen, Cooper, and Schiffer [14] discussing the microscopic reasoning for the formation of Cooper Pairs. Although he does not write down the BCS GS, it is inherent from his equations that the BCS GS is indeed the solution to the problem and is more than a simple variational solution.

8. We do not get credit for how advanced London's notion of superconductivity was. In a meeting of the Royal Society in 1935, Fritz London discussed the quantum origin of his electromagnetic equations for superconductivity. He claimed that superconductors act as a "single big diamagnetic atom". He even claimed that some force should couple electrons, so a finite energy gap between GS and excited states should exist.[7] London suggested that a rigid enough GS would have a linear response on the magnetic vector potential, explaining the Meissner effect.[281] Pippard later stated that the response of the superconductor is not directly proportional to the magnetic vector potential but to its integral in a region around the point in question, defining the coherence length.

9. The BCS ground state (2.5) can be rewritten in the following way:

$$|BCS\rangle = \prod_{\mathbf{k}} (1 + \frac{v_{\mathbf{k}}}{u_{\mathbf{k}}} \hat{c}^{\dagger}_{\mathbf{k}\uparrow} \hat{c}^{\dagger}_{\mathbf{k}\downarrow}) \, |0\rangle = \exp\left\{ - \sum_{\mathbf{k}} \frac{v_{\mathbf{k}}}{u_{\mathbf{k}}} \hat{c}^{\dagger}_{\mathbf{k}\uparrow} \hat{c}^{\dagger}_{\mathbf{k}\downarrow} \right\} |0\rangle = e^{\hat{\Lambda}^{\dagger}} \, |0\rangle \ , \quad \text{(E.1)}$$

where $\hat{\Lambda}^{\dagger}$ is the creation operator of Cooper pairs. Then, the ground state is a coherent combination of even states

$$|BCS\rangle = \sum_{n} \frac{1}{n!} (\Lambda^{\dagger})^{n} \, |0\rangle = \sum_{n} A_n \, |n\rangle \quad \text{(E.2)}$$

The BCS ground state breaks gauge invariance, so although the transformation $\hat{c}^{\dagger}_{\mathbf{k}\sigma} \to e^{i\hat{\phi}} \hat{c}^{\dagger}_{\mathbf{k}\sigma}$ does not change the ground state energy, $|BCS\rangle$ develops a phase:

$$|BCS\rangle \to |BCS, \phi\rangle = \sum_{n} A_n e^{2in\phi} \, |n\rangle \ . \quad \text{(E.3)}$$

The states $|BCS, \phi\rangle$, form a family of degenerate broken-symmetry GS. Applying the number operator to this ket

$$N \, |BCS, \phi\rangle = \sum_{n} 2n A_n e^{2in\phi} \, |n\rangle = \sum_{n} \left(-i \frac{d}{d\phi} \right) A_n e^{2in\phi} \, |n\rangle \ , \quad \text{(E.4)}$$

i.e., $\hat{N} = -id/d\hat{\phi}$, so

$$[\hat{N}, \hat{\phi}] = i \text{ or } [\hat{n}, \hat{\phi}] = 2i \ . \tag{E.5}$$

Phase and number are conjugate operators. An inverse Fourier transform of Eq. (E.3) projects the ground state to a particle-conserving state:

$$|NBCS\rangle = \frac{1}{2\pi|A_N|} \int_0^{2\pi} d\phi e^{-i\phi N} |BCS, \phi\rangle \tag{E.6}$$

$$|A_N|^2 = \int_0^{2\pi} d\phi e^{-i\phi N} \prod_{\mathbf{k}} \left(u_{\mathbf{k}}^2 + e^{2i\phi} v_{\mathbf{k}}^2\right) |0\rangle \ . \tag{E.7}$$

Where, $|A_N|$ is a probability distribution peaked around $\langle BCS| \hat{N} |BCS\rangle$.

10. Although Bardeen, Brattain and Shockley are regarded as the creators of the transistor, 20 years before their invention, Julius Edgar Lilienfeld had already patented the field-effect transistor in Canada. He could not patent it in the USA, so it was forgotten with time. Bardeen, Brattain, and Shockley proposed the point-contact transistor. It is also said that Shockley tried to take full credit for the invention of the transistor; for this reason, Bardeen and Brattain published Ref. [282] by themselves.

Bibliography

[1] J. Zaldivar. "Magnetic-impurity-induce bound stats in -Bi2Pd". PhD thesis. University of the Basque Country, 2020.

[2] K. Vaxevani et al. "Extending the spin excitation lifetime of a magnetic molecule on a proximitized superconductor". In: *Nano Letters* 22 (2022), pp. 6075–6082. DOI: 10.1021/acs.nanolett.2c00924.

[3] S. Trivini et al. "Cooper pair excitation mediated by a molecular quantum spin on a superconducting proximitized gold film". In: *Physical Review Letters* 130 (2023). Number of pages: 6 Publisher: American Physical Society, p. 136004. DOI: 10.1103/PhysRevLett.130.136004.

[4] S. Trivini. "Manipulating superconductivity at the nanoscale through magnetism and proximity effects". PhD thesis. University of the Basque Country, 2023.

[5] G. Binnig and H. Rohrer. "Scanning tunneling microscopy". In: *Surface Science* 126 (1983), pp. 236–244. DOI: 10.1016/0039-6028(83)90716-1.

[6] J. Bardeen. "Tunnelling from a Many-Particle Point of View". In: *Physical Review Letters* 6 (1961), pp. 57–59. DOI: 10.1103/PhysRevLett.6.57.

[7] J. Bardeen. "Developments of concepts in superconductivity". In: *Physics Today* 16 (1963), pp. 19–28. DOI: 10.1063/1.3050710.

[8] J. Bardeen, L. N. Cooper, and J. R. Schrieffer. "Theory of Superconductivity". In: *Physical Review* 108 (1957), pp. 1175–1204. DOI: 10.1103/PhysRev.108.1175.

[9] I. Giaever. "Electron Tunneling Between Two Superconductors". In: *Physical Review Letters* 5 (1960), pp. 464–466. DOI: 10.1103/PhysRevLett.5.464.

[10] J. Nicol, S. Shapiro, and P. H. Smith. "Direct Measurement of the Superconducting Energy Gap". In: *Physical Review Letters* 5 (1960), pp. 461–464. DOI: 10.1103/PhysRevLett.5.461.

[11] N. N. Bogoljubov, V. V. Tolmachov, and D. V. Širkov. "A New Method in the Theory of Superconductivity". In: *Fortschritte der Physik* 6 (1958), pp. 605–682. DOI: 10.1002/prop.19580061102.

[12] L. N. Cooper. "Bound Electron Pairs in a Degenerate Fermi Gas". In: *Physical Review* 104 (1956), pp. 1189–1190. DOI: 10.1103/PhysRev.104.1189.

[13] H. Fröhlich. "Theory of the Superconducting State. I. The Ground State at the Absolute Zero of Temperature". In: *Physical Review* 79 (1950), pp. 845–856. DOI: 10.1103/PhysRev.79.845.

[14] J. Bardeen, L. N. Cooper, and J. R. Schrieffer. "Microscopic Theory of Superconductivity". In: *Physical Review* 106 (1957), pp. 162–164. DOI: 10.1103/PhysRev.106.162.

[15] W. Meissner and B. Voigt. "Messungen mit Hilfe von flüssigem Helium XI Widerstand der reinen Metalle in tiefen Temperaturen". In: *Annalen der Physik* 399 (1930), pp. 892–936. DOI: 10.1002/andp.19303990803.

[16] F. London and H. London. "The electromagnetic equations of the supraconductor". In: *Proceedings of the Royal Society of London. Series A - Mathematical and Physical Sciences* 149 (1935), pp. 71–88. DOI: 10.1098/rspa.1935.0048.

[17] P. W. Anderson. "Localized Magnetic States in Metals". In: *Physical Review* 124 (1961), pp. 41–53. DOI: 10.1103/PhysRev.124.41.

[18] L. Yu. "BOUND STATE IN SUPERCONDUCTORS WITH PARAMAGNETIC IMPURITIES". In: *Acta Physica Sinica* 21 (1965), p. 75. DOI: 10.7498/aps.21.75.

[19] H. Shiba. "Classical Spins in Superconductors". In: *Progress of Theoretical Physics* 40 (1968), pp. 435–451. DOI: 10.1143/PTP.40.435.

[20] M. Ruan et al. "Epitaxial graphene on silicon carbide: Introduction to structured graphene". In: *MRS Bulletin* 37 (2012), pp. 1138–1147. DOI: 10.1557/mrs.2012.231.

[21] J. Kondo. "Resistance minimum in dilute magnetic alloys". In: *Progress of Theoretical Physics* 32 (1964), pp. 37–49. DOI: 10.1143/PTP.32.37.

[22] E. Wolf and G. Arnold. "Proximity electron tunneling spectroscopy". In: *Physics Reports* 91 (1982), pp. 31–102. DOI: https://doi.org/10.1016/0370-1573(82)90061-8.

[23] A. I. Rusinov. "On the Theory of Gapless Superconductivity in Alloys Containing Paramagnetic Impurities". In: *Soviet Journal of Experimental and Theoretical Physics* 29 (1969). Publisher: Springer ADS Bibcode: 1969JETP...29.1101R, p. 1101.

[24] A. Yazdani et al. "Probing the Local Effects of Magnetic Impurities on Superconductivity". In: *Science* 275 (1997), pp. 1767–1770. DOI: 10.1126/science.275.5307.1767.

[25] E. Majorana. "Teoria simmetrica dell'elettrone e del positrone". In: *Il Nuovo Cimento* 14 (1937), pp. 171–184. DOI: 10.1007/BF02961314.

[26] A. Y. Kitaev. "Unpaired Majorana fermions in quantum wires". In: *Physics-Uspekhi* 44 (2001), pp. 131–136. DOI: 10.1070/1063-7869/44/10S/S29.

[27] S. Nadj-Perge et al. "Proposal for realizing Majorana fermions in chains of magnetic atoms on a superconductor". In: *Physical Review B* 88 (2013), p. 020407. DOI: 10.1103/PhysRevB.88.020407.

[28] Y. Kim et al. "Helical order in one-dimensional magnetic atom chains and possible emergence of Majorana bound states". In: *Physical Review B* 90 (2014), p. 060401. DOI: 10.1103/PhysRevB.90.060401.

[29] B. W. Heinrich, J. I. Pascual, and K. J. Franke. "Single magnetic adsorbates on s -wave superconductors". In: *Progress in Surface Science* 93 (2018), pp. 1–19. DOI: 10.1016/j.progsurf.2018.01.001.

[30] K. Iwaya et al. "Full-gap superconductivity in spin-polarised surface states of topological semimetal -PdBi2". In: *Nature Communications* 8 (2017), p. 976. DOI: 10.1038/s41467-017-01209-9.

[31] M. Sakano et al. "Topologically protected surface states in a centrosymmetric superconductor -PdBi2". In: *Nature Communications* 6 (2015), p. 8595. DOI: 10.1038/ncomms9595.

[32] G. C. Ménard et al. "Coherent long-range magnetic bound states in a superconductor". In: *Nature Physics* 11 (2015), pp. 1013–1016. DOI: 10.1038/nphys3508.

[33] H. Kim et al. "Long-range focusing of magnetic bound states in superconducting lanthanum". In: *Nature Communications* 11 (2020), p. 4573. DOI: 10.1038/s41467-020-18406-8.

[34] E. Liebhaber et al. "Quantum spins and hybridization in artificially-constructed chains of magnetic adatoms on a superconductor". In: *Nature Communications* 13 (2022), p. 2160. DOI: 10.1038/s41467-022-29879-0.

[35] L. Schneider et al. *High-resolution spectroscopy of proximity superconductivity in finite-size quantized surface states*. Version Number: 1. 2024. DOI: 10.48550/ARXIV.2402.08895.

[36] F. von Oppen and K. J. Franke. "Yu-Shiba-Rusinov states in real metals". In: *Physical Review B* 103 (2021). Number of pages: 21 Publisher: American Physical Society, p. 205424. DOI: 10.1103/PhysRevB.103.205424.

[37] K. Satori et al. "Numerical renormalization group study of magnetic impurities in superconductors". In: *Journal of the Physical Society of Japan* 61 (1992), pp. 3239–3254. DOI: 10.1143/JPSJ.61.3239.

[38] R. ž žitko, O. Bodensiek, and T. Pruschke. "Effects of magnetic anisotropy on the subgap excitations induced by quantum impurities in a superconducting host". In: *Physical Review B* 83 (2011). Number of pages: 13 Publisher: American Physical Society, p. 054512. DOI: 10.1103/PhysRevB.83.054512.

[39] A. Odobesko et al. "Observation of tunable single-atom Yu-Shiba-Rusinov states". In: *Physical Review B* 102 (2020), p. 174504. DOI: 10.1103/PhysRevB.102.174504.

[40] P. W. Anderson. "A poor man's derivation of scaling laws for the Kondo problem". In: *Journal of Physics C: Solid State Physics* 3 (1970), p. 2436. DOI: 10.1088/0022-3719/3/12/008.

[41] K. J. Franke, G. Schulze, and J. I. Pascual. "Competition of Superconducting Phenomena and Kondo Screening at the Nanoscale". In: *Science* 332 (2011), pp. 940–944. DOI: 10.1126/science.1202204.

[42] A. V. Balatsky, I. Vekhter, and J.-X. Zhu. "Impurity-induced states in conventional and unconventional superconductors". In: *Reviews of Modern Physics* 78 (2006), pp. 373–433. DOI: 10.1103/RevModPhys.78.373.

[43] M. Tinkham. *Introduction to superconductivity*. 2. ed. International series in pure and applied physics. New York: McGraw-Hill, 1996.

[44] G. O. Steffensen and A. L. Yeyati. *YSR Bond Qubit in a Double Quantum Dot with cQED Operation*. Version Number: 1. 2024. DOI: 10.48550/ARXIV.2402.19261.

[45] G.-L. Ingold and Y. V. Nazarov. "Charge Tunneling Rates in Ultrasmall Junctions". In: *Single Charge Tunneling*. Ed. by H. Grabert and M. H. Devoret. Vol. 294. Series Title: NATO ASI Series. Boston, MA: Springer US, 1992, pp. 21–107. DOI: 10.1007/978-1-4757-2166-9_2.

[46] D. V. Averin and K. K. Likharev. "Coulomb blockade of single-electron tunneling, and coherent oscillations in small tunnel junctions". In: *Journal of Low Temperature Physics* 62 (1986), pp. 345–373. DOI: 10.1007/BF00683469.

[47] K. A. Matveev et al. "Parity-induced suppression of the Coulomb blockade of Josephson tunneling". In: *Physical Review Letters* 70 (1993), pp. 2940–2943. DOI: 10.1103/PhysRevLett.70.2940.

[48] P. Joyez et al. "Observation of parity-induced suppression of Josephson tunneling in the superconducting single electron transistor". In: *Physical Review Letters* 72 (1994), pp. 2458–2461. DOI: 10.1103/PhysRevLett.72.2458.

[49] E. Cortés-del Río et al. "Observation of yu–shiba–rusinov states in superconducting graphene". In: *Advanced Materials* 33 (2021), p. 2008113. DOI: https://doi.org/10.1002/adma.202008113.

[50] J. Von Delft. "Superconductivity in ultrasmall metallic grains". In: *Annalen der Physik* 513 (2001), pp. 219–276. DOI: 10.1002/andp.20015130302.

[51] J. Senkpiel et al. "Single channel Josephson effect in a high transmission atomic contact". In: *Communications Physics* 3 (2020), p. 131. DOI: 10.1038/s42005-020-00397-z.

[52] P. Joyez. "The single Cooper pair transistor: a macroscopic quantum system". PhD thesis. Université Pierre et Marie Curie - Paris, 1995.

[53] Y. Harada, H. Takayanagi, and A. A. Odintsov. "Cooper-pair tunneling in small junctions with tunable Josephson coupling". In: *Physical Review B* 54 (1996), pp. 6608–6613. DOI: 10.1103/PhysRevB.54.6608.

[54] M. H. Devoret et al. "Effect of the electromagnetic environment on the Coulomb blockade in ultrasmall tunnel junctions". In: *Physical Review Letters* 64 (1990), pp. 1824–1827. DOI: 10.1103/PhysRevLett.64.1824.

[55] M. Trahms et al. "Diode effect in Josephson junctions with a single magnetic atom". In: *Nature* 615 (2023), pp. 628–633. DOI: 10.1038/s41586-023-05743-z.

[56] J. F. Steiner et al. “Diode Effects in Current-Biased Josephson Junctions”. In: *Physical Review Letters* 130 (2023), p. 177002. DOI: 10.1103/PhysRevLett.130.177002.

[57] C. Gorter and H. Casimir. “On supraconductivity I”. In: *Physica* 1 (1934), pp. 306–320. DOI: 10.1016/S0031-8914(34)90037-9.

[58] V. Ginzburg and L. Landau. “ON THE THEORY OF SUPERCONDUCTIVITY”. In: *Collected Papers of L.D. Landau*. Elsevier, 1965, pp. 546–568. DOI: 10.1016/B978-0-08-010586-4.50078-X.

[59] E. Maxwell. “Isotope Effect in the Superconductivity of Mercury”. In: *Physical Review* 78 (1950), pp. 477–477. DOI: 10.1103/PhysRev.78.477.

[60] C. A. Reynolds et al. “Superconductivity of Isotopes of Mercury”. In: *Physical Review* 78 (1950), pp. 487–487. DOI: 10.1103/PhysRev.78.487.

[61] P. F. Dahl. “Superconductivity after World War I and Circumstances Surrounding the Discovery of a State B = 0”. In: *Historical Studies in the Physical and Biological Sciences* 16 (1986), pp. 1–58. DOI: 10.2307/27757556.

[62] J. Bardeen. “Electron-Vibration Interactions and Superconductivity”. In: *Reviews of Modern Physics* 23 (1951), pp. 261–270. DOI: 10.1103/RevModPhys.23.261.

[63] P. Coleman. *Introduction to Many-Body Physics*. 1st ed. Cambridge University Press, 2015. DOI: 10.1017/CBO9781139020916.

[64] L. Bogoliuvob. “A NEW METHOD IN THE THEORY OF SUPERCONDUCTIVITY. I”. In: *JETP Letters* 34 (1957). bogoliubov1957, pp. 58–65.

[65] Y. Nambu. “Quasi-Particles and Gauge Invariance in the Theory of Superconductivity”. In: *Physical Review* 117 (1960), pp. 648–663. DOI: 10.1103/PhysRev.117.648.

[66] L. Gor’ Kov. “On The Energy Spectrum of Superconductors”. In: *J. Exptl. Theoret. Phys.* 34 (1958), p. 735.

[67] U. Eckern, G. Schön, and V. Ambegaokar. “Quantum dynamics of a superconducting tunnel junction”. In: *Physical Review B* 30 (1984), pp. 6419–6431. DOI: 10.1103/PhysRevB.30.6419.

[68] P. K. Tien and J. P. Gordon. “Multiphoton Process Observed in the Interaction of Microwave Fields with the Tunneling between Superconductor Films”. In: *Physical Review* 129 (1963), pp. 647–651. DOI: 10.1103/PhysRev.129.647.

[69] B. Josephson. “Possible new effects in superconductive tunnelling”. In: *Physics Letters* 1 (1962), pp. 251–253. DOI: 10.1016/0031-9163(62)91369-0.

[70] V. Ambegaokar and B. I. Halperin. “Voltage Due to Thermal Noise in the dc Josephson Effect”. In: *Physical Review Letters* 22 (1969), pp. 1364–1366. DOI: 10.1103/PhysRevLett.22.1364.

[71] D. Averin, Y. Nazarov, and A. Odintsov. "Incoherent tunneling of the cooper pairs and magnetic flux quanta in ultrasmall Josephson junctions". In: *Physica B: Condensed Matter* 165-166 (1990), pp. 945–946. DOI: 10.1016/S0921-4526(09)80058-6.

[72] G. Falci, V. Bubanja, and G. Schn. "Quasiparticle and Cooper pair tenneling in small capacitance Josephson junctions: Effects of the electromagnetic environment". In: *Zeitschrift fr Physik B Condensed Matter* 85 (1991), pp. 451–458. DOI: 10.1007/BF01307643.

[73] T. A. Fulton and G. J. Dolan. "Observation of single-electron charging effects in small tunnel junctions". In: *Physical Review Letters* 59 (1987), pp. 109–112. DOI: 10.1103/PhysRevLett.59.109.

[74] W. De Haas, J. De Boer, and G. Van Dën Berg. "The electrical resistance of gold, copper and lead at low temperatures". In: *Physica* 1 (1934), pp. 1115–1124. DOI: 10.1016/S0031-8914(34)80310-2.

[75] M. P. Sarachik, E. Corenzwit, and L. D. Longinotti. "Resistivity of Mo-Nb and Mo-Re Alloys Containing 1% Fe". In: *Physical Review* 135 (1964), A1041–A1045. DOI: 10.1103/PhysRev.135.A1041.

[76] J. Friedel. "ON SOME ELECTRICAL AND MAGNETIC PROPERTIES OF METALLIC SOLID SOLUTIONS". In: *Canadian Journal of Physics* 34 (1956), pp. 1190–1211. DOI: 10.1139/p56-134.

[77] F. Pawlek and K. Reichel. "Der Einfluß von Beimengungen auf die elektrische Leitfähigkeit von Kupfer: I. Die elektrische Leitfähigkeit des reinen Kupfers, ihr Maximalwert und ihre Beeinflussung durch Beimengungen". In: *International Journal of Materials Research* 47 (1956), pp. 347–356. DOI: 10.1515/ijmr-1956-470601.

[78] B. T. Matthias et al. "Magnetic Moment of Transition Metal Atoms in Dilute Solution and Their Effect on Superconducting Transition Temperature". In: *Physical Review Letters* 5 (1960), pp. 542–544. DOI: 10.1103/PhysRevLett.5.542.

[79] J. R. Schrieffer and P. A. Wolff. "Relation between the anderson and kondo hamiltonians". In: *Physical Review* 149 (1966). Number of pages: 0 Publisher: American Physical Society, pp. 491–492. DOI: 10.1103/PhysRev.149.491.

[80] M. M. Salomaa. "Schrieffer-wolff transformation for the anderson hamiltonian in a superconductor". In: *Physical Review B* 37 (1988). Number of pages: 0 Publisher: American Physical Society, pp. 9312–9317. DOI: 10.1103/PhysRevB.37.9312.

[81] Yu Luh. "Bound state in superconductors with paramagnetic impurities". In: *Acta Physica Sinica* 21 (1965), p. 75. DOI: 10.7498/aps.21.75.

[82] A. A. Abrikosov. *Methods of quantum field theory in statistical physics*. OCLC: 933978350. Beijing: Collaege Press, University of Beijing, 1998.

[83] R. Young, J. Ward, and F. Scire. "The Topografiner: An Instrument for Measuring Surface Microtopography". In: *Review of Scientific Instruments* 43 (1972), pp. 999–1011. DOI: 10.1063/1.1685846.

[84] R. Wiesendanger. *Scanning probe microscopy and spectroscopy: methods and applications*. Cambridge [England] ; New York: Cambridge University Press, 1994.

[85] J. C. Cuevas, A. Martín-Rodero, and A. L. Yeyati. "Hamiltonian approach to the transport properties of superconducting quantum point contacts". In: *Physical Review B* 54 (1996), pp. 7366–7379. DOI: 10.1103/PhysRevB.54.7366.

[86] M. Ruby et al. "Tunneling Processes into Localized Subgap States in Superconductors". In: *Physical Review Letters* 115 (2015), p. 087001. DOI: 10.1103/PhysRevLett.115.087001.

[87] D. Averin and A. Bardas. "ac Josephson Effect in a Single Quantum Channel". In: *Physical Review Letters* 75 (1995), pp. 1831–1834. DOI: 10.1103/PhysRevLett.75.1831.

[88] E. Scheer et al. "Proximity Effect and Multiple Andreev Reflections in Gold Atomic Contacts". In: *Physical Review Letters* 86 (2001), pp. 284–287. DOI: 10.1103/PhysRevLett.86.284.

[89] J. Senkpiel et al. "Extracting transport channel transmissions in scanning tunneling microscopy using superconducting excess current". In: *Physical Review B* 105 (2022), p. 165401. DOI: 10.1103/PhysRevB.105.165401.

[90] S. Karan et al. "Superconducting quantum interference at the atomic scale". In: *Nature Physics* 18 (2022), pp. 893–898. DOI: 10.1038/s41567-022-01644-6.

[91] O. Naaman, W. Teizer, and R. C. Dynes. "Fluctuation Dominated Josephson Tunneling with a Scanning Tunneling Microscope". In: *Physical Review Letters* 87 (2001), p. 097004. DOI: 10.1103/PhysRevLett.87.097004.

[92] S.-H. Ji et al. "High-Resolution Scanning Tunneling Spectroscopy of Magnetic Impurity Induced Bound States in the Superconducting Gap of Pb Thin Films". In: *Physical Review Letters* 100 (2008), p. 226801. DOI: 10.1103/PhysRevLett.100.226801.

[93] M. Ruby et al. "End States and Subgap Structure in Proximity-Coupled Chains of Magnetic Adatoms". In: *Physical Review Letters* 115 (2015), p. 197204. DOI: 10.1103/PhysRevLett.115.197204.

[94] Y. Peng et al. "Strong Localization of Majorana End States in Chains of Magnetic Adatoms". In: *Physical Review Letters* 114 (2015), p. 106801. DOI: 10.1103/PhysRevLett.114.106801.

[95] R. Pawlak et al. "Probing atomic structure and Majorana wavefunctions in mono-atomic Fe chains on superconducting Pb surface". In: *npj Quantum Information* 2 (2016), p. 16035. DOI: 10.1038/npjqi.2016.35.

[96] M. Ruby et al. "Exploring a Proximity-Coupled Co Chain on Pb(110) as a Possible Majorana Platform". In: *Nano Letters* 17 (2017), pp. 4473–4477. DOI: 10.1021/acs.nanolett.7b01728.

[97] L. Schneider et al. "Topological Shiba bands in artificial spin chains on superconductors". In: *Nature Physics* 17 (2021), pp. 943–948. DOI: 10.1038/s41567-021-01234-y.

[98] C. Mier et al. "Atomic manipulation of in-gap states in the Bi 2 Pd superconductor". In: *Physical Review B* 104 (2021), p. 045406. DOI: 10.1103/PhysRevB.104.045406.

[99] L. Schneider et al. "Atomic-scale spin-polarization maps using functionalized superconducting probes". In: *Science Advances* 7 (2021), eabd7302. DOI: 10.1126/sciadv.abd7302.

[100] N. Hatter et al. "Magnetic anisotropy in Shiba bound states across a quantum phase transition". In: *Nature Communications* 6 (2015), p. 8988. DOI: 10.1038/ncomms9988.

[101] N. Hatter et al. "Scaling of Yu-Shiba-Rusinov energies in the weak-coupling Kondo regime". In: *Nature Communications* 8 (2017), p. 2016. DOI: 10.1038/s41467-017-02277-7.

[102] L. Farinacci et al. "Interfering Tunneling Paths through Magnetic Molecules on Superconductors: Asymmetries of Kondo and Yu-Shiba-Rusinov Resonances". In: *Physical Review Letters* 125 (2020), p. 256805. DOI: 10.1103/PhysRevLett.125.256805.

[103] S. Kezilebieke et al. "Coupled Yu–Shiba–Rusinov States in Molecular Dimers on NbSe $_2$". In: *Nano Letters* 18 (2018), pp. 2311–2315. DOI: 10.1021/acs.nanolett.7b05050.

[104] J. Brand et al. "Electron and Cooper-pair transport across a single magnetic molecule explored with a scanning tunneling microscope". In: *Physical Review B* 97 (2018), p. 195429. DOI: 10.1103/PhysRevB.97.195429.

[105] S. Kezilebieke et al. "Observation of Coexistence of Yu-Shiba-Rusinov States and Spin-Flip Excitations". In: *Nano Letters* 19 (2019), pp. 4614–4619. DOI: 10.1021/acs.nanolett.9b01583.

[106] L. Malavolti et al. "Tunable Spin–Superconductor Coupling of Spin 1/2 Vanadyl Phthalocyanine Molecules". In: *Nano Letters* 18 (2018), pp. 7955–7961. DOI: 10.1021/acs.nanolett.8b03921.

[107] C. Rubio-Verdú et al. "Coupled Yu-Shiba-Rusinov States Induced by a Many-Body Molecular Spin on a Superconductor". In: *Physical Review Letters* 126 (2021), p. 017001. DOI: 10.1103/PhysRevLett.126.017001.

[108] S. Y. Song et al. "Yu-Shiba-Rusinov bound states studied by tuning the electron density at the Fermi energy". In: *Physical Review B* 103 (2021), p. 214509. DOI: 10.1103/PhysRevB.103.214509.

[109] L. Cornils et al. “Spin-Resolved Spectroscopy of the Yu-Shiba-Rusinov States of Individual Atoms”. In: *Physical Review Letters* 119 (2017), p. 197002. DOI: 10.1103/PhysRevLett.119.197002.

[110] A. Kamlapure et al. “Engineering the spin couplings in atomically crafted spin chains on an elemental superconductor”. In: *Nature Communications* 9 (2018), p. 3253. DOI: 10.1038/s41467-018-05701-8.

[111] J. Senkpiel et al. “Robustness of Yu-Shiba-Rusinov resonances in the presence of a complex superconducting order parameter”. In: *Physical Review B* 100 (2019), p. 014502. DOI: 10.1103/PhysRevB.100.014502.

[112] S. Y. Song et al. “Visualization of Local Magnetic Moments Emerging from Impurities in Hund’s Metal States of FeSe”. In: *Physical Review Letters* 124 (2020), p. 117001. DOI: 10.1103/PhysRevLett.124.117001.

[113] X. Yang et al. “Observation of short-range Yu-Shiba-Rusinov states with three-fold symmetry in layered superconductor 2H-NbSe $_2$”. In: *Nanoscale* 12 (2020), pp. 8174–8179. DOI: 10.1039/D0NR01383H.

[114] H. Huang et al. “Quantum phase transitions and the role of impurity-substrate hybridization in Yu-Shiba-Rusinov states”. In: *Communications Physics* 3 (2020), p. 199. DOI: 10.1038/s42005-020-00469-0.

[115] H. Huang et al. “Tunnelling dynamics between superconducting bound states at the atomic limit”. In: *Nature Physics* 16 (2020), pp. 1227–1231. DOI: 10.1038/s41567-020-0971-0.

[116] H. Ding et al. “Tuning interactions between spins in a superconductor”. In: *Proceedings of the National Academy of Sciences* 118 (2021), e2024837118. DOI: 10.1073/pnas.2024837118.

[117] P. Beck et al. “Spin-orbit coupling induced splitting of Yu-Shiba-Rusinov states in antiferromagnetic dimers”. In: *Nature Communications* 12 (2021), p. 2040. DOI: 10.1038/s41467-021-22261-6.

[118] D. Chatzopoulos et al. “Spatially dispersing Yu-Shiba-Rusinov states in the unconventional superconductor FeTe0.55Se0.45”. In: *Nature Communications* 12 (2021), p. 298. DOI: 10.1038/s41467-020-20529-x.

[119] H. Huang et al. “Spin-dependent tunneling between individual superconducting bound states”. In: *Physical Review Research* 3 (2021), p. L032008. DOI: 10.1103/PhysRevResearch.3.L032008.

[120] D. Wang et al. “Spin-Polarized Yu-Shiba-Rusinov States in an Iron-Based Superconductor”. In: *Physical Review Letters* 126 (2021), p. 076802. DOI: 10.1103/PhysRevLett.126.076802.

[121] A. Kamlapure et al. “Correlation of Yu–Shiba–Rusinov States and Kondo Resonances in Artificial Spin Arrays on an s-Wave Superconductor”. In: *Nano Letters* 21 (2021), pp. 6748–6755. DOI: 10.1021/acs.nanolett.1c00387.

[122] F. Küster et al. "Long range and highly tunable interaction between local spins coupled to a superconducting condensate". In: *Nature Communications* 12 (2021), p. 6722. DOI: 10.1038/s41467-021-26802-x.

[123] M. Ruby et al. "Orbital Picture of Yu-Shiba-Rusinov Multiplets". In: *Physical Review Letters* 117 (2016), p. 186801. DOI: 10.1103/PhysRevLett.117.186801.

[124] D.-J. Choi et al. "Mapping the orbital structure of impurity bound states in a superconductor". In: *Nature Communications* 8 (2017), p. 15175. DOI: 10.1038/ncomms15175.

[125] M. Etzkorn et al. *Mapping of Yu-Shiba-Rusinov states from an extended scatterer*. Version Number: 1. 2018. DOI: 10.48550/ARXIV.1807.00646.

[126] E. Liebhaber et al. "Yu–Shiba–Rusinov States in the Charge-Density Modulated Superconductor NbSe $_2$". In: *Nano Letters* 20 (2020), pp. 339–344. DOI: 10.1021/acs.nanolett.9b03988.

[127] P. O. Sprau et al. "Discovery of orbital-selective Cooper pairing in FeSe". In: *Science* 357 (2017), pp. 75–80. DOI: 10.1126/science.aal1575.

[128] R. Sharma et al. "Momentum-resolved superconducting energy gaps of Sr $_2$ RuO $_4$ from quasiparticle interference imaging". In: *Proceedings of the National Academy of Sciences* 117 (2020), pp. 5222–5227. DOI: 10.1073/pnas.1916463117.

[129] Y. Imai et al. "Superconductivity at 5.4 K in -Bi $_2$ Pd". In: *Journal of the Physical Society of Japan* 81 (2012), p. 113708. DOI: 10.1143/JPSJ.81.113708.

[130] E. Herrera et al. "Magnetic field dependence of the density of states in the multiband superconductor Bi 2 Pd". In: *Physical Review B* 92 (2015), p. 054507. DOI: 10.1103/PhysRevB.92.054507.

[131] J. Kačmarčík et al. "Single-gap superconductivity in B i 2 Pd". In: *Physical Review B* 93 (2016), p. 144502. DOI: 10.1103/PhysRevB.93.144502.

[132] M. M. Ugeda et al. "Characterization of collective ground states in single-layer NbSe2". In: *Nature Physics* 12 (2016), pp. 92–97. DOI: 10.1038/nphys3527.

[133] A. Weismann et al. "Seeing the Fermi Surface in Real Space by Nanoscale Electron Focusing". In: *Science* 323 (2009), pp. 1190–1193. DOI: 10.1126/science.1168738.

[134] M. Rouco, F. S. Bergeret, and I. V. Tokatly. "Gap inversion in quasi-one-dimensional Andreev crystals". In: *Physical Review B* 103 (2021), p. 064505. DOI: 10.1103/PhysRevB.103.064505.

[135] M. Rouco, F. S. Bergeret, and I. V. Tokatly. "Spectral properties of Andreev crystals". In: *Physical Review B* 104 (2021), p. 064506. DOI: 10.1103/PhysRevB.104.064506.

[136] M. Ruby et al. "Wave-Function Hybridization in Yu-Shiba-Rusinov Dimers". In: *Physical Review Letters* 120 (2018), p. 156803. DOI: 10.1103/PhysRevLett.120.156803.

[137] D.-J. Choi et al. “Influence of Magnetic Ordering between Cr Adatoms on the Yu-Shiba-Rusinov States of the Bi 2 Pd Superconductor”. In: *Physical Review Letters* 120 (2018), p. 167001. DOI: 10.1103/PhysRevLett.120.167001.

[138] H. Kim et al. “Toward tailoring Majorana bound states in artificially constructed magnetic atom chains on elemental superconductors”. In: *Science Advances* 4 (2018), eaar5251. DOI: 10.1126/sciadv.aar5251.

[139] D. K. Morr and N. A. Stavropoulos. “Quantum interference between impurities: Creating novel many-body states in s -wave superconductors”. In: *Physical Review B* 67 (2003), p. 020502. DOI: 10.1103/PhysRevB.67.020502.

[140] B. Nyári et al. “Relativistic first-principles theory of Yu-Shiba-Rusinov states applied to Mn adatoms and Mn dimers on Nb(110)”. In: *Physical Review B* 104 (2021), p. 235426. DOI: 10.1103/PhysRevB.104.235426.

[141] M. E. Flatté and D. E. Reynolds. “Local spectrum of a superconductor as a probe of interactions between magnetic impurities”. In: *Physical Review B* 61 (2000), pp. 14810–14814. DOI: 10.1103/PhysRevB.61.14810.

[142] N. Y. Yao et al. “Enhanced Antiferromagnetic Exchange between Magnetic Impurities in a Superconducting Host”. In: *Physical Review Letters* 113 (2014), p. 087202. DOI: 10.1103/PhysRevLett.113.087202.

[143] S. Trivini et al. “Diluted Yu-Shiba-Rusinov arrays on the anisotropic superconductor Bi 2 Pd”. In: *Physical Review B* 110 (2024), p. 235405. DOI: 10.1103/PhysRevB.110.235405.

[144] A. Skurativska et al. *Robust spin polarization of yu-shiba-rusinov states in superconductor/ferromagnetic insulator heterostructures*. arXiv: 2302.13864 [cond-mat.supr-con]. 2023.

[145] I. Affleck, J.-S. Caux, and A. M. Zagoskin. “Andreev scattering and Josephson current in a one-dimensional electron liquid”. In: *Physical Review B* 62 (2000), pp. 1433–1445. DOI: 10.1103/PhysRevB.62.1433.

[146] E. Vecino, A. Martín-Rodero, and A. L. Yeyati. “Josephson current through a correlated quantum level: Andreev states and ¡span class=”nocase”¿¡/span¿ junction behavior”. In: *Physical Review B* 68 (2003). Number of pages: 9 Publisher: American Physical Society, p. 035105. DOI: 10.1103/PhysRevB.68.035105.

[147] M. Pita-Vidal et al. “Direct manipulation of a superconducting spin qubit strongly coupled to a transmon qubit”. In: *Nature Physics* (2023). DOI: 10.1038/s41567-023-02071-x.

[148] M. Žonda et al. “Generalized atomic limit of a double quantum dot coupled to superconducting leads”. In: *Physical Review B* 107 (2023), p. 115407. DOI: 10.1103/PhysRevB.107.115407.

[149] T. Machida, Y. Nagai, and T. Hanaguri. “Zeeman effects on Yu-Shiba-Rusinov states”. In: 4 (2022). Number of pages: 12 Publisher: American Physical Society, p. 033182. DOI: 10.1103/PhysRevResearch.4.033182.

[150] M. Uldemolins et al. *Interaction-driven quantum phase transition of a single magnetic impurity in Fe(Se,Te).* arXiv:2310.06030 [cond-mat]. 2023.

[151] K. D. Usadel. "Generalized diffusion equation for superconducting alloys". In: *Physical Review Letters* 25 (1970). Number of pages: 0 Publisher: American Physical Society, pp. 507–509. DOI: 10.1103/PhysRevLett.25.507.

[152] F. Zhou et al. "Density of states in superconductor-normal metal-superconductor junctions". In: *Journal of Low Temperature Physics* 110 (1998), pp. 841–850. DOI: 10.1023/A:1022628927203.

[153] H. le Sueur et al. "Phase controlled superconducting proximity effect probed by tunneling spectroscopy". In: *Physical Review Letters* 100 (2008). Number of pages: 4 Publisher: American Physical Society, p. 197002. DOI: 10.1103/PhysRevLett.100.197002.

[154] A. K. Gupta et al. "Anomalous density of states in a metallic film in proximity with a superconductor". In: *Physical Review B* 69 (2004). Number of pages: 4 Publisher: American Physical Society, p. 104514. DOI: 10.1103/PhysRevB.69.104514.

[155] P. Wei et al. "Superconductivity in the surface state of noble metal gold and its fermi level tuning by EuS dielectric". In: *Physical Review Letters* 122 (2019). Number of pages: 6 Publisher: American Physical Society, p. 247002. DOI: 10.1103/PhysRevLett.122.247002.

[156] L. Serrier-Garcia et al. "Scanning Tunneling Spectroscopy Study of the Proximity Effect in a Disordered Two-Dimensional Metal". In: *Physical Review Letters* 110 (2013), p. 157003. DOI: 10.1103/PhysRevLett.110.157003.

[157] L. Schneider et al. "Precursors of Majorana modes and their length-dependent energy oscillations probed at both ends of atomic Shiba chains". In: *Nature Nanotechnology* 17 (2022), pp. 384–389. DOI: 10.1038/s41565-022-01078-4.

[158] J.-C. Liu et al. *Proximity-induced superconductivity in atomically precise nanographene.* tex.copyright: Creative Commons Attribution 4.0 International. 2022. DOI: 10.48550/ARXIV.2202.00460.

[159] A. Gourdon. "On-Surface Covalent Coupling in Ultrahigh Vacuum". In: *Angewandte Chemie International Edition* 47 (2008), pp. 6950–6953. DOI: 10.1002/anie.200802229.

[160] Y. Zhao et al. "Quantum nanomagnets in on-surface metal-free porphyrin chains". In: *Nature Chemistry* (2022). DOI: 10.1038/s41557-022-01061-5.

[161] S. Mishra et al. "Collective all-carbon magnetism in triangulene dimers**". In: *Angewandte Chemie International Edition* 59 (2020), pp. 12041–12047.

[162] S. Mishra et al. "Observation of fractional edge excitations in nanographene spin chains". In: *Nature* 598 (2021), pp. 287–292. DOI: 10.1038/s41586-021-03842-3.

[163] J. Hieulle et al. “On-surface synthesis and collective spin excitations of a triangulene-based nanostar”. In: *Angewandte Chemie International Edition* 60 (2021), pp. 25224–25229. DOI: https://doi.org/10.1002/anie.202108301.

[164] J. Ortuzar et al. “Theory of a single magnetic impurity on a thin metal film in proximity to a superconductor”. In: *Physical Review B* 108 (2023), p. 024511. DOI: 10.1103/PhysRevB.108.024511.

[165] B. W. Heinrich et al. “Protection of excited spin states by a superconducting energy gap”. In: *Nature Physics* 9 (2013), pp. 765–768. DOI: 10.1038/nphys2794.

[166] B. W. Heinrich et al. “Tuning the Magnetic Anisotropy of Single Molecules”. In: *Nano Letters* 15 (2015), pp. 4024–4028. DOI: 10.1021/acs.nanolett.5b00987.

[167] P. G. de Gennes and D. Saint-James. “Elementary excitations in the vicinity of a normal metal-superconducting metal contact”. In: *Physics Letters* 4 (1963). Place: Country unknown/Code not available. DOI: 10.1016/0031-9163(63)90148-3.

[168] I. O. Kulik. “Macroscopic quantization and the proximity effect in s-n-s junctions”. In: *Soviet Journal of Experimental and Theoretical Physics* 30 (1969). tex.adsnote: Provided by the SAO/NASA Astrophysics Data System, p. 944.

[169] L. Schneider et al. “Proximity superconductivity in atom-by-atom crafted quantum dots”. In: *Nature* 621 (2023), pp. 60–65. DOI: 10.1038/s41586-023-06312-0.

[170] L. Schneider et al. *Proximity superconductivity in atom-by-atom crafted quantum dots*. tex.copyright: arXiv.org perpetual, non-exclusive license. 2022. DOI: 10.48550/ARXIV.2212.00657.

[171] G. Deutscher. “Andreev–Saint-James reflections: A probe of cuprate superconductors”. In: *Reviews of modern physics* 77 (2005). Publisher: APS, p. 109.

[172] P. G. DE GENNES. “Boundary effects in superconductors”. In: *Reviews of Modern Physics* 36 (1964). Number of pages: 0 Publisher: American Physical Society, pp. 225–237. DOI: 10.1103/RevModPhys.36.225.

[173] W. L. McMillan. “Theory of superconductor—normal-metal interfaces”. In: *Physical Review* 175 (1968). Number of pages: 0 Publisher: American Physical Society, pp. 559–568. DOI: 10.1103/PhysRev.175.559.

[174] G. Kieselmann. “Self-consistent calculations of the pair potential and the tunneling density of states in proximity contacts”. In: *Physical Review B* 35 (1987). Number of pages: 0 Publisher: American Physical Society, pp. 6762–6770. DOI: 10.1103/PhysRevB.35.6762.

[175] G. B. Arnold. “Theory of thin proximity-effect sandwiches”. In: *Physical Review B* 18 (1978). Number of pages: 0 Publisher: American Physical Society, pp. 1076–1100. DOI: 10.1103/PhysRevB.18.1076.

[176] J. Rowell and W. McMillan. “Electron interference in a normal metal induced by superconducting contracts”. In: *Physical Review Letters* 16 (1966). Publisher: APS, p. 453.

[177] W. Tomasch. “Geometrical resonance and boundary effects in tunneling from superconducting In”. In: *Physical Review Letters* 16 (1966). Publisher: APS, p. 16.

[178] C. Janvier et al. “Coherent manipulation of Andreev states in superconducting atomic contacts”. In: *Science* 349 (2015), pp. 1199–1202. DOI: 10.1126/science.aab2179.

[179] M. Hays et al. “Coherent manipulation of an Andreev spin qubit”. In: *Science* 373 (2021), pp. 430–433. DOI: 10.1126/science.abf0345.

[180] L. Bretheau et al. “Exciting Andreev pairs in a superconducting atomic contact”. In: *Nature* 499 (2013), pp. 312–315. DOI: 10.1038/nature12315.

[181] L. Grill et al. “Nano-architectures by covalent assembly of molecular building blocks”. In: *Nature Nanotechnology* 2 (2007), pp. 687–691. DOI: 10.1038/nnano.2007.346.

[182] N. Pavliček et al. “Synthesis and characterization of triangulene”. In: *Nature Nanotechnology* 12 (2017), pp. 308–311. DOI: 10.1038/nnano.2016.305.

[183] S. Mishra et al. “Synthesis and Characterization of -Extended Triangulene”. In: *Journal of the American Chemical Society* 141 (2019), pp. 10621–10625. DOI: 10.1021/jacs.9b05319.

[184] M. Vilas-Varela et al. “On-Surface Synthesis and Characterization of a High-Spin Aza-[5]-Triangulene”. In: *Angewandte Chemie International Edition* 62 (2023), e202307884. DOI: 10.1002/anie.202307884.

[185] M. Hagiwara et al. “Observation of S =1/2 degrees of freedom in an S =1 linear-chain Heisenberg antiferromagnet”. In: *Physical Review Letters* 65 (1990), pp. 3181–3184. DOI: 10.1103/PhysRevLett.65.3181.

[186] H. Schmid et al. “Quantum Yu-Shiba-Rusinov dimers”. In: *Physical Review B* 105 (2022), p. 235406. DOI: 10.1103/PhysRevB.105.235406.

[187] D. Loss and D. P. DiVincenzo. “Quantum computation with quantum dots”. In: *Physical Review A* 57 (1998), pp. 120–126. DOI: 10.1103/PhysRevA.57.120.

[188] C. Kloeffel and D. Loss. “Prospects for Spin-Based Quantum Computing in Quantum Dots”. In: *Annual Review of Condensed Matter Physics* 4 (2013), pp. 51–81. DOI: 10.1146/annurev-conmatphys-030212-184248.

[189] H. Drexler et al. “Spectroscopy of Quantum Levels in Charge-Tunable InGaAs Quantum Dots”. In: *Physical Review Letters* 73 (1994), pp. 2252–2255. DOI: 10.1103/PhysRevLett.73.2252.

[190] S. Nadj-Perge et al. “Spin–orbit qubit in a semiconductor nanowire”. In: *Nature* 468 (2010), pp. 1084–1087. DOI: 10.1038/nature09682.

[191] J. W. G. Van Den Berg et al. “Fast Spin-Orbit Qubit in an Indium Antimonide Nanowire”. In: *Physical Review Letters* 110 (2013), p. 066806. DOI: 10.1103/PhysRevLett.110.066806.

[192] M. Scheibner et al. “Optically mapping the electronic structure of coupled quantum dots”. In: *Nature Physics* 4 (2008), pp. 291–295. DOI: 10.1038/nphys882.

[193] A. Gaita-Ariño et al. “Molecular spins for quantum computation”. In: *Nature Chemistry* 11 (2019), pp. 301–309. DOI: 10.1038/s41557-019-0232-y.

[194] N. E. Bonesteel, D. Stepanenko, and D. P. DiVincenzo. “Anisotropic Spin Exchange in Pulsed Quantum Gates”. In: *Physical Review Letters* 87 (2001), p. 207901. DOI: 10.1103/PhysRevLett.87.207901.

[195] G. Burkard and D. Loss. “Cancellation of Spin-Orbit Effects in Quantum Gates Based on the Exchange Coupling in Quantum Dots”. In: *Physical Review Letters* 88 (2002), p. 047903. DOI: 10.1103/PhysRevLett.88.047903.

[196] W. A. Coish and D. Loss. “Hyperfine interaction in a quantum dot: Non-Markovian electron spin dynamics”. In: *Physical Review B* 70 (2004), p. 195340. DOI: 10.1103/PhysRevB.70.195340.

[197] J. Fischer et al. “Spin decoherence of a heavy hole coupled to nuclear spins in a quantum dot”. In: *Physical Review B* 78 (2008), p. 155329. DOI: 10.1103/PhysRevB.78.155329.

[198] S. Baumann et al. “Electron paramagnetic resonance of individual atoms on a surface”. In: *Science* 350 (2015), pp. 417–420. DOI: 10.1126/science.aac8703.

[199] F. W. Jayatilaka, M. R. Galpin, and D. E. Logan. “Two-channel Kondo physics in tunnel-coupled double quantum dots”. In: *Physical Review B* 84 (2011), p. 115111. DOI: 10.1103/PhysRevB.84.115111.

[200] W. Chang et al. “Tunneling spectroscopy of quasiparticle bound states in a spinful josephson junction”. In: *Physical Review Letters* 110 (2013). Number of pages: 5 Publisher: American Physical Society, p. 217005. DOI: 10.1103/PhysRevLett.110.217005.

[201] G. Kirš šanskas et al. “Yu-Shiba-Rusinov states in phase-biased superconductor–quantum dot–superconductor junctions”. In: *Physical Review B* 92 (2015). Number of pages: 12 Publisher: American Physical Society, p. 235422. DOI: 10.1103/PhysRevB.92.235422.

[202] Z. Scherübl et al. “Large spatial extension of the zero-energy Yu–Shiba–Rusinov state in a magnetic field”. In: *Nature Communications* 11 (2020), p. 1834. DOI: 10.1038/s41467-020-15322-9.

[203] A. Jellinggaard et al. “Tuning Yu-Shiba-Rusinov states in a quantum dot”. In: *Physical Review B* 94 (2016). Number of pages: 8 Publisher: American Physical Society, p. 064520. DOI: 10.1103/PhysRevB.94.064520.

[204] E. J. H. Lee et al. “Zero-bias anomaly in a nanowire quantum dot coupled to superconductors”. In: *Physical Review Letters* 109 (2012). Number of pages: 5 Publisher: American Physical Society, p. 186802. DOI: 10.1103/PhysRevLett.109.186802.

[205] A. Bargerbos et al. “Singlet-doublet transitions of a quantum dot josephson junction detected in a transmon circuit”. In: *PRX Quantum* 3 (2022). Number of pages: 14 Publisher: American Physical Society, p. 030311. DOI: 10.1103/PRXQuantum.3.030311.

[206] D. V. Averin and Y. V. Nazarov. “Single-electron charging of a superconducting island”. In: *Physical Review Letters* 69 (1992), pp. 1993–1996. DOI: 10.1103/PhysRevLett.69.1993.

[207] H. Grabert and M. H. Devoret, eds. *Single Charge Tunneling*. Vol. 294. NATO ASI Series. Boston, MA: Springer US, 1992. DOI: 10.1007/978-1-4757-2166-9.

[208] B. L. Altshuler, P. A. Lee, and R. A. Webb. *Mesoscopic Phenomena in Solids*. Modern Problems in Condensed Matter Sciences. Burlington: Elsevier Science, 1991.

[209] B. van Heck, R. M. Lutchyn, and L. I. Glazman. “Conductance of a proximitized nanowire in the Coulomb blockade regime”. In: *Physical Review B* 93 (2016), p. 235431. DOI: 10.1103/PhysRevB.93.235431.

[210] T. Dittrich, ed. *Quantum transport and dissipation*. Weinheim ; New York: Wiley-VCH, 1998.

[211] K. A. Matveev, L. I. Glazman, and R. I. Shekhter. “Effects of charge parity in tunneling through a superconducting grain”. In: *Modern Physics Letters B* 08 (1994), pp. 1007–1026. DOI: 10.1142/S0217984994001011.

[212] Y. Zhang et al. “Giant phonon-induced conductance in scanning tunnelling spectroscopy of gate-tunable graphene”. In: *Nature Physics* 4 (2008), pp. 627–630. DOI: 10.1038/nphys1022.

[213] A. Van Bommel, J. Crombeen, and A. Van Tooren. “LEED and Auger electron observations of the SiC(0001) surface”. In: *Surface Science* 48 (1975), pp. 463–472. DOI: 10.1016/0039-6028(75)90419-7.

[214] W. A. De Heer et al. “Large area and structured epitaxial graphene produced by confinement controlled sublimation of silicon carbide”. In: *Proceedings of the National Academy of Sciences* 108 (2011), pp. 16900–16905. DOI: 10.1073/pnas.1105113108.

[215] I. Forbeaux, J.-M. Themlin, and J.-M. Debever. “Heteroepitaxial graphite on 6 H SiC (0001) : Interface formation through conduction-band electronic structure”. In: *Physical Review B* 58 (1998), pp. 16396–16406. DOI: 10.1103/PhysRevB.58.16396.

[216] K. V. Emtsev et al. “Ambipolar doping in quasifree epitaxial graphene on SiC(0001) controlled by Ge intercalation”. In: *Physical Review B* 84 (2011), p. 125423. DOI: 10.1103/PhysRevB.84.125423.

[217] U. Starke et al. “Engineering the electronic structure of epitaxial graphene by transfer doping and atomic intercalation”. In: *MRS Bulletin* 37 (2012), pp. 1177–1186. DOI: 10.1557/mrs.2012.272.

[218] C. Brun et al. “Dynamical Coulomb Blockade Observed in Nanosized Electrical Contacts”. In: *Physical Review Letters* 108 (2012), p. 126802. DOI: 10.1103/PhysRevLett.108.126802.

[219] E. Cortés-del Río et al. “Shaping Graphene Superconductivity with Nanometer Precision”. In: *Small* 20 (2024), p. 2308439. DOI: 10.1002/smll.202308439.

[220] J. Senkpiel et al. “Dynamical Coulomb Blockade as a Local Probe for Quantum Transport”. In: *Physical Review Letters* 124 (2020). Publisher: American Physical Society, p. 156803. DOI: 10.1103/PhysRevLett.124.156803.

[221] B. Jäck et al. “Critical Josephson current in the dynamical Coulomb blockade regime”. In: *Physical Review B* 93 (2016). Publisher: American Physical Society, p. 020504. DOI: 10.1103/PhysRevB.93.020504.

[222] M. Müller et al. “Plasticity of single-atom Pb junctions”. In: *Physical Review B* 93 (2016), p. 235402. DOI: 10.1103/PhysRevB.93.235402.

[223] M. Amman et al. “Analytic solution for the current-voltage characteristic of two mesoscopic tunnel junctions coupled in series”. In: *Physical Review B* 43 (1991), pp. 1146–1149. DOI: 10.1103/PhysRevB.43.1146.

[224] A. E. Hanna and M. Tinkham. “Variation of the Coulomb staircase in a two-junction system by fractional electron charge”. In: *Physical Review B* 44 (1991), pp. 5919–5922. DOI: 10.1103/PhysRevB.44.5919.

[225] J. Kim et al. “Universal quenching of the superconducting state of two-dimensional nanosize Pb-island structures”. In: *Physical Review B* 84 (2011), p. 014517. DOI: 10.1103/PhysRevB.84.014517.

[226] S. Vlaic et al. “Superconducting parity effect across the Anderson limit”. In: *Nature Communications* 8 (2017), p. 14549. DOI: 10.1038/ncomms14549.

[227] N. F. Q. Yuan and L. Fu. “Supercurrent diode effect and finite-momentum superconductors”. In: *Proceedings of the National Academy of Sciences* 119 (2022), e2119548119. DOI: 10.1073/pnas.2119548119.

[228] R.-F. Wang et al. “Observation of Coulomb blockade and Coulomb staircases in superconducting Pr 0.8 Sr 0.2 NiO 2 films”. In: *Physical Review B* 107 (2023), p. 115411. DOI: 10.1103/PhysRevB.107.115411.

[229] I.-P. Hong et al. “Coulomb blockade phenomena observed in supported metallic nanoislands”. In: *Frontiers in Physics* 1 (2013). DOI: 10.3389/fphy.2013.00013.

[230] F. Braun and J. Von Delft. “Fixed- N Superconductivity: The Crossover from the Bulk to the Few-Electron Limit”. In: *Physical Review Letters* 81 (1998), pp. 4712–4715. DOI: 10.1103/PhysRevLett.81.4712.

[231] R. Richardson. "A restricted class of exact eigenstates of the pairing-force Hamiltonian". In: *Physics Letters* 3 (1963), pp. 277–279. DOI: 10.1016/0031-9163(63)90259-2.

[232] R. Richardson. "Application to the exact theory of the pairing model to some even isotopes of lead". In: *Physics Letters* 5 (1963), pp. 82–84. DOI: 10.1016/S0375-9601(63)80039-0.

[233] J. Dukelsky and G. Sierra. "Density Matrix Renormalization Group Study of Ultrasmall Superconducting Grains". In: *Physical Review Letters* 83 (1999), pp. 172–175. DOI: 10.1103/PhysRevLett.83.172.

[234] J. C. Estrada Saldaña et al. "Excitations in a superconducting Coulombic energy gap". In: *Nature communications* 13 (2022), p. 2243. DOI: 10.1038/s41467-022-29634-5.

[235] B. Jankó, A. Smith, and V. Ambegaokar. "BCS superconductivity with fixed number parity". In: *Physical Review B* 50 (1994), pp. 1152–1161. DOI: 10.1103/PhysRevB.50.1152.

[236] D. Golubev and A. Zaikin. "Parity effect and thermodynamics of canonical superconducting ensembles". In: *Physics Letters A* 195 (1994), pp. 380–388. DOI: 10.1016/0375-9601(94)90046-9.

[237] K. Tanabe, K. Sugawara-Tanabe, and H. Mang. "Theory of the cranked temperature-dependent Hartree-Fock-Bogoliubov approximation and parity projected statistics". In: *Nuclear Physics A* 357 (1981), pp. 20–44. DOI: 10.1016/0375-9474(81)90624-2.

[238] G. Sierra et al. "Exact study of the effect of level statistics in ultrasmall superconducting grains". In: *Physical Review B* 61 (2000), R11890–R11893. DOI: 10.1103/PhysRevB.61.R11890.

[239] J. Perenboom, P. Wyder, and F. Meier. "Electronic properties of small metallic particles". In: *Physics Reports* 78 (1981), pp. 173–292. DOI: 10.1016/0370-1573(81)90194-0.

[240] M. Ruby et al. "Experimental Demonstration of a Two-Band Superconducting State for Lead Using Scanning Tunneling Spectroscopy". In: *Physical Review Letters* 114 (2015), p. 157001. DOI: 10.1103/PhysRevLett.114.157001.

[241] T. M. Eiles, J. M. Martinis, and M. H. Devoret. "Even-odd asymmetry of a superconductor revealed by the Coulomb blockade of Andreev reflection". In: *Physical Review Letters* 70 (1993), pp. 1862–1865. DOI: 10.1103/PhysRevLett.70.1862.

[242] J. M. Hergenrother, M. T. Tuominen, and M. Tinkham. "Charge transport by Andreev reflection through a mesoscopic superconducting island". In: *Physical Review Letters* 72 (1994), pp. 1742–1745. DOI: 10.1103/PhysRevLett.72.1742.

[243] S. Skalski, O. Betbeder-Matibet, and P. R. Weiss. "Properties of Superconducting Alloys Containing Paramagnetic Impurities". In: *Physical Review* 136 (1964), A1500–A1518. DOI: 10.1103/PhysRev.136.A1500.

[244] F. Herman and R. Hlubina. "Microscopic interpretation of the Dynes formula for the tunneling density of states". In: *Physical Review B* 94 (2016), p. 144508. DOI: 10.1103/PhysRevB.94.144508.

[245] A. Abrikosov and L. Gor'kov. "Contribution to the Theory of Superconducting Alloys With Paramagnetic Impurities". In: *Soviet Phys.-JETP* 12 (1961). abrikosov1961.

[246] C. T. Black, D. C. Ralph, and M. Tinkham. "Spectroscopy of the Superconducting Gap in Individual Nanometer-Scale Aluminum Particles". In: *Physical Review Letters* 76 (1996), pp. 688–691. DOI: 10.1103/PhysRevLett.76.688.

[247] R. C. Dynes, V. Narayanamurti, and J. P. Garno. "Direct Measurement of Quasiparticle-Lifetime Broadening in a Strong-Coupled Superconductor". In: *Physical Review Letters* 41 (1978), pp. 1509–1512. DOI: 10.1103/PhysRevLett.41.1509.

[248] J. Von Delft et al. "Parity-Affected Superconductivity in Ultrasmall Metallic Grains". In: *Physical Review Letters* 77 (1996), pp. 3189–3192. DOI: 10.1103/PhysRevLett.77.3189.

[249] S. Bose et al. "Upper critical field in nanostructured Nb: Competing effects of the reduction in density of states and the mean free path". In: *Physical Review B* 74 (2006), p. 224502. DOI: 10.1103/PhysRevB.74.224502.

[250] R. H. Parmenter. "Size Effect in a Granular Superconductor". In: *Physical Review* 166 (1968), pp. 392–396. DOI: 10.1103/PhysRev.166.392.

[251] V. W. Brar et al. "Gate-controlled ionization and screening of cobalt adatoms on a graphene surface". In: *Nature Physics* 7 (2011), pp. 43–47. DOI: 10.1038/nphys1807.

[252] W. Shockley. "The Theory of *p-n* Junctions in Semiconductors and *p-n* Junction Transistors". In: *Bell System Technical Journal* 28 (1949), pp. 435–489. DOI: 10.1002/j.1538-7305.1949.tb03645.x.

[253] J. H. Scaff and R. S. Ohl. "Development of Silicon Crystal Rectifiers for Microwave Radar Receivers". In: *Bell System Technical Journal* 26 (1947), pp. 1–30. DOI: 10.1002/j.1538-7305.1947.tb01310.x.

[254] M. Davydova, S. Prembabu, and L. Fu. "Universal Josephson diode effect". In: *Science Advances* 8 (2022), eabo0309. DOI: 10.1126/sciadv.abo0309.

[255] R. Wakatsuki et al. "Nonreciprocal charge transport in noncentrosymmetric superconductors". In: *Science Advances* 3 (2017), e1602390. DOI: 10.1126/sciadv.1602390.

[256] E. Zhang et al. "Nonreciprocal superconducting NbSe2 antenna". In: *Nature Communications* 11 (2020), p. 5634. DOI: 10.1038/s41467-020-19459-5.

[257] F. Ando et al. "Observation of superconducting diode effect". In: *Nature* 584 (2020), pp. 373–376. DOI: 10.1038/s41586-020-2590-4.

[258] C. Baumgartner et al. "Supercurrent rectification and magnetochiral effects in symmetric Josephson junctions". In: *Nature Nanotechnology* 17 (2022), pp. 39–44. DOI: 10.1038/s41565-021-01009-9.

[259] B. Pal et al. "Josephson diode effect from Cooper pair momentum in a topological semimetal". In: *Nature Physics* 18 (2022), pp. 1228–1233. DOI: 10.1038/s41567-022-01699-5.

[260] I. Zapata et al. "Voltage Rectification by a SQUID Ratchet". In: *Physical Review Letters* 77 (1996), pp. 2292–2295. DOI: 10.1103/PhysRevLett.77.2292.

[261] I. Zapata et al. "Tunneling Center as a Source of Voltage Rectification in Josephson Junctions". In: *Physical Review Letters* 80 (1998), pp. 829–832. DOI: 10.1103/PhysRevLett.80.829.

[262] K. K. Likharev and A. B. Zorin. "Theory of the Bloch-wave oscillations in small Josephson junctions". In: *Journal of Low Temperature Physics* 59 (1985), pp. 347–382. DOI: 10.1007/BF00683782.

[263] H. Le Sueur and P. Joyez. "Room-temperature tunnel current amplifier and experimental setup for high resolution electronic spectroscopy in millikelvin scanning tunneling microscope experiments". In: *Review of Scientific Instruments* 77 (2006), p. 123701. DOI: 10.1063/1.2400024.

[264] V. Ambegaokar and A. Baratoff. "Tunneling Between Superconductors". In: *Physical Review Letters* 10 (1963), pp. 486–489. DOI: 10.1103/PhysRevLett.10.486.

[265] A. Barone, G. Paternò, and John Wiley & Sons, eds. *Physics and applications of the Josephson effect*. A Wiley-Interscience publication. New York: Wiley, 1982. DOI: 10.1002/352760278X.

[266] Y. M. Ivanchenko and L. Zil'berman. "The Josephson Effect in Small Tunnel Contacts". In: *Journal of Experimental and Theoretical Physics* (1969).

[267] P. Joyez. "Self-Consistent Dynamics of a Josephson Junction in the Presence of an Arbitrary Environment". In: *Physical Review Letters* 110 (2013), p. 217003. DOI: 10.1103/PhysRevLett.110.217003.

[268] A. M. van den Brink et al. "Coherent Cooper pair tunneling in systems of Josephson junctions: Effects of quasiparticle tunneling and of the electromagnetic environment". In: *Zeitschrift für Physik B Condensed Matter* 85 (1991), pp. 459–467. DOI: 10.1007/BF01307644.

[269] O. Peters et al. "Resonant Andreev reflections probed by photon-assisted tunnelling at the atomic scale". In: *Nature Physics* 16 (2020), pp. 1222–1226. DOI: 10.1038/s41567-020-0972-z.

[270] P. Kot et al. "Microwave-assisted tunneling and interference effects in superconducting junctions under fast driving signals". In: *Physical Review B* 101 (2020), p. 134507. DOI: 10.1103/PhysRevB.101.134507.

[271] J. Siebrecht et al. “Microwave excitation of atomic scale superconducting bound states”. In: *Nature Communications* 14 (2023), p. 6794. DOI: 10.1038/s41467-023-42454-5.

[272] P. M. R. Brydon et al. “Topological Yu-Shiba-Rusinov chain from spin-orbit coupling”. In: *Physical Review B* 91 (2015), p. 064505. DOI: 10.1103/PhysRevB.91.064505.

[273] T. E. Feuchtwang. “Tunneling theory without the transfer-Hamiltonian formalism. I.” In: *Physical Review B* 10 (1974). Number of pages: 0 Publisher: American Physical Society, pp. 4121–4134. DOI: 10.1103/PhysRevB.10.4121.

[274] P. Berggren and J. Fransson. “Spin inelastic electron tunneling spectroscopy on local magnetic moment embedded in Josephson junction”. In: *EPL (Europhysics Letters)* 108 (2014), p. 67009. DOI: 10.1209/0295-5075/108/67009.

[275] R. Žitko, R. Peters, and T. Pruschke. “Properties of anisotropic magnetic impurities on surfaces”. In: *Physical Review B* 78 (2008), p. 224404. DOI: 10.1103/PhysRevB.78.224404.

[276] L. Farinacci et al. “Tuning the Coupling of an Individual Magnetic Impurity to a Superconductor: Quantum Phase Transition and Transport”. In: *Physical Review Letters* 121 (2018), p. 196803. DOI: 10.1103/PhysRevLett.121.196803.

[277] N. Y. Yao et al. “Phase diagram and excitations of a Shiba molecule”. In: *Physical Review B* 90 (2014), p. 241108. DOI: 10.1103/PhysRevB.90.241108.

[278] P. Fulde. “High field superconductivity in thin films”. In: *Advances in Physics* 22 (1973), pp. 667–719. DOI: 10.1080/00018737300101369.

[279] P. G. De Gennes and M. Tinkham. “Magnetic behavior of very small superconducting particles”. In: *Physics Physique Fizika* 1 (1964), pp. 107–126. DOI: 10.1103/PhysicsPhysiqueFizika.1.107.

[280] A. J. Leggett. “Quantum tunneling in the presence of an arbitrary linear dissipation mechanism”. In: *Physical Review B* 30 (1984), pp. 1208–1218. DOI: 10.1103/PhysRevB.30.1208.

[281] F. London. *Superfluids*. Dover ed. OCLC: 499130771. New York: Dover Publications, 1961.

[282] J. Bardeen and W. H. Brattain. “The Transistor, A Semi-Conductor Triode”. In: *Physical Review* 74 (1948), pp. 230–231. DOI: 10.1103/PhysRev.74.230.

List of publications and contributions to conferences

Publications

Includede in this thesis

- **Jon Ortuzar**, Stefano Trivini, Miguel Alvarado, Mikel Rouco, Javier Zaldivar, Alfredo Levy Yeyati, José Ignacio Pascual, and F. Sebastian Bergeret. "Yu-Shiba-Rusinov states in two-dimensional superconductors with arbitrary Fermi contours." *Phys. Rev. B*, 105(24), 245403 (2022). doi: *10.1103/PhysRevB.105.245403*

- Stefano Trivini, **Jon Ortuzar**, Katerina Vaxevani, Jingchen Li, F. Sebastian Bergeret, Miguel A. Cazalilla, and Jose Ignacio Pascual. "Cooper pair excitation mediated by a molecular quantum spin on a superconducting proximitized gold film." *Phys. Rev. Lett.*, 130(13), 136004 (2023). *10.1103/PhysRevLett.130.136004*

- **Jon Ortuzar**, Jose Ignacio Pascual, F. Sebastian Bergeret, and Miguel A. Cazalilla. "Theory of a single magnetic impurity on a thin metal film in proximity to a superconductor." *Phys. Rev. B*, 108(2), 024511 (2023). doi: *10.1103/PhysRevB.108.024511*

- Stefano Trivini, **Jon Ortuzar**, Javier Zaldivar, Edwin Herrera, Isabel Guillamón, Hermann Suderow, F. Sebastian Bergeret, Jose Ignacio Pascual. "Diluted Yu-Shiba-Rusinov arrays on the β-Bi_2Pdanisotropic superconductor." *Phys. Rev. B*, 110(23), 235405 (2024). doi: *10.1103/PhysRevB.110.235405*

Further publications

- Katerina Vaxevani, Jingcheng Li, Stefano Trivini, **Jon Ortuzar**, Danilo Longo, Dongfei Wang, and Jose Ignacio Pascual. "Extending the spin excitation lifetime of a magnetic molecule on a proximitized superconductor." *Nano Letters*, 22(15), 6075-6082 (2022). doi: *10.1021/acs.nanolett.2c00924*

- Anastasiia Skurativska, **Jon Ortuzar**, Dario Bercioux, F. Sebastian Bergeret, and Miguel A. Cazalilla. "Robust spin polarization of Yu-Shiba-Rusinov states in superconductor/ferromagnetic insulator heterostructures." *Phys. Rev. B*, 107(22), 224507 (2023). doi: *10.1103/PhysRevB.107.224507*

- Andrea Aguirre, Andrés Pinar Solé, Diego Soler Polo, Carmen González-Orellana, Amitayush Thakur, **Jon Ortuzar**, Oleksandr Stesovych, Manish Kumar, Marina Peña-Díaz, Andrew Weber, Massimo Tallarida, Ji Dai, Jan Dreiser, Matthias Muntwiler, Celia Rogero, José Ignacio Pascual, Pavel Jelínek, Maxim Ilyn, and Martina Corso. "Ferromagnetic Order in 2D Layers of Transition Metal Dichlorides." *Adv. Mat.*, 2402723 (2024). doi: *10.1002/adma.202402723*

Works in Progress

- Javier Zaldívar, **Jon Ortuzar**, Miguel Alvarado, Stefano Trivini, Julie Baumard, Carmen Rubio-Verdú, Edwin Herrera, Hermann Suderow, Alfredo Levy Yeyati, F. Sebastian Bergeret, and Jose Ignacio Pascual. "Revealing inter-band electron pairing in a superconductor with spin-orbit coupling."

- **Jon Ortuzar**, Stefano Trivini, Katerina Vaxevani, Beatriz Viñas, F. Sebastian Bergeret, and Jose Ignacio Pascual. "Coulomb effects in the superconducting gap of small Pb islands."

- Jon Ortuzar, Stefano Trivini, Katerina Vaxevani, Beatriz Viñas, F. Sebastian Bergeret, and Jose Ignacio Pascual. "A reversible Cooper pair diode."

- Chen-How Huang, **Jon Ortuzar**, Jose Ignacio Pascual, F. Sebastian Bergeret, and Miguel A. Cazalilla. "Singlet Quantum Qubit in Quantum Dots on Coupled Superconducting Bath."

Contribution to conferences

Invited talks

- **Opportunities from local noise spectroscopy**. Lorentz Center, Leiden, 20-24 November (2023). "Theory of Magnetic impurities on proximitized metals"

Oral contributions

- **Fuerzas y Túnel 2023**. Fundación Rei Afonso Henriques, Zamora, 03-06 July (2023). "Pair Excitation of a Quantum Spin on a Proximitized Gold Surface."

- **DPG-SKM Spring Meeting of the Condensed Matter Section**. Technische Universitat, Berlin, 17-22 March (2024). "Theory of Magnetic impurities on proximitized metals."

- **XXXIX Reunión Bienal de la Real Sociedad Española de Física**. UPV/EHU, Donostia/San Sebastián, 15-19 Jun (2024). "Josephson Effect in the Coulomb blockade regime: A Tunable Superconducting Diode."

Poster Contributions

- **Novel Quantum Phases in Superconducting Heterostructures**. Physikzentrum Bad Honnef, 30 May - 02 Jun (2022). "Yu-Shiba-Rusinovstates in 2D superconductors with arbitrary Fermi contours"
- **QUANTUM 2021**. UPV/EHU, Bilbo, 23-25 November (2022). "Yu-Shiba-Rusinovstates in 2D superconductors with arbitrary Fermi contours"
- **II International conference on Novel 2D Materials Explored Via Scanning Probe Microscopy & Spectroscopy (2D-SPM)**. UPV/EHU, Donostia/San Sebastián, 20-24 Jun (2022). "Transition metal dihalide magnetic island on the $NbSe_2$ superconducting surface."
- **DPG-DKM Meeting 2022**. Deutsche Physikalische Gesellschaft, Regensburg, 04-09 September (2022). "Magnetic molecule as a parity sensor in entangled spin and YSR excitation on a superconductor."
- **XII Reunión de la División de Física de la Materia Condensada de la RSEF (GEFES2023)**. Salamanca, 01-03 February (2023). " Magnetic molecule as a parity sensor in entangled spin and YSR excitation on a superconductor."
- **The Third Spins on Surfaces Workshop (SoS III)**. UPV/EHU, Donostia/San Sebastián, 11-15 September (2023). "Theory of a Single Magnetic Impurity on a Thin Metal Film in Proximity to a Superconductor."
- **III International Conference on Novel 2D Materials Explored Via Scanning Probe Microscopy & Spectroscopy (2DSPM2024)**. UPV/EHU, Donostia/San Sebastián, 24-28 Jun (2024). "Control of the Superconducting Diode Effect on Pb Islands Mediated by the Coulomb Blockade."

7.0.1 Doctoral Trainings

- **Doctoral Training: Frontiers of Condensed Matter**. École de Physique, Des Houches, 10-21 November (2023).